# NANOBIOENGINEERING STRATEGIES FOR BONE REPAIR: OSTEOBLAST-DERIVED EXTRACELLULAR VESICLES AND THEIR MIMETICS

By

MATHIEU YVES BRUNET

A thesis submitted to
the University of Birmingham
for the degree of
DOCTOR OF PHILOSOPHY

Healthcare Technologies Institute
School of Chemical Engineering
College of Engineering and Physical Sciences
University of Birmingham
April 2024

# Declaration

This thesis describes research which took place at the Healthcare Technologies Institute of the School of Chemical Engineering of the University of Birmingham (UK). I declare that this thesis has been composed solely by myself and that it has not been submitted, in whole or in part, in any previous application for another degree at any other academic institution. This body of work is entirely my own unless otherwise stated with any external support found documented, referenced and acknowledged.

Mathieu Yves Brunet

*Je dédie cette thèse à Nanoue.*

# Abstract

**Introduction:** Nanobioengineering strategies combine recent advances in nanotechnologies with bioengineering methods to accelerate the development of nanotherapeutics. In the last decade, extracellular vesicles (EVs) have been intensively researched as an innovative acellular approach to overcome the current limitations of cell-based therapeutic solutions. For bone repair, EVs derived from osteoblasts have exhibited a strong osteogenic potency highlighting their potential as the next generation of bone regenerative therapy. Nevertheless, the clinical translation of EVs remains hindered by several barriers including scale-up and purity.

**Aims:** The aim of this project was to advance the development of nanotherapeutics for bone repair by harnessing the potential of osteoblast-derived EVs. Comprehensively characterised, the osteoinductive capacity of mineralising-osteoblast-derived EVs (MO-EVs) was evaluated to determine their therapeutic relevance with the development of an innovative functional assay. Based on these results, synthetic MO-EVs were then developed and produced as bioinspired mimetics overcoming translational hurdles. Finally, the formulation of a hydrogel 3D system was investigated to develop a new delivery strategy for EVs suited to bone repair applications.

**Methods:** MO-EVs were separated using differential ultracentrifugation after comparing isolation methods. MO-EVs were fully characterised to determine their physico-chemical properties, the validation of the presence of EV biomarkers as well as their storage conditions. The composition of MO-EVs was also determined with a particular focus on protein content *via* a proteomic analysis and on mineral content. The effects of MO-EVs on osteoblast migration and proliferation were assessed as well as their osteogenic potency on osteoblast cultures. To that end, an innovative biomineralisation *in vitro* assessment method was also developed harnessing the potential of μ-X-ray fluorescence spectroscopy. Using both top-down and bottom-up approaches, synthetic MO-EVs were formulated, and both were compared to the biological activity of MO-EVs. Cell-derived nanovesicles were generated from mineralising osteoblasts (MO-NVs) *via* serial extrusion, whereas proteoliposomes were formulated using the thin-film hydration method. An injectable alginate/collagen hydrogel system was developed harnessing the potential of competitive ligand exchange cross-linking gelation.

**Results:** MO-EVs were successfully isolated *via* ultracentrifugation and their extensive characterisation revealed the presence of key proteins such as annexins as well as minerals which can be mechanistically linked to their pro-osteogenic potency which was demonstrated *in vitro* on osteoblasts. Moreover, MO-EVs were found to modulate mineral production in a time- and dose- dependent manner as demonstrated by μ-XRF. Both synthetic EVs were successfully formulated presenting with MO-EVs features and the incorporation of both alkaline phosphatase (ALP) and annexin VI was validated. Nevertheless, neither of these synthetic EVs matched the activity of the MO-EVs. Finally, alginate-collagen composite hydrogels were successfully produced, and the MO-EV release kinetics was found dependent on the collagen concentration.

**Conclusion:** In this thesis, novel insights were provided supporting the therapeutic use of MO-EVs for bone repair. Through the use of bioengineering strategies, the foundations of the development of synthetic MO-EVs were laid. Associated with the successful development of an injectable hydrogel delivery system for these nanovesicles, the work presented has supported the development of MO-EV based therapies for bone repair.

**Keywords:** Extracellular Vesicles, Osteoblast, Bone Repair, Synthetic EVs, Hydrogel

# Acknowledgements

First, I would like to thank my supervisors Dr Sophie C. Cox and Dr Marie-Christine Jones to have welcomed me to join this PhD program four years ago and for their guidance and support ever since. This was definitely a life-changing journey from which I leave as a wiser person and a better scientist.

I am also very grateful to the School of Chemical Engineering of the University of Birmingham for awarding me a fully funded PhD Scholarship as well as the Engineering and Physical Sciences Research Council (EPSRC) for the research financial support.

Very special thanks to Dr Kenny Man to whom I have had the privilege to work closely with along this PhD. Thank you for having managed to become a supervisor, a mentor, and a friend, you made this journey possible!

I would also like to thank Dr David Bassett, Dr Luke Carter, Dr Paula Mendes, and Dr Guillaume Desanti for their technical support and mentoring over the years. I would like to acknowledge the valuable support received by the University of Birmingham’s wider community with, in particular, members of staff from the School of Chemical Engineering, the Queen Elisabeth Hospital, the Library and the Graduate School. Particular mentions must be given to Emma Lardner, Carissa Pausanos and Lynn Draper for their patience and continuous support.

I would like to thank all the colleagues and friends at the Healthcare Technologies Institute, past and present. To the proud members of office 03, Dr Lucy Arkinstall, Dr Thomas Robinson and Dr Victor Villapun, thank you for your support during the stressing periods of research and for our journeys to Staff House.

Special thanks to Miruna Chipara, Anna Johnston, Lucrezia Righelli, Cinzia Amieni, Aleksandar Atanasov, Adam Efrat and all the others not mentioned who have been formidable PhD companions and friends.

To my Aberdonian’s friends, Dr Laura Blaikie, Dr Teodora Stoyanova and Dr Maria Kopsida, thank you for your friendship during all these years. To Dr Marie Goua, thank you for having introduced me to research eight years ago and for your mentoring ever since!

To my friend and brother, David Barataud, your continuous support, loyalty and faith in my abilities has been one of the most valuable contributions to this adventure. I am forever grateful to you and to your fiancée Angelika Janaszkiewicz for your love and support even from across the globe.

Finally, and most importantly, I would like to thank my parents and grandparents for supporting me and believing in me despite the distance over this last decade.

## Research Outputs

---

### Publications in preparation or under-review:

- **Brunet, M.Y.**, McGuinness, A., Man, K., Jones, M.C. & Cox, S.C. (2024). Harnessing µ-X-Ray Fluorescence Spectroscopy as a Tool to Assess Extracellular Vesicle Induced Biomineralisation. *Currently under review.*

- **Brunet, M.Y.**, Man, K., Jones, M.C. & Cox, S.C. (2024). Biofabricated Osteoblast-derived Nanovesicles as Extracellular Vesicle Mimetics for Bone Repair. *In Preparation*

- **Brunet, M.Y.** & Man, K. (2024). Extracellular Vesicles and their Mimetics: Advances in Orthopaedic Nanomedicine. Book chapter part of 'Bone and Cartilage Engineering: From Modern Technology to Future Perspective' by World Scientific. *Currently under review.*

### Peer Reviewed Publications:

#### 2024

- Sanches, B. D. A., Teófilo, F. B. S., **Brunet, M. Y.**, Villapun, V. M., Man, K., Rocha, L. C., Neto, J. P., Matsumoto, M. R., Maldarine, J. S., Ciena, A. P., Cox, S. C., & Carvalho, H. F. (2024). Telocytes: current methods of research, challenges and future perspectives. Cell and tissue research, 10.1007/s00441-024-03888-5. Advance online publication. https://doi.org/10.1007/s00441-024-03888-5

#### 2023

- Robinson, T.E., **Brunet, M.Y.**, Chapple, I., Heagerty, A.H.M., Metcalfe, A.D. and Grover, L.M. (2023), Self-Delivering Microstructured Iota Carrageenan Spray Inhibits Fibrosis at Multiple Length Scales. Adv. NanoBiomed Res., 3: 2300048. https://doi.org/10.1002/anbr.202300048

- Man, K., **Brunet, M.Y.**, Lees, R., Peacock, B., & Cox, S. C. (2023). Epigenetic Reprogramming via Synergistic Hypomethylation and Hypoxia Enhances the Therapeutic Efficacy of Mesenchymal Stem Cell Extracellular Vesicles for Bone Repair. International journal of molecular sciences, 24(8), 7564. https://doi.org/10.3390/ijms24087564

**2022**

- Man, K., Joukhdar, H., Manz, X. D., **Brunet, M.Y.**, Jiang, L. H., Rnjak-Kovacina, J., & Yang, X. B. (2022). Bone tissue engineering using 3D silk scaffolds and human dental pulp stromal cells epigenetic reprogrammed with the selective histone deacetylase inhibitor MI192. Cell and tissue research, 388(3), 565–581. https://doi.org/10.1007/s00441-022-03613-0

- Luo, L., Foster, N. C., Man, K. L., **Brunet, M.Y.**, Hoey, D. A., Cox, S. C., Kimber, S. J., & El Haj, A. J. (2022). Hydrostatic pressure promotes chondrogenic differentiation and microvesicle release from human embryonic and bone marrow stem cells. Biotechnology journal, 17(4), e2100401. https://doi.org/10.1002/biot.202100401

- Man, K., **Brunet, M.Y.**, Federici, A. S., Hoey, D. A., & Cox, S. C. (2022). An ECM-Mimetic Hydrogel to Promote the Therapeutic Efficacy of Osteoblast-Derived Extracellular Vesicles for Bone Regeneration. Frontiers in bioengineering and biotechnology, 10, 829969. https://doi.org/10.3389/fbioe.2022.829969

- Man, K., Barroso, I. A., **Brunet, M.Y.**, Peacock, B., Federici, A. S., Hoey, D. A., & Cox, S. C. (2022). Controlled Release of Epigenetically-Enhanced Extracellular Vesicles from a GelMA/Nanoclay Composite Hydrogel to Promote Bone Repair. International journal of molecular sciences, 23(2), 832. https://doi.org/10.3390/ijms23020832

**2021**

- Man, K., **Brunet, M.Y.,** Louth, S., Robinson, T. E., Fernandez-Rhodes, M., Williams, S., Federici, A. S., Davies, O. G., Hoey, D. A., & Cox, S. C. (2021). Development of a Bone-Mimetic 3D Printed Ti6Al4V Scaffold to Enhance Osteoblast-Derived Extracellular Vesicles' Therapeutic Efficacy for Bone Regeneration. Frontiers in bioengineering and biotechnology, 9, 757220. https://doi.org/10.3389/fbioe.2021.757220

- Man, K., **Brunet, M.Y.**, Fernandez-Rhodes, M., Williams, S., Heaney, L. M., Gethings, L. A., Federici, A., Davies, O. G., Hoey, D., & Cox, S. C. (2021). Epigenetic reprogramming enhances the therapeutic efficacy of osteoblast-derived extracellular vesicles to promote human bone marrow stem cell osteogenic differentiation. Journal of extracellular vesicles, 10(9), e12118. https://doi.org/10.1002/jev2.12118

**2020**

- Man, K., **Brunet, M.Y.**, Jones, M. C., & Cox, S. C. (2020). Engineered Extracellular Vesicles: Tailored-Made Nanomaterials for Medical Applications. Nanomaterials (Basel, Switzerland), 10(9), 1838. https://doi.org/10.3390/nano10091838

- Hall, T.J., Villapún, V.M., Addison, O., Webber, M.A., Lowther, M., Louth, S.E.T., Mountcastle, S.E., **Brunet, M.Y.** & Cox, S.C. (2020). A call for action to the biomaterial community to tackle antimicrobial resistance. Biomaterials Science, vol. 8, no. 18, pp. 4951-4974. https://doi.org/10.1039/D0BM01160F

## Conferences and Seminars

---

- **Poster presentation** at NanoMed Europe 23 co-organised by the Nanomedicine European Technology Platform (ETPN) and hosted by the University of Liverpool, UK – June 2023.

- **Interview Seminar** at New York University, Tandon School of Engineering, Bioengineering Institute (held online) – May 2023.

- **Oral presentation** at the Tissue Engineering and Regenerative Medicine International Society (TERMIS) European Chapter Conference 2022 in Krakow, Poland – June 2022.

- **Oral presentation** at the Healthcare Technologies Institute (HTI) Winter Symposium, University of Birmingham, UK – November 2022.

- **Poster presentation** at the Tissue and Cell Engineering Society and EPSRC Doctoral Training Centre's Conference 2022 in Birmingham, UK – June 2022.

- **Oral presentation** at the Tissue Engineering and Regenerative Medicine International Society (TERMIS) 6th World Congress in Maastricht, The Netherlands (held online) – November 2021.

- **Oral presentation** at the TRAIN-EV International Conference (held online during pandemic) – June 2021.

- **Oral presentation** at the Student Network for Extracellular Vesicles (SNEV) International Conference (held online during pandemic) – June 2021.

# List of Figures

---

# List of Abbreviations

**Abbreviation - Description**

| | |
|---|---|
| ANK | Ankylosis Protein |
| ACSs | Adipose-derived Stem Cells |
| ALP | Alkaline Phosphatase |
| ARS | Alizarin Red Staining |
| ATCC | America Type Culture Collection |
| BCA | Bicinchoninic Acid |
| BMU | Basic Multicellular Units |
| BRC | Bone Remodelling Cycle |
| BTCP | β-Tricalcium Phosphate |
| Ca-EDTA | Ca-Ethylenediaminetetraacetic Acid |
| CCM | Conditioned Culture Media |
| CDNs | Cell-derived Nanovesicles |
| CLEX | Competitive Ligand Exchange of Crosslinking Ions |
| Ca Pyro | Calcium Pyrophosphate |
| DLS | Dynamic Light Scattering |
| DPPC | Dipalmitoyl phosphatidylcholine |
| DPPS | 1,2-dipalmitoyl-sn-glycero-3-phospho-L-serine |
| ECM | Extracellular Matrix |
| EDTA | Ethylenediaminetetra-acetic acid |
| EDX | Energy Dispersive X-ray Spectroscopy |
| ELISA | Enzyme-Linked Immuno Sorbent Assay |
| ESI | Electrospray Ionisation |
| EVs | Extracellular Vesicles |
| FFF | Flow Field-flow Fractionation |
| GMP | Good Manufacturing Practice |
| GN | Gene Name |

| | |
|---|---|
| GO | Gene Ontology |
| HA | Hydroxyapatite |
| hBMSCs | Human Bone Marrow Stem Cells |
| HEK | Human Embryonic Kidney |
| HEPES | (2-hydroxyethyl)-1-piperazineethanesulfonic acid |
| I-MAG | Immune-magnetic Positive Selection |
| LC-MS | Liquid Chromatography–Mass Spectrometry |
| MCPM | Monocalcium Phosphate Monohydrate |
| MEM-α | Minimum Essential Medium Alpha |
| miRNA | MicroRNA |
| MO-EVs | Mineralising Osteoblast-derived Extracellular Vesicles |
| MO-NVs | Mineralising Osteoblast-derived Nanovesicles |
| MSCs | Mesenchymal Stem Cells |
| MVs | Matrix Vesicles |
| Na Poly | Sodium Polyphosphate |
| NK | Natural Killer |
| NPP1 | Nucleotide Pyrophosphatase Type 1 |
| NTA | Nanoparticle Tracking Analysis |
| OA | Osteoarthritis |
| OB-EVs | Osteoblast-derived EVs |
| OX | Organism Identifier |
| PA | Phosphatidic Acid |
| PBS | Phosphate Buffered Saline |
| PCA | Principal Component Analysis |
| PE | Protein Existence |
| PEG | Polyethylene Glycol |
| PLA | Poly Lactic Acid |
| PPI | Protein-protein Interaction |
| PRS | Picro Sirius Red Staining |

| | |
|---|---|
| PS | Phosphatidyl Serine |
| RANKL | Receptor Activator of the nuclear factor Kappa-B Ligand |
| rhBMP-2 | Recombinant Human BMP-2 |
| RP | Reversed Phase |
| Rt | Retention time |
| RT | Room Temperature |
| SEC | Size-exclusion Chromatography |
| SEM | Scanning Electron Microscopy |
| sEVs | Small EVs |
| SP-IRIS | Single-particle Interferometric Reflectance Imaging Sensor |
| SV | Sequence Version |
| TEMs | Tetraspanin-enriched Microdomains |
| TEM | Transmission Electron Microscopy |
| TERMIS | Tissue Engineering and Regenerative Medicine International Society |
| TNAP | Tissue Non-specific Alkaline Phosphatase |
| UC | Ultracentrifugation |
| XRD | X-ray Diffraction |
| XRF | X-ray Fluorescence |

## Table of Content

# Chapter I

-

# Introduction

## 1.1. Bone

### 1.1.1. Bone tissue physiology

Bone is a complex tissue supporting a variety of functions for the human body including structural support, organ protection, minerals and growth factors reservoirs, and the marrow provides an environment for blood cells production (Clarke, 2008). This tissue multifunctionality is supported by a unique structure composed of a dense cortical outer layer maintaining mechanical strength and an inner more porous layer called the trabecular which is more metabolically active. The physiology of this mineralised tissue is regulated by three major cellular components being osteoblasts, osteoclasts, and osteocytes (Schlesinger *et al.*, 2020). Far from being an inert tissue, bone is continuously remodelled due to the action of osteoblasts and osteoclasts, respectively responsible for bone formation and bone resorption (Kenkre and Bassett, 2018). The balance between these two activities is critical to maintain bone homeostasis and it is also necessary for fracture healing and skeleton structural adjustment that can be observed through life (Florencio-Silva *et al.*, 2015).

Among bone cells, osteocytes represent more than 90% of the total cellular population and can have a 25 year lifespan (Franz-Odendaal *et al.*, 2005). Located in the bone matrix, they are not directly involved in bone remodelling, however, they play key roles as inducers of osteoclast activation, they are source of factors regulating mineral metabolism and act as mechanosensory cells (Bonewald, 2011). On the other hand, osteoblasts and osteoclasts actively participate to the bone remodelling process allowing up to 10% of the human skeleton to be replaced each year (Walsh *et al.*, 2015). Derived from mesenchymal lineage, osteoblasts only represent 5% of the bone cell population and are cuboidal in shape. The main function of osteoblasts is the production of the organic components forming the bone matrix which is why this cell type is equipped with abundant rough endoplasmic reticulum and Golgi apparatus for effective protein synthesis (Capulli *et al.*, 2014). In opposition to osteoblasts, osteoclasts are multinucleated cells which have differentiated from the hematopoietic stem cell lineage (Crockett *et al.*, 2010). Forming bonds with the matrix via adhesion proteins, osteoclasts resorb the bone by acidification which solubilises minerals and they also secrete enzymes to dissolve the matrix (Henriksen *et al.*, 2009).

Other key components of the bone include the bone matrix composed of an organic and an inorganic phase. The most abundant organic constituent are collagen fibres offering support and structure for the cellular machinery with collagen type I accounting for 90% of total collagen (Sartori *et al.*, 2015). Non-collagenous proteins are also present with notably proteoglycans, γ-carboxyglutamic acid-containing proteins and glycoproteins which participate to the regulation of bone metabolism. For example, osteonectin is a regulator of calcium release via its binding to collagen fibres whereas sialoprotein is involved with osteoblast differentiation and mineralisation initiation (Lin *et al.*, 2020). Regarding the inorganic phase of the bone matrix, it is essentially composed of hydroxyapatite (HA, $Ca_{10}(PO_4)_6(OH)_2$) which is created by the nucleation of phosphate and calcium ions. The deposition of these crystals is supported by the organic phase with structural proteins such as collagens acting like a scaffold (Datta *et al.*, 2008). Combined, these two matrix phases provide a robust framework offering the required mechanical strength to the bones.

Both osteoblasts and osteoclasts cooperate during bone remodelling to maintain homeostasis. Bone remodelling is a highly regulated cycle which was firstly described by

Eriksen (Eriksen, 1986) (Figure 1.1.). Even if the initiation event remains unclear, calcium ions level and growth factors release by osteocytes are two major factors linked to the start of the cycle. Moreover, cytokines, and particularly the receptor activator of the nuclear factor kappa-B ligand (RANKL) expressed with osteoblasts can bind to RANK receptors of osteoclasts to activate them and accelerate their maturity (Tu *et al.*, 2018). The cooperation of osteoblasts and osteoclasts is key in the remodelling process, and it begins with the creation of basic multicellular units (BMU). These groups of cells facilitate bone remodelling by forming temporarily a cylindrical structure permitting a better efficiency (Jilka, 2003). The bone remodelling sequence can be divided into 3 phases which are resorption, reversal, and formation. The resorption phases start with the accumulation of osteoclasts on site due to a stimulus with for example the induction of mechanical stress or osteocyte signalling. The osteoclasts attach to the bone surface and acidify the local environment with hydrochloric acid and cathepsin K protein. After degradation of the bone matrix, the osteoclasts detach, and macrophages cleans the area while mesenchymal stem cells are recruited on site leading to the end of the reversal phase. During the formation phase, osteoblasts progenitors differentiate, and osteoblasts starts the formation of a new matrix subsequently enriched in hydroxyapatite crystals forming a fully-restored bone tissue (Delaisse *et al.*, 2020).

With aging, this process can become less efficient leading to an unbalanced bone remodelling with for example an excessive bone resorption. Moreover, serious clinical situations such as trauma, tumours or congenital diseases can lead to greater damages to the bone and challenge its regenerative capacities.

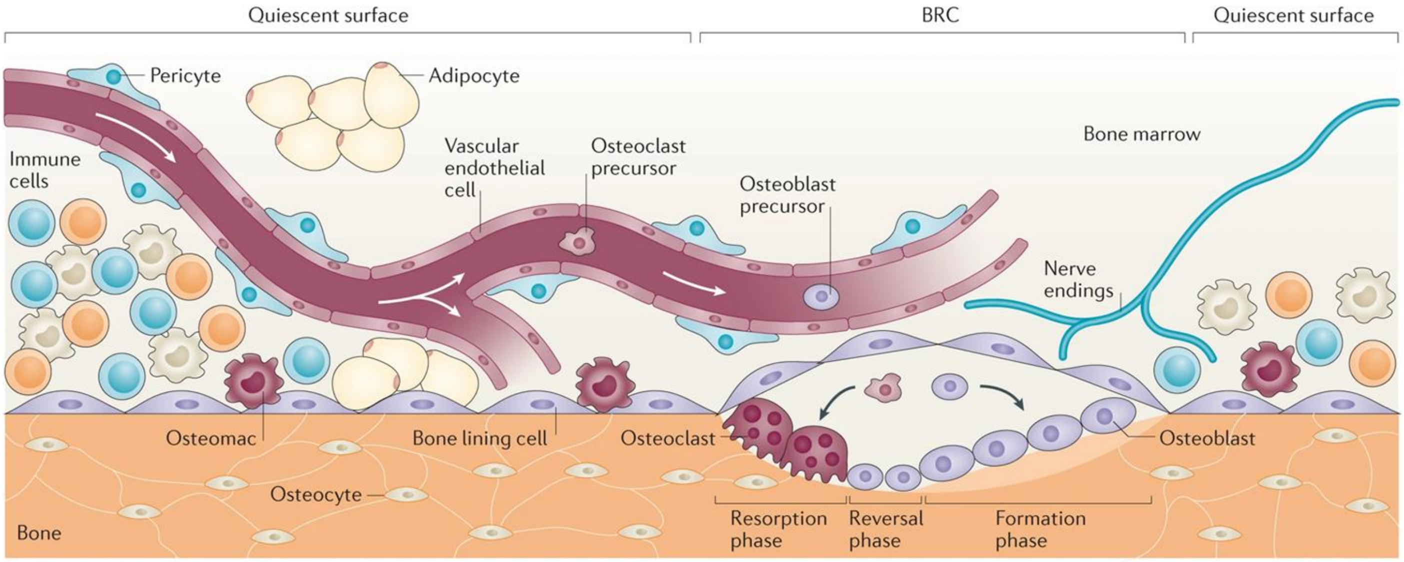

**Figure 1.1. |Schematic representation of bone physiology during the remodelling cycle (BRC).** Bone physiology is represented as a timeline from left to right with BRC following the quiescent surface stage including bone, nerve, vascular and immune cells. Adapted from Croucher *et al.* (2016).

### 1.1.2. Clinical context

Due to an ever-increasing ageing population, the risk of bone damage has increased substantially with a current estimate of 1.71 billion people living with a musculoskeletal condition as analysed by the Global Burden of Disease 2019 (Cieza *et al.*, 2021). Disorders such as osteoporosis frequently lead to fractures resulting in a significant healthcare and socio-economic burden. Osteoporotic fractures alone are estimated to occur every 3 seconds in the world (Johnell and Kanis, 2006). Furthermore, the gold standard treatments for bone repair, autologous/allogenous bone grafting, often suffer from donor site morbidity, risk of infection and limited availability (Sohn and Oh, 2019). On the other hand, total joint replacements carry the risk of aseptic loosening and implant corrosion, which can limit its lifespan. This may require multiple surgeries, especially when offered to young patients (Levent *et al.*, 2021). Therefore, the effective treatment of damaged bone tissues remains a major clinical challenge in orthopaedic field and requires the development of novel therapeutic approaches.

Due to the issues with current clinical treatment, there has been extensive investigations into the use of cell-based tissue engineering approaches to repair damaged bone (Re *et al.*, 2023; Kalamegam *et al.*, 2018). Cell-based strategies harnessing mesenchymal stem/stromal cells (MSCs) have shown promise due to their multipotent capacity, which is particularly suited to musculoskeletal regeneration as their lineage differentiation includes osteoblasts and chondrocytes which are key factors of their respective tissue. A wide range of encouraging pre-clinical and clinical studies involving MSCs demonstrated their therapeutic potential for skeletal diseases as showed by Kangari *et al.*, 2020 (Kangari *et al.*, 2020).

Nevertheless, the translation of cell-therapies remains hindered due to regulatory hurdles, cost of manufacture, ethical issues, safety (tumour formation), efficacy and immunogenicity (Riester *et al.*, 2021; Makarczyk, 2023). Moreover, with the poor survival rate of single cell suspension after injection and despite the advances of cell delivery strategies with scaffold-based approaches to generate tissue analogues, there is still numerous barriers to overcome before the development of a viable therapy (Kangari *et al.*, 2020). Despite the problems associated with direct MSC-based treatment, it was observed that MSC-secreted factors alone present in their CCM possessed an inherent potency showcasing regenerative properties. Following, these paracrine effects, innovative strategies employing cells' secretome have been investigated (Vizoso *et al.*, 2017).

### 1.1.3. The emergence of EVs as an acellular therapy

In recent years, there has been growing evidence demonstrating the influence of the cell's secretome in mediating key cellular functions (Karimian *et al.*, 2023; Buzas, 2023; De Jong *et al.*, 2014). Of these factors, cell-derived lipid nanoparticles called extracellular vesicles (EVs) have shown their role in several biological processes. EVs are defined as nanosized lipid-based particles which contain a diverse cargo of proteins, metabolites, and nucleic acids (Raposo *et al.*, 2013). These vesicles are typically classified into three types defined by their size, biogenesis, and composition. Exosomes (30 - 150 nm) are created via the endosomal route and are secreted from the plasma membrane when multivesicular bodies fuse. Microvesicles (50 - 1000 nm) are formed from the outward blebbing of the plasma membrane. Finally, apoptotic bodies (500 - 2000 nm) are produced from the plasma membrane when cell undergo programmed cell death. These three subtypes of nanovesicles have been regrouped under the term EVs as the current isolation/characterisation methods do not discriminate with precision the different EV subtypes (Veziroglu and Mias, 2020). EVs can be isolated from both conditioned cell culture media or from biological samples such as biofluids or liquid biopsy. Based on the downstream analysis required, several methods of EV isolation can be employed with the most commonly used being ultracentrifugation (differential or density gradient), size-exclusion based methods (size exclusion chromatography, flow field fractionation), immunoaffinity (immunocapture, ELISA), precipitation methods or microfluidic (Doyle et *al.*, 2019). Although not always specific, certain biomarkers are found to be enriched in EVs. Therefore, the detection of surface markers such as tetraspanins (*i.e.* CD9, CD63 or CD81) integrins or major histocompatibility complex molecules is commonly used to validate the successful EV-isolation procedure. Since 2011, the work conducted by the International Society for EVs resulted in the publication of the 'Minimal Information for Studies of

Extracellular Vesicles' guidelines providing a first step toward the standardisation of EV methodologies (Thery *et al*., 2018). In an effort to standardize terminology and experimental practices, the expert research community provides with an updated comprehensive discussion of current approaches which can be found as MISEV2023 (Welsh *et al.*, 2024).

Generally, EVs are involved in key physiological processes such as the maintenance of homeostasis and the regulation of cellular functions (Koniusz *et al.*, 2016). Several studies have reported the importance of these EV-associated bioactive factors in intercellular communication to regulate biological behaviour (Pitt *et al.*, 2016; Sánchez *et al.* 2021). The tremendous advances in the EV field in recent years, emphasise their potential influence on future healthcare technologies (Wiklander *et al.*, 2019). Therefore, the use of these cell-derived nanoparticles has attracted interest as potential therapies for regenerative orthopaedics (Li *et al*., 2022; Herrmann *et al.*, 2020; Murphy *et al.*, 2018). Employing these nanovesicles as an acellular therapy present numerous advantages such as a lower immunogenicity, a longer shelf life and storage capacity compared to cell-based therapies (Ong and Wu, 2015; Turturici et *al.*, 2014). With the promising results of MSC-based therapies, an interesting angle taken by Zavatti *et al.* has been the direct comparison of the therapeutic potency of stem cells, here human amniotic fluid stem cells, to their secreted EVs alone. In an monoiodoacetate-induced rat model of osteoarthritis (OA), they showed that EVs performed better in terms of both pain tolerance and histological score compared to the defect sites treated with amniotic fluid stem cells. Describing the defect sites as a complete restoration of cartilage after 3 weeks, these results demonstrate the potential of acellular EV-based therapies with the additional advantage of not requiring a cell injection lowering immunogenicity and ethical concerns (Zavatti *et al.*, 2020). Moreover, produced by most cells, these cell-derived nanoparticles do not demonstrate an intrinsic cytotoxicity neither the which can be found post cell transfer (Thirabanjasak *et al.*, 2010). Compared to synthetic nanoparticles which have been intensively investigated mainly as drug delivery systems, EVs present with a more complex molecular diversity which reinforce their homing ability to the target tissue especially at the membrane level (Kooijmans *et al.*, 2016). They also have been successfully repurposed as a drug delivery system mainly using electroporation-based approaches to load therapeutic compounds or nucleic acids (Du *et al.*, 2023).

In regenerative medicine, EVs have received attention as these nanoparticles showed great regenerative potential across multiple tissue types via the regulation of angiogenesis, cell proliferation or immunomodulation (Jong *et al.*, 2014). The popular use of MSCs due to their therapeutic action based on paracrine signalling led to the early study of MSC-derived EVs as potential paracrine actors overcoming the current limitation of cell-based therapies. For example, human placenta-MSC-derived EVs treated a mouse model of multiple sclerosis which showed an increased myelination within the spinal cord of treated mice for both MSCs and MSC-EV treatments. *In vitro* results supported that MSCs mechanism of action was mediated by EVs making them a promising acellular alternative treatment (Clark *et al.*, 2019). MSC-EVs from rat bone marrow also showed potency for nervous regeneration with for example, the enhanced recovery of brain function after traumatic brain injury in rat (Zhang *et al.*, 2015).

In cancer therapy, BMSC-derived EVs were studied in the context of bladder cancer and their use as a treatment prevented cancer progression and metastasis in mice model via the transfer of miR-9-3p leading to the downregulation of endothelial cell-specific molecule 1 (ESM1) (Cai *et al.*, 2019). The therapeutic and EV-mediated delivery of micro RNAs (miR) has been observed in several other cancer types with for example miR-143 in prostate cancer (Che *et al.*, 2019) or miR-133b in glioma (Xu *et al.*, 2019). In addition to their native activity, EVs can be used in combination with established cancer treatment. Liu *et al.* focused Imatinib, tyrosine kinase inhibitor, and its therapeutic potency against K562 human leukaemia cells as drug resistance can occur. Human umbilical cord-MSC-derived EVs were found to have no anti-cancer activity alone, nevertheless, the combined treatment indicated an increased sensitivity of K562 cells to Imatinib activity via the EV-mediated activation of a major apoptotic signalling pathway (*Liu et al.*, 2018a).

Applied to neurodegenerative diseases, an important factor is the capacity of EVs to pass the blood-brain barrier (BBB). Tominaga *et al.*, showed that brain metastatic cancer cells were releasing EVs capable of destroying the BBB through the transfer of microRNA-181c, thus, confirming the potential EVs circulation through BBB in a pathological context (Tominaga *et al.*, 2015). In response to inflammation, it has also been demonstrated that EV-mediated inter-cellular communication was possible between the hematopoietic system and the brain with an observed transfer of genetic material (Ridder *et al.*, 2014). Dendritic cells, which were previously transfected, produced engineered EVs harboring Lamp2b, a membrane protein which was fused to the neuron-specific RVG peptide offering an active targeting strategy. EVs were further modified and actively-loaded with exogenous siRNA. The EV based treatment in wild-type mice revealed the knockdown of BACE1, an Alzheimer's disease's target (Alvarez-Erviti *et al.*, 2011).

Alternatively in terms of diagnostic use, EVs have been studied as a biomarker reservoir as they often harbour markers present at their parental cell's level. EV isolation leads to the downstream analysis of biofluids or liquid biopsies to obtain for example, the proteomic profile of the collected EVs. In their study, Wang *et al.* evaluated EVs from patients' serum and they demonstrated that the EV-levels of the EGFR protein was an effective diagnostic marker for Glioma, a malignant primary brain tumour currently lacking from reliable diagnostic methods (Wang *et al.*, 2019). Urinary EVs have also showed great potential to identify kidney-related pathologies as the neutrophil gelatinase-associated lipocalin (NGAL) protein, a biomarker for acute kidney injury, was enriched in the EV fraction (Alvarez *et al.*, 2013). In cancer detection, EV-biomarkers can be employed for both diagnoses and disease progression monitoring. The studies of miRNA and protein levels in tumor-derived EVs have showed their great potential (Rabinowits *et al.*, 2009).

Through the development of engineering methods, researchers have enhanced EV therapeutic efficacy by modifying their composition allowing the delivery of additional molecular species or to improve the active targeting of the naturally derived EVs; further information regarding all the EV engineering routes have been recapitulated elsewhere (Man *et al.*, 2020).

The acceleration of EV research is also attributed to the discovery of EV therapeutic activities when derived from multiple cellular origin. EV composition and activity reflects both their parental cell and the physiological context of their release (Kumar *et al.*, 2024). Once in the extracellular domain, EVs can translate their activity through their uptake by a target cell which can be performed via endocytosis, membrane fusion or the binding to a surface receptor of the cell (Fig 1.2).

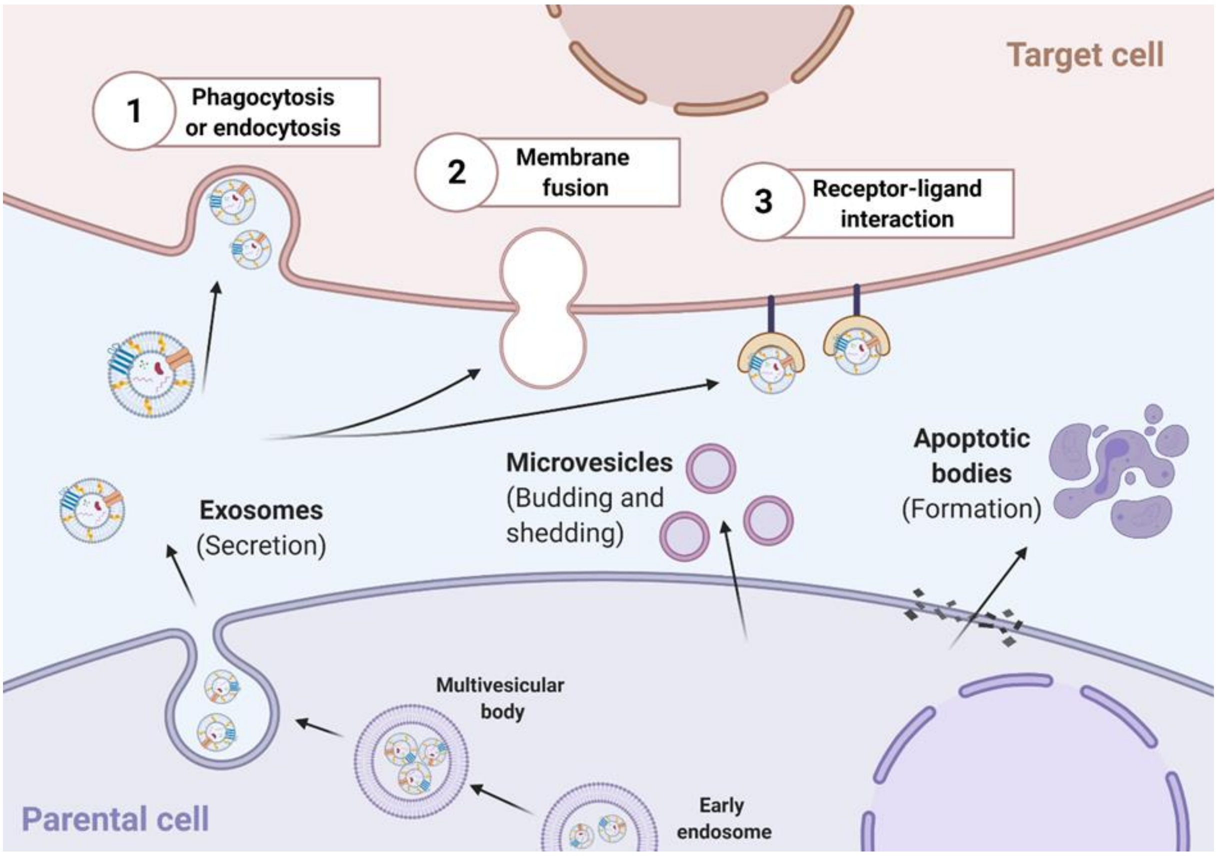

**Figure 1.2. | Representation of the release of different EV subtypes and their interaction mechanism with recipient cell.** (Created using BioRender.com). The separate biogenesis of EV subtypes (exosomes, microvesicles and apoptotic bodies) from their parental cell is represented. Once secreted, the resulting EVs are located in the extracellular matrix and can interact with a recipient cell via endocytosis, their fusion with the membrane or via a receptor-ligand interaction at the surface of the cell.

EVs are also involved in a range of pathological conditions with for example their contribution to OA pathogenesis (Liu *et al.*, 2023a) or their role in bone tumour microenvironment (Tamura et *al.*, 2020). Moreover, MSC-derived EVs were shown to have positive effects on tissue repair regulating cell senescence and proliferation (Roefs *et al.*, 2020). Despite this complex heterogeneity of activity and pathophysiological roles, the rigorous study of EV populations separated from *in vitro* cell cultures has allowed to establish the promising application of EVs in regenerative medicine. As such, the use of EVs as a potential acellular treatment has grown in recent years and will be detailed further in this chapter to focus on their bone regenerative potential.

## 1.2. EVs in bone regeneration

The implication of EVs in bone development dates back to the work of Anderson and Bonucci describing how matrix vesicles (MVs) were involved in the calcification of cartilaginous matrix (Bonucci, 1967; Anderson, 1967). Responsible for driving the biomineralisation of the extracellular matrix, a logical focus has been made for the study of osteoblast-derived EVs (OB-EVs). In terms of intercellular communications, OB-EVs were found to induce the differentiation of MSCs by influencing miR profiles in target cells and via the activation of the canonical Wnt pathway (Houschyar *et al.*, 2019). Not limited to the delivery of miRs, Ge *et al.* performed a proteomic study of OB-EVs obtained from pre-osteoblasts and detected 1536 proteins, among them 172 were associated to a bone database offering a first insights into their specific composition (Ge *et al.*, 2017). Furthermore, Davies *et al.* examined the difference of OB-EV compositions in mineralising conditions compared to basal conditions using a murine osteoblastic cell line. Mass spectrometry analysis showed the enrichment of OB-EVs in key proteins such as annexin calcium channelling proteins supporting the potential role of OB-EVs as a nucleation core for early mineral formation (Davies *et al.*, 2017). Additionally, non-mineralising osteoblasts-EVs were not found to increase mineralisation in 2D osteogenic cultures beyond control showing the important impact of cellular environment on the resulting EV populations secreted.

This EV-driven bone metabolism appears to be a complex mechanism as OB-EVs have been found to elicit a wide range of cellular response in the bone tissue. Cappariello *et al.* demonstrated *in vitro* the autocrine and paracrine effects of OB-EVs with the bone microenvironment as the addition of these vesicles to the cultures modulated the gene expression of osteoblasts while improving osteoclastic variables (size and number of nuclei per cell) (Cappariello *et al.*, 2018). Mature osteoblast-derived EVs were also found to inhibit bone formation and enhance osteoclastogenesis bringing *in vivo* evidence that these vesicles are capable to trigger the transition from a bone forming to a bone resorbing metabolic phase (Uenaka *et al.*, 2022). Taken together, these studies show the important role of OB-derived EVs in the bone microenvironment with established crosstalk between osteoblasts and osteoclasts (Deng *et al.*, 2015). Embedded in the mineralised extracellular matrix (ECM), osteocytes are also key players in the regulation of bone remodelling. These mechanosensitive cells (MLO-Y4 murine line) were found to release EVs which were responsible for an increased human mesenchymal stem cell (hMSCs) recruitment and osteogenesis once mechanically activated (Eichholz *et al.*, 2020). Moreover, when mechanically activated by $Ca^{2+}$-dependent contractions, osteocytes were also found to modulate the release of EVs delivering bone regulatory proteins such as RANKL (Morell *et al.*, 2018). As displayed in Figure 1.3., the role of bone cell-derived EVs identified to date groups a variety of bone specific cellular responses such the osteogenic differentiation of stem cells, the polarisation of resident macrophages or the regulation of the bone remodelling cycle via the modulation of osteolysis/osteogenesis (Fang *et al.*, 2024).

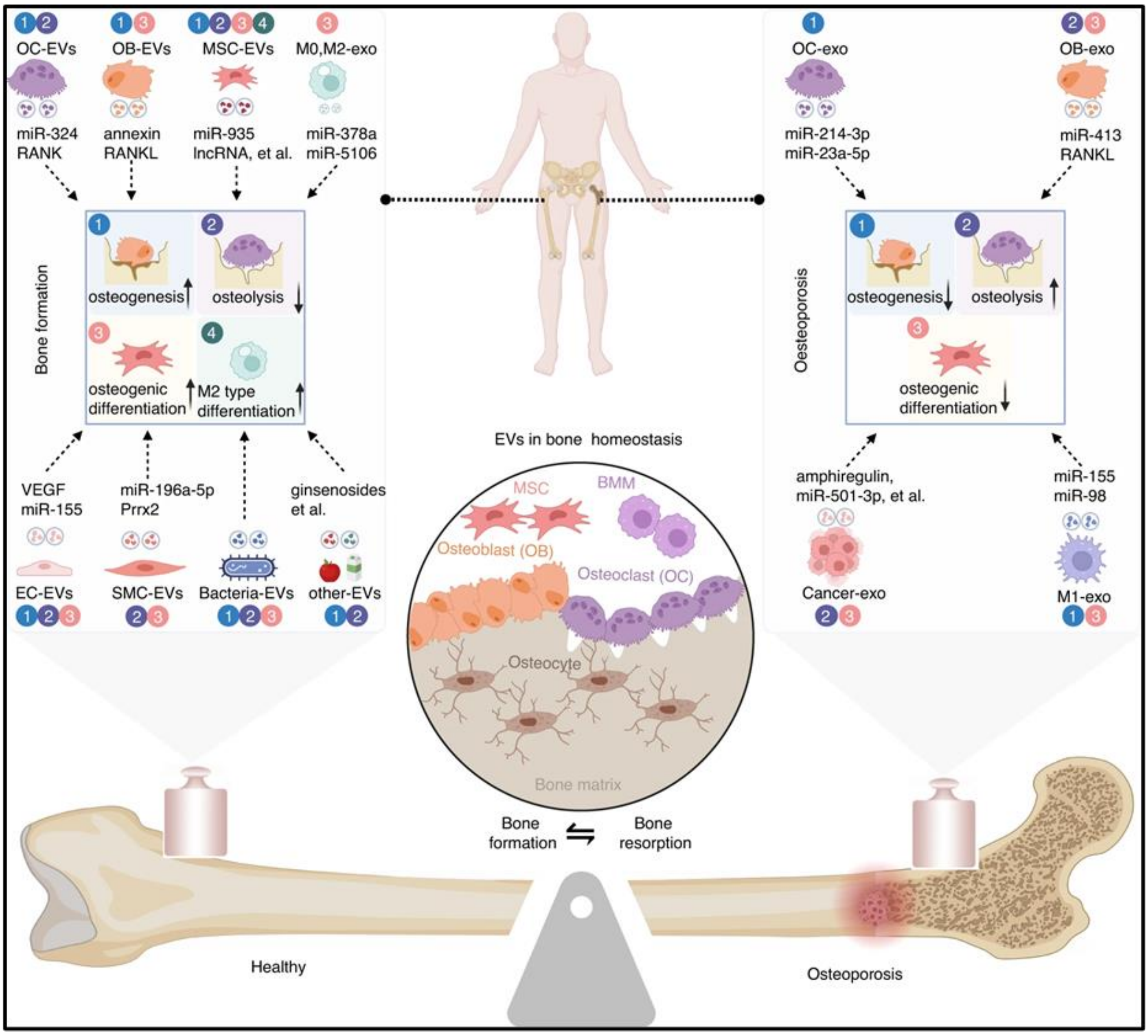

**Figure 1.3. | Schematic representation of the role of bone cell-derived EVs on both healthy and osteoporotic bone.** EV effects on bone homeostasis are separated between healthy bone (left side) and osteoporotic bone (right side). Evidence of EV potency is numbered in link with the biological effects demonstrated such as (1) osteogenesis, (2) osteolysis, (3) osteogenic differentiation and (4) M2 type differentiation with each effect associated with EV cellular origin. Adapted from Fang *et al.* (2024).

Despite accumulating evidence showing the variety of biomolecules that bone cells transfer through EV-mediated delivery such as miRNA, the precise role of these vesicles as a driver of biomineralisation remains debated. The main division in the literature is located at the level of MVs which are found embedded in the extracellular matrix. These MVs were found in bone and cartilage (Boyan *et al.*, 2022; Garcés-Ortíz *et al.*, 2013) and also in atherosclerotic plaques (Chistiakov *et al.*, 2017). They were found enriched in tissue non-specific alkaline phosphatase (ALP) and annexin proteins which has been linked to their capacity to act as an early formation site for minerals (Bottini *et al.*, 2017). More recently, the quantity of MVs were found to be reduced in osteoporotic mice when derived from femur and tibias which was associated with a reduced mineralisation potency linked to decrease level of annexin V (Su *et al.*, 2023). Mizukami *et al.* used MVs from mouse osteoblasts cultures which were administrated to femoral bone defect in mice using a gelatin hydrogel-system. These results showed a promotion of bone formation on defect site, however, these regenerative effects could not be replicated *in vitro* using a mouse osteoblast model (Mizukami *et al.*, 2023). Skelton *et al.* isolated MVs from the ECM of MG63 human osteoblast-like cells and found that these vesicles presented with a four-fold enrichment in ALP compared to plasma membranes. Additionally, these MVs were enriched in miRNA known for their anti-osteogenic and macrophage polarisation effects (Skelton *et al.*, 2023). Despite the increased effort to understand their composition, there is still a strong barrier in separating MVs subpopulations from the total secreted EVs and to understand their relative contribution to biomineralization (Balcerzak *et al.*, 2008; Ansari *et al.*, 2021). Taken together, these results show the importance of matrix vesicles and the necessity to better understand their biogenesis and fate from their cell secretion to the matrix.

From an original focus on vesicles directly influencing bone, there has been a growing interest to study the effects of these EVs on other key features of efficient bone repair such as vascularisation, nerve repair and immune response as well as the effects of these non-tissue specific cell types onto bone and cartilage repair. Regarding nerve repair, interplay between bones and the nervous system is well established as responsible of primary body functions (Minoia *et al.*, 2022). To the best of our knowledge, the effects of bone tissue-derived EVs on nerve cells remains non investigated to date. On the contrary, Zhao *et al.* showed that EVs derived from neural stem cells after traumatic brain injury were capable to facilitate osteogenesis *in vivo* in mice calvaria defect once delivered by a 3D-printed hydrogel scaffold (Zhao *et al.*, 2023). Additionally, a strong body of evidence has been described by Nasiry and Khalatbary presenting the potency of stem cell-derived EVs as a therapy for nerve injury (Nasiry and Khalatbary, 2023). Thus, this line of research offers great promise to achieve peripheral nerve repair as part of a bone regenerative strategy.

The immune homeostasis is an important parameter to consider for bone regeneration as cells such as macrophages can present different phenotypes influencing tissue remodelling (Kou and Babensee, 2011). The complex and highly regulated role of immune cells in fracture healing has been extensively described in the literature (Baht *et al.*, 2023; Wendler *et al.*, 2019). Regarding EV, their role in the immune system has been intensively researched (Buzas, 2022). Focused on bone repair, immune cell-derived EVs such as T cell- and macrophage-derived EVs have demonstrated their capacity to accelerate bone repair (Jiao *et al.*, 2024). For example, macrophage-derived EVs were identified as a promising EV population to enhance bone regeneration. The work of Kang *et al.* investigated the effects of macrophage polarisation onto the bone regenerative potency of macrophage-derived EVs. By comparing M0-EVs, M1-EVs and M2-EVs, they showed that in rat calvaria defects, M1-EVs inhibited bone repair whereas both M0 and M2 were promoting regeneration at 3 and 6 weeks (Kang *et al.*, 2020).

The vascularisation of bone tissue is also a critical component to ensure efficient healing as a sufficient nutrient supply has showed to be key for the survival of critical-sized large bone defects. Therefore, the formation of new blood vessels or angiogenesis constitute an important process of bone tissue repair which has been found to be accelerated via EVs. Endothelial progenitor cells (Jia *et al.*, 2019), bone marrow-MSCs (Zhang *et al.*, 2020a) or specialised bone cells such as osteoblast and osteocytes (Shen *et al.*, 2023) can drive blood vessel formation offer an important therapeutic approach.

In bone development, the plurality of EV-mediated bioactivities reflects the complex interplay that exists in the physiology of this tissue. Current challenges are associated to our understanding of MVs to better understand if these MVs are a secreted-EV subtype and how these anchored-vesicles drive biomineralisation. The recent increase of studies looking at readouts outside mineralisation and osteogenic differentiation such as angiogenesis or immune responses should also enlighten our comprehension of the role of EVs and their true potential as a multi-targeting therapy.

## 1.3. Synthetic EVs as bioinspired mimetics

In parallel to EVs' growing interest, nanomedicines have been increasingly researched over the last decade due to key scientific breakthroughs leading to successful clinical trials in various therapeutic areas such as cancer, infections, and neurological disorders (Anselmo & Mitragotri, 2019). Developed since the 1990's, the use of lipid-based nanocarriers have been mainly focused on the development of drug delivery systems with notably AmBisome® (liposomal delivery of amphotericin B) or Doxil® (liposomal delivery of doxorubicin) (Stone *et al.*, 2016; Patel, 1996). The use of synthetic nanoparticles has showed great clinical advantages including an improved efficacy and bioavailability as they can be tailored to each therapeutic application. Various nanotechnological platforms including both organic and inorganic nanoparticles have been developed to address the specific needs of the medical application of interest including both diagnosis and therapy. For example, iron oxide nanoparticles have been used as imaging agent for magnetic resonance imaging (Chertok *et al.*, 2008) whereas lipid nanoparticles were formulated as mRNA vaccines (Schoenmaker *et al.*, 2021).

To overcome the translational challenges associated with EVs, several strategies have been explored to create viable synthetic alternatives with the ambition to develop the next generation of nanotherapeutics. Despite the promising results of these new approaches, their clinical translation is still challenged as they use naturally-derived EVs as their foundation. In recent years, synthetic approaches have been considered using the extensive experience in the field of nanoparticle formulation to recreate EVs artificially by mimicking part of their function.

### 1.3.1. Defining EV mimetics

EV mimetics form an emerging research field which can still be confusing as the terminology used is not standardised across the literature. The terms artificial exosomes, synthetic nanovesicles, exoliposomes, semi-synthetic EV hybrids, EV mimetics or exosome-liposome hybrid vesicles are part of the vocabulary found to be used to describe similar products in the literature. To date, there is still a need to define what an EV mimetic is and to agree on a standardised classification and terminology.

In 2018, Garcia-Manrique *et al.* offered a first classification for “Bioengineered and mimetics EVs” separating semi-synthetic EVs, being bio-engineered natural EVs, and fully-synthetic EVs, describing production of de novo vesicles via bio-nanotechnology methods, not involving the use of natural EVs (Garcia-Manrique *et al.*, 2018) (Fig 1.4.). Here, the study of EV mimetics will exclude engineered EVs that were obtained by post-isolation modification such as passive/active loading or surface modification, as well as the EVs obtained from modified parental cells. Therefore, the spectrum of EV mimetics contains the lipid nanoparticles fabricated via the bottom-up approach (when precursor molecular species are used to fabricate the nanoparticles) or the top-down approach (when bulk material is reduced to smaller nanosized pieces by chemical or mechanical processing). By design, EV mimetics could be placed on a biomimicry scale or spectrum depending on how close they replicate the natural EV of interest. Composition, structure, degree of complexity, physico-chemical properties are all important EV characteristics that can be replicated into EV mimetics and design choices have to be made to determine which criteria to prioritise to obtain a functional mimetic.

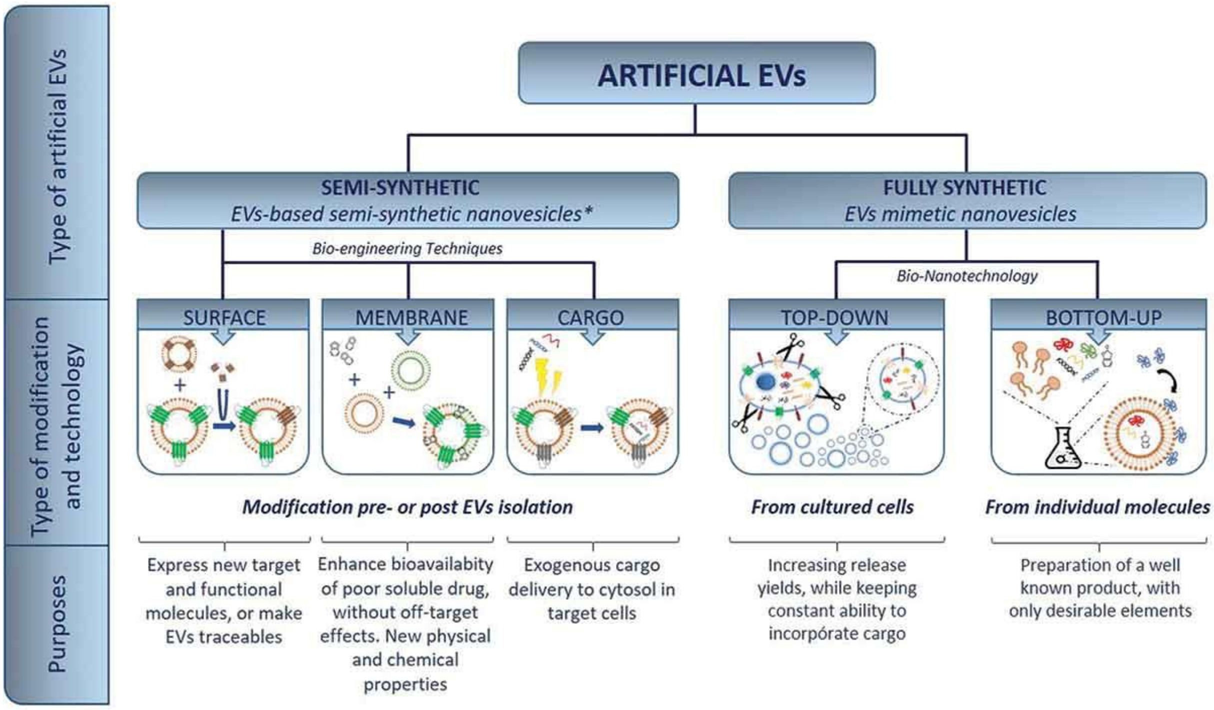

**Figure 1.4. | Schematic representation of the different approaches to develop synthetic EVs.** Artificial EVs are separated into two categories: semi-synthetic EVs and fully synthetic EVs. Semi synthetic EVs can be obtained from the modification of native EVs via surface, membrane or cargo modifications using bioengineering techniques. Fully synthetic EVs can be generated from cell using the top-down approach or via synthesis using the bottom-up approach. Adapted from (Garcia-Manrique *et al.*, 2018).

### 1.3.2. Cell-derived nanovesicles

Cell-derived nanovesicles (CDNs) are lipid nanoparticles obtained through the disruption of cells resulting in the formation of nanovesicles sharing physiochemical properties with EVs and their parental cell. The cell source to produce CDNs is usually the first question that needs to be answered as CDNs' activity is dependent on inherited biomolecules from parental cells. For example, once generated from natural killer (NK) cells, NK-CDNs were found to have a more effective anti-cancer activity than NK-derived-EVs *in vivo* on a xenograft glioblastoma mouse model (Zhu *et al.*, 2018).

In regenerative medicine, there is little evidence of the development of CDNs to date as this method remains recent and has been primarily designed towards drug delivery which is less a focus in the field. Moreover, the lack of control over the composition of these nanovesicles may lead researchers to prefer modified EVs to CDNs as long as biological potency is not established.

Targeting OA, Pang *et al.* comprehensively investigated the use of MSC-derived nanovesicles obtained via serial extrusion as EV mimetics. After directly comparing CDNs with EVs, they showed that they shared similar size and CDNs were generated at a 100-fold higher yield. They also demonstrated that these CDNs promoted the polarisation of macrophages toward an M2 phenotype *in vitro* as well as increasing chondrocyte and stem cell differentiation, proliferation, and migration. Additionally, once loaded into a gelatine methacryloyl-hydrogel, the NVs exhibited a sustained release and were able to improve OA severity in a mouse model while confirming their capacity to induce M2 macrophage polarisation (Pang *et al.*, 2023).

For bone repair, Ravi *et al.* generated CDNs from the human embryonic kidney (HEK) 293 cell line, as a well-known and low maintenance generic cell line, to study their effect on adipose-derived stem cells. The CDNs were obtained via extrusion and were loaded in the process with dexamethasone (>85% loading efficiency) which was linked to the promotion of osteogenic differentiation (Bella *et al.*, 2021). Notably, they highlighted the necessity to further monitor their biofabrication process as DNA content was still present in the resulting CDNs (~87% reduction from cells) which may have consequences regarding immunogenicity (Ravi *et al.*, 2022).

Taken together, these studies pioneered the use of CDNs for bone tissue engineering. The use of bone-specific cells to generate CDNs remains absent from the literature to date but may present great potential. Finally, determining the composition of such CDNs remains an important step towards a safe clinical translation and provide important mechanistic insights when compared to their EVs counterparts.

### 1.3.3. EV-mimetic liposomes for bone regeneration

Liposomes are engineered nanoparticles synthetically created from the self-assembly of a phospholipid-bilayer membrane enclosing an aqueous core. Originating in the 60s’, half a century of extensive research has led this technology to become an important therapeutic tool with notably, the development of drug delivery systems for chemotherapeutic agents (Gregoriadis, 2016).

To date, liposomes are by far the most popular nanotechnology used to fabricate synthetic EVs as they both share the same core vesicular structure. Using liposomes as the starting point to produce synthetic EVs appears to be the natural route to produce EV mimetics as they provide unique advantages including 1) total control over the composition, 2) possibility of large-scale production, 3) EV-vesicular structure with aqueous core, 4) ease to obtain pharmaceutical-grade product (García-Manrique *et al.*, 2018). When developing synthetic vesicles, researchers often aim to formulate a product “resembling” or “mimicking” known features of EVs. In this emerging application, it remains important to define both the characteristics of synthetic EVs and where to draw the line between liposomes and synthetic EVs.

Bone morphogenetic protein 2 (BMP-2) has been extensively used clinically to treat non-union fractures, however, the supraphysiologic doses required to stimulate effective bone repair can often lead to severe complications including hematoma, myelopathy, inflammation, heterotopic ossification (James *et al.*, 2016). The delivery of BMP-2 via liposomes (>75% loading efficiency) have been investigated. For instance, recombinant human BMP-2 (rhBMP-2) were incorporated into liposomes, which were controllably released via ultrasound stimulation and induced ectopic bone formation *in vivo*, however without direct comparison with the effects of the drug alone (Crasto *et al.*, 2016).

Li *et al.* also investigated to the development of adhesive liposomes loaded with BMP-2 which were then delivered via an injectable polyethylene glycol (PEG) hydrogel to osteoporotic femoral fracture sites in rats after 8 weeks. Compared to non-adhesive control, adhesive liposomes demonstrated stronger tissue adhesion leading to a better osteogenic differentiation as well as accelerated bone remodelling at the fracture site (Liu *et al.*, 2018b).

Outside the delivery of a biological cargo, harnessing the potential of the EV membrane itself with lipids have been investigated with development of a liposomal formulation composed of 20S-hydroxycholesterol, an osteoinductive oxysterol, and stearylamine, a cationic amphiphile. These sterasomes were found to induce the osteogenic differentiation of murine BMSCs *in vitro* without requiring the addition of therapeutic molecules (Cui *et al.*, 2017).

To achieve active targeting, acid oligopeptide-modified liposomes were formulated using Glu6, an acid oligopeptide, as this compound exhibit high binding capacity to $Ca^{2+}$ in the presence of HA. Among the range of concentration used, the highest bone-targeting activity was achieved with Glu6 at 5 mol% (Tao *et al.*, 2022).

The development of liposomes as an EV mimetic remains a new development in the EV field and is still limited in regard to bone applications. There is an unmet potential for these mimetic systems to be use as a screening platform to better understand the mechanism of action of native EVs. Additionally, more comprehensive studies comprising both EV characterisation and liposome formulation and comparing the activities of the two vesicle populations would allow to build up stronger evidence regarding this approach.

### 1.3.4. Challenges associated with both EVs and EV mimetics clinical translation

Although the study of EVs in recent years have created a path from the comprehension of pathophysiology to the development of treatment, the clinical translation of EVs into fully-approved therapies remain difficult. To date, 96 clinical studies are currently reported by the U.S National Institute of Health database (https://clinicaltrials.gov) using the research term "Extracellular vesicles".

One of the major problems in the translation of an EV product is the capacity to scale-up its production to an industrial scale following good manufacturing practice (GMP) standards and adopting clinical grade components in the culture such as serum replacement. The use of bioreactors has been investigated to produce large quantities of clinical-grade MSC-derived EVs (following GMP standards) offering a stepping stone towards EV translational feasibility (Mendt *et al.*, 2018). However, scaling-up a specific EV population depends on a range of variables including the cell source (primary cell vs cell line; variation between cell types) the culture conditions, the potential use of stimulation as well as the isolation workflow and storage method. Across the duration of the scaling-up process, changes in the EV population isolated should be carefully monitored with quality assessment and batch to batch variability evaluation (Burnouf *et al.*, 2019).

Another important issue associated with EV therapy is their storage conditions. Few studies have reported storage conditions of their EVs as the low yield obtained at the laboratory scale might assure the rapid downstream analysis of the samples. Storage experiments have confirmed that EVs remains stable at 4°C or at -80°C for up to one month with a preferential frozen storage (Deville *et al.*, 2021). However, current studies mainly look into the physico-chemical properties of EV after short storage. There is a need for dedicated long-term studies also investigating the potential change in EV therapeutic potency after storage conditions with defined storage parameters including storage temperature, freezing, and thawing cycles and storage duration, storage solutions (Yuan *et al.*, 2021). Recently, alternative process has been explored with for example the lyophilisation of EVs from adipose-derived stem cells with lyoprotectants which showed a conserved bioactivity (viability of ischemic human myoblasts) after freeze-drying (El Baradie *et al.*, 2020). The closer EVs approach clinical translation, the more storage modalities become critical, and the EV field has not yet explored the effects of storage on EV functionality mainly due to the low yields currently obtained for pre-clinical studies.

Using EVs/CDNs as a treatment, one major safety risk is the presence of contaminants. Viruses such as the human immunodeficiency virus or the hepatitis c virus are sub-200nm in size which would make them congruent to EVs and separated within the same fractions. Despite the absence of biological contaminants in their manufacture, synthetic particles such as liposomes still require to follow GMP standards into order to generate a product free of contaminants.

To avoid such risk, the use of radiation is a potential solution, however, there is a lack of evidence on the potential EV collateral damage (Rohde *et al.*, 2019). These types of additional criteria to assess on a single EV batch is increasing as steps towards clinical translation are implemented.

Synthetic EVs aims to be the solution for the clinical translation of EV-based therapies. To achieve this goal, synthetic EVs needs to be introduced to the pharmaceutical market and take into considerations the regulatory issues and principles of nanomedicine products. The main challenges to overcome are the physicochemical characterization, biocompatibility, and nanotoxicology evaluation, pharmacokinetics and pharmacodynamics assessment, process control, and scale-reproducibility (Soares *et al.*, 2018). Elkhoury *et al.* presented the development of hybrid EV-liposomes complexes using neonatal rat cystic fibrosis-derived EVs (CF-EVs) by direct-co-incubation followed by probe sonication as a proof of concept for their innovative approach without being tailored to a particular therapeutic application. These hybrids were encapsulating miRNAs which were successfully delivered. Moreover, they also integrated these innovative nanomaterials to a gelatin methacrylate hydrogel system which was bioprinted paving the way of similar bioinks for bone and cartilage tissue engineering using relevant EVs (Elkhoury *et al.*, 2022).

Importantly, the majority of bone repair studies examined here employed a small animal rodent model such as mouse and rat to look at either a critical-sized femoral or calvaria bone defect. The use of clinically appropriate defect sites and/or larger animal models needs to be further assessed on a case-by-case basis to provide greater pre-clinical evidence regarding their therapeutic potency. Finally, the clinical translation of both EVs and their mimetics lies in the development of delivery system tailored to the needs of bone repair applications.

## 1.4. EV delivery systems for bone repair

One of the major barriers to benefit from the bioactivities of EVs for bone repair is their delivery at the bone defect site. EV retention is limited and the achievement of a localised sustained presence of EVs without the use of a structural support has not been achieved (Yan *et al.*, 2020). Moreover, an *in vivo* study using a mice model have demonstrated that the intravenous injection of EVs led to their rapid clearance *via* the action of macrophages highlighting the need for innovative strategies to augment EVs half-life (Imai *et al.*, 2015). Therefore, in recent years, the bone tissue engineering community has focused its efforts to design and produce 3D-scaffolds to achieve the delivery of therapeutics of interest for bone repair (Liu *et al.*, 2023b). The use of 3D structures has been widely employed for the delivery of cells (Quarto and Giannoni, 2016) using a variety of approaches including the development of cements (Liu *et al.*, 2023a), metallic scaffolds (Alvarez and Nakajima, 2009), or mineral-based scaffolds (Nandi *et al.*, 2018). Although these materials offer great advantages from a mechanical perspective, their lack of biological recognition can negatively impact tissue regeneration and the release of the material itself through wear or corrosion may lead to cytotoxicity of inflammatory response (Banjantry *et al.*, 2022; Jacobs *et al.*, 1998). Therefore, the use of biomaterials has been explored to overcome these limitations.

In an ideal design, scaffolds should be able to support the regeneration of *de novo* mineralised tissue without disrupting or damaging its immediate surrounding area. Notably, it should also provide a degrading rate sufficiently slow to follow the rate of tissue regeneration. Therefore, such system should be biodegradable and biocompatible and present with tunable mechanical properties to achieve optimal therapeutic outcome in bone (Dixon and Gomillon, 2022). Hydrogels are 3D structures composed of a crosslinked network of hydrophilic-polymer allowing them to retain great amount of fluid while maintaining their form. In addition of overcoming the limitations of previous strategies, hydrogels grant an extended control over the composition and structure of the scaffold. They also provide with a unique porous structure mimicking the ECM suitable for the migration and proliferation of cells (Ding *et al.*, 2023). To date, a multitude of both synthetic and natural polymers have been used to produce hydrogels. Among them, sodium alginate (Hu *et al.*, 2023b), chitosan (Tian *et al.*, 2022), gelatin methacrylate (GelMA) (Zhou *et al.*, 2023) or collagen (Fan *et al.*, 2023) are among the most used to produce hydrogels for bone repair applications.

To administer EVs using a hydrogel-based system, EVs can be incorporated by several strategies including ECM-immobilisation, physical encapsulation, electrostatic interaction and covalent conjugation (Fig 1.5.) (Man et al., 2020). Important parameters to take into account designing EV-loaded hydrogels are the porosity and the scaffold degradation rate being the two major characteristics modulating the release of EVs from the scaffold. Notably, a unique feature of EVs is their reported capacity to bind to ECM components with for examples the attachment to collagen fibres *via* integrin proteins displayed as the surface of their membrane (Hao *et al.*, 2022). As such, this particular feature has been exploited to produce collagen-based delivery systems (Man *et al.*, 2022c).

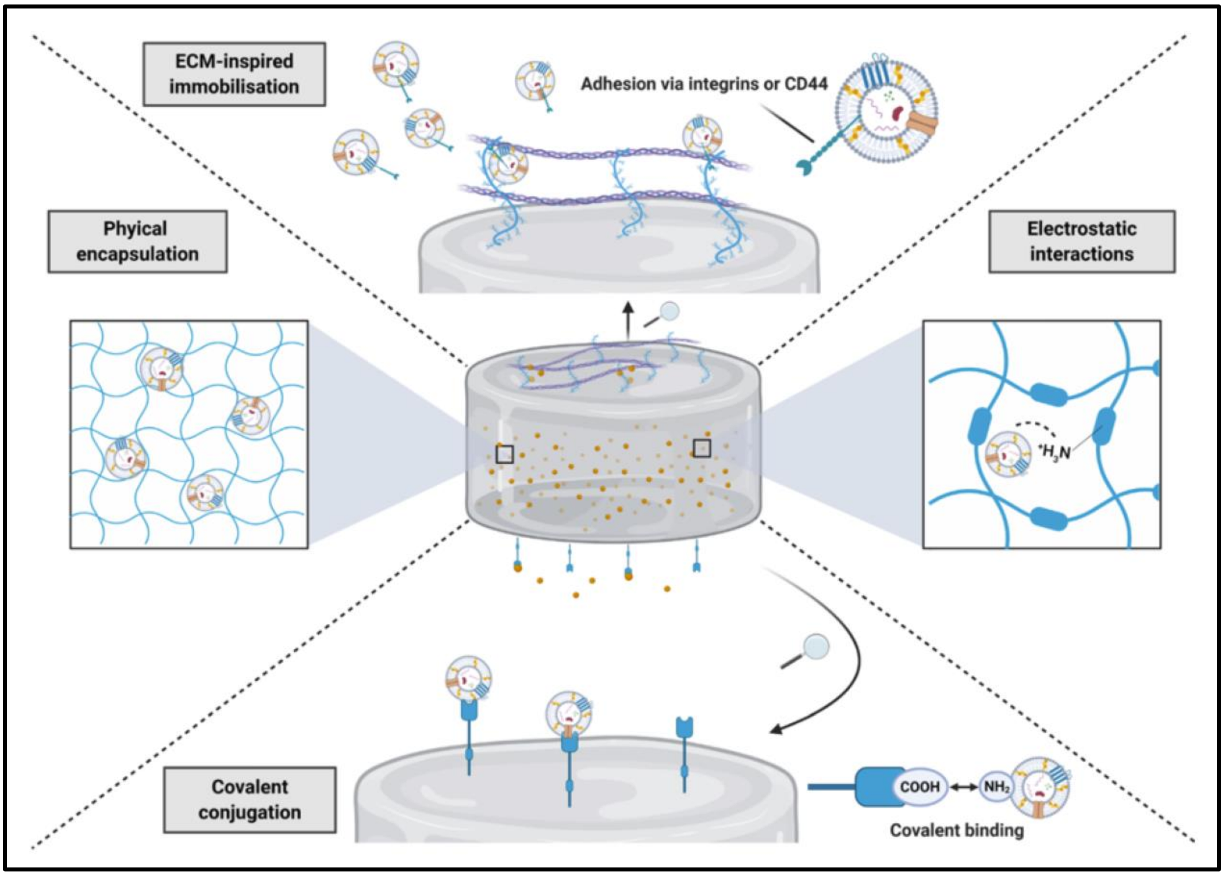

**Figure 1.5. | Schematic representation of design considerations for the incorporation of EVs to hydrogels.** Presentation of strategies to immobilise EVs within biomaterials. Methods of EVs incorporation within biomaterials include physical entrapment, extracellular matrix (ECM)-immobilisation, electrostatic interactions and covalent conjugation. (Created using Biorender.com)

Targeting bone repair, several studies have already investigated the delivery of EVs *via* the development of hydrogels. Researchers have combined epigenetically-enhanced osteoblast-derived EVs with a GelMA/nanoclay composite hydrogel to improve EV release kinetics and osteoinductive potency (Man *et al.*, 2022a). The authors showed that nanoclay inclusion improve the biomechanism of the GelMA hydrogel such as compressive strength, rheological behaviour, and 3D printed fidelity. Moreover, a dose-dependent effect on EV release was observed with nanoclay incorporation. Importantly, the Epi-EVs improve the recruitment, epigenetic activation, and osteogenic differentiation of hMSCs when compared to unmodified EVs and the EV-free scaffolds.

To improve the clinical utility of EVs, researchers have combined these nanoparticles with biomaterials systems to enhance their bioavailability at the defect site, thus improving EV-induced tissue healing. For example, Chen *et al.* developed a GelMA/ECM scaffold for the delivery of MSC-derived EVs (Chen *et al.*, 2019). The authors showed that the EV-functionalised material effectively enhanced cellular migration, supporting the polarization of macrophages to the M2 phenotype, facilitating the regeneration of osteochondral defects in rabbit. In another example, Hu *et al.* combined EVs-derived from human umbilical cord MSCs with a GelMA/nanoclay hydrogel system, showing improved cartilage regeneration via inhibiting reducing tension homolog deleted on chromosome 10 and phosphatase expression. Moreover, the addition of miR-23a-3p increased the expression of proteins kinase B, which promoted migration, proliferation, and differentiation of chondrocytes and MSCs (Hu *et al.*, 2020). MSC-derived EVs were also found to augment the regeneration of a rat calvaria defect *in vivo* using a chitosan-based thermosensitive and injectable hydrogel (Wu *et al.*, 2022).

From these examples, the therapeutic capacity of EVs after their hydrogel incorporation has been demonstrated with controlled EV localisation within the biomaterials. Nevertheless, there is still a lack of control over the tunability of EV release from these materials. Additionally, with advances in the understanding of fracture healing, there is a need to develop more complex hydrogel systems  (Schlundt et al., 2023). For example, vascularisation has been identified as major regulator of bone repair beyond the sole delivery of oxygen and nutrients  as angiogenesis has been linked to osteogenesis modulation (Di Maggio and Banfi. 2022). To this end, pro-angiogenic EVs derived from MSCs were functionalised to a decalcified bone matrix scaffold and showed augmented bone regeneration in a mice model *in vitro*.

Overall, the development of hydrogel for bone repair has only recently started and showed great promise at the pre-clinical level (Schlundt *et al.*, 2023). Difficulties are often associated with the large quantity of EVs required to develop such 3D systems leading to an effective regeneration as well as the determination of an effective dose to translate *in vitro* results into successful *in vivo* studies. While great developments have been made, novel hydrogel-based strategies are required to allow EV-based therapeutics to become a viable therapeutic appraoch for bone repair.

## 1.5. Summary and Aims

With the continuing shift towards an aging society, it is expected to cause a subsequent rise in the number of patients with bone and cartilage damage. Due to the limitations of current clinical therapies, there is an urgent need for new treatments to meet the ever-increasing demand. Based on this review of the literature, the clinical need for innovative acellular therapies to tackle bone repair has been highlighted. In the past decade, there has been growing interest in the use of EVs, as they have emerged as key regulators of musculoskeletal development, homeostasis, and repair. These nanomaterials once derived from bone cells have the potential to overcome issues hindering the translation of cell-based technologies for bone regeneration. However, their clinical translation is hampered due to the lack of fundamental understanding regarding their role in development and repair. To overcome these limitations, the development of EV-mimetic systems have been investigated to obtain a synthetic product which can be used as a model to shed light onto EV mechanisms of action or as novel candidates to support EV-based clinical translation. Finally, despite these advances in the development of nanotherapeutics, there is a strong need for the design of 3D-scaffolds to offer structural support and tailored properties allowing the localised delivery of these nanovesicles to bone defects.

The overall aim of this thesis was to investigate the potential of MO-EVs as an innovative therapeutic solution for bone repair. It was hypothesised that osteoblast-derived EVs are direct actors of biomineralisation driving osteoinduction and therefore, bone tissue regeneration.

In Chapter III, the isolation and characterisation of osteoblast-derived EVs during mineralisation was explored with their comprehensive characterisation including a compositional analysis. This was followed in Chapter IV by their *in vitro* evaluation investigating their effects on osteoblasts which was associated with the development of a novel X-ray fluorescence-based approach to assess biomineralisation *in vitro*. From the combined evidence obtained in Chapter III and IV, bioinspired synthetic EVs such as cell-derived nanovesicles and liposomes were formulated and compared to MO-EVs. Finally in Chapter VI, the hydrogel-based EV delivery system was developed as a stepping stone towards the clinical translation of these pro-osteogenic nanotherapeutics.

# Chapter II

-

# General Methodologies

## 2.1. Introduction

In this chapter, all the core methodologies used at least across more than one chapter will be reported. These mainly correspond to cell culture methods, nanoparticle characterisation techniques and methods relative to biomineralisation assessment *in vitro*. All other methods will be detailed in the method section of their respective chapter.

## 2.2. Material and methods

### 2.2.1. MC3T3-E1 culture and maintenance

Pre-osteoblastic murine MC3T3-E1 cells were used as the osteoblast model throughout this study and were obtained from the America Type Culture Collection (ATCC) and used from passage 9 to 40 (Fig 2.1.). Minimum Essential Medium Alpha (MEM-α) with GlutaMAX™ supplement (Gibco™, ThermoFisher Scientific, UK) was used as basal culture medium and was supplemented with 10% foetal bovine serum and 1% penicillin/streptomycin. Osteogenic medium was also used for mineralising cultures and correspond to basal medium supplemented with 10 mM β-glycerophosphate (Sigma-Aldrich, UK) and 50 µg/mL L-ascorbic acid (Sigma-Aldrich, UK). For EV isolation and dosing, both basal and osteogenic media were supplemented with EV-depleted FBS obtained via the ultracentrifugation of FBS for 16 h at 120,000 g using a Sorvall WX Ultra Series Ultracentrifuge (Thermo Scientific, UK) associated with a Fiberlite, F50L-8 × 39 fixed-angle rotor (Piramoon Technologies Inc., USA).

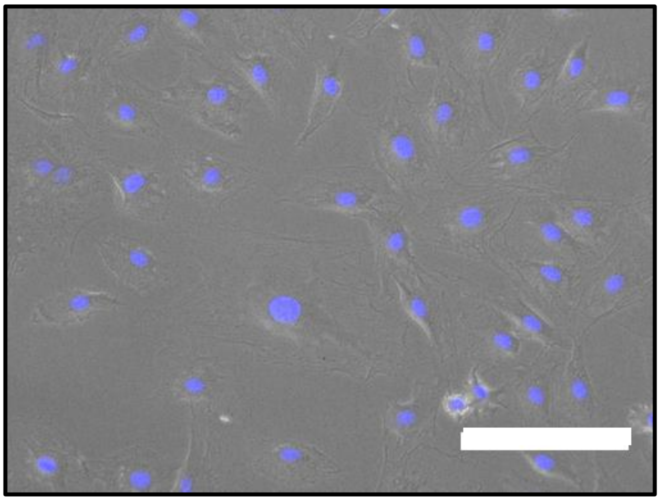

**Figure 2.1. | Microscopy observation of MC3T3-E1 cells.** DAPI was used to stain nuclei and was merged with brightfield. Scale bar = 200 µm.

### 2.2.2. EV isolation

Osteoblast-derived EVs were obtained from MC3T3-E1 cells that were cultured at scale in T175 culture flasks from which EV-enriched medium was collected and replaced every 2 days for 14 days. First, the combined conditioned culture media were spun at 2,000 x g for 20 mins to remove cells and large culture debris. The supernatant was then processed through differential ultracentrifugation using a Sorvall WX Ultra Series Ultracentrifuge (Thermo Scientific, UK) associated with a Fiberlite, F50L-8 × 39 fixed-angle rotor (Piramoon Technologies Inc., USA). EVs were separated with a first 30 min step at 10,000 g to remove large EVs followed by 120,000 x g spin for 70 mins to pellet EVs. This final step was repeated after resuspension of the EV pellet in sterile phosphate buffered saline (PBS) as a washing step. EV isolate was finally resuspended in sterile PBS and stored at 4°C for up to 7 days as used for characterisation or for *in vitro* experiments.

## 2.2.3. Nanoparticle characterisation

### *2.2.3.1. Transmission electron microscopy*

Morphological observations were obtained by transmission electron microscopy (TEM) using a JEOL JEM1400 system coupled with an AMT XR80 digital acquisition system (JEOL, Japan). Nanoparticle samples were diluted 1:20 in filtered sterile PBS prior to be drop casted on 200 mesh carbon-coated copper formvar grids (Agar Scientific, UK) to be physisorbed. A volume of 20 µL was used per grid and left to air dry prior to loading within the vacuumed sample chamber.

### *2.2.3.2. Nanoparticle tracking analysis*

Nanoparticle average diameter and concentration was obtained by nanoparticle tracking analysis (NTA) using the NanoSight LM10 Microscope (Malvern Instruments Ltd, UK) and the associated NTA software version NTA 3.3. EV samples were diluted 1:100 in sterile filtered PBS and allow to reach room temperature prior to be injected in the microscope chamber. The analysis included 5 video captures of 60 seconds recording nanoparticles in motion which were analysed frame by frame with a detection threshold set at 15 to determine the average size and concentration of the nanoparticle suspension.

### *2.2.3.3. Dynamic Light Scattering analysis*

Dynamic light scattering (DLS) analysis was performed using the Zetasizer Nano ZS (Malvern Instruments, UK). Nanoparticle suspensions were diluted 1:100 in filtered distilled water and was placed in folded capillary cell (DTS1070) for ζ-potential analysis and in 1mL micro-cuvettes (Fisher Scientific, UK) to determine size distribution, average diameter, and polydispersity index. Zeta potential (ζ-potential) is a physical property attributed to any nanoparticle suspension and corresponds to difference of potential between the dispersion medium and the stationary layer of medium attached to the nanoparticle. It is then important to note that zeta-potential is different from the electric surface potential corresponding to a different location and is here employed as an indicator of the stability behaviour of our EV colloidal suspension.

### 2.2.4. Total protein concentration

Total protein concentration was determined using the Pierce™ Bicinchoninic acid (BCA) assay kit (ThermoFisher Scientific, UK) according to the manufacturer's protocol. Briefly, 25 µL of sample or standards was loaded in a 96-well plate to which 200 µL freshly prepared BCA working solution was added (8:1 ratio). Albumin standards were prepared in the assay range of 20 to 2,000 µg/ mL. The microplate reaction was quicky shaken, incubated at 37°C for 30 min and finally measured by reading the absorbance of each well at 562 nm using a SPARK microplate reader (Tecan, Switzerland).

### 2.2.5. Biomineralisation assessment

#### *2.2.5.1. ALP activity*

ALP activity was determined using the SensoLyte® pNPP Alkaline Phosphatase Assay Kit (AnaSpec, USA) according to the supplier's protocol. At desired endpoint, cells were washed twice using assay buffer and 100 µL of Triton X-100 working solution was added to each well. After a 10 min incubation, each cell layer was mechanically disrupted in the Triton X-100 solution and were frozen at -80°C. This operation was repeated during 4 freeze-thaw cycles after which the cellular extracts were ready to be used.  ALP standards (calf intestine) were prepared in the provided dilution buffer to obtain solutions ranging from 0 to 10 ng/well with

50 µL of each standard used per well. Similarly, 50 µL of cell lysate diluted 1:2 in ALP dilution buffer was loaded into the microplate. To start the reaction, 50 µL of pNPP substrate solution was added to every well and mixed using a microplate shaker for 30 s. The plate was then incubated at 37°C to obtain an end point reading after 30 min by measuring absorbance at 405 nm using a SPARK microplate reader (Tecan, Switzerland).

#### *2.2.5.2. Alizarin red staining and semi-quantification*

Calcium deposition was evaluated by alizarin red staining. At endpoint, cells were washed with PBS before being fixed with 10% neutral buffered formalin (Merck, Germany) for 20 min. Once fixed, cells were washed 3 times using distilled water and 100 µL of alizarin red staining solution (Sigma-Aldrich, UK) was added to each well. Distilled water washes were repeated to remove the unbound dye and stained calcium was imaged using light microscopy with an EVOS™ XL Core Imaging System (Invitrogen, UK). Once imaged, samples were de-stained with 10% cetylpyridinium chloride (Sigma-Aldrich, UK) and incubated for 1 h at room temperature. Relative staining levels were then quantified by measuring the absorbance of de-stained solutions at 550 nm using the SPARK spectrophotometer.

#### *2.2.5.3. Picro sirius red staining and semi-quantification*

Collagen production was determined by picrosirius red staining. At endpoint, cells were washed with PBS before being fixed with 10% neutral buffered formalin for 20 min. Once fixed, cells were washed 3 times using distilled water and 100 µL of 0.1% picrosirius red staining solution (ScyTek Laboratories, Inc., USA) was added to each well. Once imaged, samples were de-stained using a 0.5 M acetic acid solution (Sigma-Aldrich, UK) and incubated for 1 h at room temperature. Relative staining levels were then quantified by measuring the absorbance of de-stained solutions at 590 nm using the SPARK spectrophotometer.

### 2.2.6. EV staining via lipid dye

EV staining was used in to achieve fluorescent detection of EVs in confocal microscopy. To that end, the fluorochrome PKH26 (MIDI kit, Sigma Aldrich, UK) with peak excitation (551 nm) and emission (567 nm) was employed. Freshly isolated MO-EVs were pelleted via ultracentrifugation (70 mins at 120,000 g) and the resulting pellet was resuspended with the dye at a PHK26 final concentration of 8 µM and prepared in the provided 'Diluent C' solution. After gentle mixing, staining occurred at RT for 20 min in the dark. Stained MO-EVs were then separated from unbound dye by repeating the ultracentrifugation step. The final pellet obtained was resuspended to the original amount of PBS present allowing the labelled-MO-EVs to be diluted for use in their downstream analysis.

### 2.2.7. Statistical analysis

Statistical analysis was performed using GraphPad Prism 10.1 software (GraphPad Software, San Diego, CA, USA). Statistical significance was assessed via the following:

- the student's t-test with *p<0.05, **p<0.01, ***p<0.001.

- the one-way or two-way ANOVA test followed by a Tukey's post-test with multiple comparison with *p<0.05, **p<0.01, ***p<0.001.

# Chapter III

-

# Isolation and Characterisation of Osteoblast-Derived Extracellular Vesicles

## 3.1. Introduction

### 3.1.1. Background

In recent years, the study of osteoblast-derived EVs have gathered much attention as these nanovesicles have been demonstrated to play key roles in the physiology of bone tissue (Cappariello *et al.*, 2018; Uenaka *et al.*, 2022). In order for these EV to be harnessed robust isolation and characterisation approaches are needed with a wide variety of methodologies developed in recent years (De Sousa *et al*., 2023). EVs can be derived from a range of sources, including as biofluids (Kumar *et al.*, 2024) (milk, saliva, urine, blood etc), conditioned media of *in vitro* cell cultures (Kusuma *et al.*, 2022) (cell monolayers, organoids, hydrogels, organ-on-chips etc) or directly from *in vivo* samples (Cui *et al.,* 2016). To satisfy the needs of these various formats, a plurality of separation methods has been developed, tailored to the needs of particular research projects. Ultimately, all these methods aim to separate nanoparticles in suspension from a liquid phase. This can be performed by physical separation with the use of ultracentrifugation (Chhoy *et al.*, 2021), flow field-flow fractionation (FFF) (Wu *et al.*, 2020), or chromatography (Kaddour *et al.*, 2021; Jung *et al*., 2021). EVs can also be separated by precipitation, with for example the addition of water-excluding polymers such as polyethylene glycol (PEG) (Garcia-Romero *et al.*, 2019). Possessing a variety of surface proteins, immunoaffinity-based separation methods can also be employed (Jakobsen *et al*., 2015). More recently, microfluidic-based methodologies have been used being capable of offering both physical and/or immune-based separation in a reproducible and scalable manner (Meggiolaro *et al.*, 2023).

To date osteoblast-derived EVs have been isolated from various sources using a multitude of separation workflows. For example, Cappariello, used primary osteoblasts obtained from mice skull bones and conditioned media (CCM) was collected after 24 h and processed via ultracentrifugation (Cappariello *et al.*, 2018). In another study, Unenaka *et al.* employed both primary osteoblasts and MC3T3-E1 cells to collect CCM after 48 h and using ultracentrigufation coupled with 0.22 µm filtration to generate two different fractions varying in EV size (Unenaka *et al.*, 2022). Interested in using dexamethasone as a parental cell stimulation, Zhang *et al.* maintained primary porcine osteoblasts for 14 days in osteogenic conditions and collected CCM containing EVs secreted by the mature osteoblasts between day 14 and 15, which were then separated via an ultracentrifugation protocol (Zhang *et al.*, 2023). Finally, Skelton et al. used MG63 cells as an osteoblast model isolating both secreted EVs and MVs from their culture using a protein digestion protocol followed by ultracentrifugation (Slekton *et al.*, 2023). Together, these examples show that even only looking at a single cell type, here osteoblasts, there is a plethora of approaches to obtain an EV population, which can vary from the conditions of culture, the time of collection, the volume of CCM and the isolation method to name a few. Therefore, even if osteoblast-derived EVs have been isolated before, there is a strong need for the establishment of robust parameters in this chapter to better understand the product isolated using our own experimental setup.

As heterogenous and biologically complex nanoparticles, the characterisation of EVs is fundamental to understand what population has been isolated. This characterisation starts with the physico-chemical characteristics of the nanoparticles to mainly determine their size, concentration, and morphology. For sizing analysis, DLS and NTA remain the two most widely used methods. Both are based on a similar principle known as photon correlation spectroscopy that uses a monochromatic laser going through the nanoparticle suspension

(Szatanek *et al.*, 2017). With its camera detector, NTA offers the possibility to calculate the nanoparticle concentration of a given sample, which is particularly useful to determine yield and to manipulate the quantity of EVs in downstream experiments.  To assess EV morphology, the use of TEM remains the gold standard as it offers a sub-1 nm resolution without the need for staining. However, the dehydration process coupled with the vacuumed analysis chamber can lead to a reduction of EV size. Alternatively, atomic force microscopy can be used to obtain topographical observations with a nanometre resolution (Skliar and Chernyshev, 2019; Parisse *et al.*, 2017).

Once their physico-chemical properties have been determined, the second critical aspect of EV characterisation is to obtain insights into their composition. Most methodologies currently employed are the same that can be traditionally used for cell analysis, only considering the lower amount of material found in the nanoparticles. For targeted evaluation of specific proteins of interest, methods such as immunoblotting, ELISA or flow cytometry remain the gold standards (Silva *et al.*, 2021; Logozzi *et al.*, 2020; Gul *et al.*, 2022). For a more comprehensive and untargeted approach, liquid chromatography coupled with mass spectrophotometry offers a powerful platform to gain insights into the proteome, lipidome or transcriptome of EVs (Cross *et al.*, 2023; Sun *et al.*, 2022; Schoger *et al.*, 2023). Complementary to all methods described above, biochemical assays remain the most cost-efficient and accessible assays to determine key features such as total protein, RNA or lipid content routinely used to determine dosage. However, in recent years, a clear focus has been given to the development of multi-OMICs approaches and characterisation at the single particle level with specialised equipment such as nano flow cytometry (Chiang and Chen, 2019).

Finally, due to progress towards clinical translation, a recent research focus has been put on the storage conditions of EVs as this is a key criterion to develop a product ready for therapeutic use. Due to poor yields obtained and the need for great EV numbers to sustain studies, most projects do not explore the storage conditions of their EVs of interest. Dedicated studies have demonstrated that storage conditions may affect EV features such as structural stability and EV biological functions (Bosch *et al.*, 2016; Kusuma *et al.*, 2018). Innovative strategies such as lyophilisation have showed great promise to obtain an off-the-shelf product with cryopreserved properties which will be explored in this chapter (Trenkenschuh *et al.*, 2021).

Overall, the isolation and characterisation of EVs encompass a wide range of methodologies. Due to the efforts of the International Society of Extracellular Vesicles through their MISEV guidelines, the research community has been thoroughly educated and guided to standardize the approaches used (Welsh *et al.*, 2024). Therefore, a particular effort has been made to follow guidelines and comprehensively characterise EV populations of interest.

In this chapter, EVs will solely be derived from the CCM of 2D monolayers cultures of osteoblasts. The yield and practicality of 3 workflows including ultracentrifugation, size-exclusion chromatography and immuno-separation has been investigated and compared.

Following this first assessment, MO-EVs were then comprehensively characterised by the determination of their physico-chemical properties as well as their composition (Figure 3.1.). In addition, the storage conditions of these EVs have also be explored in a 4-week long pilot study to determine the effects of various storage conditions on the stability of EVs as the length of a doctoral project required long-term perspectives.

### 3.1.2. Aim and objectives

The aim of the chapter was to culture osteoblasts in mineralising conditions and study their secretome *via* the isolation and characterisation of EVs separated from the CCM of these 2D cultures.

To achieve this aim, the following objectives were pursued:

- To validate the mineralisation status of MC3T3-E1 cells cultured in osteogenic conditions and collect their secretome.
- To compare EV isolation method and select the most appropriate approach for all subsequent MO-EV experiments.
- To validate the isolation of MO-EVs by determining their physico-chemical properties and the presence of EV biomarkers.
- To determine the composition of MO-EVs investigating both their organic and inorganic content.

### 3.1.3. Acknowledgement of contributions

The following collaborators have been critical in contributing to this body of work:

- **Dr Maria Fernandez-Rhodes & Dr Soraya Williams** from Dr Owen Davies Research Group at Loughborough University, UK – For performing the Western Blot analysis.
- **Dr Owen Davies**, from Loughborough University and **Dr Lee A. Gethings** from Waters Corporation who have run the proteomics analysis on LC/MS.

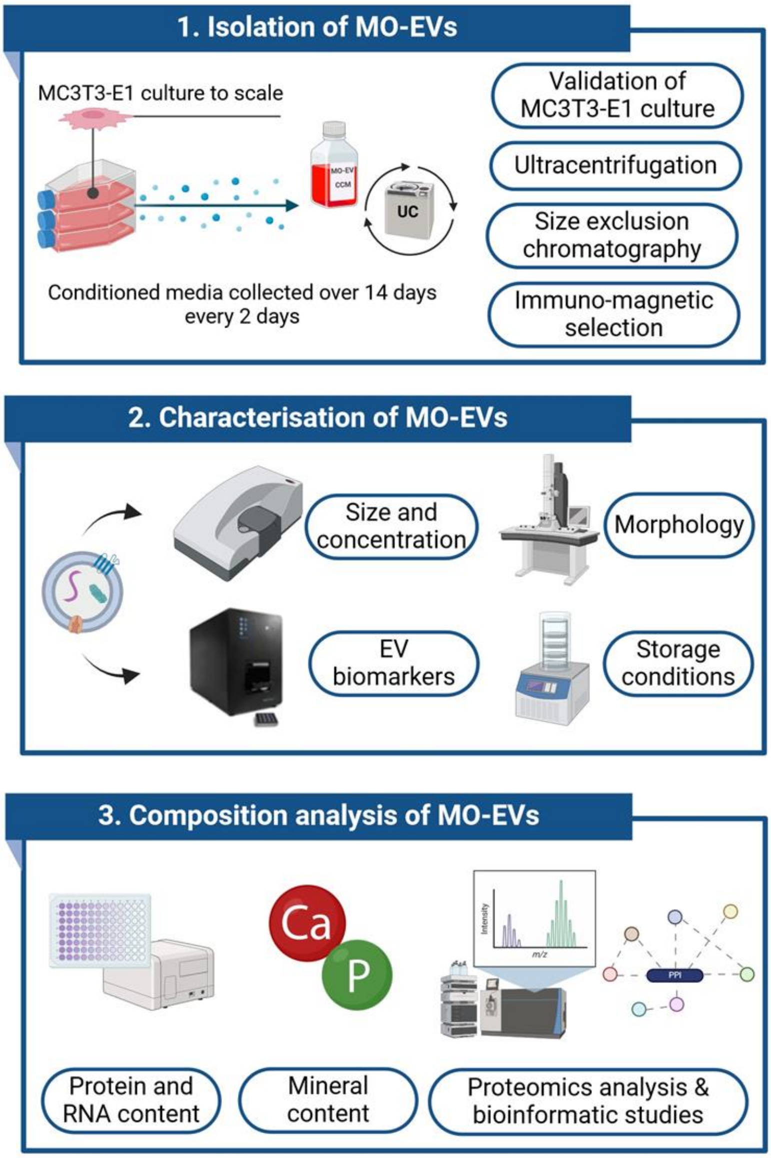

**Figure 3.1. | Schematic representation of experimental work with 1) Isolation of MO-EVs, 2) Characterisation of MO-EVs and 3) Composition analysis of MO-EVs. (Created using Biorender.com)**

## 3.2. Material and methods

Methods used in Chapter III also include methodologies described in the 'General Methodologies' Chapter II, with in particular the cell culture and maintenance of MC3T3-E1 cells (2.2.1.) as well as the Biomineralisation assessment methods (2.2.5.) such as ALP activity (2.2.5.1.), alizarin red staining (2.2.5.2.) and picro sirius red staining (2.2.5.3.).

### 3.2.1. EV isolation methods

For all the following EV isolation methods, MC3T3-E1 cells were cultured at scale in T175 flasks under osteogenic conditions for 14 days. From day 2, the CCM were collected every 48 hours replacing the existing media. After 14 days, the combined CCM collected was centrifugated at 2000 x g for 20 mins to remove cells and large debris from the media and 10,000 x g for 30 mins to remove large particles prior to the performance of the following EV isolation methods.

### 3.2.2. Size exclusion chromatography

To perform size exclusion chromatography, the EV original 70 nm series column were employed (Izon Science, NZ). In sterile conditions, the column was setup vertically and reached room temperature (RT) before use. The column was then flushed with three column volumes (10 mL) of 0.22µm-filtered PBS prior to introducing 0.5 mL of the sample into the loading frit. Using a fraction size of 0.5 mL, the buffer volume was immediately collected with the first 0.5 mL labelled as fraction 1. Each fraction was then separately stored prior to characterisation.

### 3.2.3. Immunomagnetic positive selection

The EasySep™ human pan-extracellular vesicle positive selection kit (STEMCELL Technologies, UK) was used to isolate MO-EVs from CCM. First, 2mL of CCM were incubated with 100 µL of selection cocktail (anti-CD9, -CD63, and -CD81 antibodies) for 10 mins at RT. After being vortexed, 200 µL of RapidSpheres™ solution were then added to the mix and incubated for a further 10 mins at RT. After topping-up the total volume to 2.5 mL with PBS, the tube was placed into an EasySep™ magnet for 5 mins at RT and the supernatant was then discarded by inverting the magnet-tube assembly with a continuous motion. This step was repeated 3 more times with a 1-min magnet incubation step. After removing the tube from the magnet, EVs were resuspended in filtered PBS and ready for downstream analysis.

### 3.2.4. Differential ultracentrifugation

To perform differential ultracentrifugation, CCM was processed through differential ultracentrifugation using a Sorvall WX Ultra Series Ultracentrifuge (Thermo Scientific, UK) associated with a Fiberlite, F50L-8 × 39 fixed-angle rotor (Piramoon Technologies Inc., USA). EVs were separated with a 120,000 x g spin for 70 mins to pellet EVs. This final step was repeated in sterile PBS as a washing step. MO-EV isolate was resuspended in sterile PBS and stored at 4°C for downstream analysis.

### 3.2.5. SP-IRIS analysis via the ExoView platform

The presence of EV surface tetraspanin markers CD9, CD63 and CD81 was determined via the ExoView® Tetraspanin Assay based on Single-particle Interferometric Reflectance Imaging Sensor (SP-IRIS) (NanoView Biosciences, USA) following the manufacturer’s instructions. Microarray chips were pre-scanned using the Exoview R100 (NanoView Biosciences, USA) before 35 µL of EV samples diluted 1:15,000 in incubation solution were pipetted onto each chip. The microarray chip presented with immunocapture spots for CD81, CD9 and HIgG (negative control) in triplicate. The chip was then incubated overnight for 16 h to allow EV capture, and unbound material was then washed with the provided incubation solution for 3 min using a microplate shaker. After a total of 3 washes, the provided tetraspanin antibody panel (anti-CD9, anti-CD63 and anti-CD81) was added to the chip and incubated for 1 h at room temperature under constant mixing using a microplate shaker in the dark. Antibody solution was removed, and 4 subsequent washes were performed as previously. The chip was then carefully dried and scanned using the ExoView R100 using the nScan software (NanoView Biosciences, version 2.8.10). Using IgG spots as isotype control, each spot was then analysed using the NanoViewer software (NanoView Biosciences, version 2.8.10) allowing the fluorescence imaging of captured EVs to quantify their tetraspanin phenotype.

### 3.2.6. Immunoblotting

The procedure was previously used in Immunoblotting analysis was used to confirm the presence of EV as previously described (Nikravesh et al., 2019). Briefly, following the electrophoretic separation of proteins using precast gels (4%-15% Mini-PROTEAN TBX, Biorad, UK), gels were blotted on polyvinylidene difluoride membranes (Fisher Scientific, UK) and blocked with EveryBlot blocking buffer (BioRad, UK). The blots were incubated overnight at 4°C with primary antibodies to Alix (1:1000 dilution, Santa Cruz, USA), Annexin 2 (1:2000 dilution, Abcam, UK), CD9 (1:1000 dilution, Abcam, UK) and calnexin (1:1000 dilution, Abcam, UK). The membranes were incubated with the appropriate secondary antibody, anti-rabbit for Annexin 2, CD9 and calnexin (1:3000 dilution, Cell Signaling, UK), and anti-mouse for Alix (1:3000 dilution, Cell Signaling, UK), for 1 h at room temperature. Chemiluminescence detection of bands were imaged with ChemiDoc XRS+ system (BioRad, UK) by a chemiluminescence reaction using Clarity™ Western ECL substrate (BioRad, UK) and Image Lab software (Life Science Research, BioRad, UK) following supplier's instructions.

### 3.2.7. Exo-ELISA

Enzyme-Linked Immuno Sorbent Assay (ELISA) are powerful tool in EV research usually employed as a rapid way to validate the presence of tetraspanin markers at the surface of EV suspensions without requiring the use of any specialised equipment. Here, the ExoELISA-ULTRA CD63, CD81 and CD9 kits (individual kit per target protein) were used to for the antibody-based quantification of CD63/CD81/CD9-positive EVs (System Biosciences, USA)

BCA assay is performed in order to determine the protein concentration of the EV suspension recommending 1 to 200 µg of protein per well, however, the relative quantity of CD63 in the sample ultimately remain dependent on the protein expression level.

A ExoELISA-Ultra protein standard was provided allowing to generate a standard curve using a CD63/CD81/CD9+ population of EVs of known concentration was then then used to determine the concentration of positive nanoparticles in our samples. Starting with a stock concentration of 4.56 x $10^{10}$ nanoparticles, the 6 standards were then prepared by performing a 1:2 serial dilution to reach 1:64. For both samples and standards, 50 µL of each were added in triplicate to the microtiter plate. The plate was then sealed with an adhesive film prior to start a 1-hour incubation at 37°C. Unbound samples were then removed via plate inversion and 3 subsequent washes were then performed for 5 min using 100 µl of the 1X wash buffer provided.

50 µl of anti-CD63, -CD9 or CD81 primary antibody prepared in blocking buffer (1:200) was added to each well before another 1-hour incubation and washing cycle to remove unbound antibodies. This step was then repeated with the secondary antibody diluted 1:5,000 in blocking buffer. After the final wash, the super-sensitive TMB ELISA substrate was added to each well (50 µl) and the reaction was incubated at room temperature for 15 min using a microplate shaker (low speed, 350 rpm). The reaction was ended by adding 50 µl of stop buffer

to each well and the plate was analysed using the Spark microplate reader (Tecan, CH) by determining the absorbance of each well at 450 nm. Quantitative results were then generated by determining the EV abundance of samples by reading the absorbance at 450 nm on the ExoELISA ultra standard curve.

### 3.2.8. EV storage study

For storage study, EV suspensions of 10 µg of proteins were prepared in 0.5 mL microtubes. For the 4°C and -80°C storage condition groups samples were simply stored at respective temperatures. For freeze-drying, EV samples were placed overnight -80°C after adding sucrose to the EV suspension at a final concentration of 1mM for the samples with cryoprotectant. Following freezing, samples were lyophilised overnight (Lab Series, Labfreez, UK) and dehydrated EVs were stored in a desiccator until downstream analysis where they were re-suspended in filtered PBS.

### 3.2.9. Total EV RNA content

RNA concentrations in MO-EVs was determined after RNA isolation performed using the Qiagen miRNeasy Mini Kit (Qiagen, UK) according to the manufacturers’ protocol and RNA quantity/purity assessed by measuring 260/280 nm absorbance ratio using a NanoQuant plate and a SPARK spectrophotometer.

### 3.2.10. Proteomics analysis

All methodologies below regarding proteomics analysis (3.2.10.1; 3.2.10.2; 3.2.10.3) have been adapted from our published work in Man *et al.* (2021a).

#### *3.2.10.1. Sample preparation*

Protein extraction for proteomic analysis was performed by adding 400 µl acetone (Thermo Scientific, UK) to 100 µl of EVs previously isolated and resuspended in PBS. Samples were vortexed and incubated at -80°C for 1 h. After incubation, the samples were centrifuged at 14,000 g for 10 min. The supernatant was discarded, the pellet dried by inverting and then resuspended in 0.1 M ammonium bicarbonate (Acros Organics, USA), 0.1% RapiGest (Waters Corpo., USA) in LC-MS grade water (Thermo Scientific, UK) to a final concentration of 1 µg/µl. Proteins were denatured with 1.5 µl of 1% (w/v) RapiGest in 50 mM ammonium bicarbonate and incubated at 80°C for 45 min. Following incubation, 100 mM dithiothreitol (1 µl) was added and incubated for a further 30 min at 60°C to reduce the proteins, before being alkylated with 200 mM iodoacetamide (1 µl) at room temperature for 30 min. Trypsin 1:50 (w/w) (Gold Mass Spectrometry grade, Promega, USA) was added to each sample for proteolytic digestion and left to incubate overnight at 37°C. Trifluoroacetic acid was added to a final concentration of 0.5% (v/v) to hydrolyse the RapiGest and heated for a further 45 min at 37°C, before centrifuging for 25 min at 18,000 g. The supernatant was collected and 5 µl aliquoted for LC-MS analysis. Aliquoted samples were diluted 1:4 (v/v) with 15 µl of 0.1% formic acid (v/v) to provide a working solution of 200 ng/µl.

#### *3.2.10.2. LC-MS analysis*

Extracted peptides obtained from the isolated vesicles were analysed by one dimensional nanoscale reversed-phase (RP) chromatography using an ACQUITY M-Class UPLC (Waters Corp., USA) configured for trap and elute. Peptides were loaded (1 µl injection, 200 ng on-column) onto a Symmetry C18 5 µm, 2 cm × 180 µm pre-column (Waters Corp., USA) with aqueous 0.1% (v/v) formic acid using a flow rate of 15 µl/min for 2 min. Mobile phases consisted of water with 0.1% (v/v) formic acid (mobile phase A) and acetonitrile with 0.1% (v/v) formic acid (mobile phase B). Peptides were eluted from the pre-column and separated over a 90 min gradient using a HSS T3 C18 1.7 µm, 15 cm × 75 µm analytical column (Waters Corp., USA). The gradient consisted of 3 - 40% mobile phase B over 60 min at a flow rate of 400 nl/min, whilst maintaining the analytical column temperature at 35°C. Lock mass consisting of [Glu1] -Fibrinopeptide was delivered to the reference sprayer of the MS source using the M-Class Auxiliary Solvent Manager with a flow rate of 1 µL/min.

MS data were collected on a Synapt XS mass spectrometer (Waters Corp., UK) operated in positive electrospray ionisation (ESI) mode with a nominal resolution of 25,000 FWHM (V optics). The capillary voltage was 3.2 kV, cone voltage was 35 V and source temperature was set at 100°C. Data were acquired over 50 - 2000 Da mass range with a scan time of 0.5 s. All mass spectral data were acquired in continuum mode using UDMSE to obtain fragmentation data simultaneously (Distler *et al.*, 2016; Rodriguez-Suarez *et al.*, 2013). Function one (low energy) data was collected using a constant trap and transfer energy of 6 eV whilst the second (high energy) function consisted of a transfer collision energy ramp of 19 to 45 eV. For mass accuracy, [Glu1] -fibrinopeptide (m/z = 785.8426) was acquired as lock mass at a concentration of 100 fmol/µl (in 50:50 $CH_3CN/H_2O$, 0.1% formic acid). Lock mass scans were collected every 60 s and averaged over 3 scans to perform mass correction. The time-of-flight mass analyser was externally calibrated over the acquisition mass range (50 - 2000 Da) before analysis with a NaCsI mixture (Waters API MS Calibration Solution, 2 µg/µl sodium iodide: 50 ng/µl cesium iodide in 50:50 isopropanol:water, Waters Corp., USA). These data were collected using MassLynx v 4.1 software (Waters Corp., UK) in a randomized order with three technical replicates acquired per sample.

### *3.2.10.3. LC-MS data analysis*

Progenesis QI for Proteomics (Nonlinear Dynamics, UK) was used to process all data. Retention time alignment, peak picking and normalization were conducted to produce peak intensities for retention time (Rt) and m/z data pairs. Data were searched against reviewed entries of a Mus musculus UniProt database (17,048 reviewed entries, release 2020_05) to provide protein identifications with a false discovery rate of 1%. A decoy database was generated as previously described (Li *et al.*, 2010) allowing for protein/peptide identification rates to be determined. Peptide and fragment ion tolerances were determined automatically, and searches allowed for one missed cleavage site. Carbamidomethyl of cysteines was applied as a fixed modification, whilst oxidation of methionine and deamidation of asparagine/glutamine were set as variable modifications.

### *3.2.10.4. Protein-protein interaction (PPI) network and gene ontology (GO) analysis*

Following the analysis of the raw data allowing the presentation of the most abundant proteins, protein-protein interaction network was generated using the STRING platform (https://string-db.org/cgi/input.pl) in its version 11.0. The list of the annotated list of proteins was submitted to the tool to analyse protein-protein interactions with the parameter set to the highest confidence score (0.7) to obtain the most robust evidence-based results. From the analysis, the gene ontology terms were determined and categorised based on their link with biological processes, molecular function and cellular component.

### 3.2.11. Calcium and Phosphate detection

Calcium and Phosphate detection in EV samples were performed using separate colorimetric based-assays. Calcium detection was determined using the MAK022 colorimetric calcium assay (Sigma-Aldrich, USA) following the manufacturer's instructions. Briefly, calcium standards were prepared from the provided 500 mM calcium standard stock with a concentration range from 0 to 2 µg per well. MO-EVs were diluted 1:10 in freshly filtered PBS (w/o Ca/P) for the test. In a 96-well plate, 50 µL of sample or standard were added to each well to which 90 µL of chromogenic reagent and 60 µL of calcium assay buffer were added to start the reaction. After gentle mixing on a plate shaker, the reaction was incubated for 10 min at room temperature while being protected from light. The absorbance of each well was then determined at 575 nm using the SPARK microplate reader (TECAN, CH).

Regarding phosphate detection, the MAK308 phosphate assay kit was used (Sigma-Aldrich, USA). EV samples were prepared in the same way as previously described. Phosphate standards were prepared using the provided 40 µM phosphate premix solution to obtain standards with concentrations ranging from 0 to 40 µM. In a 96-well plate, 50 µL of sample or standard were added to each well to which 100 µL of the Malachite Green Reagent was added to start the reaction. The plate was then incubated for 30 min at room temperature with the absorbance measure at 620 nm for this assay. For both test the final concentrations in calcium and phosphate were calculated using the respective standard curves.

## 3.3. Results

### 3.3.1. Validation of the mineralisation status of osteoblasts

First, the mineralisation potency of MC3T3-E1 cells was assessed to validate our culture environment comparing the effects of basal and osteogenic media. To this end, both ALP activity and calcium deposition was assessed overtime using the two different culture conditions. In Figure 3.2., an increase of ALP activity is observed overtime only under osteogenic conditions with a significantly greater ALP activity after 14 days of culture compared to 7 days only (p<0.001) (Fig 3.2.). Similarly, the quantification of alizarin red (AR) staining showed an increased amount of calcium deposition in osteogenic conditions at day 21 compared to basal conditions (p<0.001).

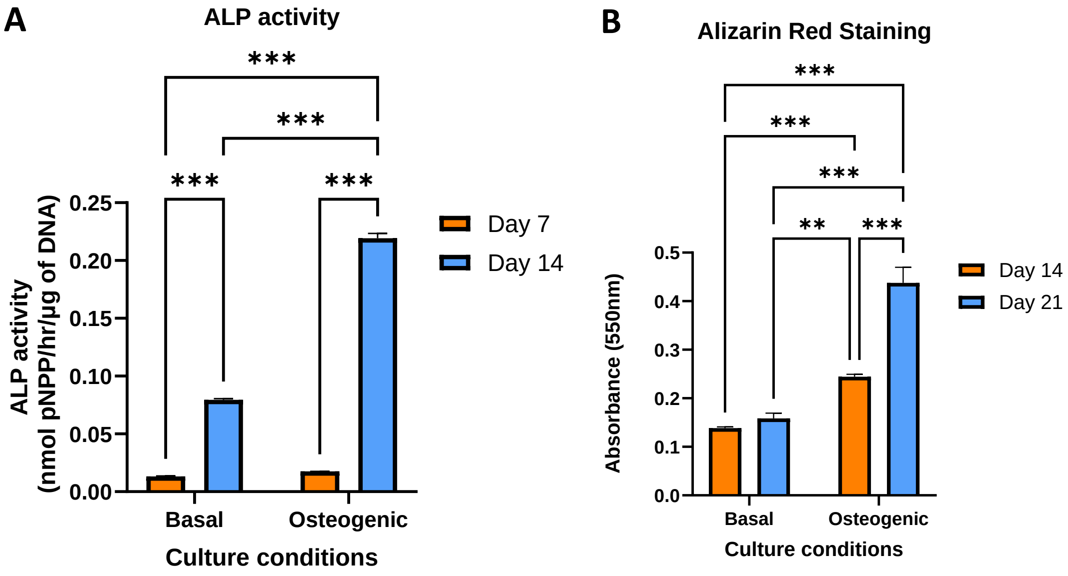

**Figure 3.2. | Validation of the mineralisation status of MC3T3-E1 cells.** Cells were treated by basal or osteogenic media every 2 days over 21 days with ALP activity assessed at Day 7 and 14 and Alizarin Red staining assessed at day 14 and 21. **A)** ALP activity after 7 and 14 days of culture. **B)** Calcium deposition via Alizarin Red staining quantification after 14 and 21 days of culture. Data are expressed as mean ± SD (n=3). *P ≤ 0.05, **P ≤ 0.01 and ***P ≤ 0.001.

### 3.3.2. Comparison of MO-EV separation methodologies

To determine the best route to consistently isolate MO-EVs, an initial screening of three methods was performed comparing the yield of ultracentrifugation (UC), size-exclusion chromatography (SEC) and immune-magnetic positive selection (I-MAG). As showed in Figure 3.3., the EV isolation via SEC resulted in the collection of 23 fractions (F) of 0.5 mL each. Both BCA and NTA analysis was performed to determine the total protein concentration and the nanoparticle concentration of each fraction, respectively. A spread distribution of protein concentrations was observed from F14 to F23 with a peak at F20 displaying a protein concentration <600µg/mL. Even if total protein concentration is usually used to quantify EVs, nanoparticle enriched fractions from F12 to F16 were detected with low protein content or even in absence of proteins in F12 or F13.

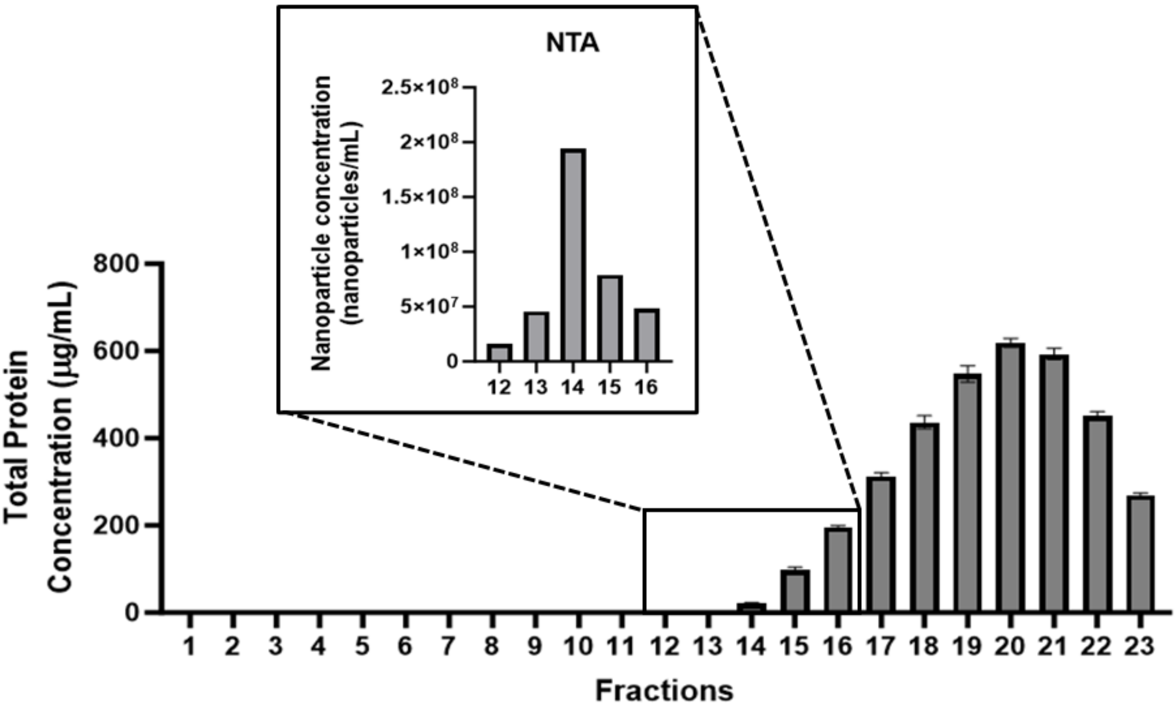

**Figure 3.3. | MO-EV isolation via size exclusion chromatography and characterisation of resulting fractions via BCA and NTA analysis.** The main graph showcases the protein concentration (BCA) of each SEC fraction whereas the insert graph displays nanoparticle concentrations (NTA) for fractions 12 to 16. Data are expressed as mean ± SD (NTA, n=1; BCA, n=3).

For both UC and I-MAG, the final step of isolation only consisted of a single pellet to resuspend. In Figure 3.4., the relative yield obtained for each separation method was compared once normalised to the volume of CCM processed. The results showed that I-MAG significantly isolated a greater number of nanoparticles compare to SEC (p<0.001) and UC (p<0.001) with over 3 x $10^9$ nanoparticles obtained per mL of CCM. UC and SEC exhibited similar yields with >10-fold decrease in yield compared to I-MAG.

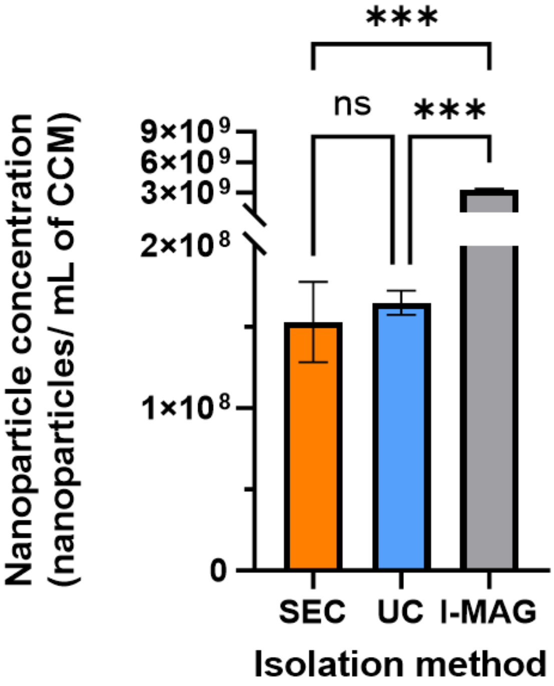

**Figure 3.4. | Comparison of the yield of UC, SEC and I-MAG for the isolation of EVs via NTA.** MO-EV conditioned medium processed using the 3 different isolation methods: size exclusion chromatography (SEC), ultracentrifugation (UC) and Immune-magnetic positive selection (I-MAG) and yield was assessed via NTA with nanoparticle concentrations being normalised to 1 mL of conditioned media for direct comparison. Data are expressed as mean ± SD (n=3). *P ≤ 0.05, **P ≤ 0.01 and ***P ≤ 0.001.

### 3.3.3. Physico-chemical properties of UC-isolated MO-EVs

Based on the comparative isolation previously performed, the ultracentrifugation method has been selected as the only procedure to separate MO-EVs. Therefore, all future MO-EV reference for the rest of this body of work has been obtained via ultracentrifugation including all the following characterisations.

#### *3.3.3.1. Transmission Electronic Microscopy*

To assess the morphological features of isolated EVs, TEM was employed to image the vesicles allowing a nanometre resolution. Without using negative staining, clear images were obtained with a good contrast from background. As presented in Figure 3.5A & 3.5B, single EVs were imaged exhibiting a round morphology with an approximate 200 nm-diameter. Additionally, the lipid bilayer membrane can also be defined upon the position of the focus knob as shown in Figure 3.5C. In rarer occasions as displayed in Figure 3.5D, the EV can be found attached to fibres which are most likely collagen fibres from the ECM as EVs are notoriously capable to bind to matrices through their surface membrane proteins such as integrins. Overall, these observations confirmed the isolation of MO-EVs via our differential ultracentrifugation protocol.

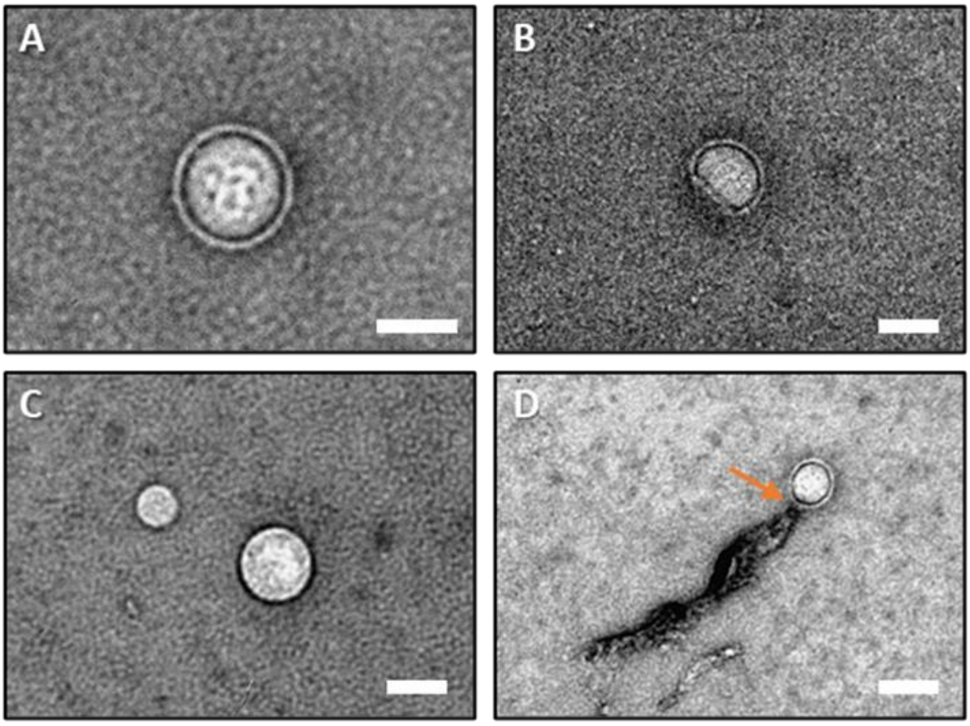

**Figure 3.5. | Transmission electron microscopy images of MO-EVs. A)B)C)** Observations of single vesicles. **D**) Observation of a vesicle associated with a fragment of extracellular matrix. The ECM fibre appears to be attached to the membrane of the vesicles (orange arrow). Scale bars = 200 nm.

#### *3.3.3.2. Concentration, Size, and ζ-potential*

To determine the nanoparticle concentration and average diameter of MO-EVs, NTA was performed with an LM10 system (Malvern, UK) allowing real-time dynamic visualisation of the nanoparticles using a laser light source to track their Brownian motion. MO-EVs exhibited a high concentration with 3 x $10^{10}$ nanoparticles per mL of EV isolate, thus, requiring dilution for the analysis. They also presented with a typical EV size with an average diameter of 213 ± 3 nm (Fig 3.6A). Using DLS, the average diameter of MO-EVs was determined at 116 ± 3 nm (Fig 3.6B) with an associated PDI of 0.226 ± 0.002 (A.U.) (Fig 3.6C). Both methods are widely used and established gold standards with expected variation in size measurements between them due to differences in terms of size distribution determination (Maguire *et al.*, 2018). After MO-EV analysis, a negative Zeta potential at – 10.9 ± 0.9 mV was measured (Fig 3.6D).

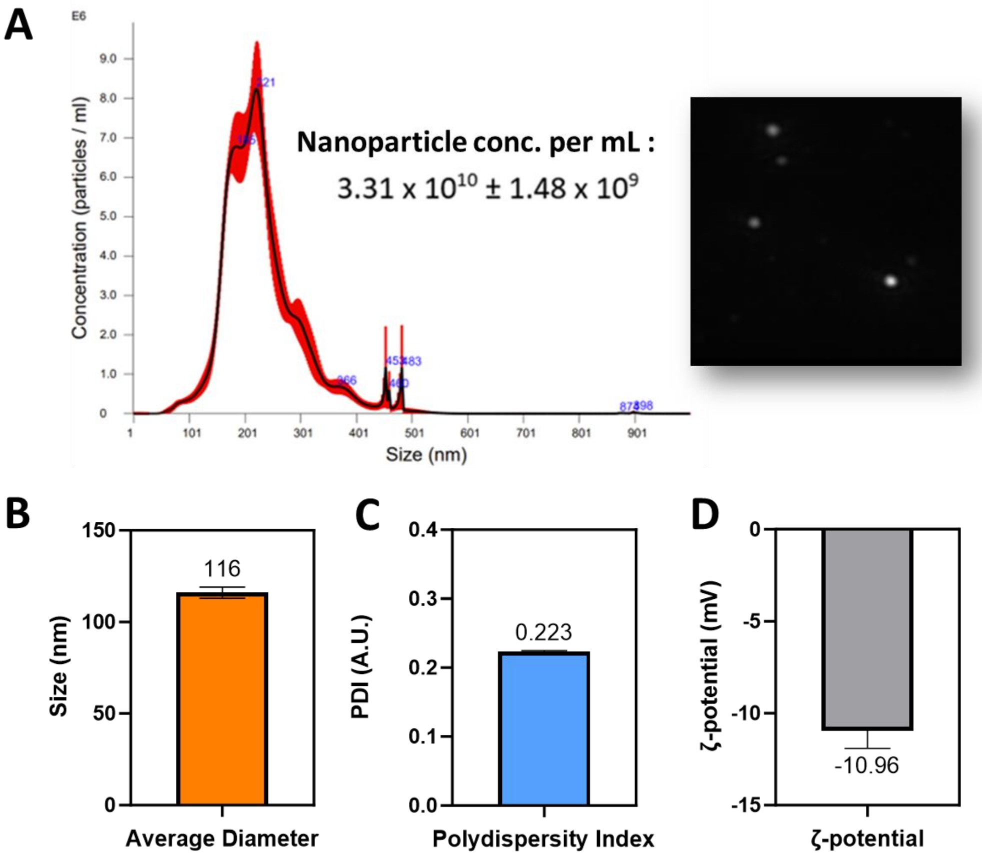

**Figure 3.6. | Determination of MO-EV concentration, size, PDI and ζ-potential via NTA and DLS.** A) Size distribution profile via NTA. B) Size via DLS. C) PDI via DLS. D) ζ-potential via DLS. Data are expressed as mean ± SD (n=3). $^{*}P \leq 0.05$, $^{**}P \leq 0.01$ and $^{***}P \leq 0.001$.

### 3.3.4. Validation of the presence of EV biomarkers

As underlined within the MISEV guidelines, further investigations need to be performed to assess the presence of makers enriched in the EV suspensions allowing to validate the isolation of the nanoparticle population of interest (Welsh *et al.*, 2024).

### *3.3.4.1. Immunoblotting*

Immunoblotting was used to determine the presence of CD9, Annexin A2 and Calnexin in both the UC-obtained MO-EV isolate and the parental cell lysate. As displayed in Figure 3.7., MO-EVs are found positive to both CD9 and Annexin A2 in the absence of Calnexin, whereas the cell lysate presented with Calnexin and Annexin A2 bands in the absence of CD9 (Fig 3.7.).

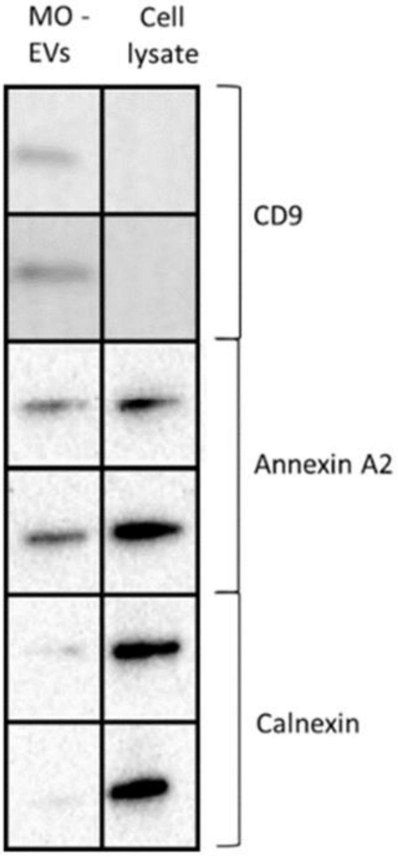

**Figure 3.7. | Comparative immunoblotting analysis of MO-EVs and their parental cell lysate for the detection of CD9, Annexin A2 and Calnexin.** Data shown allow the qualitative observation of the relative presence or absence of proteins of interest without pixel quantification (n=3).

### *3.3.4.2. Exo-ELISA*

Using an Exo-ELISA enabled the determination of tetraspanin markers at the surface of MO-EVs. The specificity of the Exo-ELISA is the existence of an EV-based standard correlating the ELISA signal to a pre-defined EV number allowing improved quantification. MO-EV analysis revealed the presence of the 3 tetraspanin proteins of interest (CD9, CD63 and CD81) with a significantly greater presence of CD81 compared to the other two proteins (P ≤ 0.01) (Fig 3.8.).

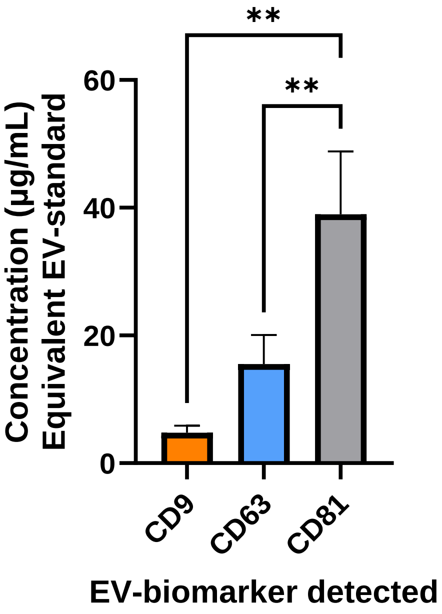

**Figure 3.8. | Exo-ELISA quantification of the presence of the tetraspanin CD9, CD63 and CD81 in MO-EVs.** Each detection was performed using a protein-specific separate kit. Data are expressed as mean ± SD (n=3). *P ≤ 0.05, **P ≤ 0.01 and ***P ≤ 0.001.

### *3.3.4.3. ExoView Platform as an EV characterisation tool*

Prior to any fluorescence detection, the presence of captured nanoparticles onto the spots of the chips have assessed using SP-IRIS detection. This analysis presented the physical attachment of nanoparticles detected at the surface of the chip at each specific capture spot.

In the absence of grafting onto the control IgG spot, nanoparticles were found to be captured onto both CD81 and CD9 spots with concentrations ranging from 2 to 6 x$10^6$ nanoparticles per mL (Fig 3.9A). Moreover, significantly more nanoparticles were capable of binding onto CD9 spots compared to CD81 (Fig 3.9B). Particle size was evaluated at around 60 nm on both capture spots (Fig 3.9B) and no traces of contaminants were found on the spots (Fig 3.9C).

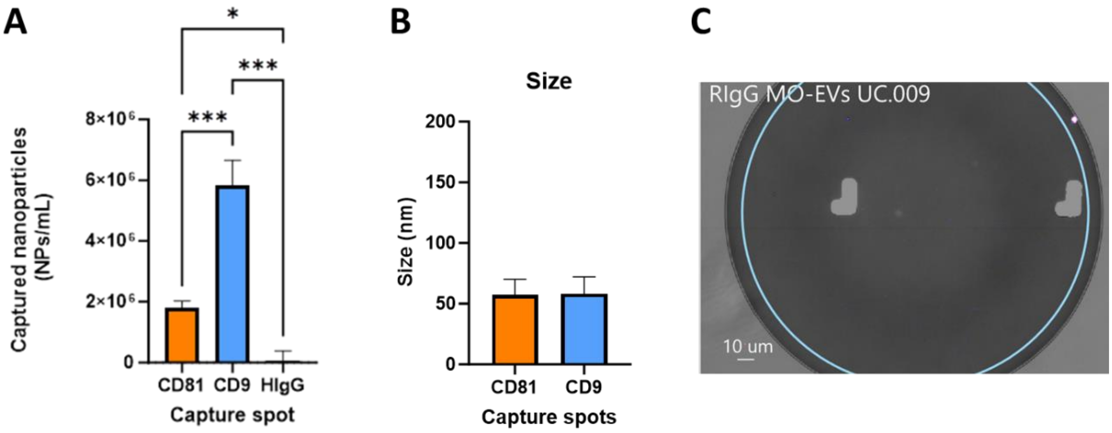

**Figure 3.9. |Interferometry analysis of the ExoView chip prior fluorescent detection.** This analysis describes the laser-based detection of MO-EVs captured onto the chip without fluorescence detection allowing to determine EV size and number. **A)** Determination of the concentration of captured nanoparticles. **B)** Nanoparticle size determined by interferometry. **C)** Post-scan image of IgG control spot. Data are expressed as mean ± SD (n=3). *P ≤ 0.05, **P ≤ 0.01 and ***P ≤ 0.001.

Following this initial assessment, fluorescence microscopy integrated to the ExoView platform was used to determine the presence of CD9, CD63 and CD81 at the surface of the captured nanoparticles. First, qualitative observations showed the presence of well-distributed fluorescent dots across the surface of each tetraspanin-decorated capture spot with no visible detection observed in IgG control (Fig 3.10A).

The quantification of the signals at the single particle level across all the spots demonstrated that both CD81 and CD9 captured particles were found positive to all 3 markers with a particular enrichment in CD81 (Fig 3.10B). Still being validated, an innovative colocalization function allowed to investigate the presence of 1, 2 or 3 markers per vesicle to determine their colocalization levels. It showed that dual-positivity was detected as less than 10% of total particles and only traces of triple-positive particles was found. (Fig 3.10C).

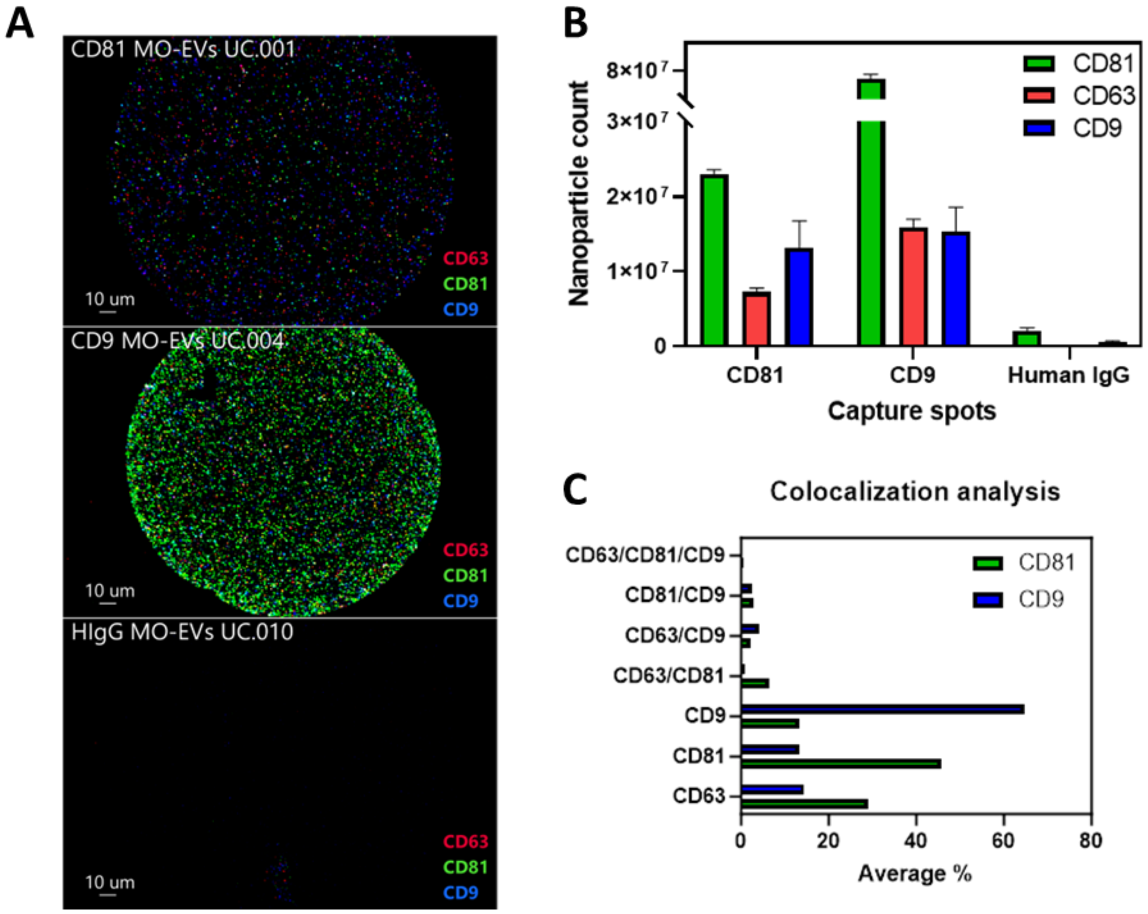

**Figure 3.10. | Determination of the presence of CD9, CD63 and CD81 at the surface of MO-EVs via SP-IRIS. A)** ExoView fluorescence images of capture spots for the detection of CD9, CD63 and CD81. **B)** ExoView analysis results and **C)** Colocalization analysis. Data are expressed as mean ± SD (n=3).

### 3.3.5. Assessment of MO-EV storage conditions

The influence of storage on MO-EVs stability has been assessed using 4 different storage conditions: in suspension at 4°C, in suspension at -80°C, freeze-dried without cryoprotectant and freeze-dried using sucrose as a cryoprotectant (1 mM). The size of MO-EVs for each storage condition was detected each week over a 4-week period. The DLS analysis performed each week showed that there was a constant augmentation of the size of the nanoparticles over the first 3 weeks for the all the storage conditions (Fig. 3.11.). However, it is after four weeks that the average diameter of the vesicle population went above the 1 µm threshold for all storage conditions except when EVs were freeze-dried using a cryoprotectant.

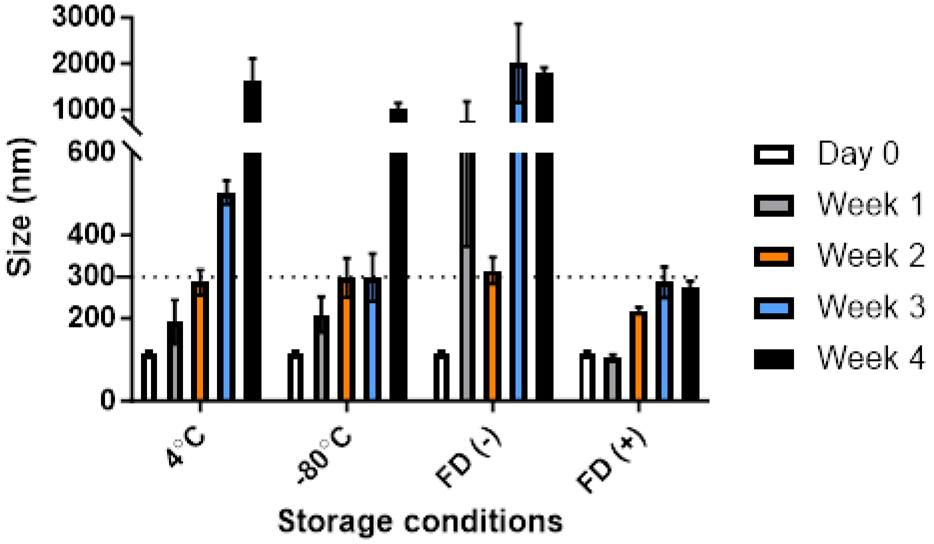

**Figure 3.11. | Storage study of MO-EVs over a 4-week period using 4 different storage conditions via A) DLS analysis and B) total protein content.** 4°C = in suspension at 4°C. -80°C = in suspension at -80°C. FD - = freeze-dried without cryoprotectant and FD + = freeze-dried using sucralose as a cryoprotectant (sucralose – 1 mM) (n=1).

### 3.3.6. MO-EV composition analysis

After the validation of the correct isolation of EVs via ultracentrifugation and the first insights obtained via confirming typical physico-chemical properties as well as the presence of EV-biomarkers, the composition of these vesicles has been investigated further by determining their protein composition as well as their mineral content to obtain a better understanding of their potential mechanism of action.

#### *3.3.6.1. Total protein and RNA content*

Total protein concentration was determined via BCA assay and MO-EVs exhibited a concentration of 601.6 ± 30.7 µg/mL (Fig 3.12A). After isolation from MO-EVs, total RNA content was calculated by measuring 260/280 nm absorbance ratio and a concentration of 1.15 ± 0.65 µg/mL was determined (Fig 3.12B).

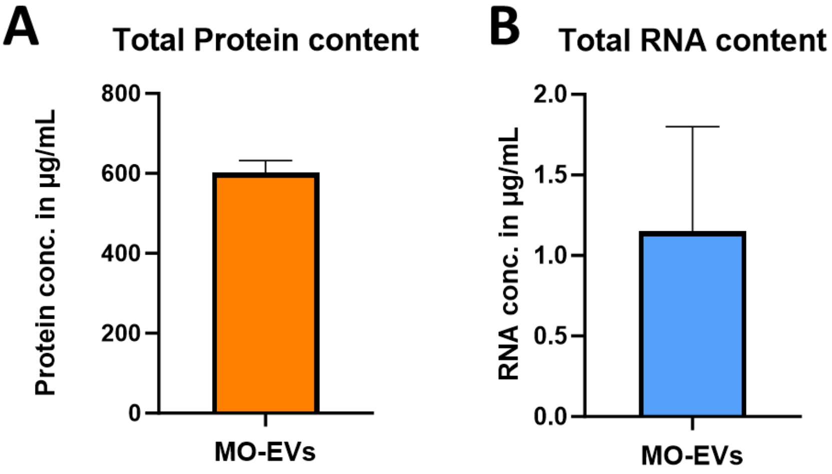

**Figure 3.12. | Quantification of total protein and RNA content in MO-EVs. A)** Total protein concentration determined via BCA assay. **B)** Total RNA concentration determined via NanoQuant™. Data are expressed as mean ± SD (n=3).

### *3.3.6.2. Proteomics analysis to obtain a detailed overview of MO-EV protein composition*

Using UC-separated MO-EV samples, the proteome of MO-EVs were determined using a label free LC/MS approach. Proteins identified were included when appearing in at least 2 samples out of three with > 2 spectral counts in at least one repeat. The use of a protein database for identification revealed the presence of a total of 1404 proteins each associated with a description name from the database and a relative abundance level (mean ± SD) ranging from 2.5 A.U. with XK-related protein 5 to 408988 A.U for COG1. To only focus on the most abundant proteins found in MO-EVs, an abundance threshold was set at 15,000 A.U. reducing the number of proteins of interest from 1404 to 279. Among them the top 15 most abundant proteins have been displayed (Fig 3.13.)

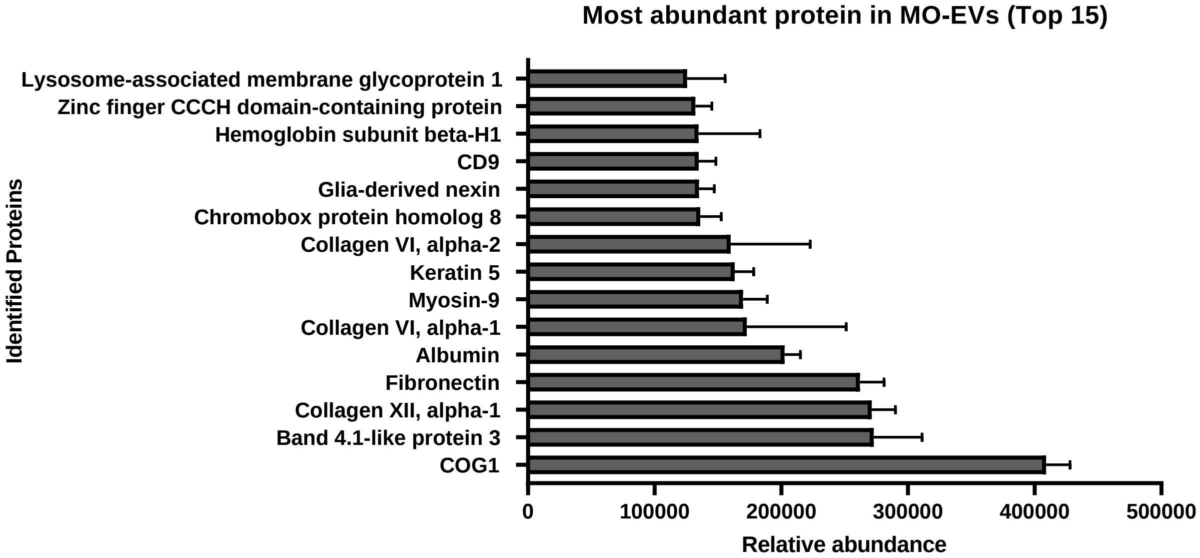

**Figure 3.13. | Most abundant proteins (top 15) determined via protemics analysis.** Data are expressed as mean ± SD (n=3).

After this shortlisting of proteins to the most abundant ones found in MO-EVs, specific proteins of interest have been grouped when belonging to the same protein family. Interestingly, 10 different tetraspanin proteins were detected including TSPAN 4, 6 and 14 as well as the cluster of differentiations 5, 9, 44, 63, 81, 109 and 151 (Fig 3.14A). Moreover, 7 members of the annexin family were found among the most abundant proteins including annexin 2, 3, 4, 5, 6 and 11 (Fig 3.14B). Finally, collagen I, VI and XII were also richly found in MO-EVs (Fig 3.14.C).

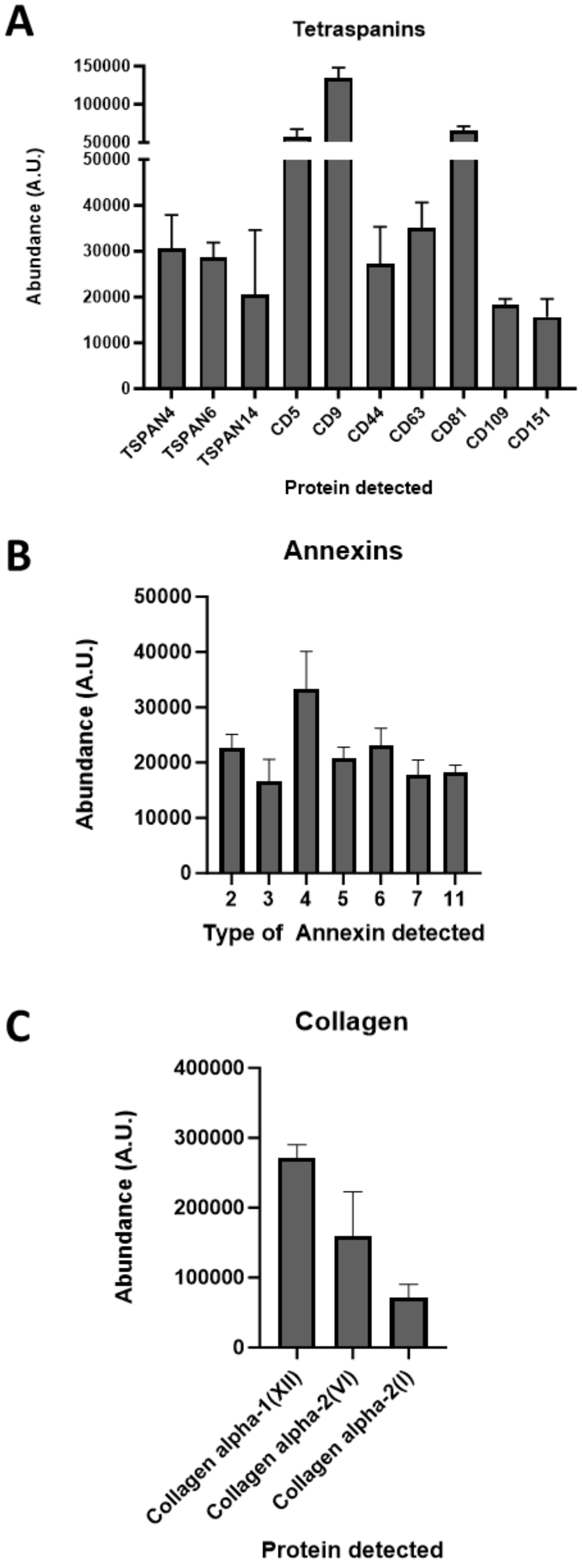

**Figure 3.14. | Relative abundances of proteins belonging to the (A) tetraspanins, (B) annexins and (C) collagen family of proteins among the most abundant proteins identified in MO-EVs.** Data are expressed as mean ± SD (n=3).

The open access databases Vesiclepedia and Exocarta have been used to obtain a list of the 100 most abundant proteins found in all EVs present in each database. By cross referencing these lists with our population of interest, a Venn diagram was produced (Figure 3.15). This revelead that the two online databases shared close to 50% of their most abundant proteins, however, when including the 279 most abundant proteins of our EV population, the three databses only shared 28 proteins in common which mainly corresponded to common EV biomarkers such as CD9, CD81 or Albumin.

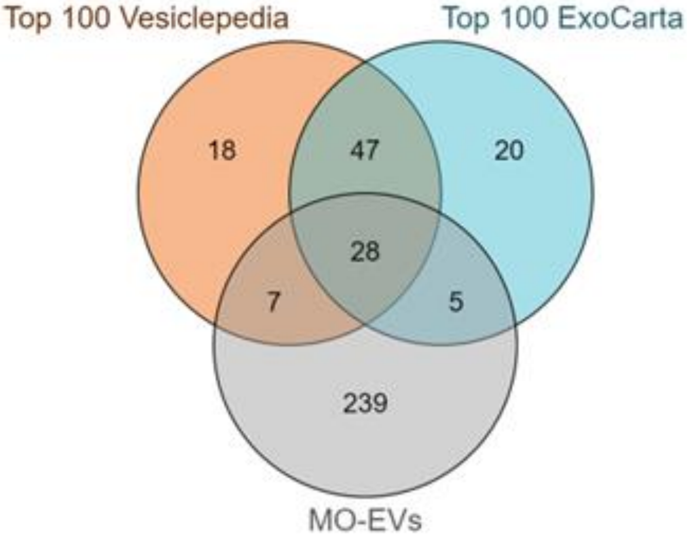

**Figure 3.15. | Venn diagram for the comparison of the most abundant proteins found in MO-EVs to the 100 most abundant proteins found in the databases Vesiclepedia and Exocarta.**

Using the list of the 279 most abundant proteins found in MO-EVs, a protein-protein interaction network was generated via the STRING platform using the highest level of evidence to connect proteins predicting associations based functional associations (Fig 3.16.) Fibronectin and albumin are the most connected proteins present at the center of the network. Most proteins are connected to a maximum of 1 or 2 other proteins leading to the absence of clear specific clusters.

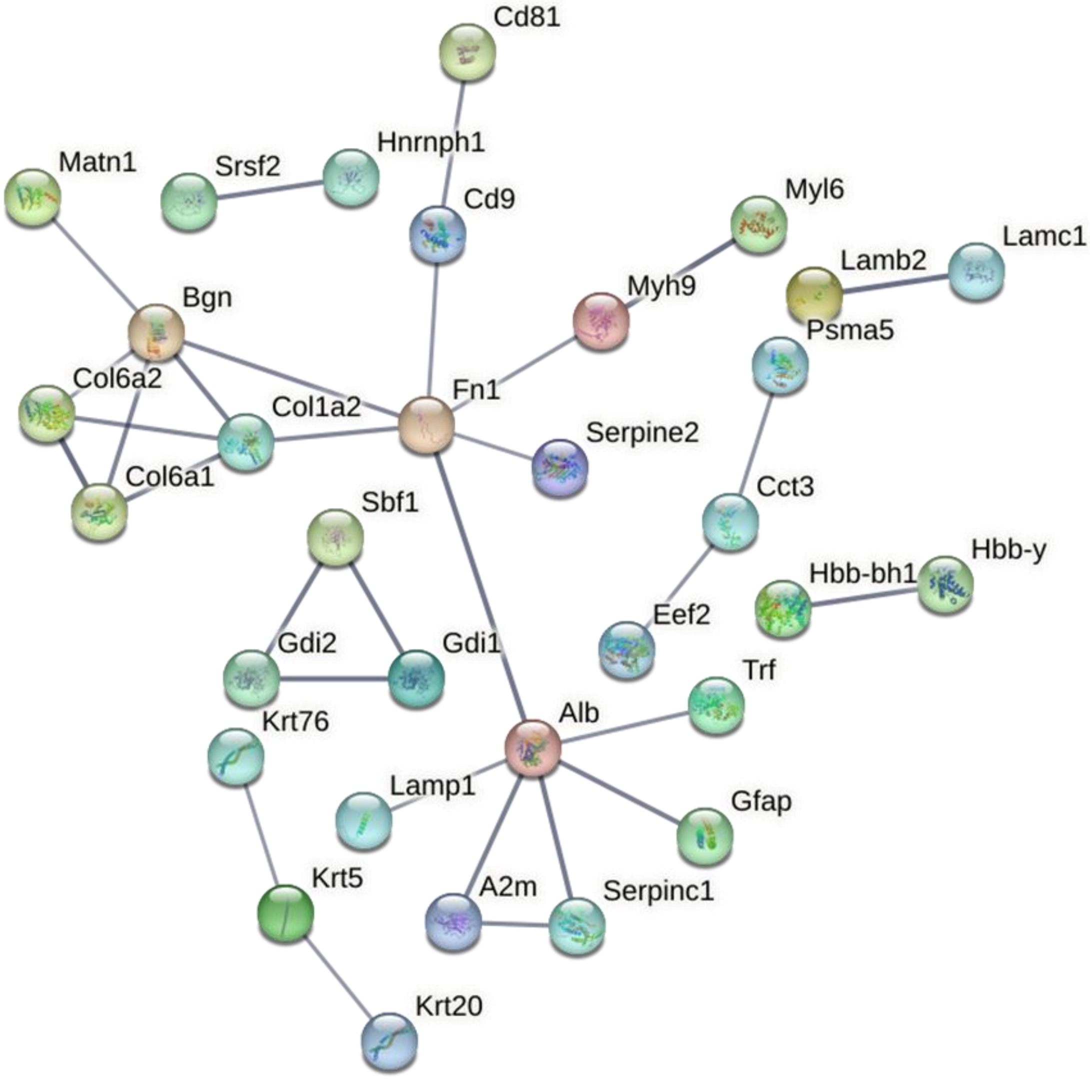

**Figure 3.16. | Protein-protein interaction network of the most abundant proteins found in MO-EVs.** The network displays 33 proteins using the strongest level of evidence and the highest level of confidence where evidence of protein interaction creates a link between the proteins' schematic representations, thus presenting a network.

Gene ontology analysis was perfomed looking at the 279 most abundant proteins found in MO-EVs. These proteins were found to be annotated with GO functional annotations. In Figure 3.17., the top 10 GO terms for biological processess (Fig 3.17A), molecular function (Fig 3.17B) and cellular component (Fig 3.17C) are presented.

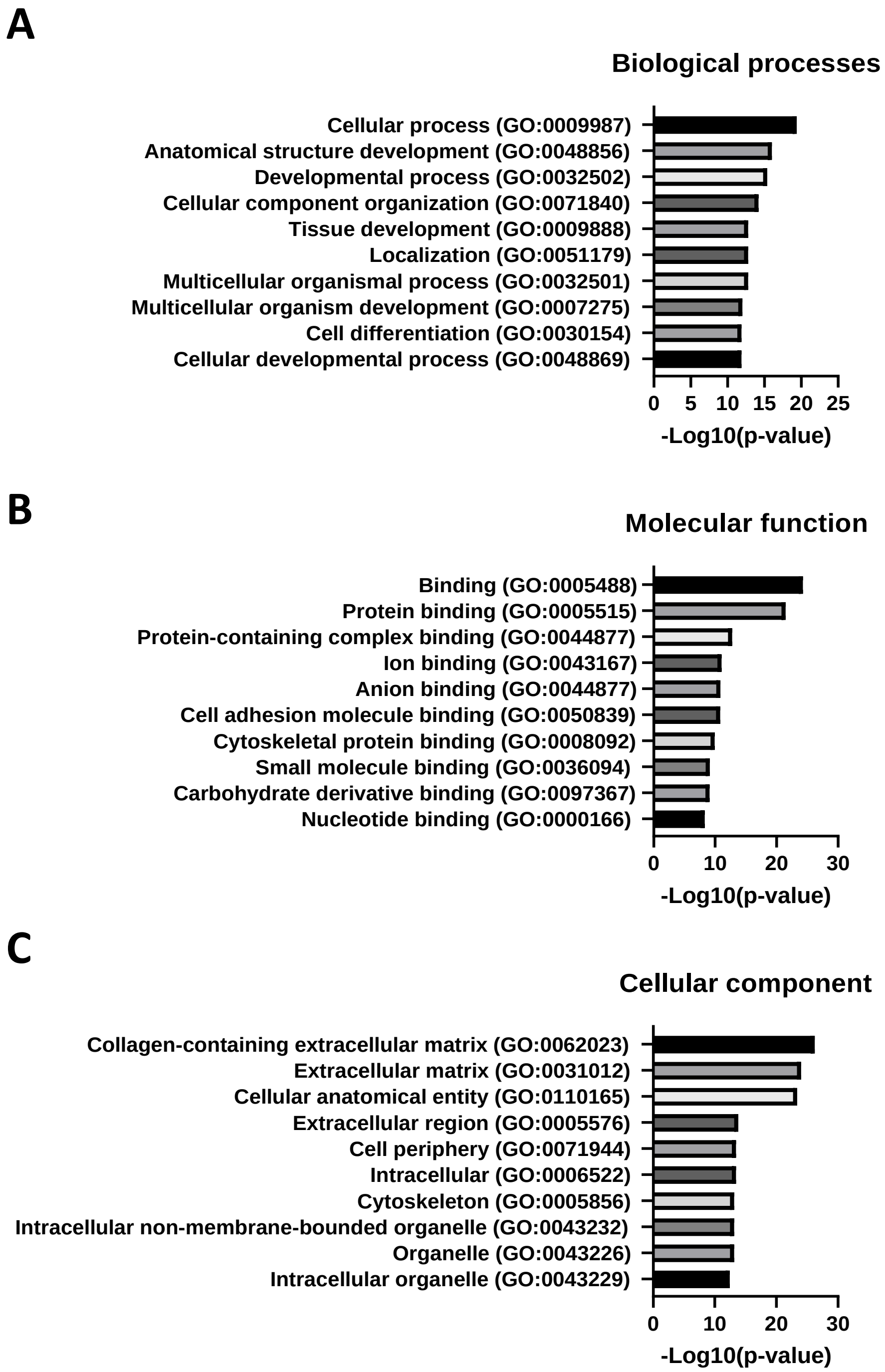

**Figure 3.17. | Gene ontology analysis of the most abundant proteins identified in MO-EVs**. Top 10 GO terms related to **(A)** Biological processes, **(B)** Molecular function and **(C)** Cellular component were presented.

### *3.3.6.3. Calcium and phosphate concentrations*

The inorganic content of MO-EVs has been investigated for the first time by assessing the presence of calcium and phosphate in the MO-EV isolate as an indicator of mineral content. PBS has been used as a control to validate the concentration detected for each component with known concentrations in calcium and phosphate in PBS(+). Calcium levels in MO-EVs were determined at 122.8 ± 30.2 mg/mL (Fig 3.18A). Regarding phosphate, the concentrations was evaluated at 963.7 ± 38.7 µM. In both cases these concentrations were significantly greater than PBS(-) (P<0.001) (Fig 3.18B).

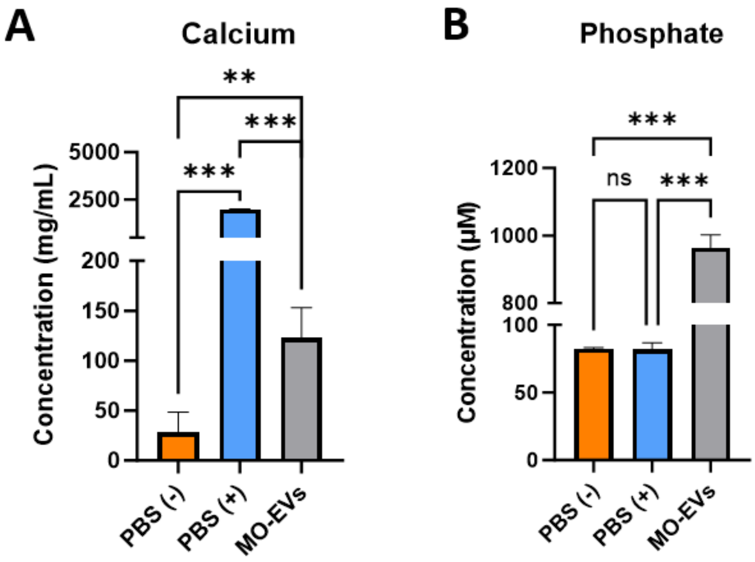

**Figure 3.18. | Determination of the mineral content of MO-EVs. A)** detemination of calcium levels **B)** determination of phosphate levels. Data are expressed as mean ± SD (n=3). *P ≤ 0.05, **P ≤ 0.01 and ***P ≤ 0.001.

## 3.4. Discussion

### ***MC3T3-E1 cells were chosen as a suitable osteoblast model validating their mineralising potency.***

The choice of using MC3T3-E1 cells as our osteoblast model was critical as it would establish the foundation for the rest of the research project.

Among alternative models, the differentiation of MSCs into osteoblasts or the direct isolation of primary osteoblasts offers more physiological relevance, however, sourcing remained limited with higher cost and lower cell numbers (Lindner *et al.*, 2010; Tanaka *et al.*, 2000). Other cell lines were also considered as potential candidates such as human immortalised osteoblast precursors h-MS(2-15) (Hicok *et al.*, 1998), murine stromal cells ST-2 having an osteoblastic phenotype (Otsuka *et al.*, 1999) or the osteosarcoma cell lines such as SAOS-2 or MG-63 (Müller *et al.*, 2016; Staehlke *et al.*, 2019).

As a cell line, MC3T3-E1 has been widely studied in terms of cellular response (Izumya *et al.*, 2021) but also in terms of the EV populations these cells secrete in osteogenic conditions from both our group (Man *et al.*, 2021a; Man *et al.*, 2022c) and beyond (Holkar *et al.*, 2024; Wei *et al.*, 2019; Davies *et al.*, 2023). As the most used model for MO-EV research, it was decided to build on the strong foundations of information present in the literature without introducing cellular origin as a new variable.

In Figure 3.2, MC3T3-E1 demonstrated their osteogneic potency *via* an increase of both ALP activity and calcium deposition under osteogenic conditions compared to basal media. From this first experiement, the mineralising capacity of MC3T3-E1 cell was validated, allowing the culture to scale in order to obtain desired CCM.

### ***Ultracentrifugation was selected as the routine method for MO-EV isolation.***

Regarding the choice of isolation methods, the comparison between size exclusion chromatography, ultracentrifugation and immuno magnetic selection showed a greater yield obtained by the latter method with a total nanoparticle concentration superior to 3 x $10^9$ nanoparticles per mL of CCM. Notably, no significant difference of yield was observed between size exclusion chromatography and ultracentrifugation, with both presenting a yield >10 fold lower than immunomagnetic separation. Despite UC not exhibiting the greatest number of EVs per mL CCM, there is numerous other reasons for selecting it as the isolation method moving forward. In the case of this study, the culture of mineralising osteoblasts over two weeks led to a need for large volumes of media, typically 500 mL for a single batch. Based on this criteria alone, ultracentrifugation is the only method allowing up to 200 mL of media to be centrifuged at once (based on rotor availability) compared to the 0.5 mL loading bay of the chromatography column or the 2 mL sample size used for the magnetic separation. Therefore this criteria made UC the only approach to process larger volumes of media in a practical way for routine isolation (Konoshenko *et al.*, 2018). Additionally, both size exclusion chromatography and immuno magnetic separation represent important consumable cost to routinely isolate vesicles especially in line with the long term needs of a doctoral project. Finally, even if separating EVs via magnetic selection was the easiest protocol to run as well as the method procuring the most nanoparticles, EVs attached to the magnetic beads via antibody binding results in a current incapacity to separate the EVs from the beads themselves, therefore preventing the use of EVs for most downstream uses aside from composition analysis. However, this is subject to evolution and new approaches utilising weaker DNA-linkers for antibody-based capture might allow the release of intact particles (Brambilla *et al.*, 2021).

Thus, despite attractive advantages regarding their purification efficiency and yield, both size exclusion chromatography and immuno-selection were excluded and all EVs moving forward were isolated using UC.

Importantly, a single pan-method for EV isolation does not exist, and here, UC has been carefully chosen based on EV final use (Clos-Sansalvador *et al.*, 2022). Nevetheless, a combination of methods might be a useful route to explore with for example the use of SEC post UC in order of obtain a purer suspension or to separate EV subpopulation by size. An example is the work of Wei *et al*. (2020) shows that particular combination improved the performance of mass-spec-based proteomic profiling in plasma-derived sEVs (Wei *et al.*, 2020).

***EV were successfully isolated from mineralising osteoblasts cultures.***

First, TEM observations showed clear round-shaped nanovesicles as displayed in Figure 3.5. With a lipid bilayer membrane observable in 3.5A and 3.5B, more opaque vesicles could also be observed as showed in Fig 3.5C. These observations are rarely comparable between studies as each preparation and TEM system will induce variability in the quality of the images obtained, as highlighted by Rikkert *et al.* (2019). Even so, the images presented in Figure 3.5. displayed EVs of typical size (50-300 nm) and morphology. Interestingly, the observation of the attached fiber to a vesicle indicate the MO-EV interaction with the ECM (Patel *et al.*, 2023). Although satisfactory morphological analysis was obtained without staining or advanced protocol, state-of-the art method have been developed in recent years to obtain an even greater resolution (Chuo *et al.*, 2018). For example, immuno-gold labeling associated with cryo-electron microscopy allowed the identification of different EV subtypes within a population of platelet-derived EVs (Brisson *et al.*, 2017).

After isolation from conditioned media, MO-EVs were extensively characterized. The evaluation of MO-EV average size found at 213 nm, which confirmed the isolation of nanoparticles exhibiting a regular EV diameter (50-300nm). According to MISEV guidelines, they can be been referred to as small EVs (sEVs). With a PDI below 0.25, the EV preparation was considered as a monodispersed suspension showing that the differential ultracentrifugation method allowed the specific isolation of nanoparticles of a defined size range from the CCM of osteoblasts (Thery *et al.*, 2018; Danaei *et al.*, 2018). DLS and NTA are two complementary techniques as DLS provides a wider range of size analysis whereas NTA offers a higher resolution, which explains the slight variability observed between the two sizing methods (Szatanek *et al.*, 2017). The negative ζ-potential value of -10.96 mV obtained suggests that the suspension is below the threshold of agglomeration of -10mV providing a first indication of the stability of this colloidal system due to electrostatic repulsions between EVs (Midekessa *et al.*, 2020). TEM images exhibited round-shaped EVs and it showed an observed size slightly smaller than 100 nm. This variation of size between TEM or other methods such as NTA/DLS can be explained by the dehydration of EVs during sample preparation which can often appear cup-shaped (Chuo *et al.*, 2018).

The immunoblotting revealed the presence of both CD9 and annexin II in the absence of calnexin, thus, the presence of these EV-biomarkers confirmed the successful isolation of MO-EVs. The absence of calnexin is important information as this endoplasmic reticulum protein is considered a strong exclusion marker as its intracellular location prevent it from being involved in EV biogenesis (Wang *et al.*, 2020). This result was confirmed by Exo-ELISA validating the presence of CD9, CD81 and CD63, three EV enriched tetraspanin markers (Figure 3.8.). Finally, these results were further confirmed using nano flow cytometry as displayed in Appendix 3.2 allowing resolution at the single particle level.

### ***SP-IRIS showed great promise as an all-in one EV-characterisation platform.***

Adapted for the first to the characterisation of MO-EVs, the ExoView platform offered formidable advantages towards the characterisation of MO-EVs allowing to determine particle size, particle concentration and the detection of EV biomarkers with supportive imaging in and all-in-one format. The optimisation of this method revealed that EVs can also be detected with the same precision directly from media before purification and this will allow a more efficient screening of EV-markers. For example, Jung *et al.* have studied the cytokine profiling of serum-derived EVs and Im *et al.* explored variation of EV concentration using the grafting detection (Jung *et al.*, 2020; Im *et al.*, 2020). This method also has the potential be useful to determine the mechanism of action of EVs by probing other proteins both at the surface and inside the EV-cargo as showed by Silva *et al.* (2021) engineering cells (Expi293F) to express GFP-tagged proteins in secreted EVs which was then characterised using the ExoView platform.

Important limitations to note are that size assessement performed by the system might not correlate with other methods such as DLS or NTA due to the final drying step causing vesicle shrinkage (Bachurski *et al.*, 2019). Addtionally, by being dependent on an antibody-binding, only a number of event can be analysed as no marker would yield the capture of the totality of an EV population. As such the development of lipid-binding subtrates could offer great potential to capture total EV populations as well as other types of lipid nanoparticles.

Overall, SP-IRIS appeared as a strong characterisation method provide a multitude of insights from a single analysis including EV cargo analysis applications which have not yet been extensively developed.

### ***Lyophilisation of MO-EVs in the presence of cryoprotectant indicate a greater stability for long-term storage.***

The pilot storage study performed has presented lyophilisation associated with the use of cryoprotectant as the most suitable method for long term EV storage. Due to poor yield and the need for large quantities of EVs for a majority of studies, most projects isolated and use EVs in a tight-flow manner with a single freezing step reported post-isolation to routinely store EVs. However, with the advances of EVs towards clinical translation, storage conditions are becoming more important to be able to delivery a nanotherapeutic following the requirement of the pharmaceutical industry. In this pilot study, first evidence was obtained by evaluating size stability, however, a complete study should include a functional assessement to evaluate the effects of the storage consition on the EV bioactivity. This wasn't performed here, due to the great number of EVs required to run biomineralisation studies validating their activity. Such pioneering studies have been performed by Levy *et al* (2023) showing that MSC-derived EVs retained their bioactivity after both freezing and lyophilisation for up to 6 weeks, also confirming the preserved functionality of nucleic acids in a wound healing model. Alternatively, Görgens *et al.* (2022) presented their discoveries regarding EV storage buffer as standard PBS showed a severely reduced recovery rate which was improved by the addition of trehalose and albumin. Based on our findings, MO-EVs were always freshly isolated to perform *in vitro* studies and part of the batch was kept frozen at -80°C for characterisation purposes.

### ***The protein composition of MO-EVs provides unique mechanical insights to understand their role in biomineralisation.***

The composition of MO-EVs was first evaluated in terms of total content of both proteins and RNA. Protein content was found in line with previous isolating MO-EVs from MC3T3-E1 cells (Man *et al.*, 2021a). Interestingly, the concentration of protein compared to RNA was found >600-fold compared to RNA levels, which were found very low. From this analysis alone, we could hypothesise that MO-EVs were richer in proteins linking their bioactivity to their high protein content. Thus, this led to a deeper investigation of their protein composition via proteomic analysis.

Proteomic analysis revealed the presence of over 1,000 proteins within our single MO-EV population of interest. First, it is important to note that inter-vesicle variability is expected in such a complex nanoparticle sample with only a few proteins found per 100-nm large nanovesicle. This leads to the possibility of existing subpopulations with define bioactivities which can't be currently discriminated via UC alone.

Among the most abundant proteins of interest, the top 15 most abundant proteins have been presented in Figure 3.14. and their role will be discussed briefly. LAMP1 is a lysosomal protein associated with exosome biogenesis and found in CD63 positive EVs (Mathieu *et al.*, 2021). CD9 have been employed as an EV biomarker and has been found to be linked to the formation of TEMs in exosomes (Baghban *et al.*, 2023). The presence of albumin, fibronectin and collagen VI and XII revealed the strong link of MO-EVs to the ECM linking the presence of these proteins to the potential binding of EVs to fibronectin or collagen fibers via their adhesion surface proteins (Buzás *et al.*, 2018).

Separately, 3 protein families were well represented with annexin, tetraspanin and collagen protein families all found among the most abundant proteins. Annexins are calcium chelators transmembrane proteins capable to bind to acidic phospholipids such as phosphatidyl serine in the presence of calcium ions. Annexins are important at the cellular level as these proteins have various roles including membrane trafficking, ion channelling or cytoskeletons regulation (Enrich *et al.*, 2022). More specifically in bone cell-derived EVs, annexins have been found enriched within mineralising vesicles. Su *et al.* (2023) studied osteoblast MVs in osteoporosis and reported annexin V as a mineralisation mediator (Su *et al.*, 2023). Davies *et al.* (2017) compared MO-EVs to non-MO-EVs and showed an upregulation of annexins I, II and VI in MO-EVs specifically (Davies *et al.*, 2017).

Absent from all proteomics results and also non-detectable via enzymatic activity, ALP was found absent from MO-EVs. This complete lack of phosphatase enzyme shows a clear difference between our secreted MO-EVs and matrix-bound vesicles studied in the literature and found enriched in proteins such as ALP (Boyan *et al.*, 2022).

In addition to the presence of annexins, collagen type I, VI and XII was also found in the most abundant proteins. Given their nature, it is expected that the detection of these protein is related to the binding of collagens to EVs via binding proteins and not the presence of collagen-loaded MO-EVs. Harvesting EVs over 2 weeks in mineralising cultures, EVs collected might have attached and been release from the ECM over the collection period. The presence of these ECM components is very important at several levels. Collagen I is the most abundant proteins of the bone ECM and is essential to biomineralisation indicating the affinity of MO-EVs to its binding. Furthermore, collagen VI and VII have been established as coordinators of

ECM formation forming complexes linked to osteoblast-osteoblast communication during osteogenesis (Izu *et al.*, 2016).

Although the presence of tetraspanin markers validate the detection of these EV biomarkers, it also highlight the importance of this family of proteins in EV suspension beyond their use as markers. Organised in specialized tetraspanin-enriched microdomains, tetraspanins are involved in EV biogenesis as well as the modulation of EV cargo (Andreu *et al.*, 2014). Moreover, these proteins can interact laterally with other receptors involved in signalling such metalloproteinases or adhesion proteins such as integrins (Yáñez-Mó *et al.*, 2009). This is further supported by the gene ontology analysis presented in Figure 3.17. as all 10 GO terms related to molecular functions were found associated to a binding function including ion and protein binding. Together, this shows how an untargeted approach to study EV composition may lead to interesting mechanistic insights and the discovery of new proteins of interests.

Importantly, beyond the protein composition of MO-EVs, their lipid composition has also been investigated as the role of lipids in EV activity has been emerging in recent years and remains poorly understood (Skotland *et al.*, 2020). Preliminary lipidomics data (showed in Appendix 3..3) revealed a significant enrichment in phosphatidyl serine (PS) in MO-EVs. Recent evidence has showed the participation of PS-enriched EVs in the innate defense against pathogens (Groß *et al.*, 2024) or its use a cancer biomarker as tumor cell-derived EVs were showed to externalize PS (Perez *et al.*, 2023).

### ***MO-EVs contain calcium and phosphate indicating the presence of mineral cargo.***

For the first time, the mineral content of MO-EVs was assessed via biochemical assays to determine the levels of calcium and phosphate within the secreted vesicles of osteoblasts. After an attempt of detemining MO-EV compositional signature using Raman spectroscopy

(Appendix 3.1.), the use of biochemical assays was preferred. Interestingly, both calcium and phosphate levels were detected in MO-EVs, however an important limitation to note here is that, without direct comparison with EVs isolated from non-mineralising cultures, mineral content could also be linked to a co-isolation of minerals.

The initiation of mineral formation within EVs serving as a nucleation site still lack of mechanistic understanding. Using coarse-grained simulations, Pokhrel *et al.* (2018) performed *in silico* investigations and showed that $Ca^{2+}/HPO_4^{2-}$ and PS was initiators of mineral nucleation. Importantly, the presence of minerals within MO-EVs could be linked to the mechanistic attributes of MVs with the presense of a mineral rich core within mature vesicles attached to the matrix. To the best of our knowledge, this is the first time that the presence of Ca/P is reported in total secreted EV population which provide a key marker to determine the importance of MVs as a subpopulation. Interestingly, the accumulation of calcium and phosphorus witihn cell-derived vesicles have already been reported in osteoblast mithochondrial granules and intracellular vesicles. The mithochondria being a calcium rich organelle, Boonrungsiman *et al.*, (2012) highlighted the link between intracellular calcium phosphate content in osteoblast to ECM mineralisation which could be driven by cell-derived nanovesicles. Nevertheless, the link between these cytoplasmic nanoparticles and the secreted EV populations has not yet been investigated. A major aspect of future work lies in understanding if mineral are transported from cells to the ECM or if these vesicles continue to drive Ca/P within their cargo once attached to the ECM.

## 3.5. Conclusion

The overall aim of this chapter was to investigate the isolation and characterisation of EVs from the CCM of mineralising osteoblasts obtained from a 2D *in vitro* culture. This was achieved via a comparative investigation of isolation methods from which differential ultracentrifugation was selected as a method of choice. Using a wide range of characterisation methodologies, the isolation of MO-EVs was validated presenting a population of nanoparticles positive to CD9, CD63 and CD81 with a typical EV size range (50-300 nm) and morphology. Notably, the use of SP-IRIS was adapted for the first to the successful detection of tetraspainin markers which was confirmed using immunoblotting and ExoELISAs. Pilot data regarding MO-EV storage conditions suggested the potential of the use of lyophilisation to enhance the structural stability of these nanovesicles. Importantly, compositional analysis revelead the richness and diversity of the content of the nanoparticles isolated. It was demonstrated that MO-EVs, in addition of their lipid membrane rich in PS, contained both nucleic acids, proteins and minerals. Interestingly, proteomic analysis revelead the presence of key proteins with annexins and collagens observed among the most abundant proteins indicating that at least a subpopulation of MO-EVs can mediate biomineralisation acting as nucleation site for mineral formation.

Together, these initial findings established the foundation of this research project focused on MO-EVs providing, validating the isolation of these nanovesicles of interest. The key characteristics determined associated with new methods adapted such as SP-IRIS and the extensive compositional analysis provide decisive insights to better understand MO-EVs and their bioactivity which has been evaluted in the following chapter.

# Appendices – Chapter III

## Appendix 3.1.

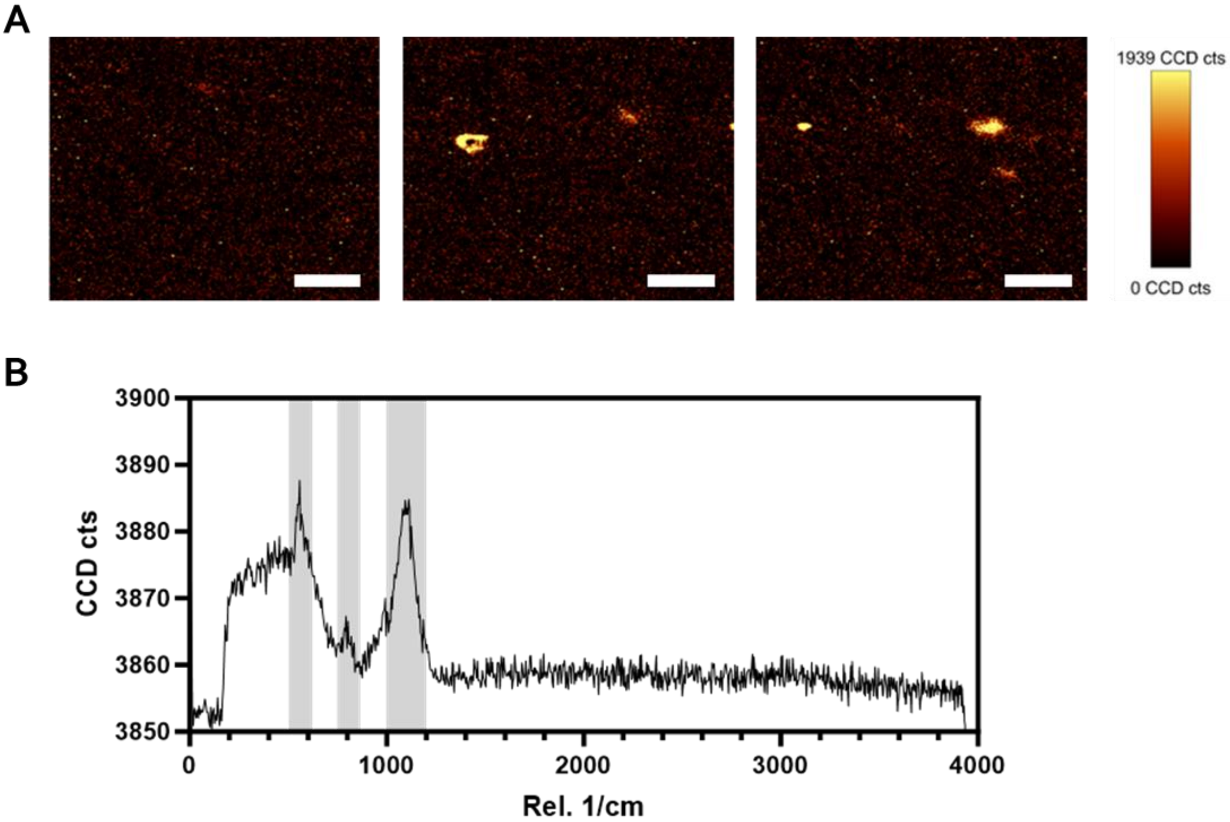

**Appendix 3.1. | Confocal Raman spectroscopy analysis of MO-EVs with A) Raman confocal imaging and B) Raman spectrum.** Scale bars = 10 µm.

## Appendix 3.2.

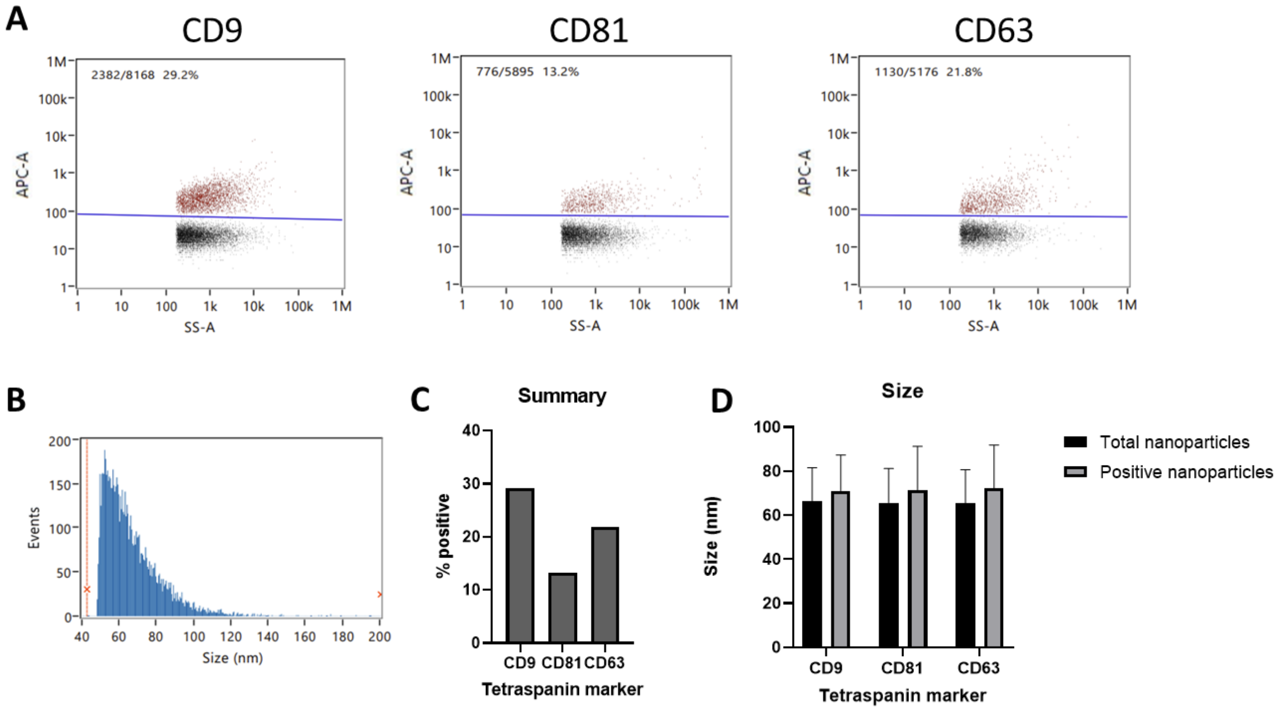

**Appendix 3.2. | Nanoflowcytometry analysis of MO-EVs with A) Flow cytometry dot plots presenting the respective detection of CD9, CD81 and CD63. B) Example of a size distribution profile. C) Summary of the quantificxation of % positive particles. D) Average sizes of total and positive nanoparticles.** Data are expressed as mean ± SD (n=1). *P ≤ 0.05, **P ≤ 0.01 and ***P ≤ 0.001.

**Appendix 3.3.**

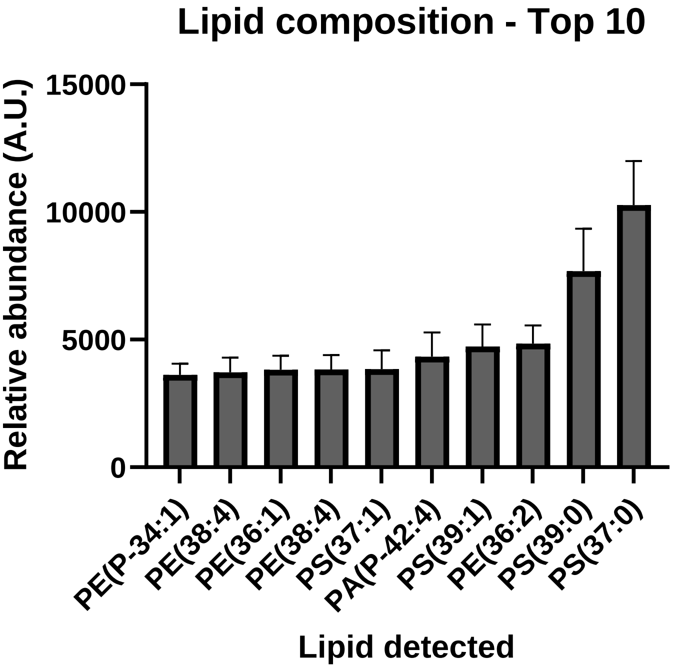

**Appendix 3.3. | Lipidomic analysis of MO-EVs reporting the top 10 most abundant lipids found in the negative ion analysis.** Phosphatidylethanolamine (PE), phosphatidic acid (PA), phosphatidylserine (PS) were the three lipid species identified. Data are expressed as mean ± SD (n=3).

## Appendix 3.4.

All 279 most abundant proteins have been presented in the table below. In the first column, their number correspond to their abundance ranking with 1, the most abundant protein and 279, the least abundant one. All protein decriptions follows NCBI guidelines with FASTA headers for UniProtKB.

Description is made as follow Protein Name – Organism Name/ Species (OS) – Organism Identifier (OX) – Gene Name (GN) – Protein Existence (PE) – Sequence Version (SV)

**Appendix 3.4. | Descriptive list of the most abundant proteins found in MO-EVs.**

| № | Description |
|---|---|
| 1 | Conserved oligomeric Golgi complex subunit 1 OS=Mus musculus OX=10090 GN=Cog1 PE=1 SV=3 |
| 2 | Band 4.1-like protein 3 OS=Mus musculus OX=10090 GN=Epb41l3 PE=1 SV=1 |
| 3 | Collagen alpha-1(XII) chain OS=Mus musculus OX=10090 GN=Col12a1 PE=2 SV=3 |
| 4 | Fibronectin OS=Mus musculus OX=10090 GN=Fn1 PE=1 SV=4 |
| 5 | Albumin OS=Mus musculus OX=10090 GN=Alb PE=1 SV=3 |
| 6 | Collagen alpha-1(VI) chain OS=Mus musculus OX=10090 GN=Col6a1 PE=1 SV=1 |
| 7 | Myosin-9 OS=Mus musculus OX=10090 GN=Myh9 PE=1 SV=4 |
| 8 | Keratin_ type II cytoskeletal 5 OS=Mus musculus OX=10090 GN=Krt5 PE=1 SV=1 |
| 9 | Collagen alpha-2(VI) chain OS=Mus musculus OX=10090 GN=Col6a2 PE=1 SV=3 |
| 10 | Chromobox protein homolog 8 OS=Mus musculus OX=10090 GN=Cbx8 PE=1 SV=1 |
| 11 | Glia-derived nexin OS=Mus musculus OX=10090 GN=Serpine2 PE=1 SV=2 |
| 12 | CD9 antigen OS=Mus musculus OX=10090 GN=Cd9 PE=1 SV=2 |
| 13 | Hemoglobin subunit beta-H1 OS=Mus musculus OX=10090 GN=Hbb-bh1 PE=2 SV=3 |
| 14 | Zinc finger CCCH domain-containing protein 13 OS=Mus musculus OX=10090 GN=Zc3h13 PE=1 SV=1 |
| 15 | Lysosome-associated membrane glycoprotein 1 OS=Mus musculus OX=10090 GN=Lamp1 PE=1 SV=2 |
| 16 | T-complex protein 1 subunit gamma OS=Mus musculus OX=10090 GN=Cct3 PE=1 SV=1 |
| 17 | Ninein OS=Mus musculus OX=10090 GN=Nin PE=1 SV=4 |
| 18 | Leucine-rich repeat-containing protein 17 OS=Mus musculus OX=10090 GN=Lrrc17 PE=2 SV=1 |
| 19 | Elongation factor 2 OS=Mus musculus OX=10090 GN=Eef2 PE=1 SV=2 |
| 20 | Kinesin-like protein KIF9 OS=Mus musculus OX=10090 GN=Kif9 PE=1 SV=2 |
| 21 | Nuclear exosome regulator NRDE2 OS=Mus musculus OX=10090 GN=Nrde2 PE=1 SV=3 |
| 22 | Pigment epithelium-derived factor OS=Mus musculus OX=10090 GN=Serpinf1 PE=1 SV=2 |
| 23 | Matrilin-4 OS=Mus musculus OX=10090 GN=Matn4 PE=1 SV=1 |
| 24 | Nucleolar GTP-binding protein 2 OS=Mus musculus OX=10090 GN=Gnl2 PE=1 SV=2 |
| 25 | Protein bassoon OS=Mus musculus OX=10090 GN=Bsn PE=1 SV=4 |

| | |
|---|---|
| 26 | Cell surface hyaluronidase OS=Mus musculus OX=10090 GN=Cemip2 PE=1 SV=1 |
| 27 | Laminin subunit gamma-1 OS=Mus musculus OX=10090 GN=Lamc1 PE=1 SV=2 |
| 28 | Ras-related protein Rab-7L1 OS=Mus musculus OX=10090 GN=Rab29 PE=1 SV=1 |
| 29 | Guanine nucleotide-binding protein subunit alpha-12 OS=Mus musculus OX=10090 GN=Gna12 PE=1 SV=3 |
| 30 | Phospholipid scramblase 1 OS=Mus musculus OX=10090 GN=Plscr1 PE=1 SV=1 |
| 31 | Alpha-2-macroglobulin-P OS=Mus musculus OX=10090 GN=A2m PE=2 SV=2 |
| 32 | Heterogeneous nuclear ribonucleoprotein H OS=Mus musculus OX=10090 GN=Hnrnph1 PE=1 SV=3 |
| 33 | Protein ZGRF1 OS=Mus musculus OX=10090 GN=Zgrf1 PE=1 SV=2 |
| 34 | Keratin_ type II cytoskeletal 2 oral OS=Mus musculus OX=10090 GN=Krt76 PE=1 SV=1 |
| 35 | Synaptotagmin-15 OS=Mus musculus OX=10090 GN=Syt15 PE=2 SV=1 |
| 36 | Proteasome subunit alpha type-5 OS=Mus musculus OX=10090 GN=Psma5 PE=1 SV=1 |
| 37 | Pleckstrin homology domain-containing family G member 3 OS=Mus musculus OX=10090 GN=Plekhg3 PE=1 SV=2 |
| 38 | Centrosome-associated protein 350 OS=Mus musculus OX=10090 GN=Cep350 PE=1 SV=1 |
| 39 | GRB10-interacting GYF protein 2 OS=Mus musculus OX=10090 GN=Gigyf2 PE=1 SV=2 |
| 40 | Soluble calcium-activated nucleotidase 1 OS=Mus musculus OX=10090 GN=Cant1 PE=2 SV=1 |
| 41 | Rab GDP dissociation inhibitor beta OS=Mus musculus OX=10090 GN=Gdi2 PE=1 SV=1 |
| 42 | Forkhead-associated domain-containing protein 1 OS=Mus musculus OX=10090 GN=Fhad1 PE=2 SV=1 |
| 43 | Collagen alpha-2(I) chain OS=Mus musculus OX=10090 GN=Col1a2 PE=1 SV=2 |
| 44 | Glial fibrillary acidic protein OS=Mus musculus OX=10090 GN=Gfap PE=1 SV=4 |
| 45 | Unconventional myosin-Va OS=Mus musculus OX=10090 GN=Myo5a PE=1 SV=2 |
| 46 | Serine/arginine-rich splicing factor 2 OS=Mus musculus OX=10090 GN=Srsf2 PE=1 SV=4 |
| 47 | Ribosomal RNA-processing protein 8 OS=Mus musculus OX=10090 GN=Rrp8 PE=1 SV=1 |
| 48 | Keratin_ type I cytoskeletal 20 OS=Mus musculus OX=10090 GN=Krt20 PE=1 SV=1 |
| 49 | Coiled-coil domain-containing protein 80 OS=Mus musculus OX=10090 GN=Ccdc80 PE=1 SV=2 |
| 50 | Coiled-coil domain-containing protein 186 OS=Mus musculus OX=10090 GN=Ccdc186 PE=1 SV=2 |
| 51 | Transgelin-2 OS=Mus musculus OX=10090 GN=Tagln2 PE=1 SV=4 |
| 52 | CD81 antigen OS=Mus musculus OX=10090 GN=Cd81 PE=1 SV=2 |
| 53 | Disks large-associated protein 3 OS=Mus musculus OX=10090 GN=Dlgap3 PE=1 SV=1 |
| 54 | Oxysterol-binding protein-related protein 6 OS=Mus musculus OX=10090 GN=Osbpl6 PE=1 SV=1 |
| 55 | Biglycan OS=Mus musculus OX=10090 GN=Bgn PE=1 SV=1 |
| 56 | Antithrombin-III OS=Mus musculus OX=10090 GN=Serpinc1 PE=1 SV=1 |
| 57 | Tenascin OS=Mus musculus OX=10090 GN=Tnc PE=1 SV=1 |
| 58 | Ras-related protein Rab-25 OS=Mus musculus OX=10090 GN=Rab25 PE=1 SV=2 |
| 59 | CD5 antigen-like OS=Mus musculus OX=10090 GN=Cd5l PE=1 SV=3 |
| 60 | Myotubularin-related protein 5 OS=Mus musculus OX=10090 GN=Sbf1 PE=1 SV=2 |
| 61 | Laminin subunit beta-2 OS=Mus musculus OX=10090 GN=Lamb2 PE=1 SV=2 |
| 62 | Protein THEMIS2 OS=Mus musculus OX=10090 GN=Themis2 PE=1 SV=2 |
| 63 | Peroxiredoxin-2 OS=Mus musculus OX=10090 GN=Prdx2 PE=1 SV=3 |
| 64 | Histone H4 OS=Mus musculus OX=10090 GN=H4c1 PE=1 SV=2 |
| 65 | Histone H1.2 OS=Mus musculus OX=10090 GN=H1-2 PE=1 SV=2 |
| 66 | Lactadherin OS=Mus musculus OX=10090 GN=Mfge8 PE=1 SV=3 |
| 67 | Scaffold attachment factor B2 OS=Mus musculus OX=10090 GN=Safb2 PE=1 SV=2 |

| | |
|---|---|
| 68 | Arf-GAP with coiled-coil_ ANK repeat and PH domain-containing protein 2 OS=Mus musculus OX=10090 GN=Acap2 PE=1 SV=2 |
| 69 | Sushi-repeat-containing protein SRPX OS=Mus musculus OX=10090 GN=Srpx PE=2 SV=1 |
| 70 | Serine/threonine-protein phosphatase 2A regulatory subunit B'' subunit gamma OS=Mus musculus OX=10090 GN=Ppp2r3c PE=1 SV=2 |
| 71 | Teneurin-4 OS=Mus musculus OX=10090 GN=Tenm4 PE=1 SV=2 |
| 72 | Dynein heavy chain 3_ axonemal OS=Mus musculus OX=10090 GN=Dnah3 PE=1 SV=2 |
| 73 | Phospholipid transfer protein OS=Mus musculus OX=10090 GN=Pltp PE=1 SV=1 |
| 74 | Hemoglobin subunit alpha OS=Mus musculus OX=10090 GN=Hba PE=1 SV=2 |
| 75 | Lysosomal-associated transmembrane protein 4A OS=Mus musculus OX=10090 GN=Laptm4a PE=1 SV=1 |
| 76 | Moesin OS=Mus musculus OX=10090 GN=Msn PE=1 SV=3 |
| 77 | Myosin light polypeptide 6 OS=Mus musculus OX=10090 GN=Myl6 PE=1 SV=3 |
| 78 | Hemoglobin subunit epsilon-Y2 OS=Mus musculus OX=10090 GN=Hbb-y PE=1 SV=2 |
| 79 | Beta-1_4-glucuronyltransferase 1 OS=Mus musculus OX=10090 GN=B4gat1 PE=1 SV=1 |
| 80 | Centromere-associated protein E OS=Mus musculus OX=10090 GN=Cenpe PE=1 SV=1 |
| 81 | Serotransferrin OS=Mus musculus OX=10090 GN=Tf PE=1 SV=1 |
| 82 | Keratin_ type II cytoskeletal 75 OS=Mus musculus OX=10090 GN=Krt75 PE=1 SV=1 |
| 83 | Cartilage matrix protein OS=Mus musculus OX=10090 GN=Matn1 PE=2 SV=2 |
| 84 | Toll-interacting protein OS=Mus musculus OX=10090 GN=Tollip PE=1 SV=1 |
| 85 | Proto-oncogene tyrosine-protein kinase ROS OS=Mus musculus OX=10090 GN=Ros1 PE=1 SV=1 |
| 86 | Soluble scavenger receptor cysteine-rich domain-containing protein SSC5D OS=Mus musculus OX=10090 GN=Ssc5d PE=1 SV=1 |
| 87 | Ubiquitin carboxyl-terminal hydrolase 24 OS=Mus musculus OX=10090 GN=Usp24 PE=1 SV=1 |
| 88 | Ras-related protein Rap-2a OS=Mus musculus OX=10090 GN=Rap2a PE=1 SV=2 |
| 89 | OTU domain-containing protein 7A OS=Mus musculus OX=10090 GN=Otud7a PE=1 SV=1 |
| 90 | Proteasome adapter and scaffold protein ECM29 OS=Mus musculus OX=10090 GN=Ecpas PE=1 SV=3 |
| 91 | Cingulin OS=Mus musculus OX=10090 GN=Cgn PE=1 SV=1 |
| 92 | Voltage-dependent anion-selective channel protein 1 OS=Mus musculus OX=10090 GN=Vdac1 PE=1 SV=3 |
| 93 | Ras-related protein Rab-3A OS=Mus musculus OX=10090 GN=Rab3a PE=1 SV=1 |
| 94 | Serine protease 23 OS=Mus musculus OX=10090 GN=Prss23 PE=2 SV=2 |
| 95 | 1-phosphatidylinositol 4_5-bisphosphate phosphodiesterase epsilon-1 OS=Mus musculus OX=10090 GN=Plce1 PE=1 SV=3 |
| 96 | Asporin OS=Mus musculus OX=10090 GN=Aspn PE=1 SV=1 |
| 97 | Rab GDP dissociation inhibitor alpha OS=Mus musculus OX=10090 GN=Gdi1 PE=1 SV=3 |
| 98 | Syntenin-1 OS=Mus musculus OX=10090 GN=Sdcbp PE=1 SV=1 |
| 99 | Golgi-associated plant pathogenesis-related protein 1 OS=Mus musculus OX=10090 GN=Glipr2 PE=1 SV=3 |
| 100 | Trinucleotide repeat-containing gene 18 protein OS=Mus musculus OX=10090 GN=Tnrc18 PE=1 SV=2 |
| 101 | Basement membrane-specific heparan sulfate proteoglycan core protein OS=Mus musculus OX=10090 GN=Hspg2 PE=1 SV=1 |
| 102 | EH domain-containing protein 2 OS=Mus musculus OX=10090 GN=Ehd2 PE=1 SV=1 |
| 103 | Junction-mediating and -regulatory protein OS=Mus musculus OX=10090 GN=Jmy PE=1 SV=1 |
| 104 | CD63 antigen OS=Mus musculus OX=10090 GN=Cd63 PE=1 SV=2 |
| 105 | Afamin OS=Mus musculus OX=10090 GN=Afm PE=1 SV=2 |

| | |
|---|---|
| 106 | Ras-responsive element-binding protein 1 OS=Mus musculus OX=10090 GN=Rreb1 PE=1 SV=2 |
| 107 | Eukaryotic initiation factor 4A-II OS=Mus musculus OX=10090 GN=Eif4a2 PE=1 SV=2 |
| 108 | Prothrombin OS=Mus musculus OX=10090 GN=F2 PE=1 SV=1 |
| 109 | Flotillin-1 OS=Mus musculus OX=10090 GN=Flot1 PE=1 SV=1 |
| 110 | Gelsolin OS=Mus musculus OX=10090 GN=Gsn PE=1 SV=3 |
| 111 | Centrosomal protein of 128 kDa OS=Mus musculus OX=10090 GN=Cep128 PE=1 SV=2 |
| 112 | Espin OS=Mus musculus OX=10090 GN=Espn PE=1 SV=2 |
| 113 | Annexin A4 OS=Mus musculus OX=10090 GN=Anxa4 PE=1 SV=4 |
| 114 | Unconventional myosin-XVIIIa OS=Mus musculus OX=10090 GN=Myo18a PE=1 SV=2 |
| 115 | Haptoglobin OS=Mus musculus OX=10090 GN=Hp PE=1 SV=1 |
| 116 | DNA-dependent protein kinase catalytic subunit OS=Mus musculus OX=10090 GN=Prkdc PE=1 SV=3 |
| 117 | Phospholipid-transporting ATPase ID OS=Mus musculus OX=10090 GN=Atp8b2 PE=2 SV=2 |
| 118 | Protein Daple OS=Mus musculus OX=10090 GN=Ccdc88c PE=1 SV=1 |
| 119 | Clathrin heavy chain 1 OS=Mus musculus OX=10090 GN=Cltc PE=1 SV=3 |
| 120 | Adenosylhomocysteinase OS=Mus musculus OX=10090 GN=Ahcy PE=1 SV=3 |
| 121 | Beta-1_3-galactosyl-O-glycosyl-glycoprotein beta-1_6-N-acetylglucosaminyltransferase 3 OS=Mus musculus OX=10090 GN=Gcnt3 PE=2 SV=2 |
| 122 | Calmodulin-1 OS=Mus musculus OX=10090 GN=Calm1 PE=1 SV=1 |
| 123 | Centrosomal protein of 290 kDa OS=Mus musculus OX=10090 GN=Cep290 PE=1 SV=2 |
| 124 | Non-receptor tyrosine-protein kinase TYK2 OS=Mus musculus OX=10090 GN=Tyk2 PE=1 SV=3 |
| 125 | Integrin alpha-3 OS=Mus musculus OX=10090 GN=Itga3 PE=1 SV=1 |
| 126 | Decaprenyl-diphosphate synthase subunit 2 OS=Mus musculus OX=10090 GN=Pdss2 PE=1 SV=2 |
| 127 | Actin_ cytoplasmic 1 OS=Mus musculus OX=10090 GN=Actb PE=1 SV=1 |
| 128 | Keratin_ type II cytoskeletal 1 OS=Mus musculus OX=10090 GN=Krt1 PE=1 SV=4 |
| 129 | Tetraspanin-4 OS=Mus musculus OX=10090 GN=Tspan4 PE=1 SV=1 |
| 130 | Ribosomal protein S6 kinase delta-1 OS=Mus musculus OX=10090 GN=Rps6kc1 PE=1 SV=2 |
| 131 | Centriolin OS=Mus musculus OX=10090 GN=Cntrl PE=1 SV=2 |
| 132 | Alstrom syndrome protein 1 homolog OS=Mus musculus OX=10090 GN=Alms1 PE=1 SV=2 |
| 133 | Centrosome and spindle pole associated protein 1 OS=Mus musculus OX=10090 GN=Cspp1 PE=1 SV=2 |
| 134 | ATPase family protein 2 homolog OS=Mus musculus OX=10090 GN=Spata5 PE=1 SV=2 |
| 135 | Supervillin OS=Mus musculus OX=10090 GN=Svil PE=1 SV=1 |
| 136 | Disintegrin and metalloproteinase domain-containing protein 10 OS=Mus musculus OX=10090 GN=Adam10 PE=1 SV=2 |
| 137 | RNA helicase Mov10l1 OS=Mus musculus OX=10090 GN=Mov10l1 PE=1 SV=1 |
| 138 | Gem-associated protein 2 OS=Mus musculus OX=10090 GN=Gemin2 PE=2 SV=1 |
| 139 | Transmembrane 9 superfamily member 3 OS=Mus musculus OX=10090 GN=Tm9sf3 PE=1 SV=1 |
| 140 | DNA polymerase zeta catalytic subunit OS=Mus musculus OX=10090 GN=Rev3l PE=1 SV=3 |
| 141 | Cofilin-2 OS=Mus musculus OX=10090 GN=Cfl2 PE=1 SV=1 |
| 142 | Endoplasmic reticulum chaperone BiP OS=Mus musculus OX=10090 GN=Hspa5 PE=1 SV=3 |
| 143 | Unconventional myosin-Id OS=Mus musculus OX=10090 GN=Myo1d PE=1 SV=1 |
| 144 | Testis-expressed protein 52 OS=Mus musculus OX=10090 GN=Tex52 PE=2 SV=1 |
| 145 | Tetraspanin-6 OS=Mus musculus OX=10090 GN=Tspan6 PE=1 SV=1 |
| 146 | Keratin_ type I cytoskeletal 19 OS=Mus musculus OX=10090 GN=Krt19 PE=1 SV=1 |
| 147 | Major vault protein OS=Mus musculus OX=10090 GN=Mvp PE=1 SV=4 |
| 148 | Fascin OS=Mus musculus OX=10090 GN=Fscn1 PE=1 SV=4 |

| | |
|---|---|
| 149 | H-2 class I histocompatibility antigen_ alpha chain (Fragment) OS=Mus musculus OX=10090 PE=2 SV=1 |
| 150 | Ras-related protein Ral-A OS=Mus musculus OX=10090 GN=Rala PE=1 SV=1 |
| 151 | HIV Tat-specific factor 1 homolog OS=Mus musculus OX=10090 GN=Htatsf1 PE=1 SV=1 |
| 152 | Angiopoietin-2 OS=Mus musculus OX=10090 GN=Angpt2 PE=2 SV=2 |
| 153 | AP-4 complex subunit epsilon-1 OS=Mus musculus OX=10090 GN=Ap4e1 PE=1 SV=3 |
| 154 | Nidogen-2 OS=Mus musculus OX=10090 GN=Nid2 PE=1 SV=2 |
| 155 | P2X purinoceptor 4 OS=Mus musculus OX=10090 GN=P2rx4 PE=1 SV=1 |
| 156 | CD44 antigen OS=Mus musculus OX=10090 GN=Cd44 PE=1 SV=3 |
| 157 | Profilin-1 OS=Mus musculus OX=10090 GN=Pfn1 PE=1 SV=2 |
| 158 | Ankyrin repeat domain-containing protein 11 OS=Mus musculus OX=10090 GN=Ankrd11 PE=1 SV=1 |
| 159 | AT-rich interactive domain-containing protein 1A OS=Mus musculus OX=10090 GN=Arid1a PE=1 SV=1 |
| 160 | Serine/threonine-protein kinase TAO3 OS=Mus musculus OX=10090 GN=Taok3 PE=1 SV=2 |
| 161 | DNA polymerase epsilon catalytic subunit A OS=Mus musculus OX=10090 GN=Pole PE=1 SV=3 |
| 162 | Kinectin OS=Mus musculus OX=10090 GN=Ktn1 PE=1 SV=1 |
| 163 | Complement factor H OS=Mus musculus OX=10090 GN=Cfh PE=1 SV=2 |
| 164 | Band 4.1-like protein 2 OS=Mus musculus OX=10090 GN=Epb41l2 PE=1 SV=2 |
| 165 | A-kinase anchor protein 13 OS=Mus musculus OX=10090 GN=Akap13 PE=1 SV=1 |
| 166 | Serine protease HTRA1 OS=Mus musculus OX=10090 GN=Htra1 PE=1 SV=2 |
| 167 | Golgin subfamily A member 4 OS=Mus musculus OX=10090 GN=Golga4 PE=1 SV=2 |
| 168 | Cell division cycle 7-related protein kinase OS=Mus musculus OX=10090 GN=Cdc7 PE=1 SV=2 |
| 169 | Nucleoside diphosphate kinase A OS=Mus musculus OX=10090 GN=Nme1 PE=1 SV=1 |
| 170 | CCAAT/enhancer-binding protein zeta OS=Mus musculus OX=10090 GN=Cebpz PE=1 SV=2 |
| 171 | MORN repeat-containing protein 3 OS=Mus musculus OX=10090 GN=Morn3 PE=2 SV=2 |
| 172 | Eukaryotic initiation factor 4A-I OS=Mus musculus OX=10090 GN=Eif4a1 PE=1 SV=1 |
| 173 | Epidermal growth factor receptor kinase substrate 8-like protein 1 OS=Mus musculus OX=10090 GN=Eps8l1 PE=1 SV=1 |
| 174 | Dynein heavy chain 1_ axonemal OS=Mus musculus OX=10090 GN=Dnah1 PE=1 SV=1 |
| 175 | 4F2 cell-surface antigen heavy chain OS=Mus musculus OX=10090 GN=Slc3a2 PE=1 SV=1 |
| 176 | Cytochrome P450 26B1 OS=Mus musculus OX=10090 GN=Cyp26b1 PE=1 SV=1 |
| 177 | Annexin A6 OS=Mus musculus OX=10090 GN=Anxa6 PE=1 SV=3 |
| 178 | Heat shock protein HSP 90-alpha OS=Mus musculus OX=10090 GN=Hsp90aa1 PE=1 SV=4 |
| 179 | ATP-binding cassette sub-family A member 8-A OS=Mus musculus OX=10090 GN=Abca8a PE=1 SV=2 |
| 180 | Bone sialoprotein 2 OS=Mus musculus OX=10090 GN=Ibsp PE=2 SV=2 |
| 181 | Transcription factor TFIIIB component B'' homolog OS=Mus musculus OX=10090 GN=Bdp1 PE=2 SV=2 |
| 182 | DDB1- and CUL4-associated factor 6 OS=Mus musculus OX=10090 GN=Dcaf6 PE=1 SV=1 |
| 183 | Dynein regulatory complex protein 11 OS=Mus musculus OX=10090 GN=Iqca1 PE=2 SV=2 |

| | |
|---|---|
| 184 | Annexin A2 OS=Mus musculus OX=10090 GN=Anxa2 PE=1 SV=2 |
| 185 | Angiopoietin-related protein 6 OS=Mus musculus OX=10090 GN=Angptl6 PE=2 SV=1 |
| 186 | Transitional endoplasmic reticulum ATPase<br>OS=Mus musculus OX=10090 GN=Vcp PE=1 SV=4 |
| 187 | Vimentin OS=Mus musculus OX=10090 GN=Vim PE=1 SV=3 |
| 188 | Semaphorin-6A OS=Mus musculus OX=10090 GN=Sema6a PE=1 SV=2 |
| 189 | Histone H3.2 OS=Mus musculus OX=10090 GN=H3c2 PE=1 SV=2 |
| 190 | Histone H2B type 1-A OS=Mus musculus OX=10090 GN=H2bc1 PE=1 SV=3 |
| 191 | Calpain-6 OS=Mus musculus OX=10090 GN=Capn6 PE=1 SV=2 |
| 192 | Thyroid adenoma-associated protein homolog<br>OS=Mus musculus OX=10090 GN=Thada PE=1 SV=1 |
| 193 | Polycystic kidney disease and receptor for egg jelly-related protein<br>OS=Mus musculus OX=10090 GN=Pkdrej PE=2 SV=1 |
| 194 | Ras-related protein Rab-7a OS=Mus musculus OX=10090 GN=Rab7a PE=1 SV=2 |
| 195 | Lymphocyte antigen 75 OS=Mus musculus OX=10090 GN=Ly75 PE=1 SV=2 |
| 196 | Ras-related protein Rab-5C OS=Mus musculus OX=10090 GN=Rab5c PE=1 SV=2 |
| 197 | Sortilin-related receptor OS=Mus musculus OX=10090 GN=Sorl1 PE=1 SV=3 |
| 198 | 26S proteasome non-ATPase regulatory subunit 11<br>OS=Mus musculus OX=10090 GN=Psmd11 PE=1 SV=3 |
| 199 | Complement C3 OS=Mus musculus OX=10090 GN=C3 PE=1 SV=3 |
| 200 | Annexin A5 OS=Mus musculus OX=10090 GN=Anxa5 PE=1 SV=1 |
| 201 | Tetraspanin-14 OS=Mus musculus OX=10090 GN=Tspan14 PE=1 SV=1 |
| 202 | Guanine nucleotide-binding protein G(I)/G(S)/G(T) subunit beta-2<br>OS=Mus musculus OX=10090 GN=Gnb2 PE=1 SV=3 |
| 203 | Cadherin-10 OS=Mus musculus OX=10090 GN=Cdh10 PE=1 SV=3 |
| 204 | Tudor domain-containing protein 7 OS=Mus musculus OX=10090 GN=Tdrd7 PE=1 SV=1 |
| 205 | Programmed cell death 6-interacting protein<br>OS=Mus musculus OX=10090 GN=Pdcd6ip PE=1 SV=3 |
| 206 | 26S proteasome regulatory subunit 10B OS=Mus musculus OX=10090 GN=Psmc6 PE=1 SV=1 |
| 207 | Calcium-activated chloride channel regulator 3A-1<br>OS=Mus musculus OX=10090 GN=Clca3a1 PE=1 SV=1 |
| 208 | E3 ubiquitin-protein ligase listerin OS=Mus musculus OX=10090 GN=Ltn1 PE=1 SV=3 |
| 209 | Coagulation factor VIII OS=Mus musculus OX=10090 GN=F8 PE=2 SV=2 |
| 210 | Receptor-type tyrosine-protein phosphatase kappa<br>OS=Mus musculus OX=10090 GN=Ptprk PE=1 SV=1 |
| 211 | Serpin H1 OS=Mus musculus OX=10090 GN=Serpinh1 PE=1 SV=3 |
| 212 | Lysyl oxidase homolog 4 OS=Mus musculus OX=10090 GN=Loxl4 PE=2 SV=2 |
| 213 | Serine/threonine-protein phosphatase PP1-beta catalytic subunit<br>OS=Mus musculus OX=10090 GN=Ppp1cb PE=1 SV=3 |
| 214 | Pregnancy zone protein OS=Mus musculus OX=10090 GN=Pzp PE=1 SV=3 |
| 215 | Nik-related protein kinase OS=Mus musculus OX=10090 GN=Nrk PE=1 SV=2 |
| 216 | Histone H2B type 2-B OS=Mus musculus OX=10090 GN=Hist2h2bb PE=1 SV=3 |
| 217 | Laminin subunit beta-1 OS=Mus musculus OX=10090 GN=Lamb1 PE=1 SV=3 |
| 218 | Plexin-A3 OS=Mus musculus OX=10090 GN=Plxna3 PE=1 SV=2 |
| 219 | Vacuolar protein sorting-associated protein 13A<br>OS=Mus musculus OX=10090 GN=Vps13a PE=1 SV=1 |
| 220 | Alpha-2-HS-glycoprotein OS=Mus musculus OX=10090 GN=Ahsg PE=1 SV=1 |

| | |
|---|---|
| 221 | Peroxiredoxin-5_ mitochondrial OS=Mus musculus OX=10090 GN=Prdx5 PE=1 SV=2 |
| 222 | Tropomyosin alpha-3 chain OS=Mus musculus OX=10090 GN=Tpm3 PE=1 SV=3 |
| 223 | Uveal autoantigen with coiled-coil domains and ankyrin repeats OS=Mus musculus OX=10090 GN=Uaca PE=1 SV=2 |
| 224 | Annexin A11 OS=Mus musculus OX=10090 GN=Anxa11 PE=1 SV=2 |
| 225 | CD109 antigen OS=Mus musculus OX=10090 GN=Cd109 PE=1 SV=1 |
| 226 | Fibromodulin OS=Mus musculus OX=10090 GN=Fmod PE=2 SV=1 |
| 227 | Fibrinogen alpha chain OS=Mus musculus OX=10090 GN=Fga PE=1 SV=1 |
| 228 | Glutaryl-CoA dehydrogenase_ mitochondrial OS=Mus musculus OX=10090 GN=Gcdh PE=1 SV=2 |
| 229 | 60S ribosomal protein L4 OS=Mus musculus OX=10090 GN=Rpl4 PE=1 SV=3 |
| 230 | Transmembrane domain-containing protein TMIGD3 OS=Mus musculus OX=10090 GN=Tmigd3 PE=2 SV=1 |
| 231 | Dual specificity mitogen-activated protein kinase kinase 1 OS=Mus musculus OX=10090 GN=Map2k1 PE=1 SV=2 |
| 232 | Heat shock 70 kDa protein 1A OS=Mus musculus OX=10090 GN=Hspa1a PE=1 SV=2 |
| 233 | Annexin A7 OS=Mus musculus OX=10090 GN=Anxa7 PE=1 SV=2 |
| 234 | TBC1 domain family member 9 OS=Mus musculus OX=10090 GN=Tbc1d9 PE=2 SV=2 |
| 235 | Ferritin heavy chain OS=Mus musculus OX=10090 GN=Fth1 PE=1 SV=2 |
| 236 | Disks large homolog 5 OS=Mus musculus OX=10090 GN=Dlg5 PE=1 SV=1 |
| 237 | Matrix Gla protein OS=Mus musculus OX=10090 GN=Mgp PE=3 SV=1 |
| 238 | Adenylate cyclase type 5 OS=Mus musculus OX=10090 GN=Adcy5 PE=1 SV=2 |
| 239 | cAMP and cAMP-inhibited cGMP 3'_5'-cyclic phosphodiesterase 10A OS=Mus musculus OX=10090 GN=Pde10a PE=1 SV=2 |
| 240 | Syntaxin-7 OS=Mus musculus OX=10090 GN=Stx7 PE=1 SV=3 |
| 241 | Hemoglobin subunit beta-2 OS=Mus musculus OX=10090 GN=Hbb-b2 PE=1 SV=2 |
| 242 | Complement factor B OS=Mus musculus OX=10090 GN=Cfb PE=1 SV=2 |
| 243 | Catenin alpha-1 OS=Mus musculus OX=10090 GN=Ctnna1 PE=1 SV=1 |
| 244 | 60S ribosomal protein L18a OS=Mus musculus OX=10090 GN=Rpl18a PE=1 SV=1 |
| 245 | Glyceraldehyde-3-phosphate dehydrogenase OS=Mus musculus OX=10090 GN=Gapdh PE=1 SV=2 |
| 246 | Adenylate kinase isoenzyme 1 OS=Mus musculus OX=10090 GN=Ak1 PE=1 SV=1 |
| 247 | Lysine-specific demethylase 3A OS=Mus musculus OX=10090 GN=Kdm3a PE=1 SV=1 |
| 248 | Matrilin-2 OS=Mus musculus OX=10090 GN=Matn2 PE=2 SV=2 |
| 249 | 40S ribosomal protein SA OS=Mus musculus OX=10090 GN=Rpsa PE=1 SV=4 |
| 250 | Retina-specific copper amine oxidase OS=Mus musculus OX=10090 GN=Aoc2 PE=2 SV=2 |
| 251 | Annexin A3 OS=Mus musculus OX=10090 GN=Anxa3 PE=1 SV=4 |
| 252 | EH domain-containing protein 1 OS=Mus musculus OX=10090 GN=Ehd1 PE=1 SV=1 |
| 253 | Centrin-1 OS=Mus musculus OX=10090 GN=Cetn1 PE=1 SV=1 |
| 254 | Keratin_ type I cytoskeletal 18 OS=Mus musculus OX=10090 GN=Krt18 PE=1 SV=5 |
| 255 | Sperm motility kinase Z OS=Mus musculus OX=10090 GN=Gm4922 PE=2 SV=1 |
| 256 | GPALPP motifs-containing protein 1 OS=Mus musculus OX=10090 GN=Gpalpp1 PE=1 SV=2 |
| 257 | Tumor necrosis factor receptor superfamily member 18 OS=Mus musculus OX=10090 GN=Tnfrsf18 PE=1 SV=1 |
| 258 | MORC family CW-type zinc finger protein 3 OS=Mus musculus OX=10090 GN=Morc3 PE=1 SV=1 |
| 259 | Coagulation factor V OS=Mus musculus OX=10090 GN=F5 PE=1 SV=1 |
| 260 | Centrosome-associated protein CEP250 OS=Mus musculus OX=10090 GN=Cep250 PE=1 SV=4 |
| 261 | Small integral membrane protein 1 OS=Mus musculus OX=10090 GN=Smim1 PE=1 SV=1 |

| | |
|---|---|
| 262 | Disintegrin and metalloproteinase domain-containing protein 8 OS=Mus musculus OX=10090 GN=Adam8 PE=1 SV=3 |
| 263 | Matrix metalloproteinase-21 OS=Mus musculus OX=10090 GN=Mmp21 PE=1 SV=1 |
| 264 | Integrin beta-3 OS=Mus musculus OX=10090 GN=Itgb3 PE=1 SV=2 |
| 265 | Thioredoxin-like protein 4A OS=Mus musculus OX=10090 GN=Txnl4a PE=1 SV=1 |
| 266 | Laminin subunit alpha-4 OS=Mus musculus OX=10090 GN=Lama4 PE=1 SV=2 |
| 267 | Keratin_ type I cytoskeletal 15 OS=Mus musculus OX=10090 GN=Krt15 PE=1 SV=2 |
| 268 | Kinesin-like protein KIF16B OS=Mus musculus OX=10090 GN=Kif16b PE=1 SV=1 |
| 269 | Aldehyde oxidase 2 OS=Mus musculus OX=10090 GN=Aox2 PE=1 SV=2 |
| 270 | CD151 antigen OS=Mus musculus OX=10090 GN=Cd151 PE=1 SV=2 |
| 271 | 60S ribosomal protein L9 OS=Mus musculus OX=10090 GN=Rpl9 PE=2 SV=2 |
| 272 | Catenin beta-1 OS=Mus musculus OX=10090 GN=Ctnnb1 PE=1 SV=1 |
| 273 | Terminal uridylyltransferase 4 OS=Mus musculus OX=10090 GN=Tut4 PE=1 SV=2 |
| 274 | Early endosome antigen 1 OS=Mus musculus OX=10090 GN=Eea1 PE=1 SV=2 |
| 275 | Prolyl 4-hydroxylase subunit alpha-1 OS=Mus musculus OX=10090 GN=P4ha1 PE=1 SV=2 |
| 276 | Unconventional myosin-Ic OS=Mus musculus OX=10090 GN=Myo1c PE=1 SV=2 |
| 277 | Keratin_ type II cytoskeletal 6A OS=Mus musculus OX=10090 GN=Krt6a PE=1 SV=3 |
| 278 | Actin_ cytoplasmic 2 OS=Mus musculus OX=10090 GN=Actg1 PE=1 SV=1 |
| 279 | Sorcin OS=Mus musculus OX=10090 GN=Sri PE=1 SV=1 |

# Chapter IV

-

# In Vitro Evaluation of the Effects of Osteoblast-derived EVs on Biomineralisation

# Chapter IV

# *In Vitro* Evaluation of the Effects of Osteoblast-derived EVs on Biomineralisation

## 4.1. Introduction

### 4.1.1. Background

Apart from the determination of EV-inner features, the functional characterisation of EVs remains one of the most important challenges to obtain a clear understanding of their therapeutic potency. MO-EVs have been increasingly studied in recent years and have demonstrated their osteogenic potency in MSCs. An important line of work on MO-EVs has been conducted of MC3T3-E1-derived EVs starting with Ge *et al. (2015)* who isolated these mouse EVs for the first time and provided insights into their protein composition (Ge *et al.*, 2015). This initial study was explored further by Davies *et al.* who compared osteoblast-derived EVs from mineralising or non-mineralising cultures and demonstrated that MO-EVs only were able to induce mineralisation in MSC cultures. Additionally, it was showed that these MO-EVs were enriched in annexin calcium channelling proteins supporting the potential role of MO-EVs as early sites of mineral nucleation (Davies *et al.*, 2017). Despite the existence of several studies indicating the pro-osteogenic potential of MO-EVs, their effects on the biomineralisation of MC3T3-E1 osteoblasts remains unexplored to date in the literature which we identified as an important gap. As MC3T3-E1 cells are the parental cells of these EVs of interest, it makes them a very physiologically relevant osteoblast model to study their secreted EVs.

For most therapeutic applications, the development of potency assays remains an unmet need and current approaches remains non-standardised with a variety of biological models and dosing regimen used (Garcia *et al.*, 2024). To date, the evaluation of the mineralisation level of cell cultures *in vitro* has been performed by the staining of calcium deposits via alizarin red or von Kossa reagents whereas the quantification of matrix production was determined by collagen staining such as picro sirius red. Additionally, colorimetric analysis has also been employed to determine the concentration of calcium or phosphate in mineralising cultures by spectrophotometry. Alternatively, the activity of ALP or the expression of osteogenesis-related genes may be assessed as an indirect marker of osteoblastic activity. Although reliable and sensitive methods, these protocols constitute single-target approaches and are limited by the quantification of an average effect from a culture without providing information regarding the spatial or structural development of the mineral phase or the chemical composition of the calcium-phosphate compounds present in the developing matrix. The major component of mature bones is HA, a calcium-phosphate mineral, which is responsible for skeletal strength and is the result of the nucleation of ions followed by crystal growth forming the inorganic phase of bone tissues.

X-ray fluorescence spectroscopy is an analytical method used to determine the elemental composition of a wide variety of samples within plant science (Montanha *et al.*, 2020), forensic science (Pringle *et al.*, 2022), mining (Jang *et al.*, 2021) and biomedicine (Borjesson *et al.*, 1995). It is based on the use of radiations emitted by a primary X-ray source that bombards the atoms of a given sample causing an unstable state of high energy at the atomic level. High-energy electrons are then displaced from inner to outer orbital shells while releasing a signature x-ray energy, which can be attributed to a specific element. Modern systems have democratised the laboratory use of X-ray fluorescence (XRF) spectrophotometer thanks to the development of polycapillary lenses and automated scanning providing 2D-area elemental mapping capabilities with spot sizes below 20 µm offering a high resolution.

There is a current need for novel functional assays evaluating the osteogenic potential of EVs taking in consideration the impact of EV concentration on the biological response monitored. In this study, we exploited µ-XRF to conduct an in-depth analysis of mineral developing *invitro* osteoblast cultures treated with EVs. This study aimed to develop a novel approach to gain insights on how these nanovesicles modulate and accelerate biomineralisation with the isolation and characterisation of MO-EVs from 2D cultures in mineralising conditions followed by the *in vitro* validation of their osteogenic potency. Finally, µ-XRF was used as an innovative approach to determine the impact of a concentration range of EVs on biomineralisation against osteoblasts (Figure 4.1.).

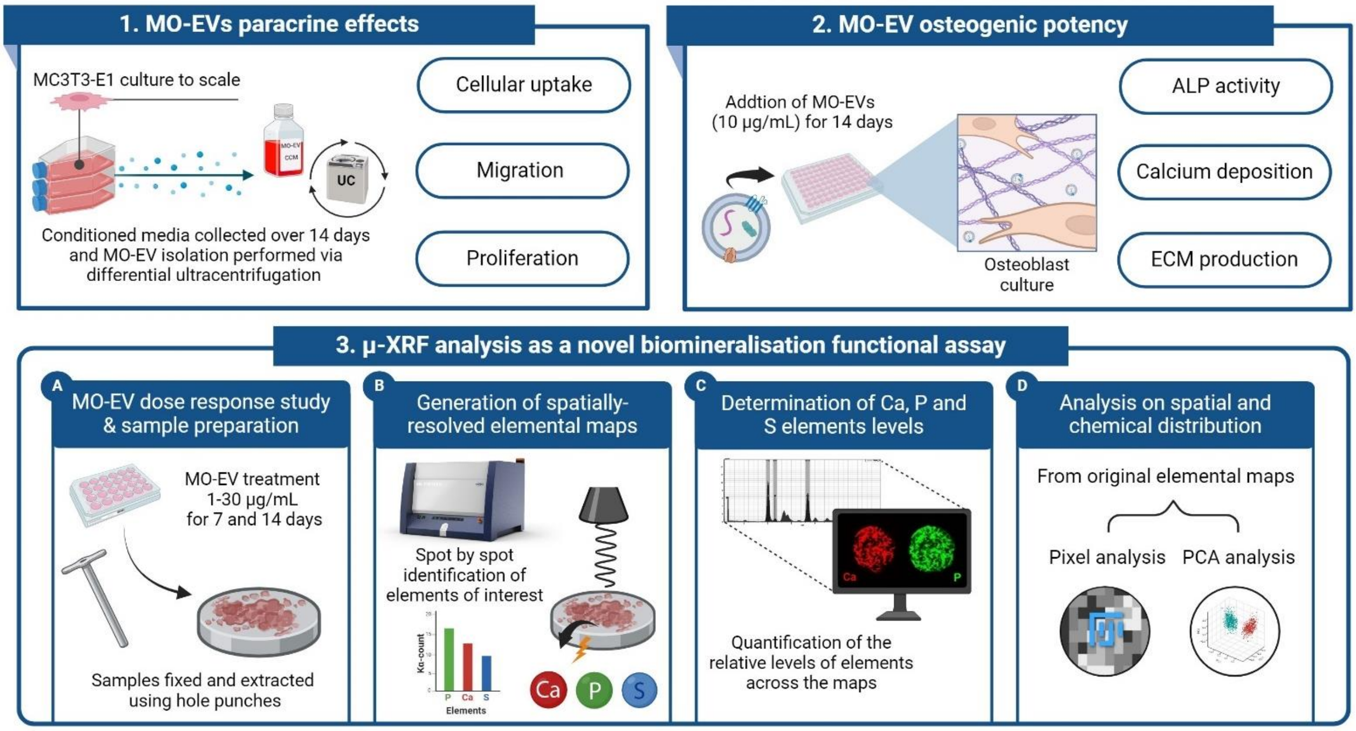

**Figure 4.1. | Schematic representation of Chapter IV experimental work with 1) the paracrine effects of MO-EVs. 2) the osteogenic potency of MO-EVs and 3) the use of μ-XRF is an innovative tool to assess biomineralisation *in vitro* (created using Biorender.com).**

### 4.1.2. Aim and objectives

The aim of this chapter was to evaluate the effects of MO-EVs on osteoblasts with a particular focus on *in vitro* biomineralisation via the development of an innovative µ-XRF based-method.

To achieve this aim, the following objectives were pursued:

- To evaluate the effects of MO-EVs on osteoblasts migration and proliferation.
- To determine the osteoinductive properties of MO-EVs on osteoblasts.
- To develop an innovative method based on µ-XRF spectroscopy to obtain greater insights on MO-EV induced biomineralization in a dose response study.

### 4.1.3. Acknowledgement of contributions

The following collaborators have been critical in contributing to this body of work:

- **Dr Adam McGuinness**, from the University of Birmingham, to have provided the analysis to obtain the standard curve presented in Figure 4.11.
- **Dr Victor Manuel Villapun**, from the University of Birmingham, for his support in the optimisation of the macrophage culture presented in Appendix 4.1.

## 4.2. Methods

### 4.2.1. Cellular uptake

To confirm the uptake of MO-EVs into MC3T3-E1 cells, a stock solution EVs were freshly labelled with the PKH26 lipid membrane dye. MC3T3-E1 cells were seeded at $1 \times 10^4$ cells/cm$^2$ in a 48-well plate in basal medium and incubated for 24 h. The following day, EV treatment (10 µg/mL) was then prepared in basal medium and added to the desired wells replacing the existing media. After 2 h, cells were fixed with 10% (v/v) neutral buffered formalin (NBF, Cellpath, United Kingdom) and stained with DAPI (Thermo Scientific, United Kingdom) to label the nuclei. Cultures were then imaged with an EVOS fluorescent inverted microscope (M5000, Thermo Scientific, UK).

### 4.2.2. Migration

To assess the migration rate of osteoblasts, the scratch assay was performed. MC3T3-E1 cells were seeded at $0.3 \times 10^4$ cells/cm$^2$ in a 48-well plate in basal medium and incubated for 24 h. The scratch was created manually using a 200 µL pipette tip to obtain a straight line across each well. EV treatment (10 µg/mL) was then prepared in basal medium and added to the desired wells replacing the existing media for 3 days. Microscopy images were obtained at day 0 to determine the baseline and the percentage of area recovered by cells was determined using Image J (v1.52) and its wound healing tool.

### 4.2.3. Proliferation

To assess the proliferation of osteoblasts, the AlamarBlue assay was employed to evaluate the metabolic activity of osteoblasts. MC3T3-E1 cells were seeded at $0.3 \times 10^4$ cells/cm$^2$ in a 48-well plate in basal medium and incubated for 24 h. Existing medium was then replaced by fresh basal medium containing MO-EVs at desired concentrations. After 7 days of treatment, AlamarBlue reagent (Thermo Scientific, UK) was added to the wells and incubated for 4 hours at 37°C. Using the TECAN SPARK plate reader, fluorescence signals were obtained at an excitation/emission wavelength of 540/590 nm.

### 4.2.4. µ X-ray fluorescence analysis

#### *4.2.4.1. Analysis parameters*

The M4 Tornado µ-X-ray fluorescence (µ-XRF) system (Brucker Nano Gmbh, Germany) was used to perform elemental analysis of 2D cultures of mineralising osteoblasts using the same culture conditions and seeding densities as previously described. The system is equipped with a rhodium µ-focus X-ray tube used as the primary X-ray source. Using a polycapillary lens, the X-rays can be focused on 25 µm spots providing the resolution of the analysis across the sample. The X-ray tube voltage was set to 50kV whereas the tube current was set to 400 µA. Regarding the acquisition parameters, the pixel time was set to 5 ms/pixel with a stage speed of 14.4 mm/s allowing a high-throughput analysis. The chamber was also placed under vacuum at 20 mbar before the start of the analysis. The elements of interest established were calcium (C), phosphorous (P) and sulphur (S).

#### *4.2.4.2. Sample preparation*

*In vitro* experiments were performed in 48-well plate at a cell density of $3 \times 10^3$ cells/cm$^2$ and EV treatments were performed as described in section 4.2.1. At endpoint, cells were washed with PBS before being fixed with 10% neutral buffered formalin for 20 min. Once fixed, cells were washed 3 times using distilled water and left to air dry. For a plate to be analysed using µ-XRF, the bottom of each well had to be extracted from the plate as the walls would prevent the sample to be close enough from the instrument for a successful analysis. Therefore, using a heated hole punch with a 10 mm-diameter fitting in the 48-well plate format, each disk corresponding to the bottom of a well was successfully extracted. To improve the practicality of sample loading, a 3D-printed grid with holes at the dimensions of the 48-well plate disks was manufactured. The disk was then inserted into the grid during the analysis to simplify the loading onto the stage as well as obtaining an even spacing between the disk on the final mapping.

#### *4.2.4.3. Data analysis*

µ-XRF scans were used to generate, in real time, spatially resolved elemental maps of the sample grid for the detection of calcium, phosphorus and sulphur defined as the elements of interest to observe the mineralised matrix. From the elemental spectrum of each spot, the system generated an image for which the number of X-ray counts/second per electronvolt (eV) determined at the Kα emission line of each element was proportional to the pixel intensity (Fig 4.2.).

Pixel analysis was also performed on Ca/P elemental map to determine the spatial distribution of mineral across each disk. Fiji software, an open-source platform for biological-image analysis, was used to transform the µ-XRF map exported as a JPEG file into a black and white image (Schindelin *et al.*, 2012). First, the original image was changed into a 16-bit grayscale image which then allowed the conversion to black and white. Using the ROI manager, objects were defined around each disk to obtain the same circle diameter for each sample which was based on the diameter of the smallest disk. Finally, the amount of black and white pixels was extracted for each sample allowing the determination of the percentage of sample area mineralised.

The autophase function of the µ-XRF proprietary software was used to identify specimen regions of similar composition. Edges and sensitivity parameter were set to 100 and the minimum phase area was set to 1%. Principle component analysis (PCA) of the spectra was performed for the selected Ca, P and S elements, thus, generating a new hypermap highlighting different regions with similar mineralisation profiles with similar levels of Ca, P and S in phase 1, 2 or 3.

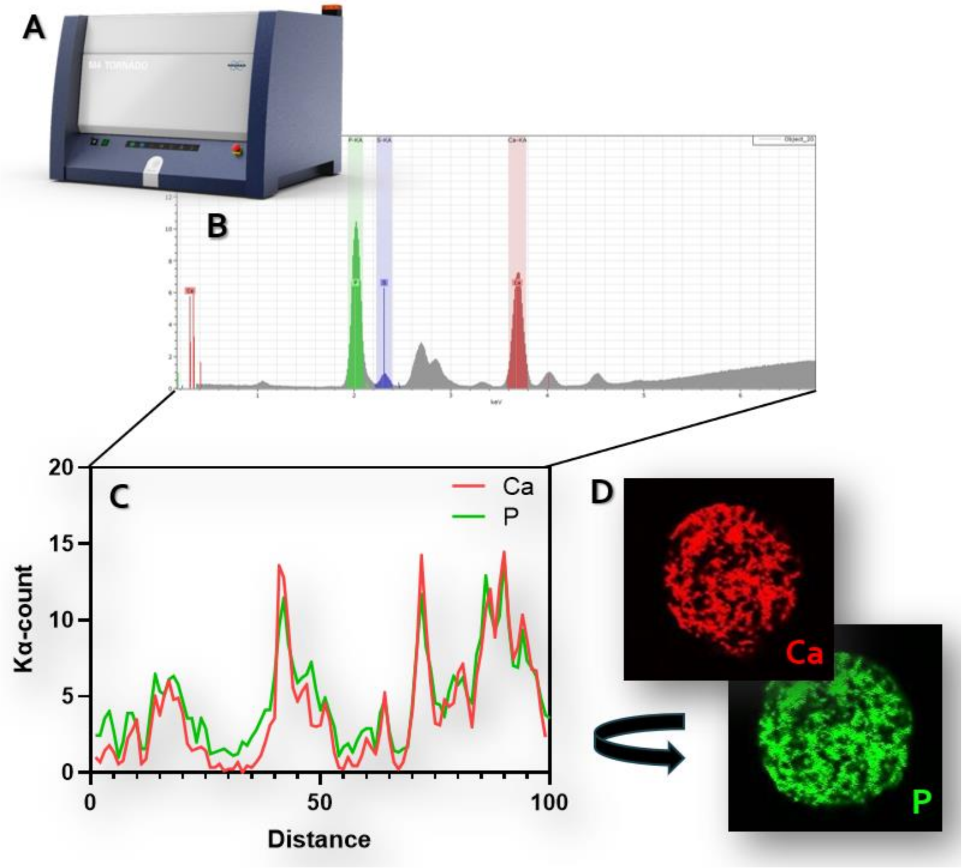

**Figure 4.2. | Schematic representation of the µ-XRF spectroscopy method analysis. A)** Prepared samples are placed in the analysis chamber of the M4 Tornado system. **B)** For each spot analysis a full elemental spectrum is obtained and the relative levels of elements of interest is isolated. **C)** Using the system software, elemental levels can be colocalised across the surface of the sample and elemental 2D maps can then be generated for each element **(D)**.

## 4.3. Results

### 4.3.1. Validation of the cellular uptake of MO-EVs in osteoblasts

First, after having decided to focus on the use of MC3T3 as the main model for this *in vitro* study, MO-EVs were labelled using a lipid membrane dye, PKH26, to be able to confirm their cellular uptake after treatment. As highlighted in Figure 4.3, MO-EVs were found to be localised within osteoblasts as early as after 2 h of treatments. Using fluorescence microscopy, large fluorescence signal indicates an accumulation of EVs within the cytoplasm.

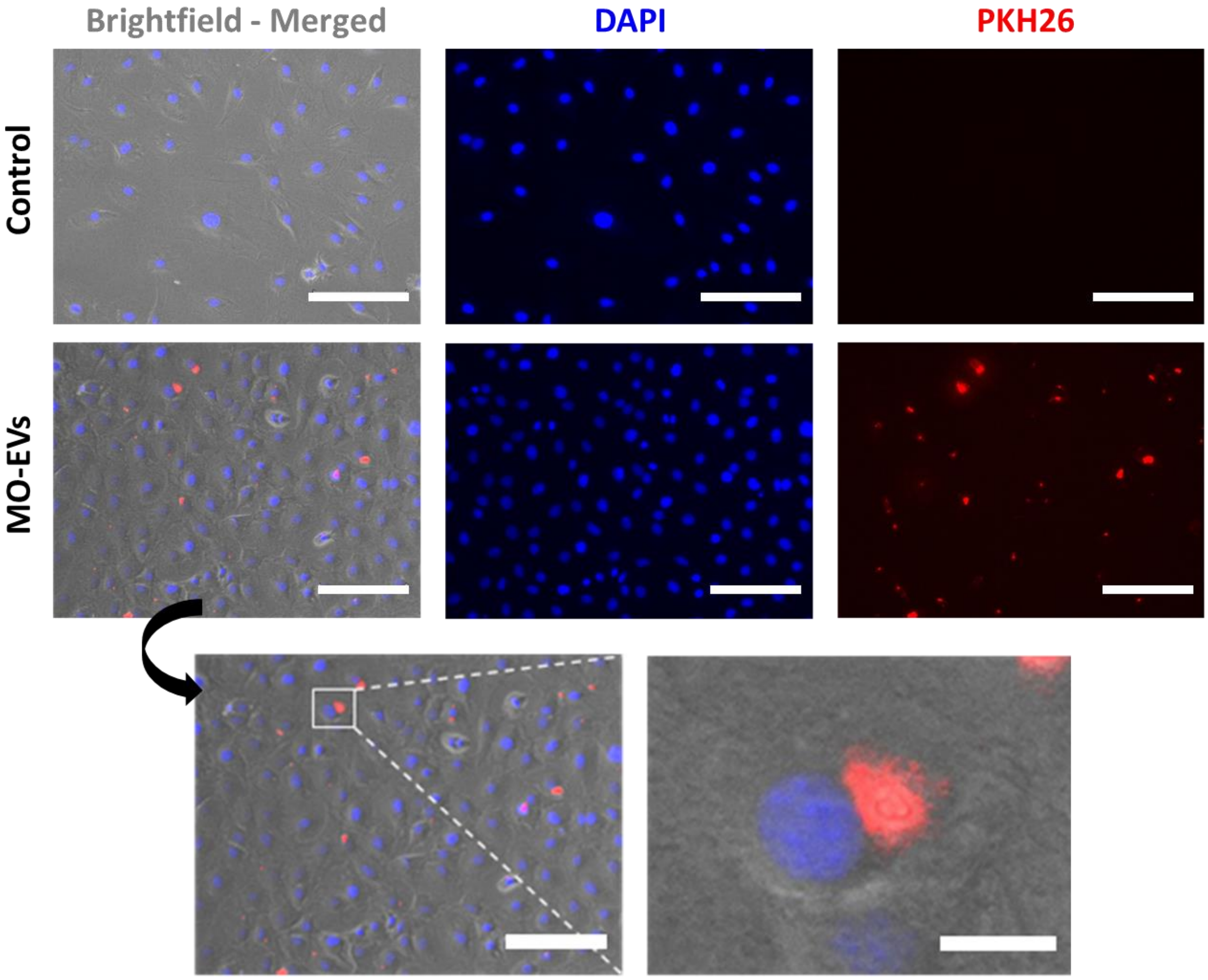

**Figure 4.3. | MO-EV uptake by osteoblasts after a 2 h-treatment in basal media.** Brightfield microscopy images merged with the fluorescent detection of nuclei (DAPI) and MO-EVs (PKH26). Scale bars = 200 µm.

### 4.3.2. Evaluation of the effects of MO-EVs on cell migration

The paracrine effects of MO-EVs were first assessed via the scratch assay in order to determine the influence of EVs on the migration of osteoblasts with visible scratches presented in Figure 4.4. Compared to untreated conditions at Day 0, the scratched area reduced at Day 3 for both untreated and MO-EV treated groups ($p<0.01$). However, no significant differences were observed after MO-EV treatment showing the absence of MO-EV effects on the migration of osteoblasts (Figure 4.4B).

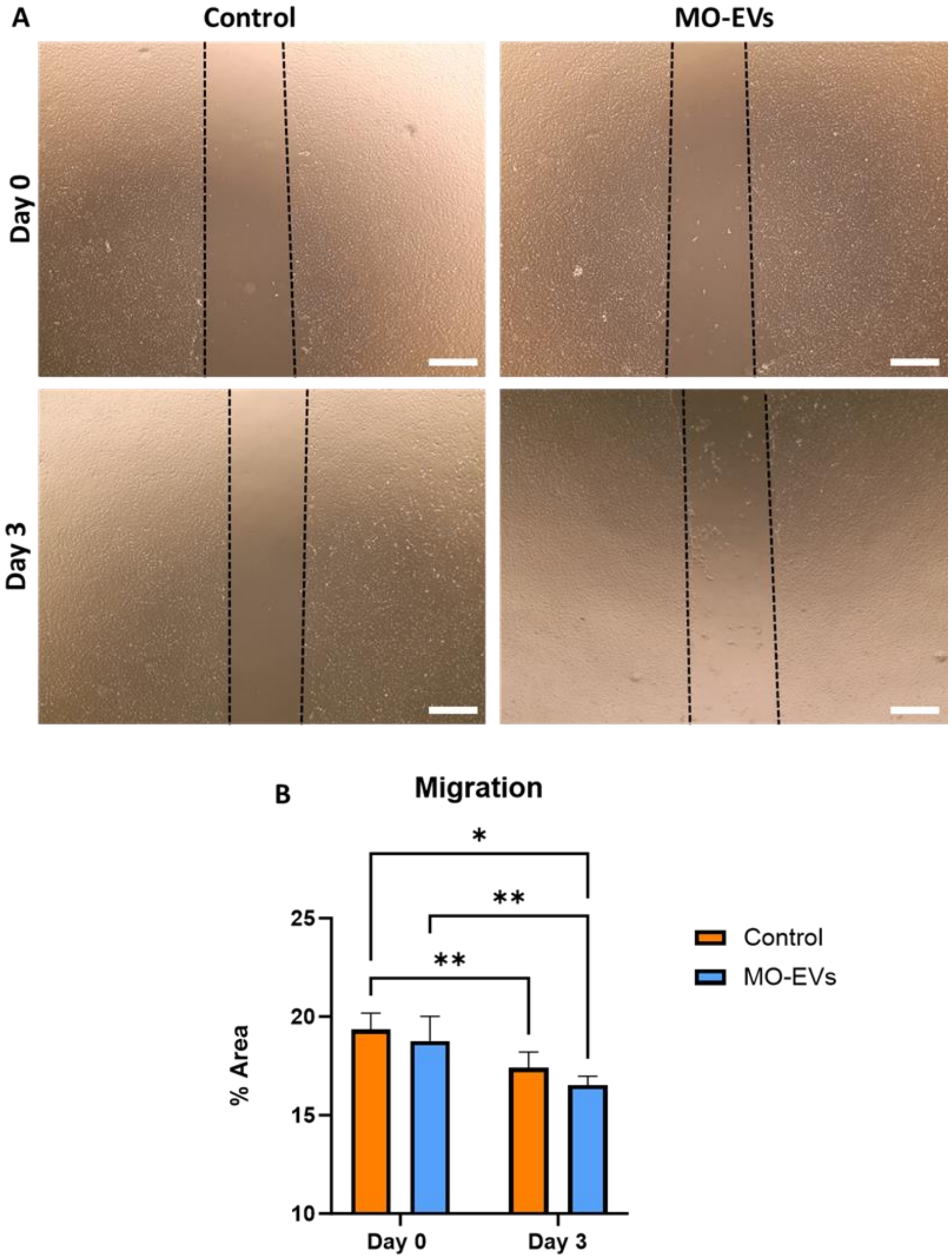

**Figure 4.4. | Effects of MO-EVs on osteoblast migration.** MO-EV treatment (10 µg/mL) was used on MC3T3-E1 cells and cell migration was assessed using the scratch assay after 3 days. **A)** Brightfield microscopy images. Scale bars = 200 µm. **B)** Quantification of the percentage of the area clear of cells. Data expressed as average ± SD. *p ≤ 0.05, **p ≤ 0.01, and ***p ≤ 0.001.

### 4.3.3. Evaluation of the effects of MO-EVs on cell metabolic activity

The evaluation of cellular metabolic activity was performed using the AlamarBlue assay. After a pilot study using 10 µg/mL showing no response, the experiment was repeated using the concentration range employed in further biomineralisation assessment. After 7 days of MO-EV treatment, osteoblasts treatment with 20 and 30 µg/mL were the only treatment groups observing a significant increase in metabolic activity compared to control (p<0.01) (Fig 4.5.).

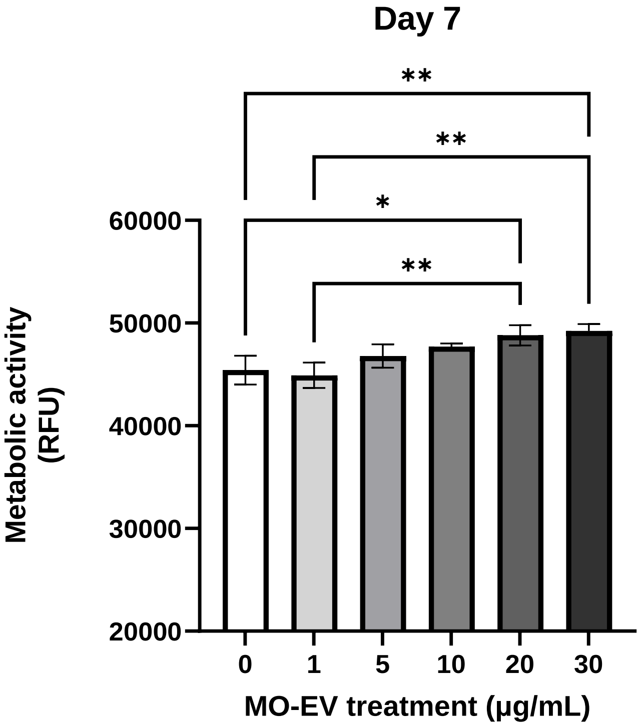

**Figure 4.5. | Effects of MO-EVs on the metabolic activity of osteoblasts after 7 days of treatment (10 µg/mL).** Data expressed as average ± SD (n=3). *p ≤ 0.05, **p ≤ 0.01, and ***p ≤ 0.001.

### 4.3.4. Determination of the osteogenic potency of osteoblasts

Changes in mineralisation were assessed via the quantification of calcium deposition, collagen production and ALP activity after two weeks of culture. MC3T3-E1 cells were cultured in basal media, osteogenic media (basal media + osteogenic supplements) or MO-EVs (EV suspension at 10 µg/mL in osteogenic media). As observed in Figure 4.6A, osteogenic conditions were necessary to induced mineralisation with the absence of staining in basal conditions for both (Fig 4.6.A). Alizarin red staining (ARS) and Picro Sirius red staining (PRS) staining (Fig 4.6.A). Furthermore, the semi-quantification performed after de-staining revealed that MO-EV treatment induced a significant increase ($p<0.05$) in both calcium deposition and collagen production compared to EV-free osteogenic conditions (Fig 4.6B & C). Similarly, ALP activity was found to be significantly increased by MO-EV addition to osteoblasts in osteogenic conditions ($p<0.05$) (Fig 4.6D).

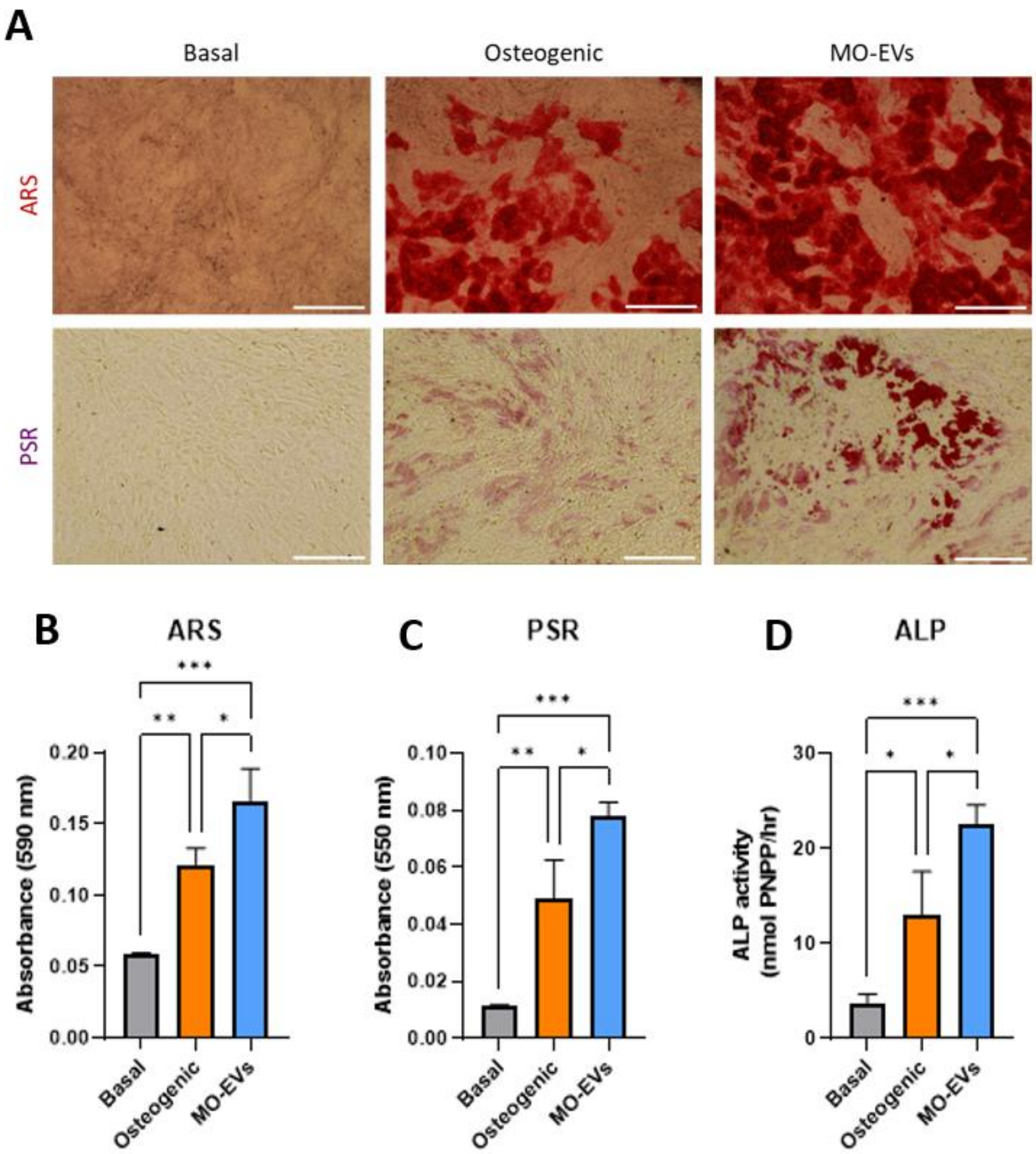

**Figure 4.6. | *In vitro* validation of MO-EVs' osteogenic potency.** MO-EVs were used at a concentration of 10 µg/mL treating MC3T3-E1 osteoblasts every 2 days over a 14-day period in basal media (growth media), osteogenic media (growth media with osteogenic supplements) or MO-EVs (EV suspension in osteogenic media). **A)** Alizarin red staining (ARS) and picrosirius red staining (PSR) to evaluate calcium and collagen deposition respectively after 14 days of EV treatment. Scale bars = 1 mm **B)** Alizarin red staining semi-quantification. **C)** Picrosirius red staining semi-quantification. **D)** ALP activity after 14 days of culture. Data expressed as average ± SD (n=3). $^{*}p \le 0.05$, $^{**}p \le 0.01$, and $^{***}p \le 0.001$.

### 4.3.5. Advanced biomineralisation assessment via µ-XRF

µ-XRF analysis was performed to analyse the influence of MO-EV dosing on biomineralisation. Dosing in the context of EV-research is of utmost importance as standardisation in pre-clinical studies remains an issue and determining the effective concentration range for EV treatments is key for their clinical translation. The dose response study was performed with MO-EV protein concentrations ranging from 1 to 30 µg/mL, which were added to osteoblast cultures under osteogenic conditions for 7 and 14 days. The first qualitative assessment shows the presence of calcium and phosphorus elements at both day 7 and day 14 across all conditions with a clear visual increase of calcium deposition at day 14 compared to day 7 (Fig 4.7A). From this elemental mapping, quantification of the levels of elements of interest was conducted. The integration of the photon counts at the emission line of each element provided the number X-ray counts at Kα lines and was used to quantitatively assess the relative presence of each element as an average for each well. Interestingly, as observed in figure 4.7B, the highest concentration of MO-EV has augmented the level of phosphorus at day 14 compared to all other concentrations with p value $< 0.001$ compared to control. Regarding calcium levels at day 14, they are only significantly increased between 1-20 and 1-30 µg/mL (Fig 4.7B).

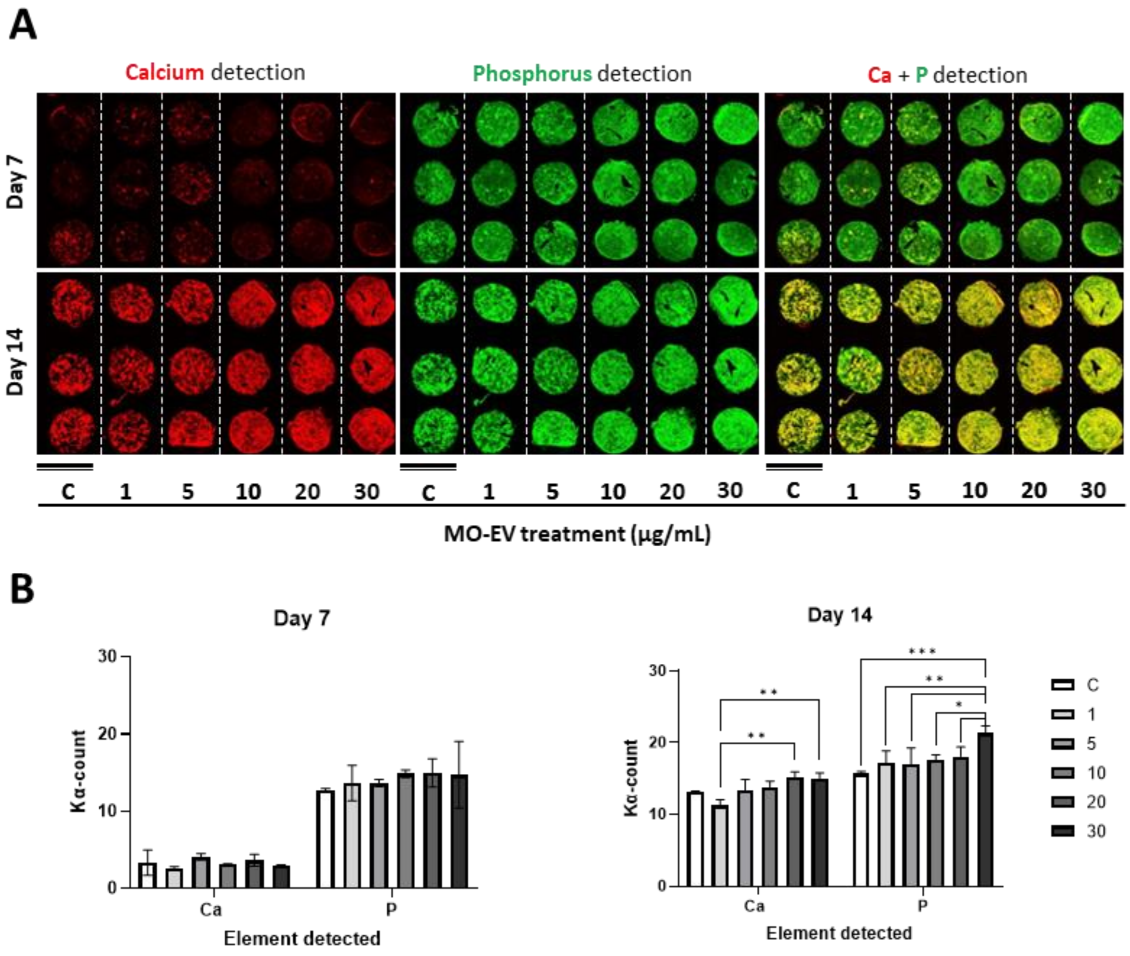

**Figure 4.7. | MO-EV dose response study using µ-XRF. A)** Elemental mapping of MC3T3-E1 cultures *via* the detection of calcium and phosphorus elements after 7 or 14 days of MO-EV treatment from 1 to 30 µg/mL. Scale bars = 10 mm. **B)** Calcium and phosphorus quantification from elemental maps. Data expressed as average ± SD (n=3). *p ≤ 0.05, **p ≤ 0.01, and ***p ≤ 0.001.

Additionally, the influence of MO-EV treatment range on ECM production was also evaluated (Fig 4.8.). First as presented in Fig 4.8A, PSR staining was used to stain for collagen I as a marker of ECM production. The semi quantification of the staining showed that EV treatment had no significant effect on the amount of ECM produced at day 7, however, all EV concentrations from 1 µg/mL induced a significant increase of ECM production ($p<0.001$) (Fig 4.8B). Moreover, only 20 and 30 µg/mL treatment groups showed a significant increase of ECM between day 7 and day 14 (20, $p<0.05$; 30, $p<0.001$) (Fig 4.8C).

Sulphur detection was performed using µ-XRF analysis on the stained samples to provide insights into ECM levels as sulphur atoms are particularly enriched in a protein dense sample such as the extracellular matrix. Sulphur elements were detected across all samples (Fig 4.8D). A significant time-dependent increase was observed with all groups showing significantly higher sulphur levels at day 14 compared to day 7, however, no significant changes were detected in a dose-dependent manner (Fig 4.8E).

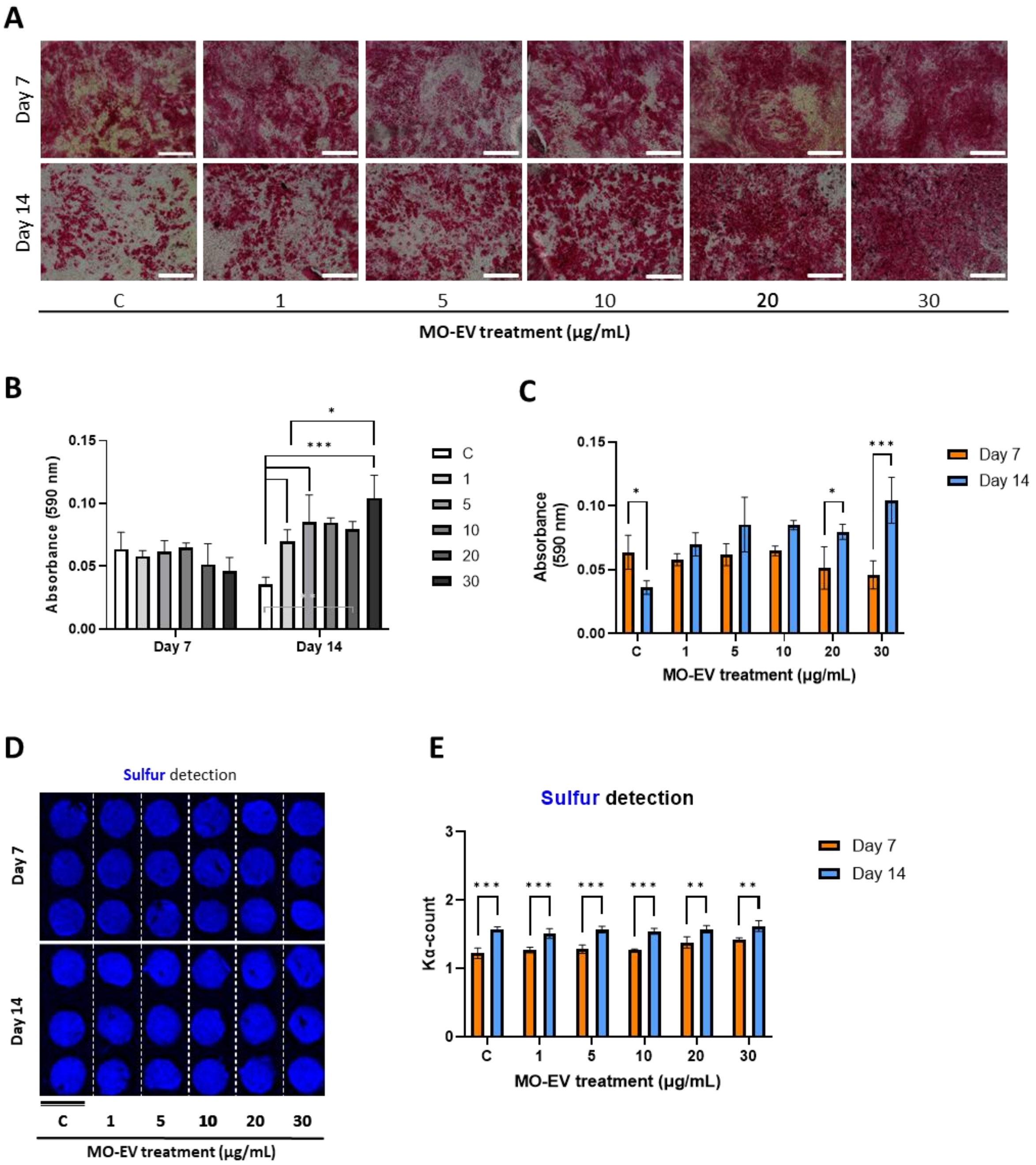

**Figure 4.8. | Influence of MO-EV treatment on ECM development. A)** Picrosirius red staining of µ-XRF samples post-analysis. Scale bars = 1 mm **B)C)** Semi-quantification of PRS staining. **D)** Elemental mapping of MC3T3-E1 cultures via the detection of sulphur after 7 or 14 days of MO-EV treatment from 1 to 30 µg/mL. Scale bars = 10 mm. **E)** Sulphur quantification. Data expressed as average ± SD (n=3). $*p \leq 0.05$, $**p \leq 0.01$, and $***p \leq 0.001$.

### 4.3.6. MO-EVs influenced the mineralised phase coverage in osteoblast cultures

Pixel analysis was conducted on the Ca/P elemental map to determine the percentage of mineral coverage across each 2D culture by separating mineralised area labelled in white from unmineralized area labelled in black (Fig 4.9A). The quantification of the white pixels allowed to determine the percentage of area occupied by mineral deposition colocalising Ca and P (Fig 4.9A). After both 7 and 14 days, MO-EV concentrations of 10, 20 and 30 µg/mL induced a significant increase of mineral deposition compared to untreated cells and 1 µg/mL MO-EV treatment ($p<0.05$) (Fig 4.9B). Although the mineral distribution increase pattern is similar between MO-EV concentration and untreated control, there is a significant temporal change in terms of the percentage of area mineralised with values ranging from 25 to 50% at day 7 and from 50% and reaching values superior to 90% with the highest MO-EV concentrations (Fig 4.9C). Notably, mineral coverage increased for all groups between day 7 and day 14 ($p< 0.001$).

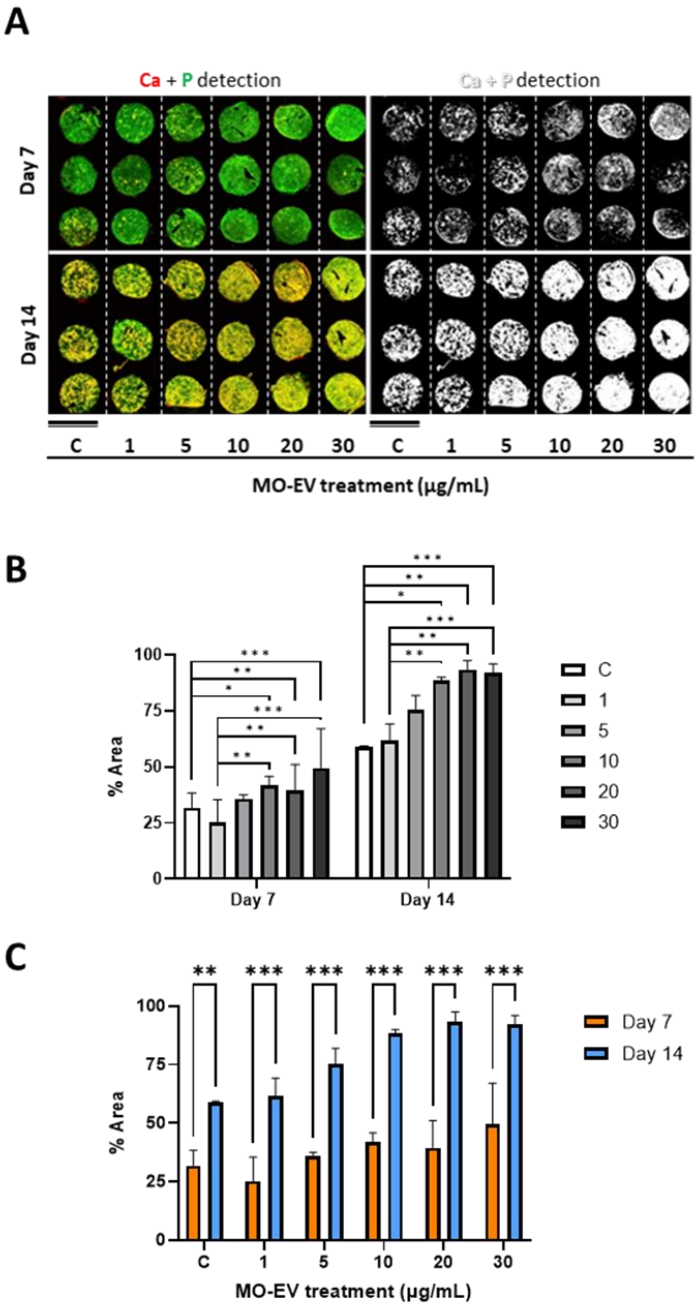

**Figure 4.9. | Pixel analysis on µ-XRF elemental maps. A)** Elemental mapping comparison between original image and black & white version. Scale bars = 10 mm. **B)** Quantification of mineralised area between day 7 and day 14. **C)** Quantification of mineralised area between MO-EV treatments and untreated cells. Data expressed as average ± SD (n=3). $^{*}p \le 0.05$, $^{**}p \le 0.01$, and $^{***}p \le 0.001$.

### 4.3.7. MO-EVs influence the composition of the mineralised matrix of osteoblast cultures in a time- dose-dependent manner

Using the autophase function on µ-XRF analysis software, principal component analysis (PCA) hypermaps were generated, allowing for distinct mineralisation phases to be identified based on the similarity of their composition in calcium, phosphorus, and sulphur elements. A gold standard in the chemical analysis of minerals is X-ray diffraction (XRD) which can provide an in-depth structural and chemical analysis via X-ray scattering or diffraction beyond the capacity of XRF used for elemental analysis. Using that autophase function, the PCA analysis allows to transform the elemental maps generated into phase maps identifying regions with similar levels of selected elements. Therefore, this complementary approach provides important insights which are not readily accessible via conventional XRF analysis.

Three mineralisation phases were identified using PCA analysis alone and presented in Figure 4.10A. Phase 1 appeared to be the most preponderant phase present at day 7 with an increased presence following MO-EV concentration. At day 14, the 3 phases are present with a clear contrast between phase 1 and 3 as the presence of the first decrease as MO-EV concentration increases whereas phase 3 follows the opposite pattern. Regarding phase 2, it is present across the conditions at day 14 only (Fig 4.10C). Following, this original analysis data binning was applied to the PCA, which accented the composition phase separation leading to the generation of two clear phases. At day 7 and across all groups, phase 1 was the major component across all samples with only traces of phase 2 detected. However, from day 14, the two phases co-exist in a 1:1 ratio for control and 1 µg/mL MO-EV treatment and the percentage of phase 2 then increase significantly with the EV concentration reaching over 90% from 10 µg/mL as quantified via pixel analysis. In Figure 4.10D, the relative levels of Ca, P and S attributed to each phase were obtained showing that phase 2 exhibited higher levels of both

Ca and P compared to phase 1. Moreover, this increased level of Ca and P in phase 2 appears to be linked to a higher Ca/P ratio as showed in Figure 4.10E which can be linked to a higher degree of mineral maturity increasing with both time and MO-EV concentration.

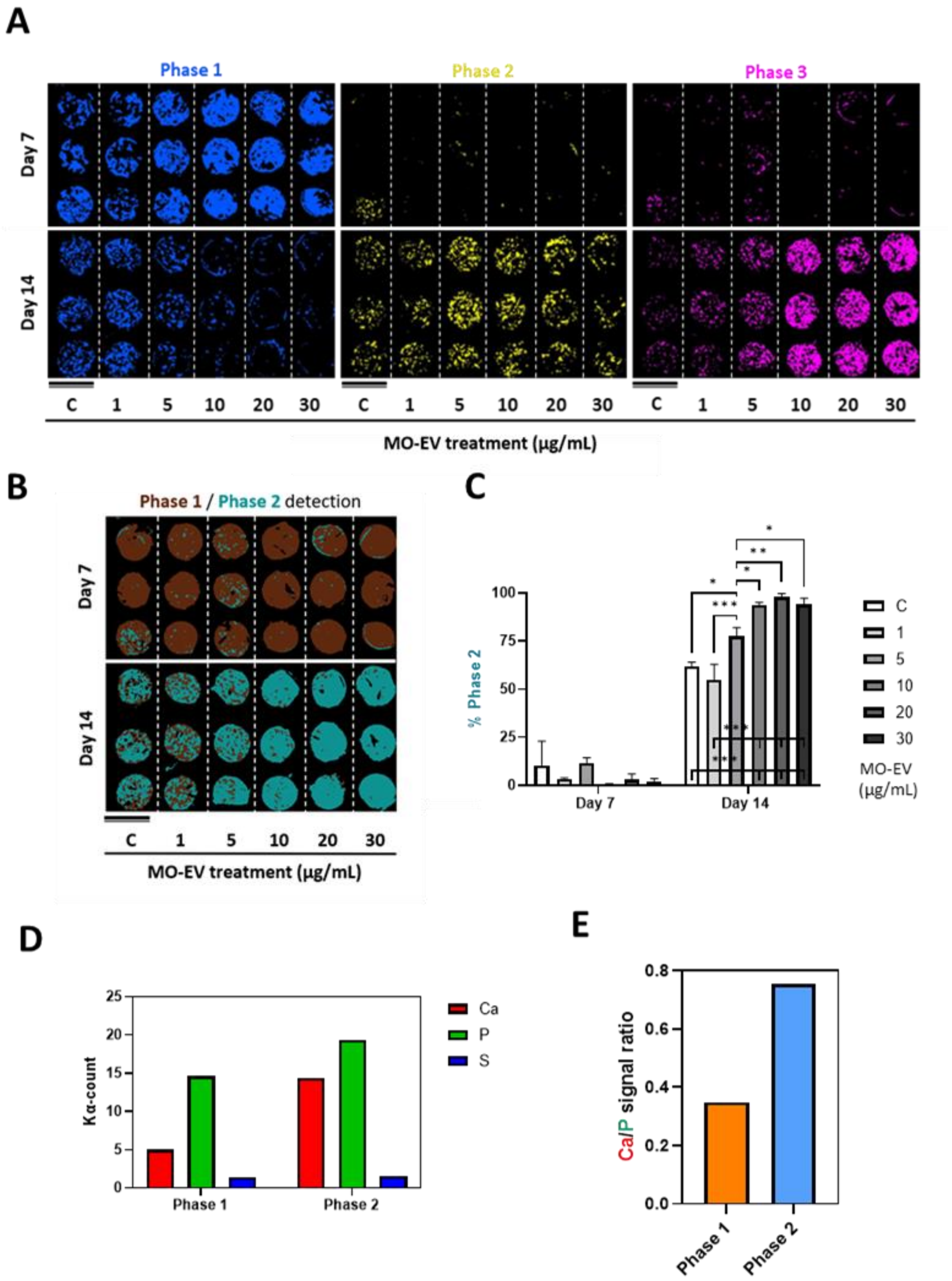

**Figure 4.10. | Mineralised phases identified on elemental maps via PCA analysis A)** Hypermap obtained from PCA analysis alone. Scale bars = 10 mm. **B)** Hypermap obtained from PCA analysis with data binning. Scale bars = 10 mm. **C)** Quantification of the percentage of phase 2 by pixel analysis determined by PCA analysis with data binning**. D)** Calcium, phosphorus and sulphur composition of the established phases obtained via PCA analysis with data binning. **E)** Ca/P ratio of phases determined by PCA analysis with data binning. Data expressed as average ± SD (n=3). *p ≤ 0.05, **p ≤ 0.01, and ***p ≤ 0.001.

### 4.3.8. Generation of a standard curve to facilitate µ-XRF interpretation for biomineralisation

The relative comparison of a range of Ca/P compounds including sodium polyphosphate (Na Poly; $(NaPO_3)_n$), monocalcium phosphate monohydrate (MCPM; $Ca(H_2PO_4)_2$), brushite ($CaHPO_4$), calcium pyrophosphate (Ca Pyro; $Ca_2P_2O_7$), β tricalcium phosphate (BTCP; $Ca_3(PO_4)_2$) and hydroxyapatite (HA; $Ca_{10}(PO_4)_6(OH)_2$) has provided with an expected increase of Ca/P signal ratio when analysed by µ-XRF analysis. Thus, by plotting the determined Ca/P signal ratio against the known Ca/P atomic ratio, a Ca/P compound standard curve has been established with $R^2=0.984$ (Fig 4.11.). This curve can then be used to determine the Ca/P atomic ratio of a sample based on the Ca/P ratio determined via µ-XRF analysis widening considerably the analytical output to interpret mineral maturity in *in vitro* studies. Here, with signal ratios of <0.4 for phase 1 and <0.8 for phase 2 (Fig 4.10E), Ca/P atomic ratios <0.25 are then found.

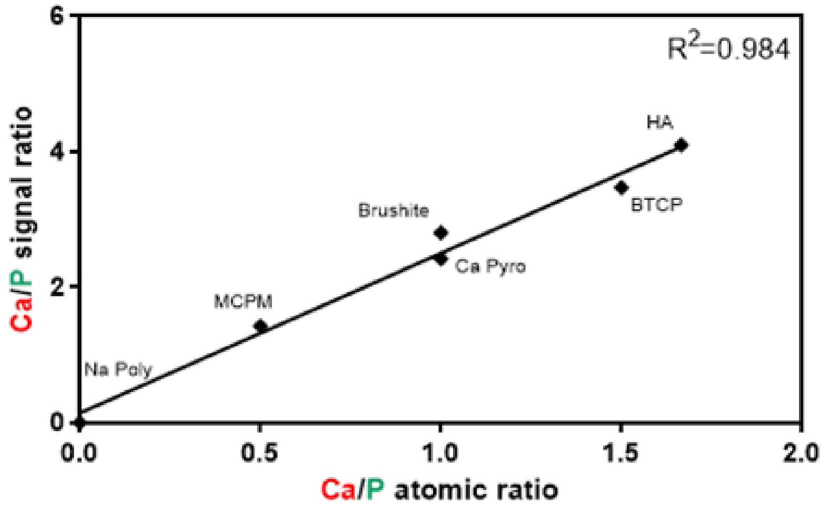

**Figure 4.11. | Standard curve of calcium-phosphate compounds of reference to determine the relationship between Ca/P signal ratio and Ca/P atomic ratio.**

## 4.4. Discussion

### ***Rapidly uptaken by osteoblasts, high concentrations of MO-EVs increased osteoblast proliferation.***

In the first section of this Chapter, we investigated the paracrine effects of EVs on the migration and proliferation of osteoblasts. It was first demonstrated that MO-EVs were uptaken by osteoblasts as an aggregation of PKH26-labelled vesicles were observed after only 2 h of incubation. However, in the absence of an ECM in early time points of culture, no conclusion can be drawn regarding the ability of these particles to preferably bind to the matrix. Using the scratch assay, MO-EVs did not significantly augment the migration of osteoblast within 3 days of cultures. A greater concentration range and longer time points might be required to observe difference between groups. However, the rapid doubling time of the MC3T3-E1 cell line appeared to completely close the wound at beyond Day 3 (data not shown). Interestingly, after having not observed any effects of MO-EVs on proliferation at 10 µg/mL, the MO-EV dose response experiment was repeated including a MO-EV concentration range reaching 30 µg/mL. The highest concentration at 20 and 30 µg/mL did show a significant increase of the metabolic activity of MO-EVs after 7 days. To be able to clearly link this change of metabolic activity to proliferation, a need for additional experimental work including DNA quantification or cell counting would be required to confirm these results. Compared to a previous study performed by Man *et al.* (2021a), they found that MO-EVs were able to significantly accelerate migration after 3 days and proliferation after 7 days using MC3T3-E1-MO-EVs on hBMSCs, thus, suggesting a difference in cellular response upon the type of recipient cell employed.

### ***MO-EVs increased early biomineralisation in osteogenic cultures of MC3T3-E1 osteoblasts.***

With the *in vitro* validation, the effect of MO-EVs on the induction of mineralisation was reported for the first time on their own parental cells. Additionally, this allowed to continue the investigation of MO-EVs obtained from MC3T3-E1 cells in line with existing literature. We showed that at the same EV-protein concentration of 10 µg/mL that was previously found potent on hBMSCs (Davies *et al.*, 2017), MO-EVs were also potent against MC3T3-E1 cells with a significant increase of ALP activity, calcium deposition and collagen production after 14 days of culture ($p \leq 0.05$). These results might open the possibility of an increased testing capacity *in vitro* as the cellular response might be more reproducible against an established cell line compared to hMSCs which can be limited by their access and the donor variability. Finally, by conserving an existing EV isolation protocol across multiple previous studies, we are trying to implement a standardisation strategy to work on the same population of MO-EVs with similar treatment regimen overtime (Man *et al.*, 2021b; Man *et al.*, 2022b). Together, these findings demonstrated the osteoinductive properties of MO-EVs. From the assessment of this bulk effect from osteoblast 2D cultures, the µ-XRF methodology developed was then used to obtain additional insights into MO-EV driven biomineralisation.

### ***The potential of µ-XRF was successfully harnessed to develop an innovative method to study biomineralisation in vitro.***

Current approaches to assess biomineralisation and evaluate MO-EVs' influence in this context are limited by their resolution as most methods employed only evaluate a quantitative effect as an average level from an entire well. For example, the semi-quantification of calcium staining will provide with a level of calcium stained per well without taking into account localised Ca/P ratio or determining the presence of mineral nodules. Moreover, these methods usually result in the destruction of the sample at a given endpoint leading to labour-intensive studies already being performed on long time-points. As an example, in their most recent studies on dexamethasone-stimulated osteoblast-derived EVs, Zhang *et al.* (2023) relied on alizarin red and von Kossa staining coupled with an osteogenic marker gene expression study to determine MO-EV groups' effect on biomineralisation describing the morphology of nodules from staining only which correspond to the most commonly used robust methodology (Zhang *et al.*, 2023). Alternative X-rays based methods have been employed for many years to identify mineral composition such as XRD or scanning electron microscopy with energy dispersive X-ray spectroscopy (SEM/EDX). Although powerful, these approaches are more suited to identify the chemical composition of the samples with high definition and cannot be integrated to the workflow of a biolaboratory to run entire culture microplates.

Here, we developed a novel approach harnessing the potential of µ-XRF spectroscopy to quantitatively assess biomineralisation in a comparative manner between in vitro samples permitting to look into calcium, phosphorus and other elements of interest from a single elemental mapping. Additionally, these benchtop instruments are consumable-free reducing the cost of analysis, although the instrument itself can be very expensive to acquire. It also enables high-throughput analysis as the automated mapping in cycles of multiple plates can be performed overnight, also reducing variability between acquisitions.

Regarding the first detection of Ca/P (Fig 4.7.), the MO-EV concentration comparison only showed a significant increase of signal for high MO-EV concentrations which is higher than the potent EV-concentration assessed *in vitro* (20 and 30 µg/mL). This suggests that average detection across the sample surfaces does not take into consideration important parameters such as nodule formation or mineral density as the treated groups with no significant difference compared to control still displayed visuals insights into the difference of Ca/P levels across the matrix indicating an EV-effect non linked to the quantity of elements but to their association or distribution. Using a standard PSR staining, a significant increase was demonstrated with all MO-EVs concentrations compared to untreated control ($p<0.001$). This confirmed previous investigations using 10 µg/mL only with, notably, no significant difference in ECM levels between all EV concentrations.

The detection of sulphur elements as a marker of ECM deposition appeared to be useful to assess temporal changes, however, additional experiments would be necessary to determine the resolution level that this approach may offer with for example the use of collagen coatings of increased concentrations to be used as standards. Nevertheless, in more complex samples, sulphur elements co-localised to Ca/P may allow to only identify regions where the mineral is located in ECM.

**Computational approaches such as pixel analysis and phase composition analysis augmented the quality of µ-XRF analysis outputs.**

Pixel analysis was utilised on the generated elemental maps to determine the coverage of minerals across the 2D surface looking at regions where Ca and P were co-localised. This analysis revealed a clear time- and concentration-dependent effect observed after addition of MO-EVs from 5 µg/mL with a continuous increase of mineralised area following EV concentration. Interestingly this effect was observable at day 7 indicating that MO-EV treatment is impactful even at the very early stages of biomineralisation. With groups approaching 100% coverage at day 14, the use of large surface of culture might be required for longer time points not to be limited by the culture format to see differences between EV concentrations or time points. This image analysis post µ-XRF analysis appears to be a useful complement, maximising the data output by exploring potential mechanism of actions. Importantly, this analysis also enabled to distinguish the efficacy of different treatment dosages which was not initially highlighted by the µ-XRF analysis alone. This suggested that a more intricate mechanism of action is revealed as mineral coverage appear to significantly vary with MO-EVs without significant changes in terms of either ECM or Ca/P levels.

Nevertheless, from this mineral coverage assessment alone, the reason behind MO-EV increasing mineral coverage still needs to be investigated as this change could be linked to either change in mineral spatial distribution in the matrix, the creation of more mineral dense regions or simply the acceleration of the mineralisation process to an increased osteoblastic activity.

In Figure 4.10., the mineral phase containing Ca, P and S was evaluated using the autophase function of the proprietary software which consisted of the generation of new hypermaps based on the levels of Ca, P and S creating different phases of these 3 elements via PCA. After data binning, two clear phases were generated showing that the mineralised phases presented higher levels of Ca/P at day 14 compared to day 7 with a doubled Ca/P ratio. Although the increased mineralisation overtime was expected, there is a 50/50 ratio in the presence of these two identified phase in the control group at day 14. This more mature phase then increases with EV concentration being the unique phase present from 10µg/mL. These results shows that this phase follows the mineral coverage pattern observed before in figure 4.9. indicating that the increased mineral coverage is not only due to mineral spreading across the matrix after EV treatment but to the generation of a more mature mineral phase presenting higher levels of Ca/P.

Investigating early bone formation, understanding the Ca/P ratio across a given sample is key as the colocalization of Ca and P at the microscale allow us to evaluate the progression and the maturity of the mineralised phase. Here, we produced a standard curve of calcium-phosphate compounds to match the Ca/P signal ratio obtained via µ-XRF analysis to the atomic Ca/P ratio of the known compounds (Fig 4.11.). The standard curve produced was satisfactory as a coefficient of determination of 0.984 was obtained. This allowed us to determine that a maximum Ca/P atomic ratio identified in the study remained below 0.25. This underlined that early mineralisation *in vitro* did not generate a matured calcified matrix with crystals of higher Ca/P ratio, showing the potential of µ-XRF for the analysis of mineralised phases over longer periods of time while obtaining insights into the degree of maturity of these minerals. Nevertheless, important limitations to note are that the sample preparation described here is required to extract samples from well plates (dried and flat surface) and the quantification remains relative as it is performed standardless, thus limiting the absolute quantitative comparison between studies. Other alternative methods are used for elemental detection with high resolution and for the detection of lighter elements such as SEM coupled with energy-dispersive X-ray spectroscopy or inductively coupled plasma mass spectrometer workflows. Nevertheless, with its high throughput and its ease-of-use µ-XRF remains a more ideal benchtop instrument to include in a biolab workflow.

Although, exclusively used on 2D cell cultures here, there is a great potential for µ-XRF to be applied to the assessment of biomineralisation in different experimental settings. For example, the determination of mineral deposition on metallic surfaces for implants remains difficult using regular microscopy method (Liu *et al.*, 2015) and the development of hydrogel systems for the delivery of extracellular examples is yet to be another area to explore for tissue engineering applications (Gkioni *et al.*, 2010). Future work includes the robust validation of the quantitative approach by creating reproducible standards to quantify the elements of interest using the same sample format. Exploring new application of *in vitro* analysis beyond biomineralisation and using a variety of format such as spheroids cultures, hydrogels, or 3D-printed metal scaffolds (Vermeulen *et al.*, 2023).

Overall using this novel µ-XRF method, we demonstrated that MO-EVs were not only capable of increasing osteoblast driven mineralisation but also to modulate the coverage and distribution of these minerals across the ECM produced which was also linked to a more mature mineral phase. Although requiring great amounts of MO-EVs, longer time points should be investigated next in order to observe these changes in more mature cultures such as day 21 or 28. Additionally, preliminary results were obtained to study the influence of temporal effect on MO-EVs by isolating separately the vesicles after 1, 2 or 3 weeks of mineralising cultures (Appendix 4.2.). This pilot study is encouraging as first results showed a MO-EV dose-dependent effect on the ALP activity of recipient hMSCs with an interesting variation observed between EVs isolating from different weeks of culture (Appendix 4.3.). This opens the way to extensive further studies investigating the different populations of EVs that can be released overtime during mineralisation as well as the impact of the maturity of osteoblasts on the resulting EVs secreted.

Moreover, to better understand the plurality of MO-EV mechanism of action, their effects should be investigated on different recipient cells. As displayed in Appendix 4.1., a pilot study was performed to evaluate the effects of MO-EVs on macrophage polarisation as these immune cells are responsible for osteoblastic stimulation during bone fracture healing (Frade *et al.*, 2023). Using the potent MO-EV concentration used earlier, only 30 µg/mL appeared to have an effect on macrophages adopting an M1 phenotype. However, no conclusion can be drawn for these preliminary results alone.

## 4.5. Conclusion

In this chapter, a wide range of cellular response to MO-EVs have been evaluated in osteoblasts. Importantly, using a reference 10 µg/mL concentration, MO-EVs demonstrated for the first time their capacity to increase biomineralisation with ALP activity, calcium deposition and ECM production found significantly augmented after a 2-week MO-EV treatment. From these encouraging results, a novel µ-XRF methodology was developed in order to further understand the influence of MO-EVs on biomineralisation. Overall, this dose response showed that MO-EVs were capable to increase the mineral coverage in 2D cultures and increased ECM deposition as well as influencing the composition of the mineralised matrix of osteoblast cultures in a time- dose-dependent manner. Notably, highest doses of MO-EVs, 20 and 30 µg/mL, were found able to increase osteoblast metabolic activity which may suggest that the uptake of MO-EVs by osteoblast results in an increased mineralising activity.

# Chapter IV – Appendices

## Appendix 4.1.

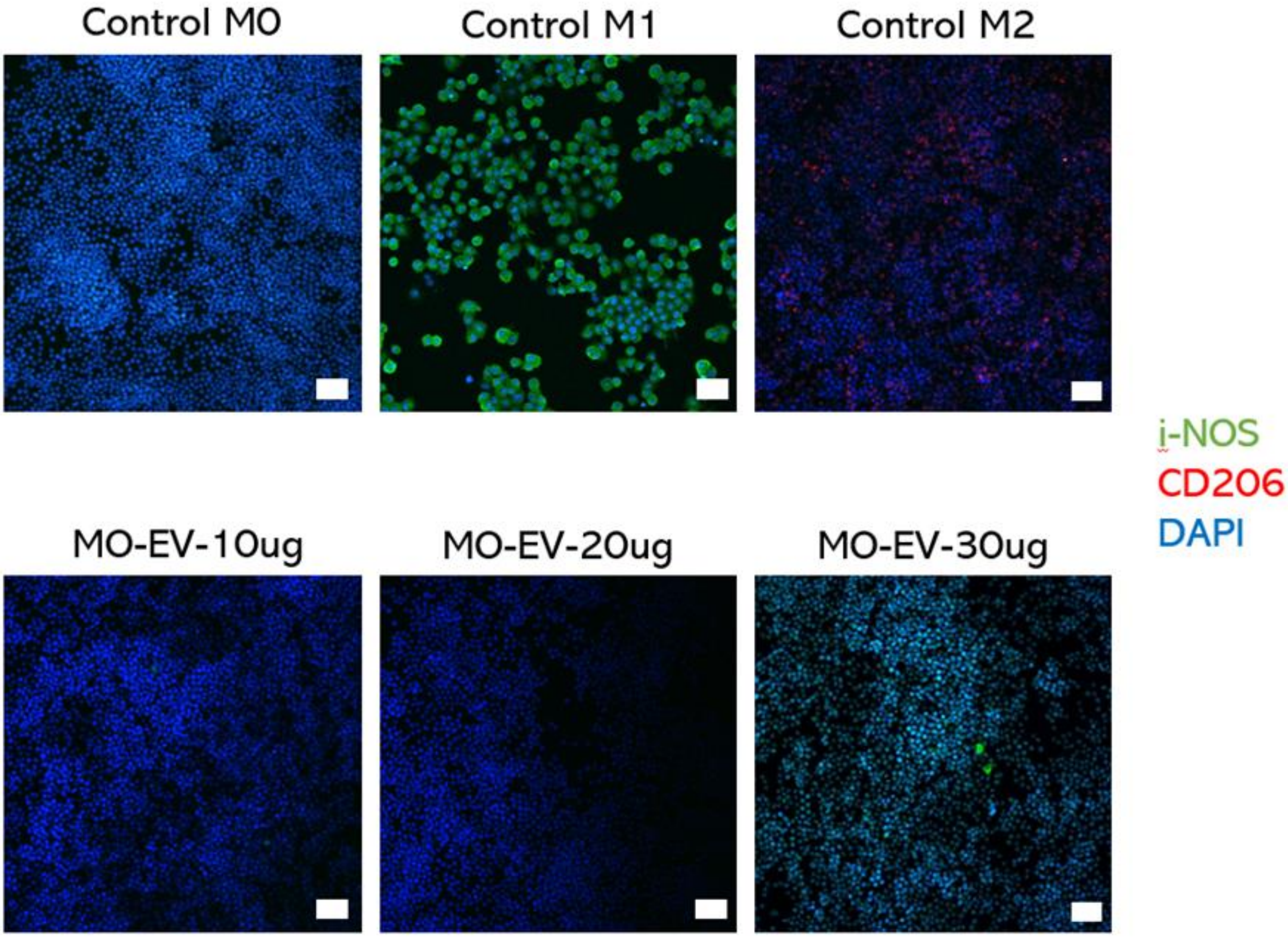

**Appendix 4.1. | Evaluation of the effects of MO-EVs on macrophage polarisation (RAW 264.7 cells).** Confocal microscopy images were obtained after a 72 h-MO-EV treatment using i-NOS as marker of M1 macrophage phenotype and CD206 as a marker of M2 macrophage phenotype. DAPI was used to stain nuclei. Scale bars = 200 µm.

# Appendix 4.2.

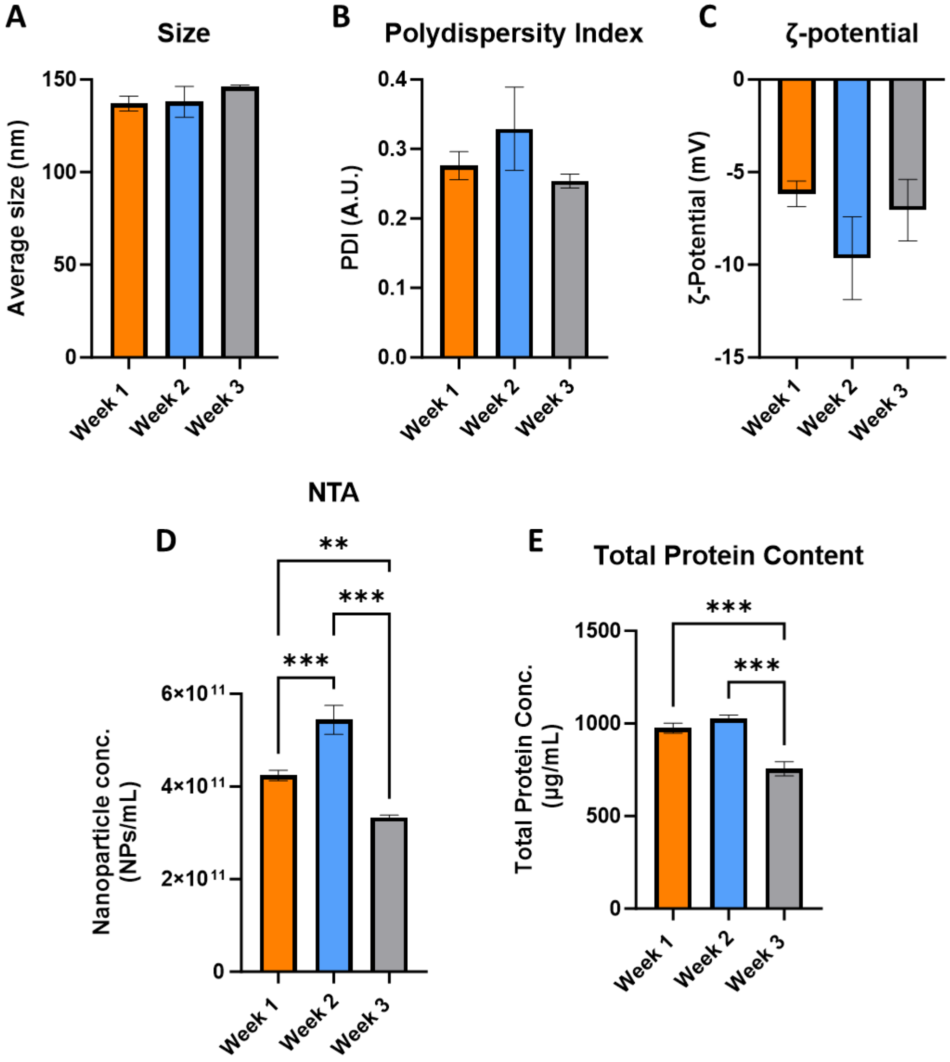

**Appendix 4.2. | Characterisation of MO-EVs isolated from the CCM collected separately for week 1, week 2 and week 3.** A) Average size via DLS. B) Polydispersity Index via DLS. C) ζ-potential via DLS. D) Nanoparticle concentration via NTA. E) Total protein content via BCA assay.

**Appendix 4.3.**

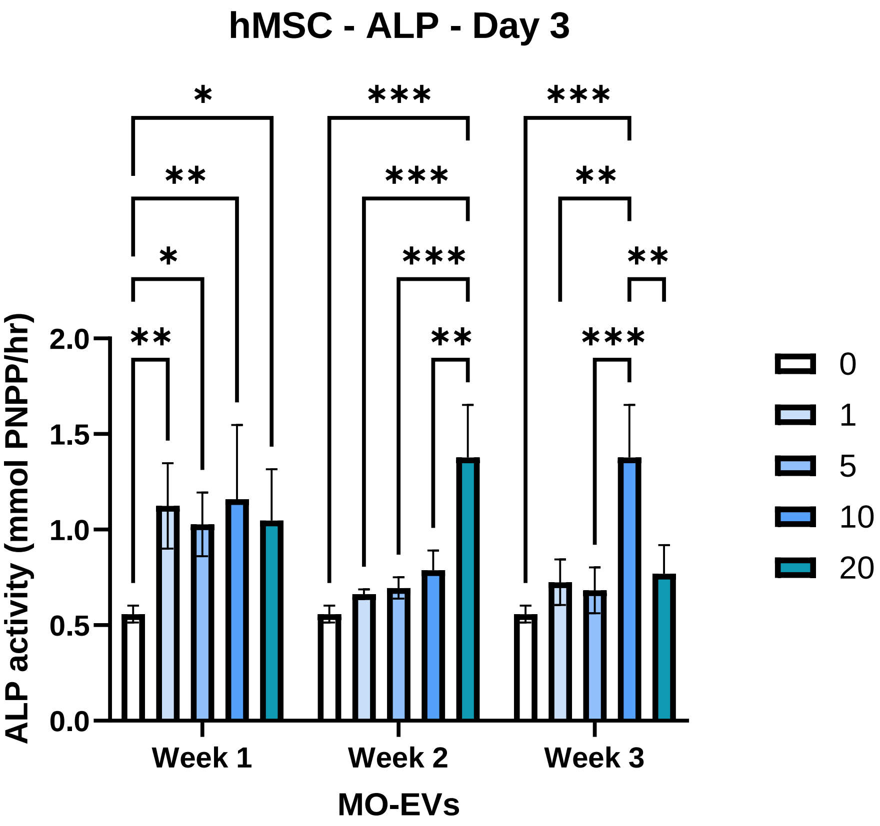

**Appendix 4.3. | ALP activity of MO-EVs isolated from the CCM collected separately for week 1, week 2 and week 3 after 3 days of treatment on osteoblasts.**

# Chapter V

-

# Development of Bioinspired Synthetic Extracellular Vesicles

## 5.1. Introduction

### 5.1.1. Background

EV derived from osteoblasts have been shown to play a significant role in cell-to-cell communication in the bone microenvironment as well as their therapeutic potential for bone repair (Cappariello *et al.*, 2018; Man et *al.*, 2022c). Despite these encouraging findings, the clinical translation of EVs remains limited by various barriers including difficulties with (i) standardised sourcing (ii) scalability or (iii) heterogeneity (Ghodasara *et al.*, 2023). To overcome these obstacles, the use of bioengineering methods and in particular the development of engineered EVs have showed great promise to develop a new class of biomimetic nanotherapeutics (Man *et al.*, 2020).

Beyond their translational advantages, EV mimetics also offers a unique platform to study the mechanism of action of natural EVs by isolating a single or several features (Staufer *et al.*, 2021). Additionally, they can be used as a mimetic delivery system aiming to partially replicate the surface complexity of EVs for delivery purposes (Herrmann *et al.*, 2021). In this chapter both a top-down approach through the biofabrication of CDNs and a bottom-up approach with the formulation of proteoliposomes has been investigated to generate bioinspired synthetic MO-EVs.

### 5.1.2. Development of cell-derived nanovesicles as synthetic EVs

CDNs or NVs have been suggested in recent years as a new class of EV-biomimetic delivery systems (DS). These NVs are fabricated using a top-down approach based on in the physical disruption of whole cells to form self-assembled nanovesicles, thus, creating EV mimetics directly from their parental cells. This alternative to naturally-derived EVs present great advantages as extrusion-based methods are scalable and only limited to the cell number available. Moreover, Goh *et al.* (2017) showed that NVs shared the physical attributes of EVs and harboured the membrane protein configuration of their parental cells. Importantly, during the self-assembly process post plasma membrane disruption, exogenous therapeutic molecules can also be loaded into the cargo of the NVs which be used to further enhance their therapeutic use (García-Manrique *et al.*, 2018).

The use of CDNs has already been investigated for a variety of medical applications. For example, MSC-NVs were added to a microneedle patch to promote wound healing (Hu *et al.*, 2023a) or monocyte-like U937-derived NVs were loaded with doxorubicin as a novel anti-cancer therapy (Goh *et al.*, 2017). Bioengineering approaches have also been developed to further improve these CDNs with for example, the formulation of ‘EXOPLEXs’ corresponding to the fusion of CDNs with synthetic lipid nanoparticles such as liposomes. In this study, they reported a resulting high loading efficiency >65% of doxorubicin with enhanced cytotoxicity compared to liposome delivery alone (Goh *et al.*, 2018). In another study, the lyophilisation of NVs was investigated and the use of cryoprotectants allowed to both maintain the vesicular integrity and the biological activity of U937-derived NVs as well as demonstrating the cardioprotective effects of these NVs after 24 h in an *in vivo* mouse model of myocardial ischemia/reperfusion injury (Neupane *et al.*, 2021). To date, only one study has investigated the use of CDNs for bone repair by generating them from the HEK 293 cell line. After being loaded with dexamethasone, a pro-osteogenic drug, they explored the effects of these HEK-derived CDNs on adipose-derived stem cells (ASCs). They demonstrated that the CDN treatment promoted osteogenic differentiation of these ASCs when loaded with the drug highlighting the capabilities of NVs as a delivery system (Ravi *et al.*, 2022).

Together, these findings showed the growing development of NVs as novel nanotherapeutics. However, to date, this approach has not been explored with any bone cells which could be more challenging as they exist in a mineralised extracellular matrix. Therefore, in this study, we have investigated the generation of MO-EV mimetic, named MO-NVs, from mineralising osteoblasts with a direct comparison with the MO-EV secreted by the same cells in an osteogenic culture (Fig 5.1). We aimed to develop a viable biomimetic alternative to osteoblast-derived EVs to accelerate the clinical translation of these nanovesicles.

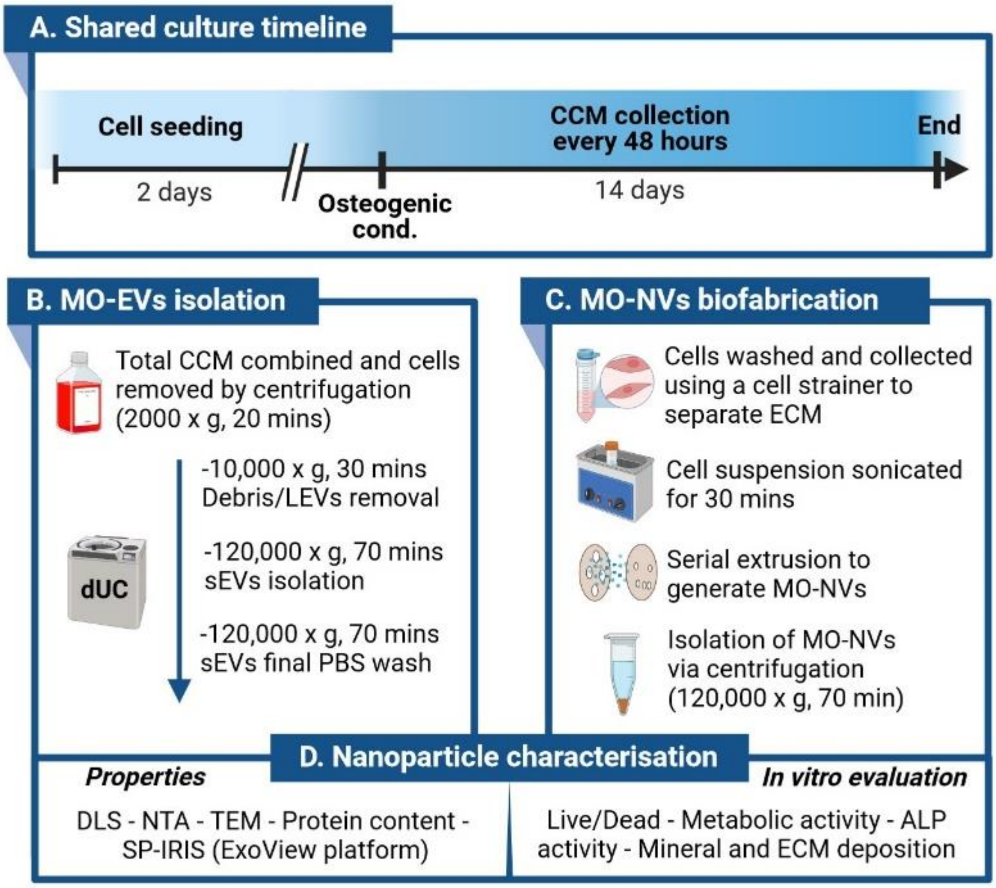

**Figure 5.1. | Schematic representation of the experimental design for the comparison of MO-EVs to biofabricated MO-NVs. A) Shared culture timeline. B) MO-EV isolation. C) MO-NV biofabrication and D) Nanoparticle characterisation (Created using Biorender.com).**

### 5.1.3. Development of proteoliposomes as synthetic EVs

Proteoliposomes correspond to liposomes incorporating protein in their composition. Initially, these nanoparticles were produced to study the biophysical interactions of lipids and proteins to mimic the cell lipid bilayer membrane (Ciancaglini *et al.*, 2012). Proteins can either be loaded inside the aqueous cargo of the liposome, embedded in its membrane, or inserted at the surface depending on the protein function or its required delivery (Scalise *et al.*, 2013).

A variety of proteoliposomes have been successfully formulated to date with for example the reconstitution of aquaporin-1 (Henderson *et al.*, 2023), TMEM16 (Brunner *et al.*, 2019) or Riboflavin Transporter-2 (Console *et al.*, 2019) to name a few, however, these studies only incorporated a single protein of interest with the unique aim of assessing their function.

Sharing the core structural features of EVs, recent efforts have been directed towards the application of proteoliposomes to mimic EVs (Rosso and Cauda, 2023). Using the simplest approach, the liposome conjugation with peptide has been the most widely reported method to generate synthetic EVs (Li *et al.*, 2021). For example, Martinez-Lostao *et al.* (2010) found that APO2L/TRAIL was present in the EVs derived from the synovial fluid. After conjugation to the membrane of liposomes, they demonstrated an increase in bioactivity compared to the soluble protein in a rabbit model of rheumatoid arthritis.

Due to the inherent complexity of EVs, it was not possible to aim for the development of a liposomal system mimicking a number of MO-EVs features. Additionally, there is still no strong mechanistic evidence of a particular set of protein being responsible for MO-EV osteoinductive activity. Therefore, there is a great opportunity to use proteoliposomes to generate synthetic EVs isolating specific features of interest.

In this chapter, annexin VI and ALP were the two proteins of interest selected as both were identified as major actors of osteoblast-EV-driven biomineralisation (Balcerzak *et al.*, 2003). Via the formulation of proteoliposomes, the development of MO-EV mimetics was investigated in an attempt to obtain greater insight into the mechanism of action of MO-EVs by mimicking specific features of pro-osteogenic EVs as presented in Figure 5.2.

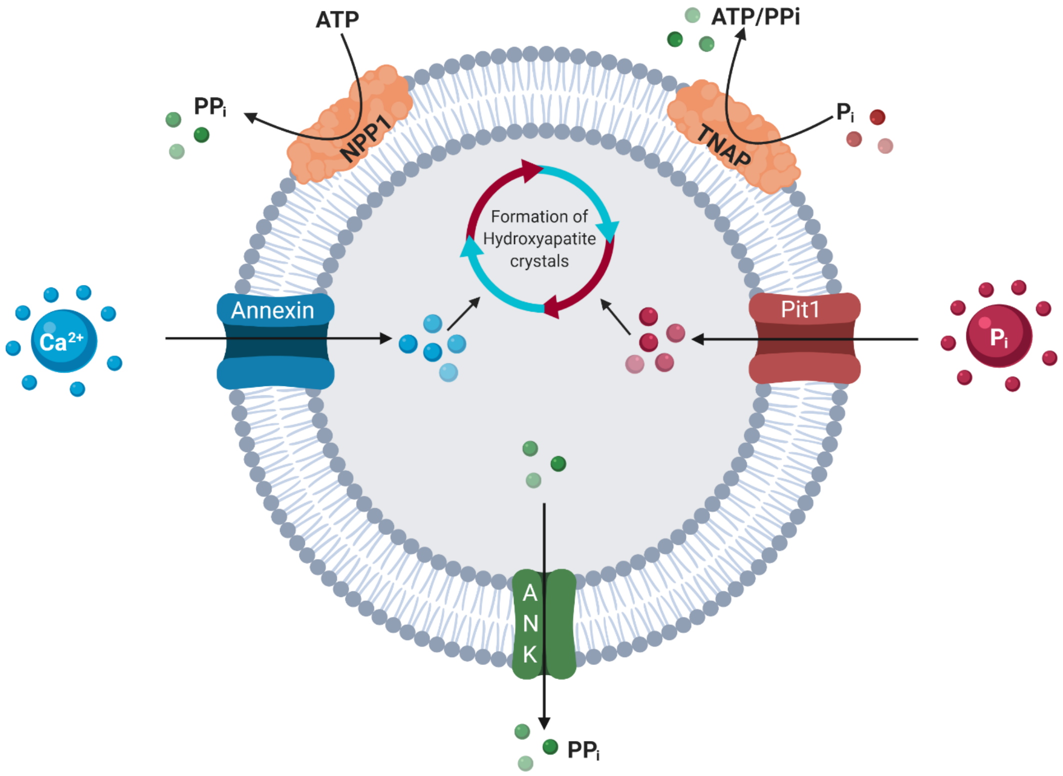

**Figure 5.2. | Schematic representation of EVs acting as a mineralisation core.** The schematic display a single pro-mineralising vesicle with its proposed mechanism of action. Nucleotide pyrophosphatase 1 (NPP1) and tissue non-specific alkaline phosphatase (TNAP) are two key surface proteins regulating phosphorus' availability locally. Other proteins such as Annexin and Pit1 are transmembrane protein channels allowing the transport of $Ca^{2+}$ and Pi, respectively, into the vesicle cargo allowing the acceleration of mineral formation. Other proteins such ankylosis protein (ANK) can also regulate the intravesicular pyrophosphate level. (Created using Biorender.com).

ALP is widely known in bone research as a marker of osteoblastic activity (Sabokbar *et al.*, 1994; Wrobel *et al.*, 2016; Darjanki *et al.*, 2023) as this membrane bound glycoprotein is produced by osteoblast to modulate phosphate levels in bone ECM (Sharma *et al.*, 2014). In recent years, ALP has also been found enriched in osteoblast-EVs (Sanchez *et al.*, 2020; Sekaran *et al.*, 2021). By hydrolysing pyrophosphate which inhibits bone mineralisation, ALP provides phosphate ions to the ECM used for mineral formation, thus modulate the ECM microenvironment (Hessle *et al.*, 2002).

On the other hand, annexins are a family of phospholipid binding proteins dependent on $Ca^{2+}$ which plays an important role in membrane organisation and trafficking, cell division, apoptosis, autophagy, or exocytosis to name a few (Gerke and Moss, 2002; Mussunoor *et al.*, 2008; Xi *et al.*, 2020). Annexin VI has been linked to EVs as Williams *et al.* showed that Annexin VI mediated exosome secretion after plasma membrane damage (Williams *et al.,* 2023). Moreover, its associated gene has been identified as a potential target as a therapeutic approach for ECM mineralisation (Yang *et al.*, 2023). Found enriched in matrix-bound vesicles but also in secreted EVs, the role of annexins have been a central point of interest to explain the direct action of vesicles in the biomineralisation process (Cmoch *et al.*, 2011; Davies *et al.*, 2017). Acting as a calcium channel inserted in the membrane of nanovesicles, the drive of $Ca^{2+}$ in the cargo of vesicles is linked to calcification as these vesicles would act as an early nucleation core for mineral formation (Genge *et al.*, 2007).

Based on the current evidence on the biomineralisation process mediated by matrix EVs, key involved protein has been identified. As a first step towards the fabrication of osteogenic synthetic EVs, Simão *et al.* reported the formulation of EV-inspired proteoliposomes displaying ALP and NPP1 (nucleotide pyrophosphatase/phosphodiesterase-1) at the membrane level

(Simão *et al.*, 2010). Clearly identifying this model as only a first step towards more complex and biomimetic liposomes, they successfully reported the reconstitution of ALP and NPP1 by direct insertion in DPPC liposomes. They also studied the kinetic interplay of the two surface membrane proteins using ATP and PPi as substrates. Their study was functionality-driven with the incorporation of a small number of selected proteins in liposomes based on the evidence of previous EV studies, and the validation of their activity post-insertion.

Interestingly, it was also found that, when both enzymes were present, ALP activity was predominant showing the key role of ALP suggested as controlling  Pi/PPi ratio in ECM to regulate the biomineralisation process. This was further confirmed by this same group as Ciancaglini *et al.* compared the kinetics of ALP, NPP1 or PHOSPHO1 inserted in liposomes compared to native matrix EVs and ALP, NPP1, or PHOSPHO1-deficient MVs in the presence of ATP, ADP, and PPi, at physiologic pH (Ciancaglini *et al.*, 2010). They highlighted that the absence of ALP had the most significant impact on all substrate tested whereas the absence of NPP1 did not significantly alter the hydrolysis of the substrates. In a following study, Boolean *et al.*, reported the formulation of proteoliposomes with ALP and Annexin V. Two lipid composition were investigated (DPPC only and DPPC: DPPS; 90%:10%) and the best catalytic efficiency was observed when DPPS was present.  They showed that $Ca^{2+}$ transport was effective, however, the presence of Annexin V affected ALP activity. (Bolean *et al.*, 2015). Together, these initial results showed the potential of proteoliposomes incorporating annexin and ALP as a first candidate for the development of an MO-EV mimetic using the bottom-up approach.

### 5.1.4. Aim and objectives

The aim of this chapter was to explore the development of synthetic EV bioinspired by their MO-EV natural equivalent previously comprehensively characterised (Chapter III & IV) (Fig 5.3.).

To achieve this aim, the following objectives were pursued:

- To investigate if CDNs could be generated from a culture of mineralising osteoblasts.
- To characterise these MO-NVs directly against MO-EVs.
- To compare MO-EVs and MO-NVs biocompatibility and biomineralisation competency.
- To formulate biomimetic proteoliposomes incorporating ALP and annexin A6.
- To characterise the effect of protein addition to the liposomes.
- To assess the osteogenic potential of the proteoliposomes formulated.

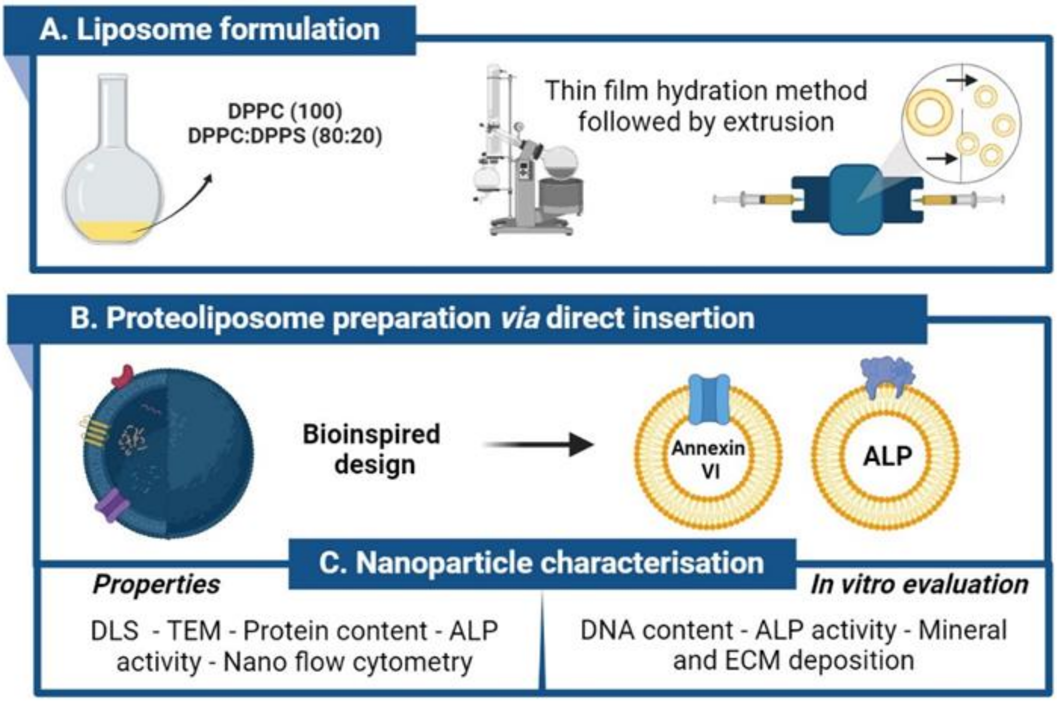

**Figure 5.3. | Schematic representation of the experimental design for the formulation of proteoliposomes. A)** Liposome formulation. **B)** Proteoliposome preparation via direct insertion (Created using Biorender.com).

## 5.2. Materials and methods

### 5.2.1. Biofabrication of MO-NVs

After a 2-week culture time under osteogenic conditions, the whole 2D-layer of culture (cells & ECM) was collected using a cell scraper (Corning, USA) to minimise cell damage and was mechanically dissociated 3 times with sterile filtered PBS through a 40 µm cell strainer adapted to 50 mL conical tubes (Corning, USA). The cell suspension was then centrifuged at 200 x g for 5 mins and the pellet obtained was resuspended in PBS prior to cell counting using a TC20 automated cell counter (Bio-Rad, Ireland). Cell suspension was then diluted to reach a concentration of 1 million cells per mL of PBS before being sonicated for 30 min to disrupt lipid bilayer membranes. Following sonication, 1 mL of the biological mix was extruded using the Avanti® Polar Lipids Mini Extruder kit using two glass gas-tight syringes (Avanti Polar Lipids, USA) and was passed first 21 times through a 1 µm membrane first. After extruder cleaning, the procedure was repeated using a 0.2 µm membrane (Whatman™ Nucleopore Hydrophilic Membrane, USA). The resulting nanoparticle suspension was then centrifugated at 120,000 *g* spin for 70 mins to pellet the MO-NVs while removing debris (Fig 5.4.)

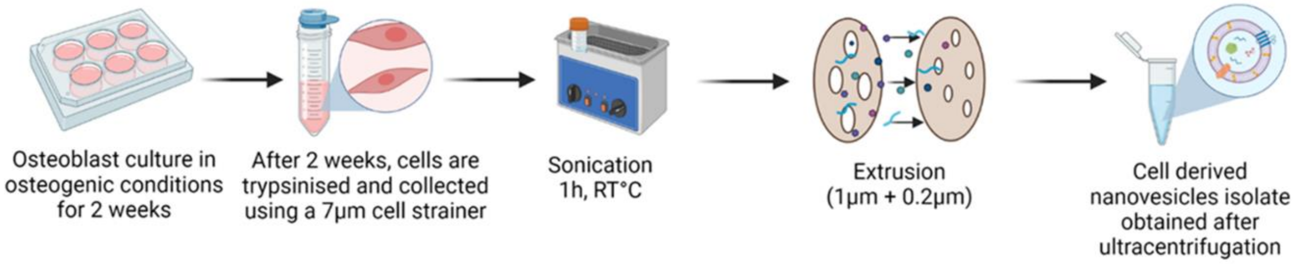

**Figure 5.4. Schematic representation of the MO-NV biofabrication process**. NVs are obtained by the mechanical disruption of cells collected and strained post-trypsin treatment. The resulting cell suspension is then sonicated and extruded to obtain an homogeneous suspension of nanovesicles (Created using Biorender.com).

### 5.2.2. Detection of tetraspanin markers

The presence of surface tetraspanin markers CD9, CD63 and CD81 was assessed via the ExoView® Tetraspanin Assay (NanoView Biosciences, USA) following the manufacturer's instructions. Microarray chips were pre-scanned using the ExoView R100 (NanoView Biosciences, USA) before 35 µL of nanoparticle samples diluted 1:1000 in the provided incubation solution were pipetted onto each chip. The microarray chip presented with immunocapture spots for CD81, CD9 and HIgG (negative control) in triplicate. The chip was then incubated overnight for 16 h to allow nanoparticle capture, and unbound material was washed with the provided incubation solution for 3 min using a microplate shaker. After a total of 3 washes, the provided tetraspanin antibody panel (anti-CD9, anti-CD63 and anti-CD81) was added to the chip and incubated for 1 h at room temperature under constant mixing using a microplate shaker in the dark. The antibody solution was removed, and 4 subsequent washes were performed as previously described. The chip was then carefully dried and scanned using the ExoView R100 using the nScan software (NanoView Biosciences, version 2.8.10). Using IgG spots as isotype control, each spot was then analysed using the NanoViewer software (NanoView Biosciences, version 2.8.10) allowing the fluorescence imaging of captured nanovesicles to quantify their tetraspanin phenotype.

### 5.2.3. Cell viability assessments

MC3T3-E1 cells were seeded in a 96-well plate at a $3 \times 10^3$ cells/cm$^2$ density with basal medium followed by a 24 h incubation. Existing medium was then replaced by MO-EVs or MO-NVs at both a low (1 µg of EV protein equivalent/mL) or high (10 µg of EV protein equivalent /mL) concentrations with basal medium alone used as control. These concentrations were calculated as EV protein concentrations which was normalised between EVs and NVs using nanoparticle concentrations obtained via NTA to ensure that both EVs and NVs were used at the same nanoparticle concentrations for their direct comparison. For example, for a 10 µg/mL EV treatment, BCA assay was used to determine the protein concentration of EV stock suspension. NTA was then used to determine how many nanoparticle per mL correspond to 10 µg of EV proteins and this nanoparticle concentration was then used to also prepare the NV suspension for comparison. Treatments were replaced every 48 h until endpoint at day 7 to mimic regular dosing regimen over a week.

AlamarBlue solution (Thermo Fisher Scientific, UK) was added to the wells at endpoint (1:10 dilution in media) and was incubated for 4 h at 37°C. Using a SPARK plate reader (Tecan, CH), fluorescence readouts were obtained (excitation/emission, 540/590 nm).

In parallel, Live/Dead staining was performed using the blue/green ReadyProbes™ cell viability imaging kit (Thermo Fisher Scientific, UK). Both NucBlue® Live reagent (excitation/emission: 360/460 nm) and NucGreen® Dead reagent (excitation/emission: 504/523 nm) were added at a concentration of 2 drops/mL of basal medium according to the manufacturer's instructions. After a 15 min incubation period, images were obtained using the EVOS™ M5000 imaging system (Thermo Fisher Scientific, UK). Percentages of cells alive or dead was then quantified by cell counting using the ImageJ software (v 1.53k) (NIH, USA).

### 5.2.4. Liposome preparation

Liposomes composed of dipalmitoylphosphatidylcholine (DPPC) and/or 1,2-dipalmitoyl-sn-glycero-3-phospho-L-serine (DPPS) were prepared using the thin film hydration method. Lipids at desired molar ratio were dissolved in chloroform in a 25mL round bottom flask. The organic solvent was removed on a rotary evaporator (Rotary evaporator RV 10 auto V-C, IKA, Germany) for 2 h under vacuum (100 mbar) and mixing (170 rpm). The procedure was performed at a temperature of 65°C, above the critical phase transition temperature of the lipids. Lipids were rehydrated with 0.9% NaCl solution and mixed for a further 2 h using the rotary evaporator. The resulting suspension was then sonicated for 30mins prior to be extruded 21 times through a 100 nm filter to create monodispersed liposomes (Avanti Mini Extruder, Avanti Polar Lipids, USA). Size determination using DLS was performed following the liposome production to control the quality of the product.

### 5.2.5. Proteoliposomes preparation

Protein addition to liposomes was performed post- liposome preparation adapting the method introduced by Bolean *et al.* (2017). Annexin VI and/or ALP were diluted in sterile distilled water to reach the concentration of 0.02 mg/mL. Liposome suspension (10 mg/mL) and protein solutions were then incubated in equal volumes (100 µL) and were mixed together at room temperature. After incubation, the suspension was centrifuged at 17,000 *g* for 1 h. The pellet was then resuspended in PBS to its original volume. To determine encapsulation efficiency, total protein content of the pellet was determined using BCA assay. The encapsulation efficiency was then calculated using the ratio of the total amount of protein in the pellet and the total amount of protein initially added to the mix.

### 5.2.6. Determination of protein binding efficiency by flow cytometry

Prior to any analysis, the flow cytometer (Cytoflex, Beckman Coulter, Inc, USA) was primed and cleaned and operated using CytExpert Software v1.2. Specific to nanoparticle analysis, the configuration was modified for Violet-SSC detection for higher resolution suited for nanoparticle detection.

Freshly prepared proteoliposomes were separated from unbound proteins via ultracentrifugation and were resuspended in an equal amount of PBS (100 µL) containing a 1:200 dilution of each antibody. Annexin VI was detected via an annexin VI AF488-conjugated antibody (R&D systems, UK) and ALP *via* a PE-conjugated antibody (R&D systems, UK). For each analysis a fixed injection volume of 25 µL was used for comparable analysis and control liposomes without proteins were used for quality control of detection. The gating strategy is illustrated in Figure 5.5. with a simple separation of nanoparticles from background using the violet-SSC-H detection with a threshold set at 10,000. All particles detected beyond threshold were then included in the fluorescence detection.

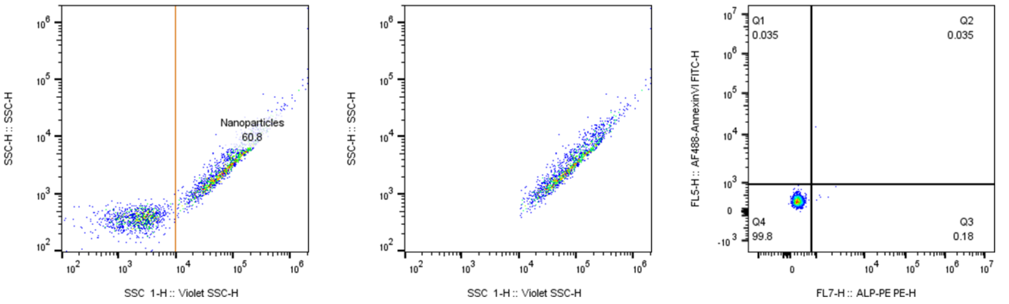

1. X-axis gating
SSC-H *vs* Violet SSC-H

2. Isolation of NPs
SSC-H *vs* Violet SSC-H

3. Fluorescence detection
Annexin VI *vs* ALP

**Figure 5.5. | Flow cytometry plot presenting the gating strategy operated for proteoliposomes detection.** 1) Nanoparticle detection threshold is set on Violet SSC-H separating nanoparticles of interest from background using PBS as negative control. 2) The selected nanoparticle population is then gated and isolated. 3) The selected population is then analysed to determine positivity to either annexin VI or ALP based on the fluorescence of their respective antibodies.

### 5.2.7. Biomineralisation evaluation

The biomineralisation study performed in this chapter employs methodologies previously described in Chapter II regarding the evaluation of ALP activity, ARS and PSR which can be found at the sections 2.2.5.1., 2.2.5.2. and 2.2.5.3., respectively. When employing synthetic

EV treatments, the nanoparticle suspension was diluted to the MO-EV nanoparticle concentration corresponding to 1 or 10 µg/mL of EV protein concentration using NTA results. Moreover, the quantification of double stranded DNA  was performed using the Quant-iT PicoGreen DNA assay (Invitrogen, Life Technologies, UK). Briefly, cells were lysed following three freeze-thaw cycles in 0.1% Triton™ X-100 in PBS. 90 µl of TE (10 mM Tris-HCl, 1 mM EDTA) buffer was added to 10 µl of cell lysate in a 96-well plate (Corning, UK). 100 µl of PicoGreen reagent was added to all samples and then incubated at 37°C for 5 min. The fluorescence was then measured in a SPARK spectrophotometer at an excitation/emission wavelength of 480/520 nm.

## 5.3. Results

### 5.3.1. Mimicking MO-EVs via the top-down approach and the generation of cell-derived nanovesicles

NVs were generated from a culture of mineralising osteoblasts after 14 days in osteogenic conditions. MO-EVs were also isolated as previously to obtain a direct comparison between the two nanovesicle populations throughout this section.

#### *5.3.1.1. Physico-chemical properties of MO-NVs compared to MO-EVs*

Sharing the same culture timeline (Fig 5.1A), NVs were obtained from the same EV-secreting mineralising osteoblasts allowing a direct comparison between the two nanoparticle populations. EVs were successfully isolated from the culture media of mineralising osteoblasts displaying an average size of 109 nm which was found consistent with previous isolations. Remarkably, NVs were found to harbour a similar size showing that the NV-generation process successfully replicated MO-EV size (Fig 5.6A and 5.6C). Both type of nanovesicles also presented with a similar polydispersity index remaining lower than 0.2 (Fig 5.6D).

Both ζ-potentials were found to be neutral to slightly negative with average values between -10 and 0 mV with MO-NVs presenting a statistically less negative potential compared to MO-EVs (Fig 5.6E).

The total nanoparticle concentration was evaluated by NTA and found to be significantly higher for MO-EVs than MO-NVs. However, it is important to note that may be caused by a difference in the experimental design where EVs are collected over 14 days while, NVs are produced following extrusion of one million cells only. With a scalable and repeatable serial extrusion process, the generation of NVs is far more efficient than the isolation of MO-EVs as estimated in Figure 5.6G, with an estimated ~5 times greater yield obtained for NVs.

Morphological observations by TEM presented two vesicular nanoparticles of similar diameter with a visually distinguishable lipid bilayer membrane (Fig 5.6B).

Finally, the total protein content was determined for NVs and EVs and was normalised to nanoparticle concentration for both (Fig 5.6H). NVs were found significantly less enriched in proteins compared to MO-EVs with a 3-fold difference ($p<0.001$) (Fig 5.6H). It is important to note that without further investigation, no conclusions can be drawn from their respective protein content as MO-EVs obtained from differential ultracentrifugation may present with protein contaminants.

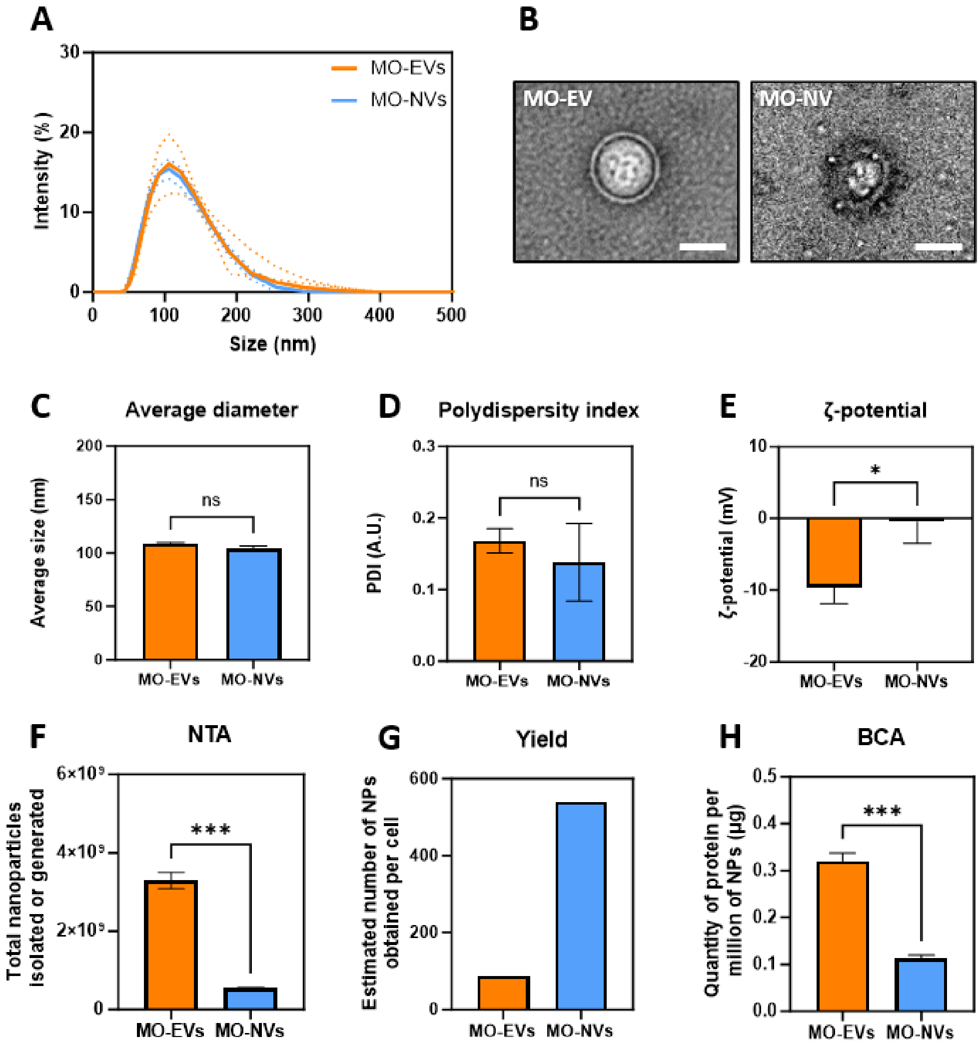

**Figure 5.6. | Comparison of the physicochemical properties of MO-EVs and MO-NVs.** Dynamic Light Scattering analysis provided **(A)** Size distribution profiles (SD around the curves represented by coloured dotted lines). **(B)** TEM images with scale bars = 100 nm **(C)** Average diameters **(D)** Polydispersity index **(E)** ζ-potential. **(F)** Nanoparticle concentrations obtained via nanoparticle tracking analysis. **(G)** Calculated yield of nanoparticles obtained per parental cell. **(H)** Total protein concentration normalized by nanoparticle number. Data presented as mean ± SD (n=3) with statistical significance presented as *P ≤ 0.05, **P ≤ 0.01 and ***P ≤ 0.001.

#### *5.3.1.2. Detection of tetraspanin markers*

In this study, SP-IRIS was used to assess MO-EVs and MO-NVs respective tetraspanin phenotype presenting a new way to compare EVs and their biomimetics. Both EVs and NVs showed the capacity to bind to the immuno-capture spots. However, a greater number of EVs (>100-fold) adhered to the tetraspanin capture spots compared to MO-NVs (Fig 5.7A & 5.7B). MO-EVs were positive for all tetraspanin markers tested (CD63, CD81 and CD9). Interestingly, the small number of NVs which were successfully captured on the CD9 spot were also positive to all tetraspanin markers targeted and only traces of NV capture on CD81 spots was observed.

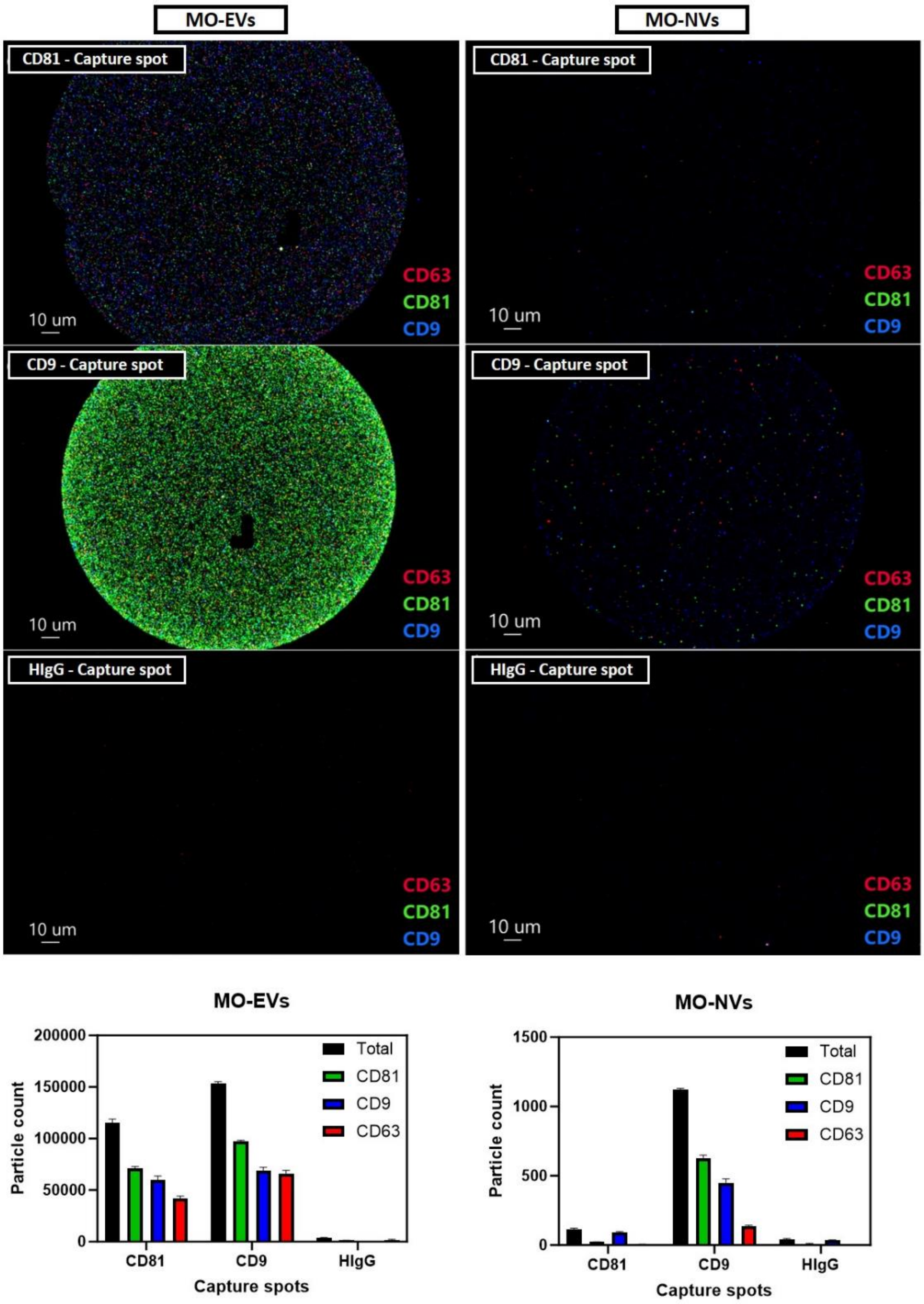

**Figure 5.7. | Detection of tetraspanin markers CD63 CD81 and CD9 by single particle interferometric reflectance imaging sensor using the ExoView™ platform. (A)** ExoView™ fluorescence microscopy detection of CD81, CD63 and CD9 expressed by MO-EVs or MO-NVs captured on CD81, CD9 or HigG immunospots. Scale bars = 10 µm. **(B)** Quantification of tetraspanins expression for MO-EVs and MO-NVs marker. One chip was used per group, with 3 technical capture spot replicates per capture marker analysed per chip, no statistical analysis performed.

### *5.3.1.3. Cell viability evaluation*

The effects of NVs on osteoblasts' viability and metabolic activity was assessed and compared to MO-EVs. Cell viability was assessed via Live/Dead staining whereas the metabolic activity of osteoblasts was evaluated using the AlamarBlue assay. Neither treatment was found to induce significant cell death after 7 days of culture at low and high concentrations (Fig 5.8A and 5.8B). In contrast, the addition of both NVs and EVs resulted in a significant reduction of the metabolic activity of osteoblasts, compared to control for both concentrations tested ($p<0.01$) (Fig 5.8C).

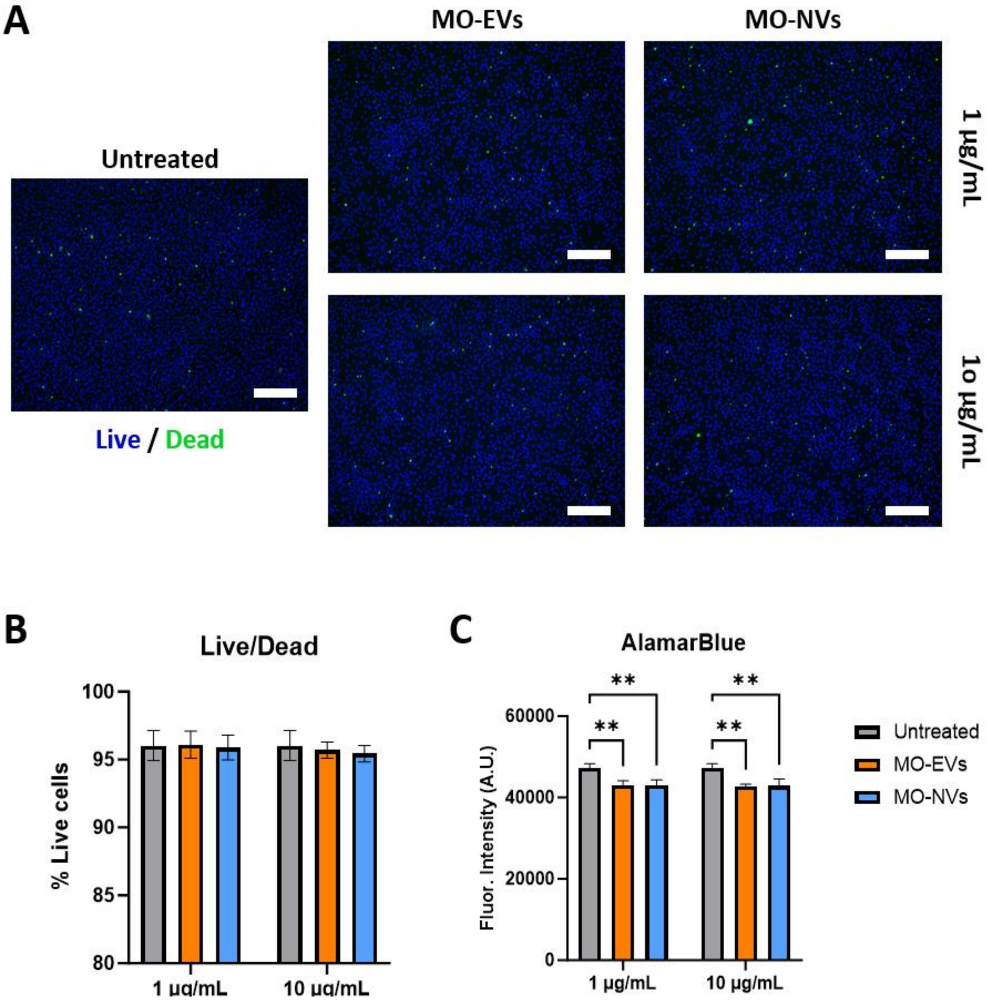

**Figure 5.8. | Cell viability assessment after MO-EV and MO-NV treatments. (A)** Fluorescence microscopy images of MC3T3-E1 cells with Live/Dead staining after 7 days of NP-treatment. **(B)** Quantification of the percentage of live cells from images. **(C)** Metabolic activity assessment by AlamarBlue assay after 7 days of treatment. Data presented as mean ± SD (n=3) with statistical significance presented as *P ≤ 0.05, **P ≤ 0.01 and ***P ≤ 0.001.

### *5.3.1.4. Comparative biomineralisation study*

To compare the therapeutic potency of MO-EVs and -NVs, an *in vitro* study was performed on osteoblast to determine their effects on ALP activity, calcium deposition and collagen production as illustrated in Figure 5.9A. At day 7, the activity of ALP was increased by treatment with MO-EVs at both 1 µg/mL (p<0.01) and 10 µg/mL (p<0.05), compared to untreated control; whereas MO-NVs treated cells exhibited a reduced ALP activity compared to all groups ($p<0.001$) (Figure 5.9B). All groups produced a collagen-rich matrix with the staining quantification displaying an increased collagen production after MO-EVs treatments as expected (Fig 5.9C&E). This trend was not found statistically significant compared to the other groups. Finally, calcium deposition was assessed via alizarin red staining (ARS) (Fig 5.9D&E). Quantification revealed no difference between groups by Day 14, whereas on Day 21, high concentration MO-EVs (10 µg/mL) significantly enhanced calcium deposition compared to the untreated control ($p<0.05$) and to MO-NVs (1 µg/mL, $p<0.05$; 10 µg/mL, $p<0.01$). Overall, MO-EVs were found to demonstrate a pro-mineralising activity in osteoblast cultures contrary to MO-NVs which had no effects on both mineral and matrix deposition and reduced ALP activity when directly compared with MO-EVs at the same nanoparticles concentrations within the respective timeframe tested.

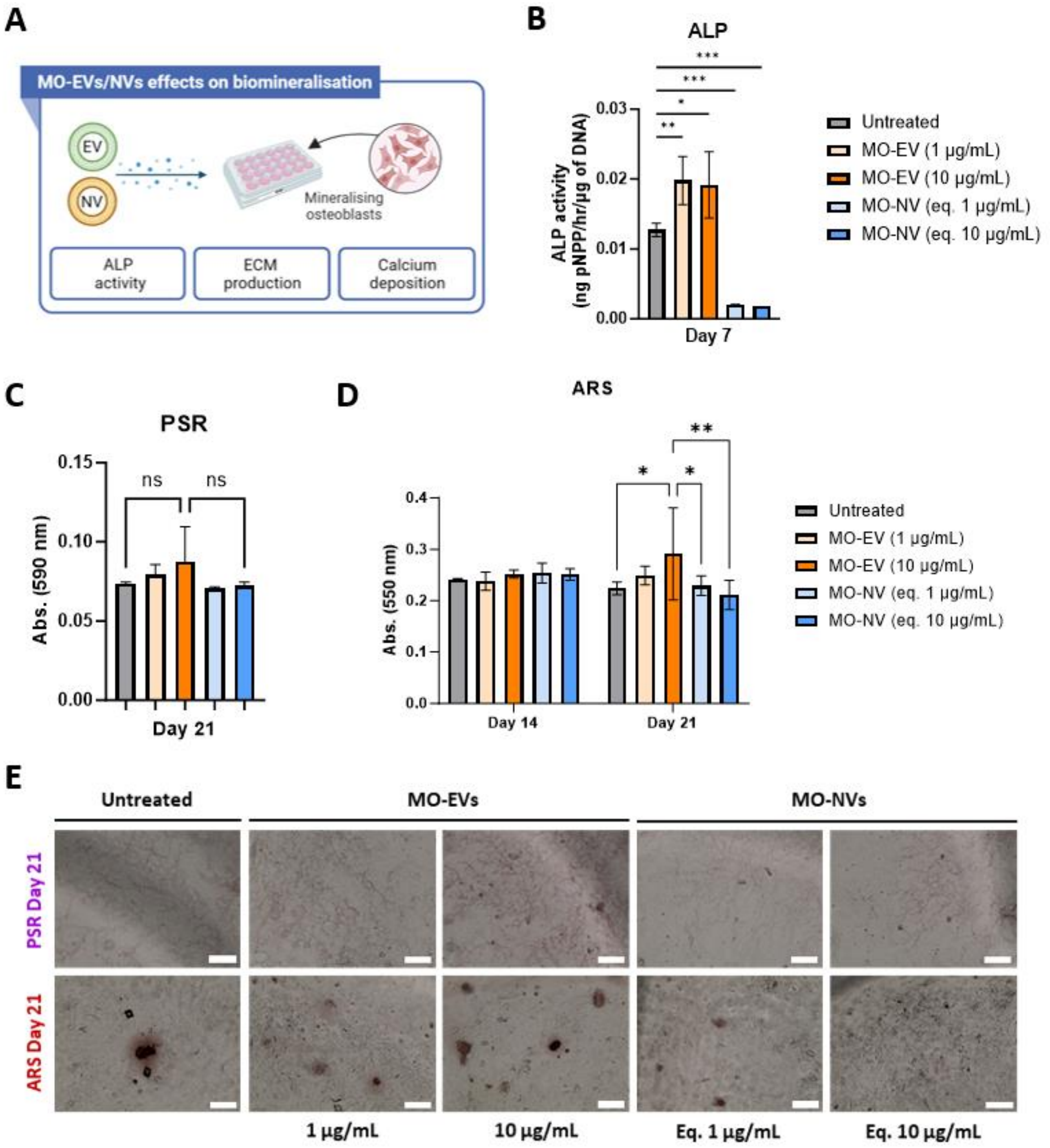

**Figure 5.9. | The influence of MO-EVs and MO-NVs on osteoblast mineralisation (A)** Graphical representation of experimental design. The effects of MO-EVs and MO-NVs on **(B)** ALP activity **(C)** collagen production (PSR) and **(D)** calcium deposition (ARS). **(E)** Light microscopy images of ARS and PSR staining. Data presented as mean ± SD (n=3) with statistical significance presented as *P ≤ 0.05, **P ≤ 0.01 and ***P ≤ 0.001.

### 5.3.2. Mimicking MO-EVs via the bottom-up approach and the formulation of proteoliposomes.

#### *5.3.2.1. Physico-chemical properties of liposomal formulations*

Liposomes composed of either 100% DPPC or DPPC:DPPS (molar ratio of 80:20) were manufactured using the thin film hydration method. DLS analysis revealed that both liposome formulations exhibited a uniform size distribution (Fig 5.10A). The addition of DPPS causing a slight reduction of liposome sizes (from 127.7 ± 2.1 to 101.0 ± 0.4 nm; $p<0.001$) (Fig 5.10B) and increase in PDI (from 0.166 ± 0.004 to 0.355 ± 0.030 ; $p<0.001$) (Fig 5.10C). Notably, both liposomes presented a negative ζ-potential which was found significantly more negative in in the presence of 20% DPPS, as expected (Fig 5.10D).

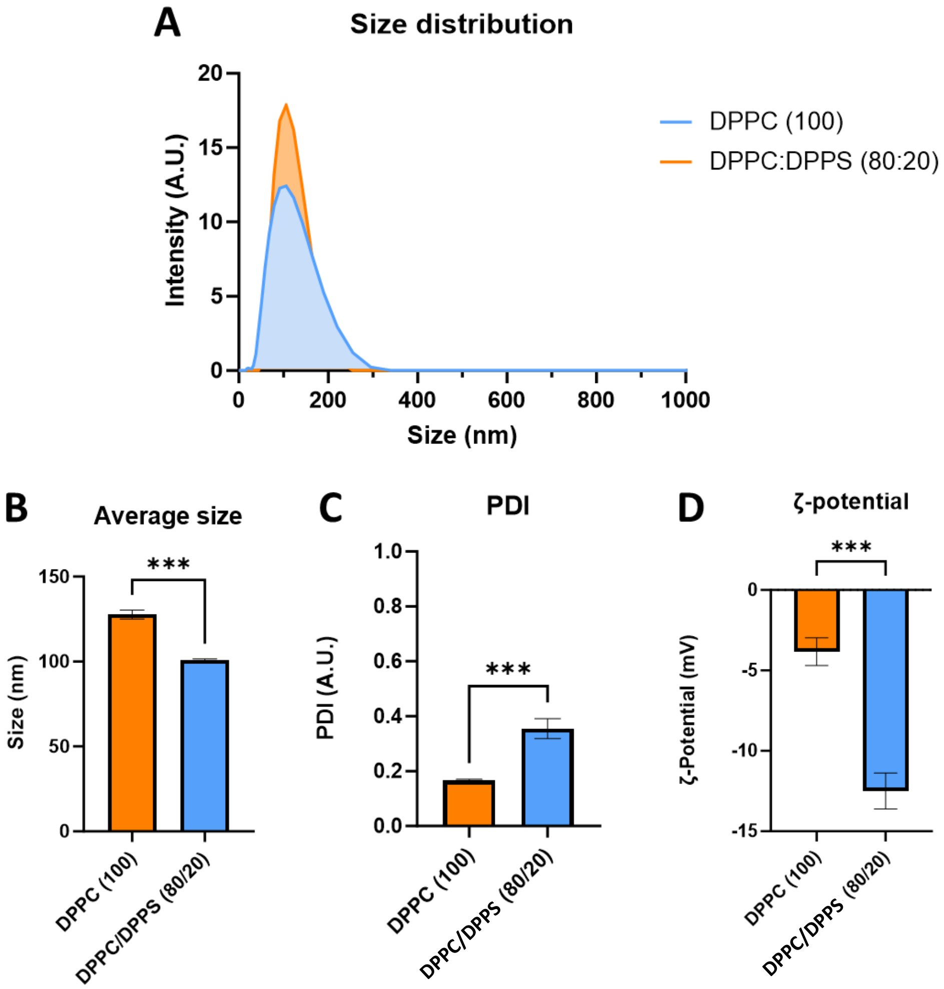

**Figure 5.10. | DLS analysis of DPPC liposomes in the presence or absence of DPPS. A)** Size distribution profile**. B)** Average size **C)** PDI and **D)** ζ-potential. Data presented as mean ± SD (n=3) with statistical significance presented as *P ≤ 0.05, **P ≤ 0.01 and ***P ≤ 0.001.

### *5.3.2.2. Validation of proteoliposome preparation*

The insertion of annexin VI and ALP was performed separately on both liposomal formulations. Protein quantification after centrifugation confirmed the presence of both proteins in the liposomes. Binding efficiency for ALP was ca. 30%, with no noticeable impact of liposome composition (Fig 5.11.). In contrast, addition of DPPS significantly increase annexin VI binding (p<0.001) with efficiency reaching ca. 50% for DPPC:DPPS liposomes.

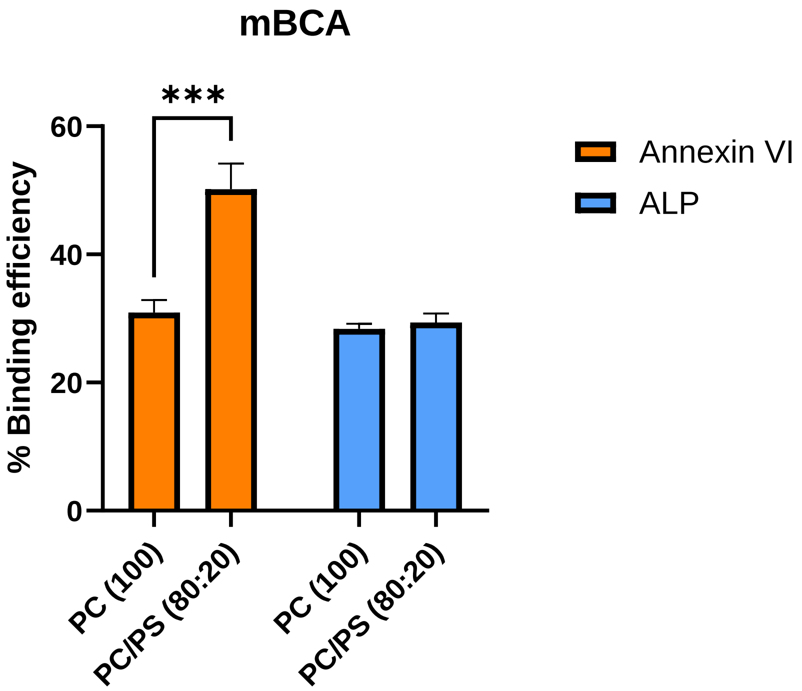

**Figure 5.11. | Determination of binding efficiency of proteins to liposomes via quantifying protein content after 30 min incubation.** Liposomes' lipid compositions are indicated in x-axis and the percentage of binding efficiencies were calculated based on the protein concentration determined in the final proteoliposome suspension obtained after the reaction (microBCA). Data presented as mean ± SD (n=3) with statistical significance presented as *P ≤ 0.05, **P ≤ 0.01 and ***P ≤ 0.001.

The activity of the ALP-liposomes was assessed after purification to remove unbound protein. ALP activity was found positive across all groups with no significant differences observed between liposome composition nor incubation time (Fig 5.12.). The activity of annexin VI post-insertion was not investigated due to the absence of an effective method for the detection of calcium uptake inside the cargo of nanoparticles.

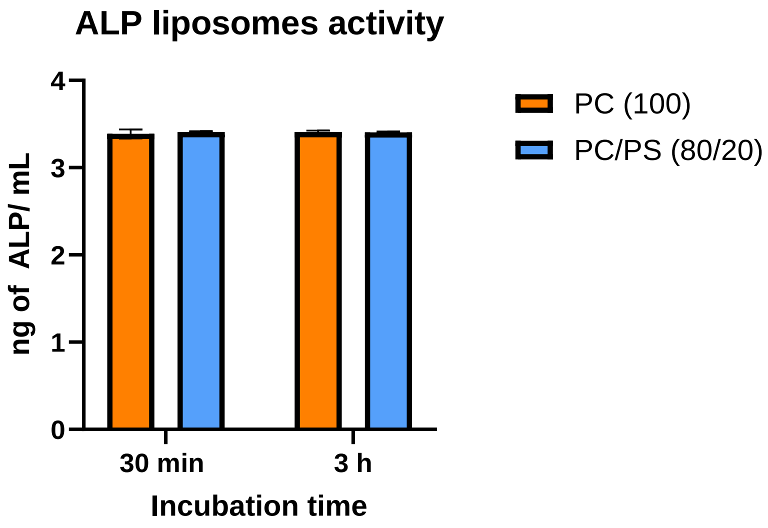

**Figure 5.12. | Determination of ALP activity of ALP liposomes after 30 min or 3 h incubation.** Two lipid compositions, PC (100) or PC/PS (80/20), were used with protein binding reaction occurring over 30 min or 3 h before determining the ALP activity of the resulting proteoliposomes. Data presented as mean ± SD (n=3) with statistical significance presented as *P ≤ 0.05, **P ≤ 0.01 and ***P ≤ 0.001.

### *5.3.2.3. Effects of protein insertion on resulting proteoliposomes size*

After incubation with each protein of interest, DLS analysis was performed to assess the effect of the protein insertion on the size of the liposomes (DPPC/DPPS; 80/20). The size distribution profile of the resulting proteoliposomes can be observed in Figure 5.13A for 30 min and in Figure 5.13B for 3 h incubation with the only qualitative difference observed for annexin VI + ALP only after 3 h incubation. This result is confirmed after the quantification of the average size (Figure 5.13C). No significant changes of particle size were observed across all groups after 30 min incubation. However, annexin VI + ALP proteoliposomes were found significantly larger, between 140 and 150 nm in diameter, compared to all three other groups with a notable large size distribution (p<0.001) (Fig 5.13C).

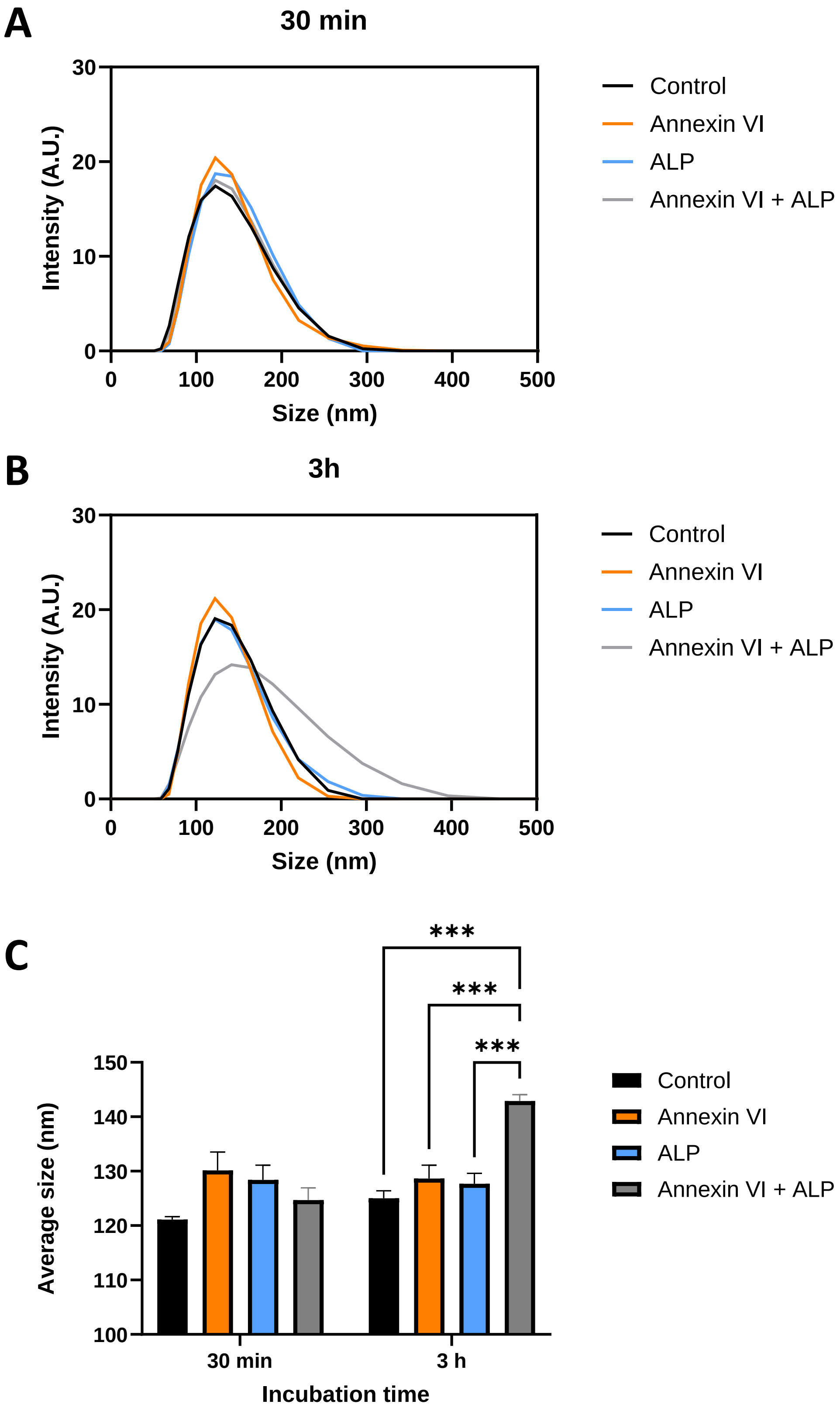

**Figure 5.13. | Evaluation of the proteoliposomes (DPPC/DPPS; 80/20) size after protein insertion via DLS analysis.** A) Size distribution profiles after 30 min incubation. B) Size distribution profiles after 3h incubation. C) Summary of average size measured for both 30 min and 3h incubation. Data presented as mean ± SD (n=3) with statistical significance presented as *P ≤ 0.05, **P ≤ 0.01 and ***P ≤ 0.001.

#### *5.3.2.4. Single particle analysis via flow cytometry to investigate the effects of incubation time on protein binding.*

Using a flow cytometry detection, proteoliposomes were separated from unbound proteins by centrifugation and resuspended in PBS containing fluorescent antibodies specific to both ALP and annexin VI. In Figure 5.14., an example of flow cytometry dot pots highlighting the detection of annexin VI (y-axis) compared to ALP (x-axis) to which a cross-gate has been applied to separate the detection of annexin VI positive liposome from ALP positive liposomes to dual positives nanoparticles (Fig 5.14A). Following analysis, the quantification of the percentage of events gated for each condition was presented for a 30 min incubation (Fig 5.14B) and a 3 h incubation (Fig 5.14C).

Annexin VI liposomes and annexin VI + ALP liposomes both showed a significant presence of annexin VI with over 60 % of nanoparticles gated found positive to the protein of interest. However, the ALP detection was considerably lower compared to annexin VI with detection across all groups remaining below 1 %. The two different incubation times did have any effects on the protein detection levels.

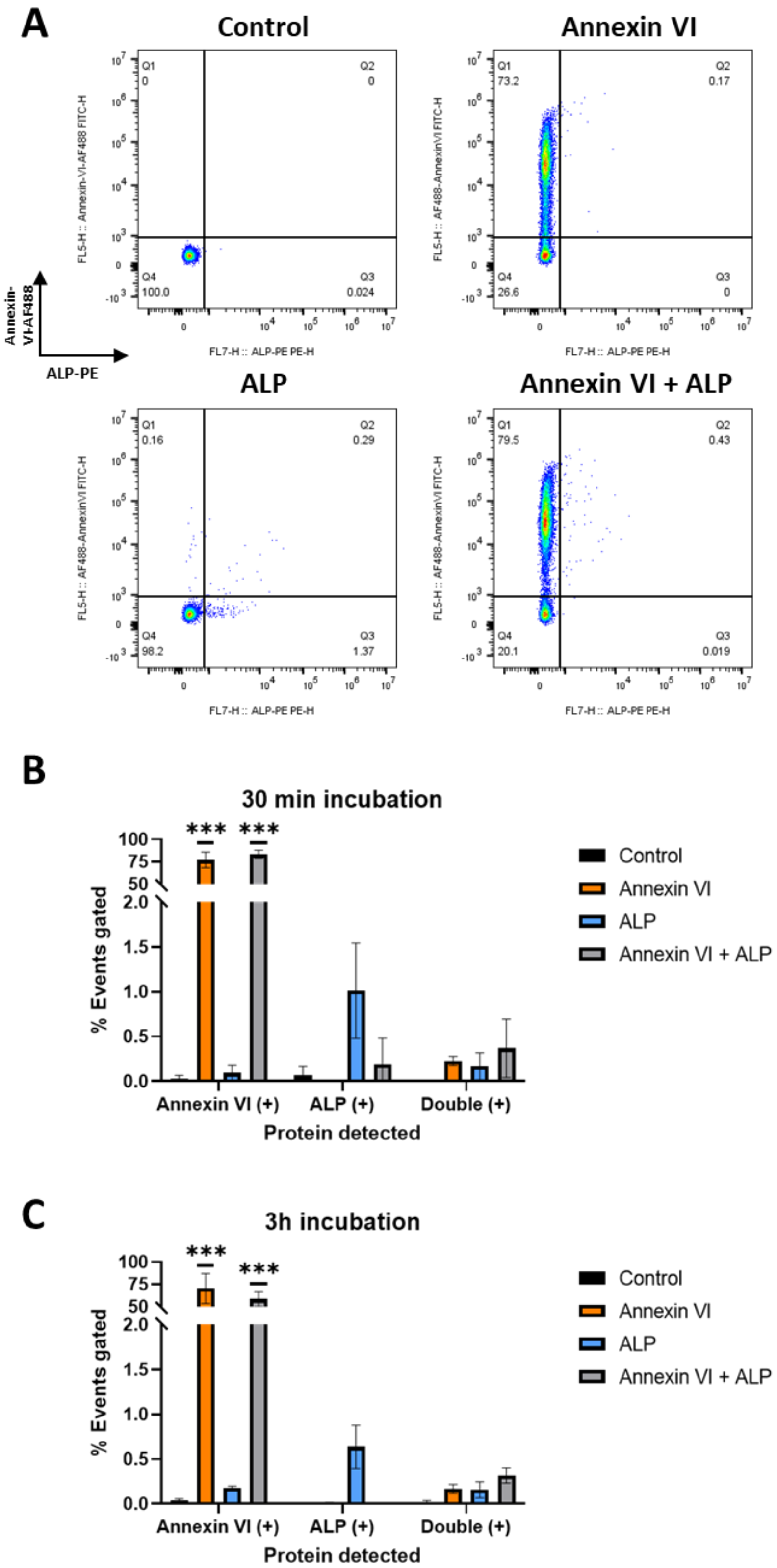

**Figure 5.14. | Determination of protein binding affinity via flow cytometry.** All proteoliposomes were formulated using the DPPC/DPPS (80/20) lipid composition. **A)** Flow cytometry dot plots. Quantification of protein binding after **B)** 30 min incubation or C) 3h incubation with proteins. Data expressed as mean ± SD (n=3). with statistical significance presented as *P ≤ 0.05, **P ≤ 0.01 and ***P ≤ 0.001.

#### *5.3.2.5. TEM imaging of proteoliposomes*

TEM observations were made for all groups at the two different incubation times (Fig 5.15.). For all conditions, intact vesicles with a preserved structure were observed. Interestingly, ALP proteoliposomes showed the presence a granular structure in the centre of the vesicles. Moreover, these vesicles appeared larger (>300 nm) and presented with a membrane curvature.

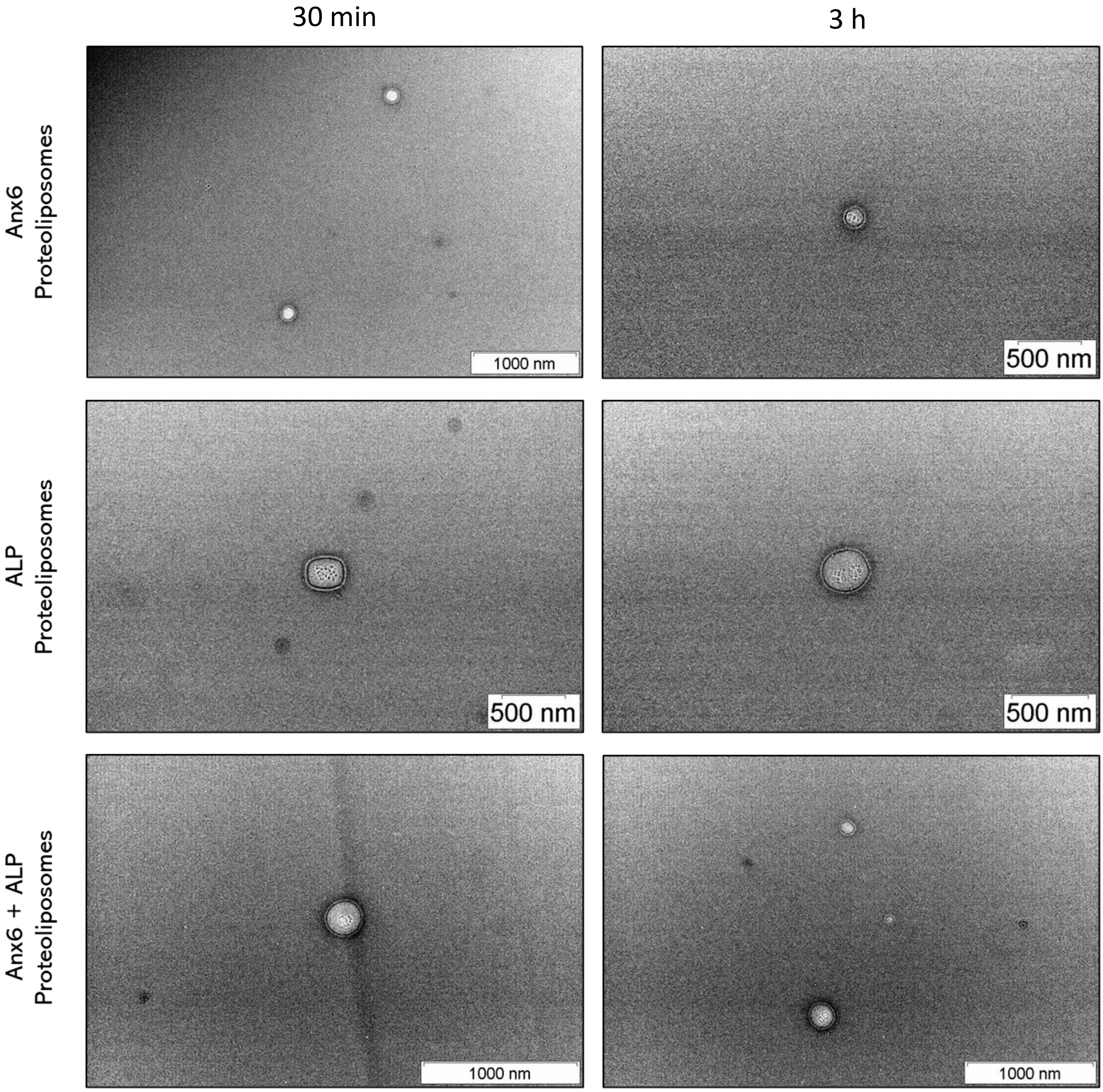

**Figure 5.15. | TEM observations of proteoliposomes obtained after 30 min and 3 h incubation with ALP and annexin VI using the DPPC/DPPS (80/20) lipid composition.** TEM observations performed in high resolution to observe single vesicles. Granular structures within or at the surface of the liposomes can be observed.

### *5.3.2.6. Evaluation of proteoliposomes osteogenic potency*

To screen the osteogenic potency of manufactured liposomes harboring either ALP or annexin VI, their concentration was adjusted to match the particle concentration of MO-EVs used to treat for 10 µg of EV protein/mL. Neither treatment had an effect on cell proliferation after 7 days; however, at day 14, annexin VI liposomes induced a reduction in cell number compared to both controls ($p<0.01$) and ALP liposomes ($p<0.05$) (Fig 5.16A). Once normalised to DNA amounts, no differences of ALP activity were found between groups at day 7 (Fig 5.16B). Interestingly, calcium deposition was significantly reduced by both liposome treatments at day 14 compared to both controls ($p<0.01$) (Fig 5.16C) with no significant variations of ECM produced across all groups (Fig 5.16D). A contraction of ECM was observed in all conditions except in basal conditions with very subtle mineral staining observed across all cultures (Fig 5.16E).

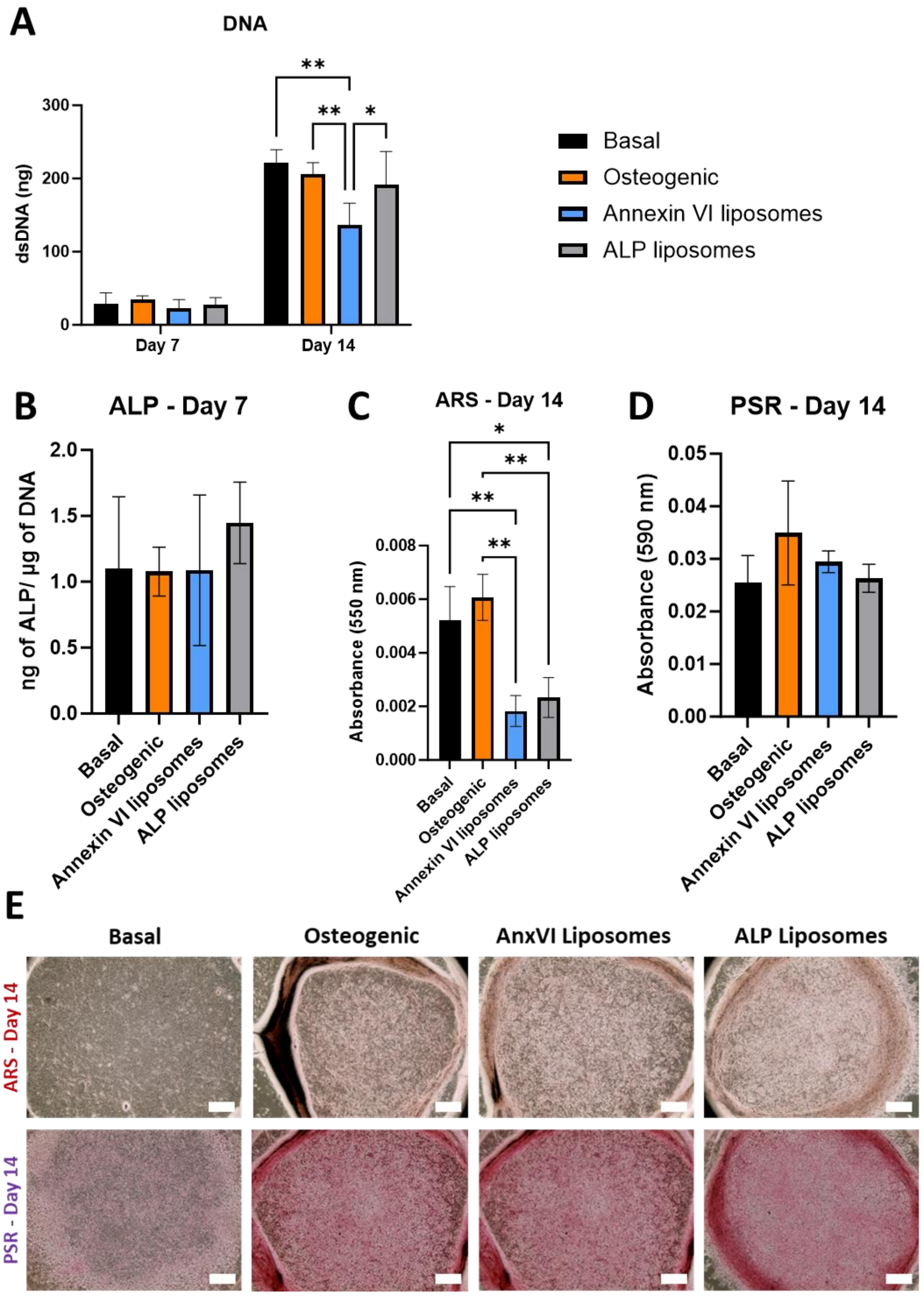

**Figure 5.16. | Biomineralisation assessment of both annexin VI and ALP liposomes on osteoblasts.** Proteoliposomes were obtained after 3 h incubation with ALP and annexin VI using the DPPC/DPPS (80/20) lipid composition (MO-EV 10µg/mL concentration equivalent). **A)** DNA quantification at day 7 and 14, **B)** ALP activity at day 7, **C)** Calcium deposition at day 14, **D)** Collagen production at day 14 and **E)** Images of Alizarin red staining at day 14. Data expressed as mean ± SD (n=3). with statistical significance presented as *P ≤ 0.05, **P ≤ 0.01 and ***P ≤ 0.001.

## 5.4. Discussion

### ***Cell-derived nanovesicles were successfully biofabricated from mineralising osteoblasts sharing structural features with MO-EVs.***

Osteoblast-derived EVs are still limited in their pre-clinical evaluation, therefore, obtaining alternative to naturally-derived EV is an important step towards their clinical translation. EVs obtained from mineralising osteoblast presented with characteristics in line with previous studies and Chapter III with a sub-200-nm diameter and rounded shape with apparent lipid bilayer membrane (Man *et al.*, 2021a). Sharing morphological characteristics, we demonstrated for the first time the possibility to generate cell-derived nanovesicles as EV mimetics. Comparing workflows, generating MO-NVs has proven to be inexpensive, time efficient as well as providing a high yield consistent with NV generation from other cell types such as MDA-MB-231 (~200-fold higher; Wen *et al.*, 2022) or adipose-derived stem cells (~20-fold higher; Sun *et al.*, 2022). Moreover, as both EVs and NVs can be obtained from the same parental cells, there is a clear synergistic approach remaining unexploited in experimental designs as most cells can be processed into NVs after endpoint of CCM collection for EV isolation. This means that most studies involving the collection of CCM for EV isolation could use EV-parental to generate NVs as a by-product. Additionally, we also showed that NVs were less enriched in proteins with a ~3-fold decrease compared to EVs which can be linked to EV specific biogenesis, to the manufacturing method of NVs or to the potential protein contaminants co-isolated with EVs during ultracentrifugation. This is an important point as many EV-dosing regimen relies on protein concentration which will need to be normalised for direct comparison with NVs. Although we showed that the naturally-derived and synthetic populations had similar properties, their direct comparison would greatly benefit from more in-depth composition analysis such as multi OMICs. Important considerations need to be made regarding the composition of NVs, resulting from the extrusion of whole cells, there is very little control over content heterogeneity. Moreover, genomic DNA can also be found in the CDN suspensions which requires further investigation to assess the safety of their clinical translation in terms of immunogenicity.

***The successful capture and characterisation of MO-NVs via SP-IRIS opens promising possibilities for synthetic EV characterisation.***

Used for the first time on both MO-EVs and on any NVs, SP-IRIS not only represent a viable alternative to other gold standard methods to detect EV-biomarkers such as western blot, ELISA or flow cytometry, but also represent an innovative way to characterise NVs as, once captured onto the chip by their tetraspanin, other secondary antibodies could be used to assess the presence of other targets at the surface of NVs with or without a direct comparison with EVs. The comparative analysis showed that MO-EVs were enriched in tetraspanin markers compared to MO-NVs with over 100 times more particles detected via fluorescence detection for a same number of particles incubated onto the chip. These results can be partially explained by the reduced protein number per particle as described previously, nevertheless, it demonstrates the EV-specific enrichment in these markers. Moreover, NVs could potentially be used as a control for EV-biomarker analysis as methods outside Western Blot do not allow the direct comparison with the parental cells.

### ***MO-NVs did not exhibit osteoinductive properties highlighting the specific native function of EVs.***

After treatment on osteoblasts, the effects of both NVs and EVs showed a good biocompatibility with no significant changes in cell viability, however, both nanoparticle treatments did reduce the metabolic activity in the cultures at all concentrations ($p<0.01$). This could be explained by the stress caused by the addition of a high concentration of nanoparticles. As no apparent cytotoxicity was presented after live/dead staining, additional experiment such as the evaluation of DNA content is necessary to confirm if the metabolic activity reduction is due to a reduced proliferation rate.

The biomineralisation study confirmed the pro-mineralising potency of MO-EVs against osteoblasts with a significant increase of both ALP activity (1 and 10 µg/mL) and mineral deposition (10 µg/mL) confirming their therapeutic potency and their use as a valid control. However, the direct comparison with MO-NVs revealed that, at the same nanoparticle concentration, the NVs did not increase mineral deposition and were even found to significantly decrease ALP activity at both concentrations at Day 7. These results shows that NVs are not inherently potent with no apparent therapeutic effects. As NVs were derived from the first time from bone-cells, no biomineralisation studies using NVs were found in the literature. This comparison highlights that the potential of NVs may lie in their use as an innovative drug delivery platform or as a template for nanobioengineering by adding therapeutic molecules of interest to NVs (Goh *et al.*, 2017).

The immediate next steps to further study MO-NVs would be to compare them to MO-EVs via OMICs analysis to obtain important insights into their different compositions. Finally, NVs generated from different bone cells or exploring parental cells stimulations represent promising routes to obtain NVs with a potent therapeutic activity (Erwin *et al.*, 2023).

### ***A biomimetic liposome sharing MO-EV key features was successfully formulated incorporating annexin VI and ALP.***

After the isolation and characterisation of MO-EVs demonstrating their osteogenic potency *in vitro*, the design and formulation of EV-inspired liposomes were performed to develop suitable candidates to model MO-EVs. Davies *et al.*, demonstrated in his study that MO-EVs were enriched with annexin I, II and VI and the recent proteomics data obtained from our MO-EVs sample reported the presence of annexin II, III, IV, V, VI, VII, XI in our EV population (Davies *et al.*, 2017). This result suggests that isolated after two-weeks of osteogenic cultures, MO-EVs are equipped to act as a nucleation core via the channelling of calcium ions in the lumen (Chen *et al.*, 2008). From this data, annexin VI were chosen to be the first protein to be incorporated to the liposomes as annexin II, V and VI were the protein found to be enriched in most MVs (Kapustin *et al.*, 2011). ALP was also chosen to act as a supportive protein maintaining a phosphate supply which has been described as augmenting the initiation of HA crystal formation by MVs (Anderson, 2003).

Two liposomes formulations were successfully formulated using two different lipid compositions with DPPC (100%) or DPPC/DPPS (80%:20%). These lipid compositions have been chosen as a previous study by Veschi *et al.* reported that the addition of DPPS in liposome were enhancing the adhesion of annexin VI which is specifically binding to PS (Veschi *et al.*, 2020). As showed in Figure 5.10., the addition of PS increased the average size of the liposomes by close to 30 nm and also significantly raised the PDI, although these increases remains acceptable to generate EV mimetic with a PDI remaining below 0.4. As a negatively charged phospholipid, DPPS has been found to modify the membrane asymmetry which can be responsible for these variations (Scott *et al.*, 2019). Interestingly, the decrease of ζ-potential observed with the addition of PS matched the potential found in MO-EVs at – 11 mV which can be linked to their high PS content as showed by the lipidomic pilot study (Appendix 4.3.).

Both ALP and annexin VI were successfully incorporated in both formulations evaluating the incorporation by determination of total protein content. Interestingly, an 2-fold increase of binding efficiency of annexin VI was observed in presence of DPPS which confirmed the essential addition of this lipid specie to improve the insertion as described by Veschi *et al.* (2020). Based on the absence of change in the binding efficiency of ALP to either formulations, the DPPS-containing liposomes (DPPC/DPPS, 80%/20%) were then used across all future experiments.

Furthermore, due to its enzymatic activity, the activity of ALP post insertion was easily monitored using a ALP activity assay. This experiment showed that proteoliposomes composition has no influence on ALP activity confirming the bonding efficiency results. Moreover, the incubation time of ALP to the proteoliposomes did not appear to enhance the insertion rate. Adapting a method from Fiori *et al.* using a calcium fluorescent probe named FLuo-5N, the tracking of the calcium intake within annexin VI liposomes was attempted without success linked to the detection threshold of analysis (Data not shown) (Fiori *et al.*, 2012).

### *The incorporation of ALP and annexin VI liposomes was confirmed via flow cytometry*

To date, the characterisation of proteoliposomes was mostly limited to the study of a bulk detection of the proteins of interest with for example Simão *et al.* validating the presence of recombinant ALP and NPP1 from proteoliposomes via immunoblotting (Simão *et al.*, 2010). This approach coupled with enzymatic activity was deemed sufficient to validate protein incorporation. However, this approaches shows clear limits as unbound proteins may never be completely removed from a proteoliposomes suspension. Moreover, it is important the understand which percentage of the total nanoparticle population incorporate the protein of interest in order to adjust formulation parameters. In this study, the first evaluation of ALP activity post insertion was performed using flow cytometry. Once inserted to liposomes, fluorescent antibodies specific to our two proteins of interest were used to label the nanoparticles. In this experiment, the use of two incubation times (30 min and 3 h) was proposed and the addition of both protein to a single liposome population was attempted. The data provided (Fig 5.14.) brought important additional insights as a poor presence of ALP was detected with less than 1% of total nanoparticles were found ALP-positive across all groups. Moreover in Figure 5.13., DLS analysis did not reveal a variation of size after incubation with the proteins of interest which could explain these results. This low binding could be due to the lack of specificity of the antibody purchased, however it is likely that the liposome-to-ALP ratio needs to be augmented.

Regarding annexin VI, high binding efficiency was found >75% across all groups. Importantly, the incubation time had no effect on the binding efficiency of the proteins and the presence of ALP had no negative impact on the binding of annexin VI. Overall, this high throughput method is a great stepping-stone for proteoliposomes characterisation offering a single particle resolution. With limited quantities of proteins available due to their high cost, the formulation was not optimised further. However, an important next step would be to generate a series of liposomes with an increase protein to liposome ratio to determine if incorporation can be enhanced.

TEM images of our proteoliposomes were then obtained to assess morphological changes after protein insertion. Stable vesicular structures of desired size were observed. Importantly, ALP proteoliposomes appeared to display an unusual curvature as well as the presence of nano sized granules at their surface which are hypothesised to be ALP aggregates. No reference in the literature was found showcasing similar structural changes. However, the presence of aggregates may potentially lead to the unavailability of ALP binding sites for the antibodies, thus, limiting ALP detection using flowcytometry. With limited quantities of proteins available due to their high cost, the formulation was not optimised further.

### ***Annexin VI and ALP liposomes did not show osteoinductive properties in osteoblast cultures.***

A comparative biomineralisation study was finally attempted to determine the osteoinductive potency of proteoliposomes (Fig 5.16.). Interestingly, annexin VI liposomes appeared to reduce osteoblast proliferation between 7 and 14 days of treatment. As presented for the first time by Theobald *et al.*, annexin VI is capable of suppressing proliferation which may be of concern as a potential side effect (Theobald *et al.*, 1994). Both annexin VI and ALP liposomes showed no effect on neither ALP activity or ECM production compared to control, however, they were both found to significantly decrease mineral production (Fig 5.16C). In their study on ALP proteoliposomes, Simão et al. showed that their formulation was capable of inducing the formation of apatite minerals *via* a turbidity assay in the absence of cells (Simão et al., 2019). This suggests that the uptake of ALP or even annexin VI liposomes by the cells did not served their proposed mechanism of action. Embedding this vesicles within a 3D matrix or treating more matured 2D cultures, having already developed an ECM, might consitute interesting strategies to re-assess the effects of both ALP and annexin VI proteoliposomes activity on osteoblasts.

Importantly, strong conclusions cannot be drawn from this biomineralisation study as quality limitations in these experiments needs to be reported. The osteogenic control did not develop mineral nodules despite the presence of a rich ECM developed across all osteogenic conditions. This shows a degree of variability in the osteoblast response to its culture conditions which needs to be elucidated prior to perform further studies. The variability of MC3T3-E1 cells in terms of osteogenic performance has been discussed by Hwang and Horton (2019) showing that different subclones can trigger various osteogenic responses, which may be linked to changes of phenotypes across passages. Investigations were conducted for troubleshooting (Appendix 5.1). Dexamethasone was added as an osteogenic supplement for the first time to compare the influence of an earlier passage number P15 compared to P40 used in this experiment. Two media manufacturers and the addition of MO-EVs were also added to the comparison and the calcium deposition was evaluated after 7, 10 and 14 days of treatment as showed in Appendix 5.1. The comparison of basal and osteogenic control showed that no mineralisation occurred at day 3 and 7, however, MO-EVs were found potent at day 10 using the new media supplier tested. Mineralisation at day 14 was saturated for all conditions as dexamethasone enhance the osteoinductive capacity of the cell. From these experiments, a new batch of cells was procured from ATCC for work and the use of dexamethasone will be considered for future studies (Zhang *et al.*, 2023).

## 5.5. Conclusion

In this Chapter, the development of synthetic MO-EVs was investigated for the first time. Using both the top-down approach with the generation of MO-NVs or the bottom-up approach with the formulation of proteoliposomes, we demonstrated the possibility to create MO-EV mimetics as strategy to overcome the current translational barriers of EV-based therapies. However, their osteoinductive potency could not be demonstrated and further investigations are required to make synthetic EVs a viable therapeutic solution for bone repair.

## Appendix 5.1.

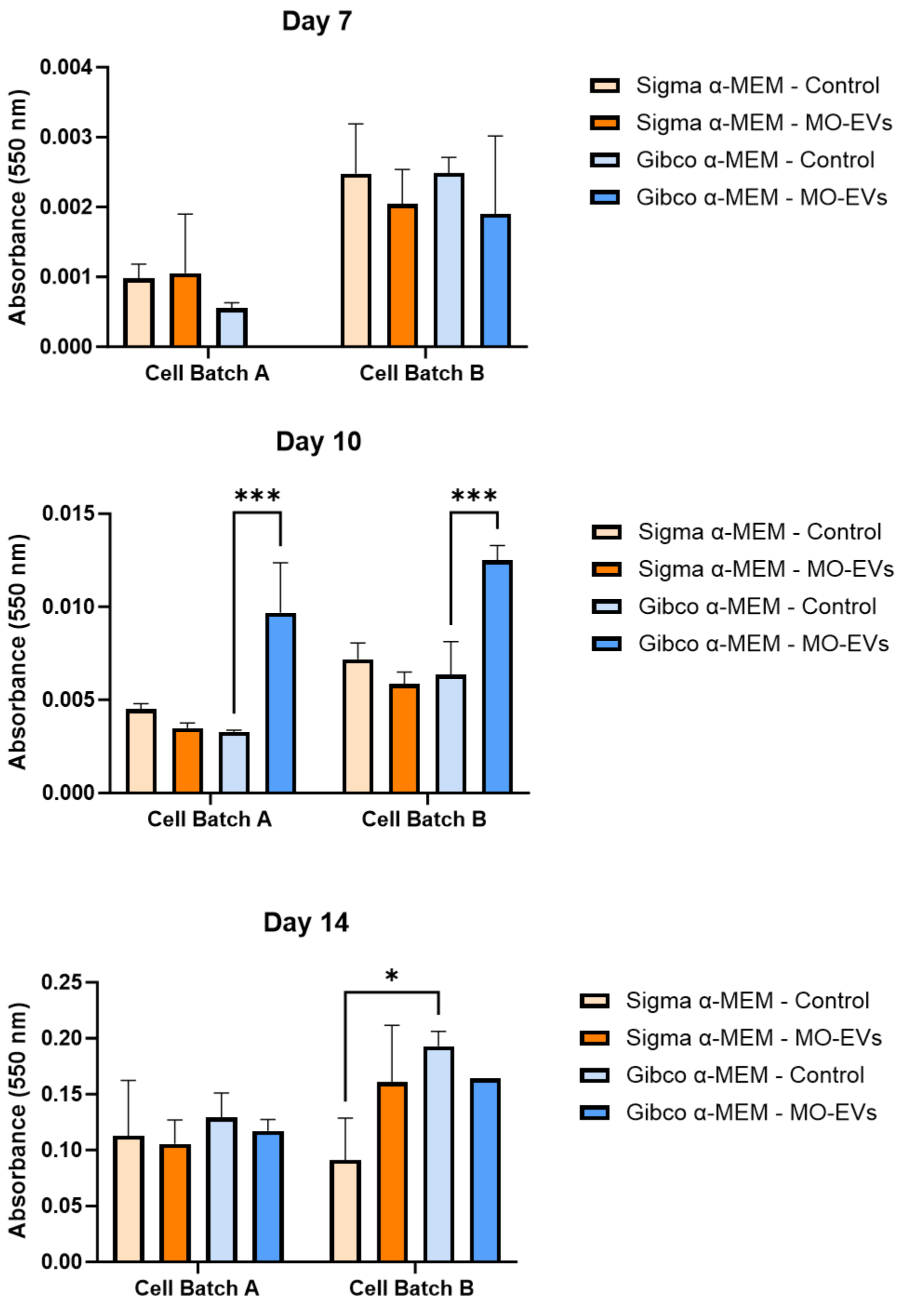

**Appendix 5.1. | Troubleshooting experiment evaluating the calcium deposition in osteoblast cultures after 7, 10 and 14 days**. Cultures were performed using dexamethasone to boost mineral formation comparing the influence of two cell culture media suppliers and two vials of MC3T3-E1 cells at passage 15 (cell batch A) and 40 (cell batch B). Data expressed as mean ± SD (n=3). with statistical significance presented as *P ≤ 0.05, **P ≤ 0.01 and ***P ≤ 0.001.

# Chapter VI

-

# Development of an hydrogel MO-EV-delivery system

## 6.1. Introduction

### 6.1.1. Background

The field of bone tissue engineering has made important advances in recent years in the development of biomaterials tailored to support bone repair. Initially, a strong focus had been placed onto inorganic scaffolds due to their excellent mechanical properties and stability (Lee *et al.*, 2022). Ceramic-based scaffolds, but also mineral-based or metal-based approaches have been employed to guide bone regeneration. However, in the last decade, the research focus has shifted towards biomaterials to obtain superior biocompatibility, as well as biomimetic environment more favourable to cells migration. Both natural and synthetic polymers have been utilised for their intrinsic anti-bacterial or osteogenic properties (Bai *et al.*, 2018). Synthetic polymers, commonly polyethylene glycol (PEG) or poly lactic acid (PLA), offers great tunability as they can be designed to obtain desired features such as porosity, mechanical properties, or functionalisation capacity (Ju *et al.*, 2023). To obtain augmented properties, single component hydrogels have become rarer, preferring the combination of several material to obtain combined advantages.

In addition to these intrinsic properties, the insertion of cells to osteoinductive biomaterials to promote bone repair has been widely investigated (Iijima and Otsuka, 2020; Zhang *et al.*, 2020b; Bahraminasab *et al.*, 2022). With the growth of the potential of nanotherapeutics for bone repair, there is need for a technology to deliver these nanoparticles to the fracture site. Specific to needs of bone fractures, traditional pre-formed hydrogels present with challenges due to the irregularities and complexities of defects (Cao *et al.*, 2024). To solve this issue, the development of injectable hydrogels has been favoured as they are allowed to fill the defect. Moreover, these systems have started to include therapeutic molecules to enhance the regenerative properties of the materials with for example the controlled and local delivery of drugs (Rizzo and Kehr, 2021).

To take advantage of the demonstrated bioactivity of EVs for bone repair, hydrogel-based systems have been developed to deliver these vesicles to the defect site offering a release *in situ* (Ju *et al.*, 2023). Importantly, EVs have demonstrated their capacity to remain in the ECM (Turner *et al.*, 2022). The demonstration of this anchorage has led to the study of matrix-bound nanovesicles to better understand the influence of these nanoparticles in the physiology of the tissues (Huleihel *et al.*, 2016).

Based on a previous study in our group, we demonstrated that a thermosensitive chitosan-collagen composite enhanced the therapeutic potency of MO-EVs, however, its design was limited due to the need for long gelation times at 37°C and the rapid degradation rate observed for hydrogels containing a high collagen percentage. Therefore, alginate was chosen to be used as the main template of this EV-hydrogel system (Man *et al.*, 2022c)

Alginate is a natural polysaccharide which has been widely employed in hydrogel systems. This hydrophilic and anionic biomaterial is obtained from the cultures of brown seaweed and can be derived from a variety of algae species as well as bacteria (Fernando *et al.*, 2020). Crosslinking of alginate is primarily performed ionically *via* the addition of divalent cations, although alternative strategies such as molecular entanglements, covalent crosslinking and self-assemblies have also been demonstrated (Zhang *et al.*, 2020b). Due to their high biocompatibility, low cost and ease of crosslinking, alginate-based hydrogels have rapidly become one of the most popular formulations using alginate as the main matrix template (Lee *et al.*, 2012). Moreover, alginate offers a wide range of molecular weight offering a simple way to tune the physical properties of the hydrogels formed (Kong *et al.*, 2004).

Due to difficulties linked to the rapid ionic crosslinking of alginate to control gelation, Bassett *et al.* (2016) developed a novel competitive ligand exchange of crosslinking ions (CLEX) approach to crosslink alginate which was chosen as the crosslinking method of choice in this study. Based on its molecular weight, alginate contains various amounts of the M residue ((1-4)-linked β-d-mannuronate) and the G (C-5 epimer α-l-guluronate) residue, both forming the polymeric structure. The negatively charged G residues are able to crosslink in the presence of cations to form a solid hydrogel in an aqueous solution. Favoured due to its non-toxicity, $Ca^{2+}$ is the most widely used cation employed (Bassett et al., 2013). The principle of CLEX gelation (Fig 6.1.) is to chelate the crosslinking ion such as Ca-Ethylenediaminetetraacetic acid (EDTA) preventing the gelation of alginate. In a second solution, an exchange ion having a greater affinity to EDTA, here $Zn^{2+}$ is also chelated forming a Zn-Bicine complex. When the two solutions are mixed together, the $Zn^{2+}$ then preferably binds to EDTA, thus releasing the crosslinking ion *in situ* triggering gelation (Yamamoto *et al.*, 2019). Having been recently developed, this approach has not yet been extensively used, Nevertheless, it has already been successfully applied with for example the preparation of hydrogel beads at the microscale for cell encapsulation using microfluidic technology (Håti *et al.*, 2016).

Overall this approach shows great promise to obtain better control of gelation offering great foundations to explore the incorporation of collagen and MO-EVs to a CLEX-alginate scaffold.

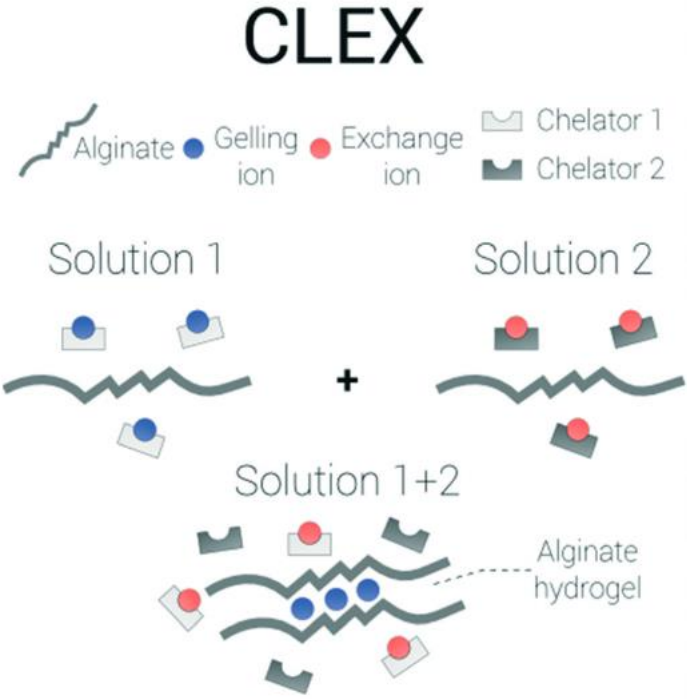

**Figure 6.1. | Schematic representation of the principle of CLEX gelation.** Before reaction, solution 1 is composed of gelling ions bonded to chelator 1 whereas exchange ions are bonded to chelator 2 in solution 2, both solutions containing sodium alginate. When the two solutions are mixed together, exchange ions will preferably bind to chelator 1 leading to the release of gelling ions, consequently crosslinking the alginate *in situ*. Adapted from Håti *et al.* (2016).

### 6.1.2. Aims and objectives

The aim of this chapter is to investigate the development of an innovative 3D-hydrogel delivery system for MO-EVs (Fig 6.2.).

- To formulate alginate/collagen hydrogels via the CLEX crosslinking method
- To determine the release profile of MO-EVs from the produced hydrogels
- To assess the printability and the control of the structure of the hydrogels

### 6.1.3. Acknowledgement of contributions

The following collaborators have been critical in contributing to this body of work:

- **Dr David Bassett** for his guidance and support towards this work with CLEX hydrogels as he led the discovery of this innovative crosslinking process.
- **Dr Aleksandar Atanasov,** for his support with 3D-printing and for allowing me to use his custom 3D-printer system.

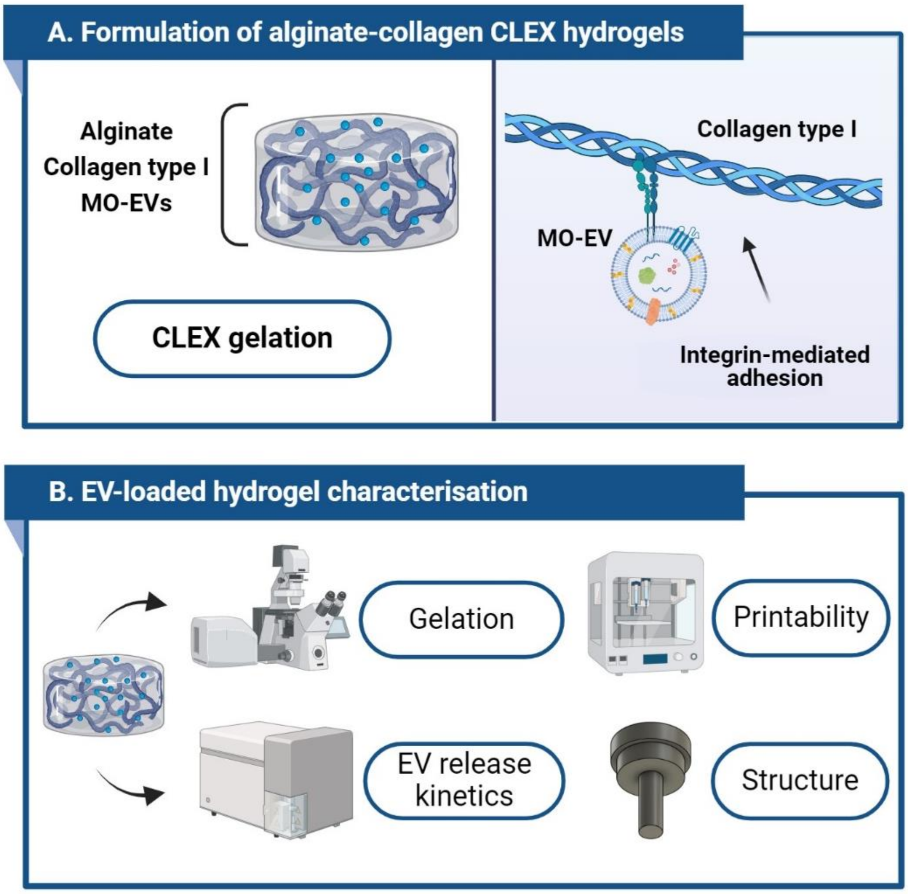

**Figure 6.2. | Schematic representation of the experimental workflow. A)** Formulation of alginate-collagen CLEX hydrogels. **B)** EV-loaded hydrogel characterisation (Created using Biorender.com).

## 6.2. Materials and methods

### 6.2.1. Preparation of Collagen I and Alginate solutions

To produce Collagen I hydrogels, rat tail collagen I (High conc. 3.55 mg/mL; Corning, UK) was used. Required for crosslinking, neutralisation of collagen I was performed by dilution collagen stock into a 20% 4-(2-hydroxyethyl)-1-piperazineethanesulfonic acid (HEPES) solution (1M stock; Sigma-Aldrich) prepared in de-ionised water.

Sodium alginate (Medium viscosity; Merck, Germany) was prepared at 2% (w/v) in de-ionised water by autoclaving (0.1 MPa, 121°C, 60 mins) offering a homogenous dissolution as well as sterility.

### 6.2.2. Preparation of CLEX solutions

All CLEX solutions were prepared in de-ionized water freshly filtered to limit the number of nanoparticle contaminants. Crosslinking ion chelator solutions named CLEX-A was prepared by mixing $CaCl_2$ (60 mM) with ethylenediaminetetra-acetic acid (EDTA) (60mM) (Sigma-Aldrich, UK) and 30 mM HEPES (pH 7.4-7.6) (Invitrogen, UK). Exchange ion chelator solutions named CLEX-B were prepared in the same way by replacing $CaCl_2$ by $Zn(CH_3CO_2)_2$ and EDTA by Bicine. Both solutions were then adjusted to pH 7.6 using an NaOH solution with final concentrations obtaining adjusting the final volumes using de-ionized water. Solutions were made freshly at every use to ensure stable chelation of the ionic solutions. Sodium alginate was then diluted in each CLEX solution to prepare hydrogels and, when needed, MO-EVs were added to CLEX-A at desired concentration.

### 6.2.3. Hydrogel moulding

To prepare hydrogel, an adapted ‘bottomless’ 48-well plate was designed, and a computer-aided design (CAD) file generated with Autodesk Fusion360 (v2.0.15). Structure was 3D-printed using a Creality CR20 Pro printer (Creatility3D, UK). This simple design following the standardised size of a 48-well plate allowed to gently push the hydrogel outside the mould by the bottom of the well. A sterile and filmed foam pad was also place under the plate to prevent any leakage prior to crosslinking. CLEX-A and -B were both added simultaneously drop by drop alternating the two solutions.

To create the core structure presented In Figure 6.16., an additional insert was designed by CAD and was generated by with Autodesk Fusion360 as displayed in Figure 6.3. The inserts were printed using the same printer as the mould ensuring a great fit with the same printing resolution (Figure 6.4.).

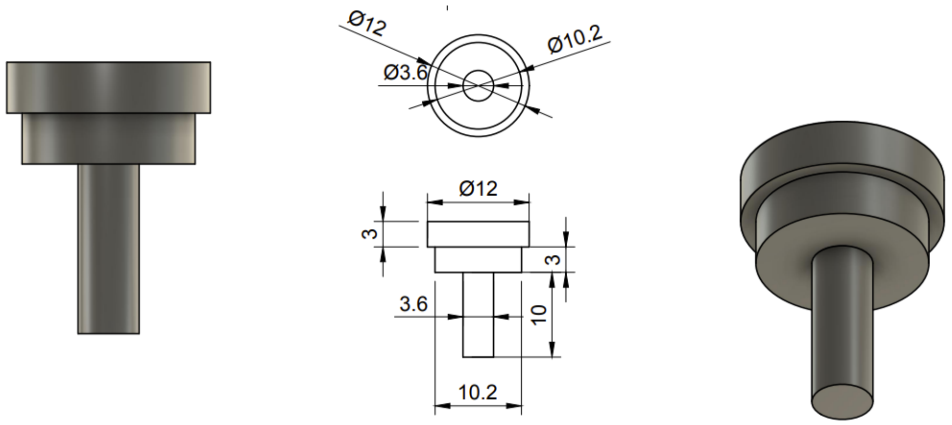

**Figure 6.3. | Schematic and technical representation of the manufactured inserts.** Values in displayed in mm.

**Figure 6.4. | 3D-rendered illustration of the hydrogel mould system with insert.**

### 6.2.4. Fluorescent labelling of rat tail collagen

Collagen I was labelled via the method developed by Doyle *et al.* (Doyle *et al.*, 2018) and was kindly provided by Dr David Bassett. Type I rat-tail collagen (Corning, UK) was stained at a final final concentration of 10 mg/mL and was mixed with unlabelled type I collagen solution at 10% (v/v) before being added to CLEX solutions.

### 6.2.5. Hydrogel fluorescence imaging

To observe both collagen I and MO-EVs inside the 3D-system, hydrogels were prepared inside µ-Slide 8 Well (Ibidi, Germany) chambered coverslip for higher optical quality. Images were obtained using an ECLIPSE Ti 2 inverted microscope allowing super-resolution imaging (Nikon, Japan). Nikon EZ-C1 FreeViewer and Fiji softwares were used to process the images.

### 6.2.6. MO-EV release study

The release kinetics of MO-EVs from hydrogels was performed by adding 20 µg of MO-EVs (mass of protein quantified by BCA assay) to each 200 µL hydrogel (100 µg/mL). Release study was performed in PBS at pH = 7.4 and within a cell incubator at 37°C. For all release studies, the totality of the release medium (100 µL) surrounding each hydrogel was collected at defined time points and replaced by the same volume. Collected release media samples were stored at 4°C until downstream analysis. The quantification of MO-EVs was performed using either BCA assay for total protein content, flow cytometry for the unlabelled quantification of all nanoparticles detected and via the CD63 ExoELISA based on the methods described previously.

### 6.2.7. Printability assessment

To 3D-print our CLEX solutions, a CAD file was first developed with Autodesk Fusion360; saved in. stl format. .stl file processed with a slicer software Ultimaker Cura to produce files which can be read by the firmware of the custom 3D bioprinter (.gcode). A custom 3D-printer system based on the Duplicator i3 printer model (Wanhao, UK) was then employed. The bioinks were then combined extemporaneously in the syringe leaving the printer a 15 min window for printing before observing pre-extrusion crosslinking. The extrusion rate (measured in steps of the extruder motor per mm of travel in the code) was set at 2 mm/s with a 20-gauge needle. Constructs were printed in a 12-well plate for ease of hydrogel recovery.

## 6.3. Results

### 6.3.1. Validation of the crosslinking properties of starting materials

The capacity of collagen I to crosslink was validated by producing 100% collagen hydrogels with concentrations ranging from 1 to 3 mg/mL. Crosslinking at 37°C was monitored at 405 nm and hydrogels at both 1 and 2 mg/mL showed crosslinking initiation at 10 min. At 2 mg/mL, plateau was reached after 20 min of incubation whereas an additional 10 min was required at 1mg/mL (Fig 6.5.).

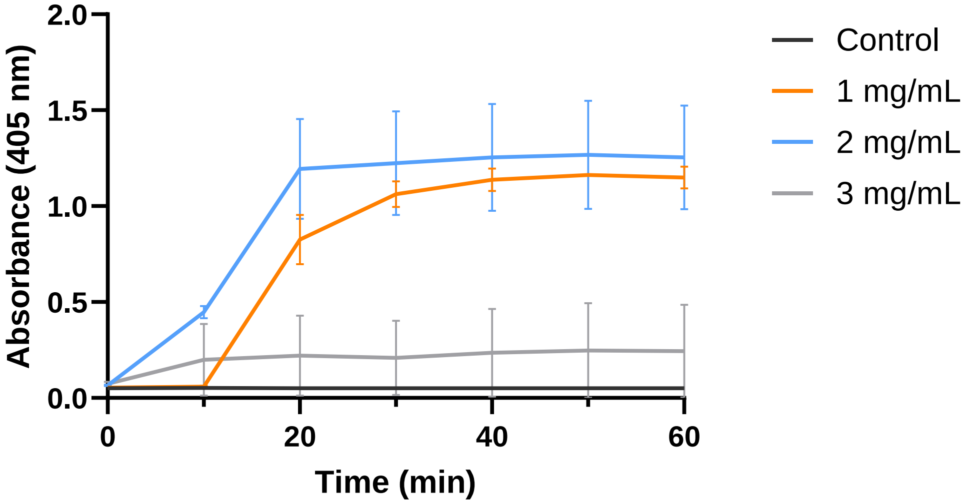

**Figure 6.5. | Evaluation of Collagen I gelation time**. Gelation time was evaluated by spectrophotometry at 405 nm using $H_2O$ (no collagen) as a control. Data expressed as mean ± SD (n=3).

Following collagen, I, the gelation time of a solution of 1% sodium alginate in contact with $CaCl_2$ was also assessed and also monitored at 405 nm with 5 min intervals. As showed in Figure 6.6., a rapid crosslinking was observed within the first minutes and reaching a plateau after 10 mins.

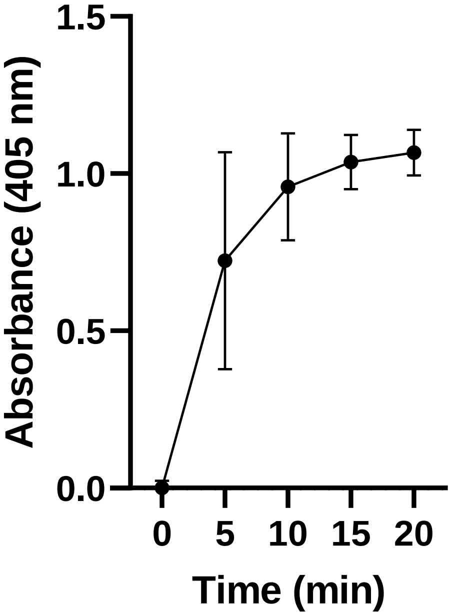

**Figure 6.6. | Evaluation of sodium alginate gelation time.** Data expressed as mean ± SD (n=3).

### 6.3.2. Validation of sodium alginate and collagen I to CLEX solutions

Once all the CLEX solutions were prepared, sodium alginate was then added to each or both CLEX solutions combined to assess pH stability. No significant pH variation was observed with all pH remaining between 7.5 and 8. (Fig 6.7.)

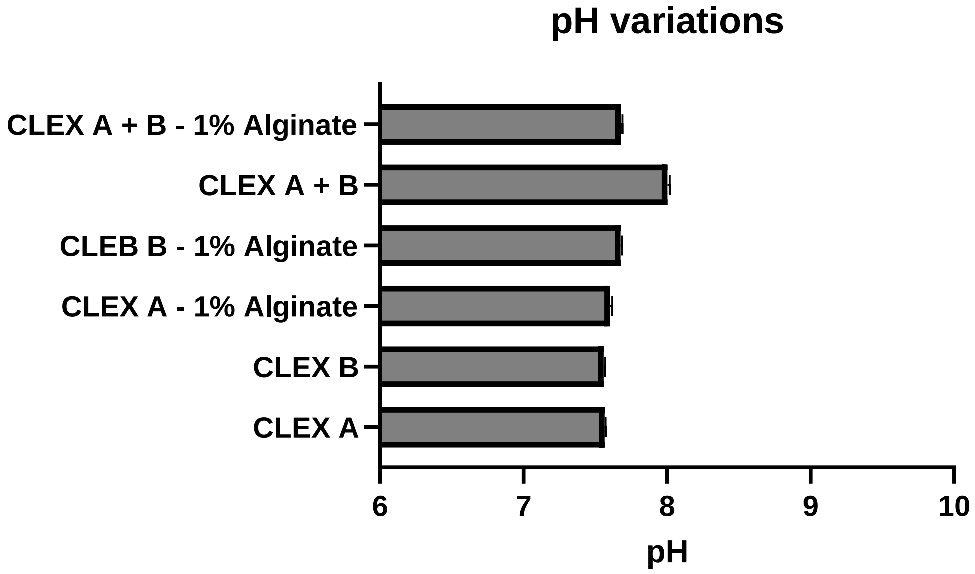

**Figure 6.7. | Evaluation of pH variations following the addition of sodium alginate to CLEX solutions.** Measurements were obtained using the mini-probe of a standard pH meter immediately after mixing when two solutions were assessed**.** Data expressed as mean ± SD (n=3).

A range of collagen concentration (v/v %) was added to CLEX solutions (A and B). Interestingly, it was showed that all concentrations of collagen significantly increased the pH levels in both CLEX A and CLEX B (p<0.001) (Fig 6.8.) Importantly, no crosslinking was observed after the addition of collagen to CLEX A or B showing that the presence of collagen alone was not disruptive, allowing collagen to be added to the CLEX solutions and maintaining the desired stable pH range between 7.4 and 8.0.

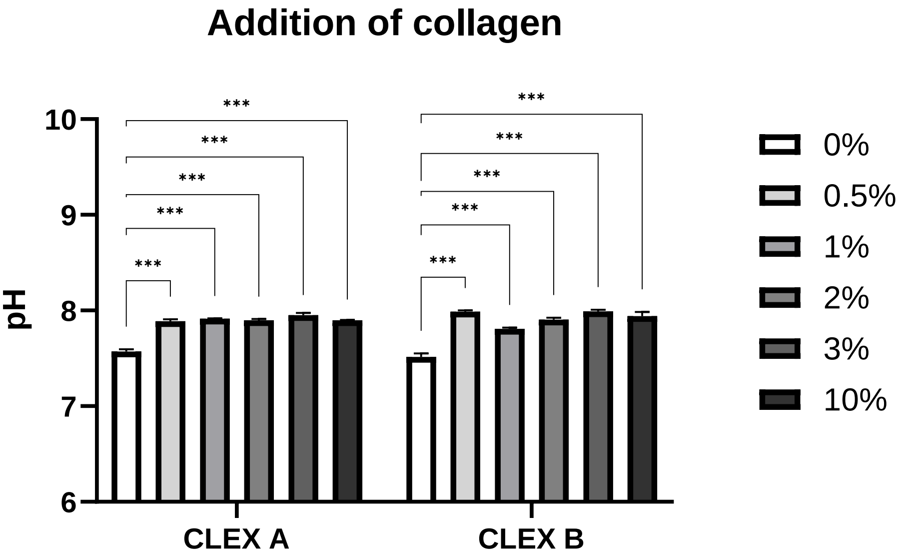

**Figure 6.8. | Evaluation of the effects of the addition of collagen to CLEX solutions on pH.** Data presented as mean ± SD (n=3) with statistical significance presented as *P ≤ 0.05, **P ≤ 0.01 and ***P ≤ 0.001.

Using CLEX A and B containing 1% alginate, the incorporation of collagen I was then assessed after mixing the 2 CLEX solutions triggering crosslinking. A range of % of collagen was used to evaluate the impact of the amount of collagen on crosslinking. Using 100% collagen hydrogel as a control, absorbance spectrum (0-1000 nm) was obtained after 20 min of crosslinking and reported in Figure 6.9. Interestingly, only hydrogel containing 10% collagen were found to have a visible increase of absorbance.

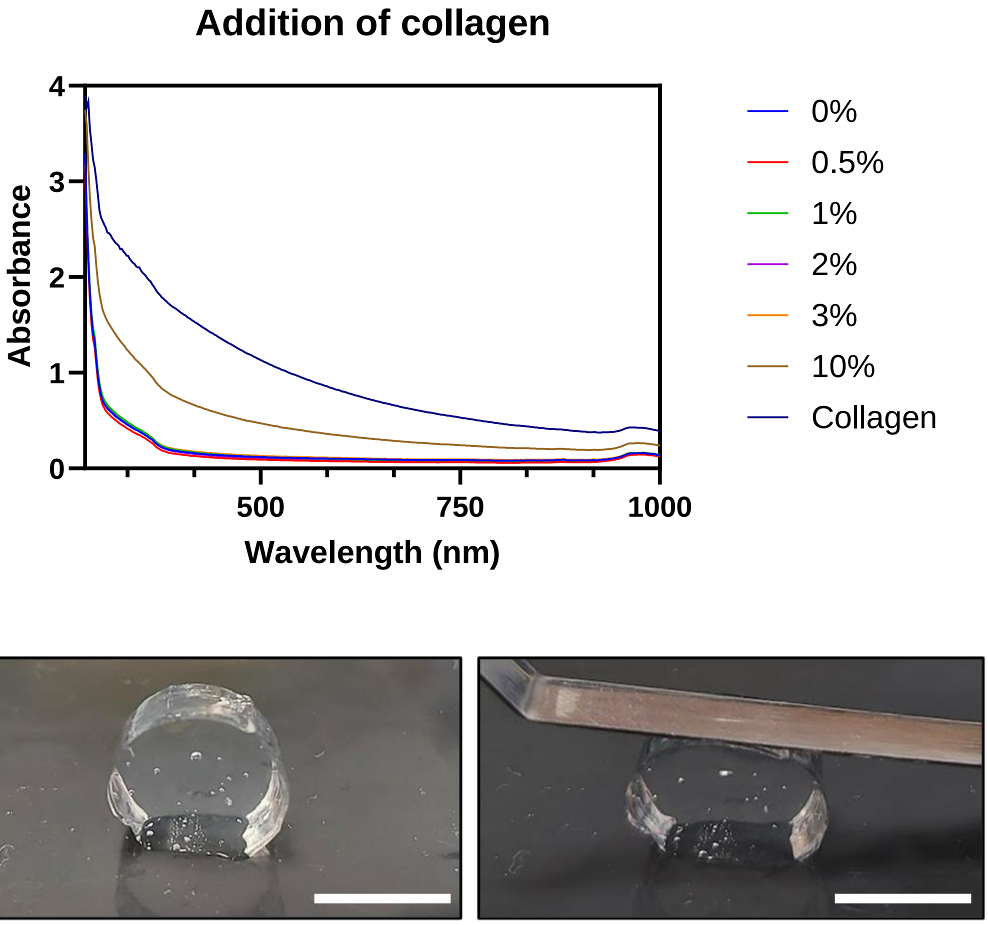

**Figure 6.9. | Evaluation of the gelation of 1%-alginate-CLEX solutions after addition of collagen.** Macroscopic images correspond to the 10%-collagen hydrogel. Scale bars = 10 mm

Following this test, the hydrogel containing 10% collagen was generated once more with the addition of fluorescent collagen to the bioink. Using confocal microscopy (Fig 6.10.), the formation of collagen fibrils was confirmed.

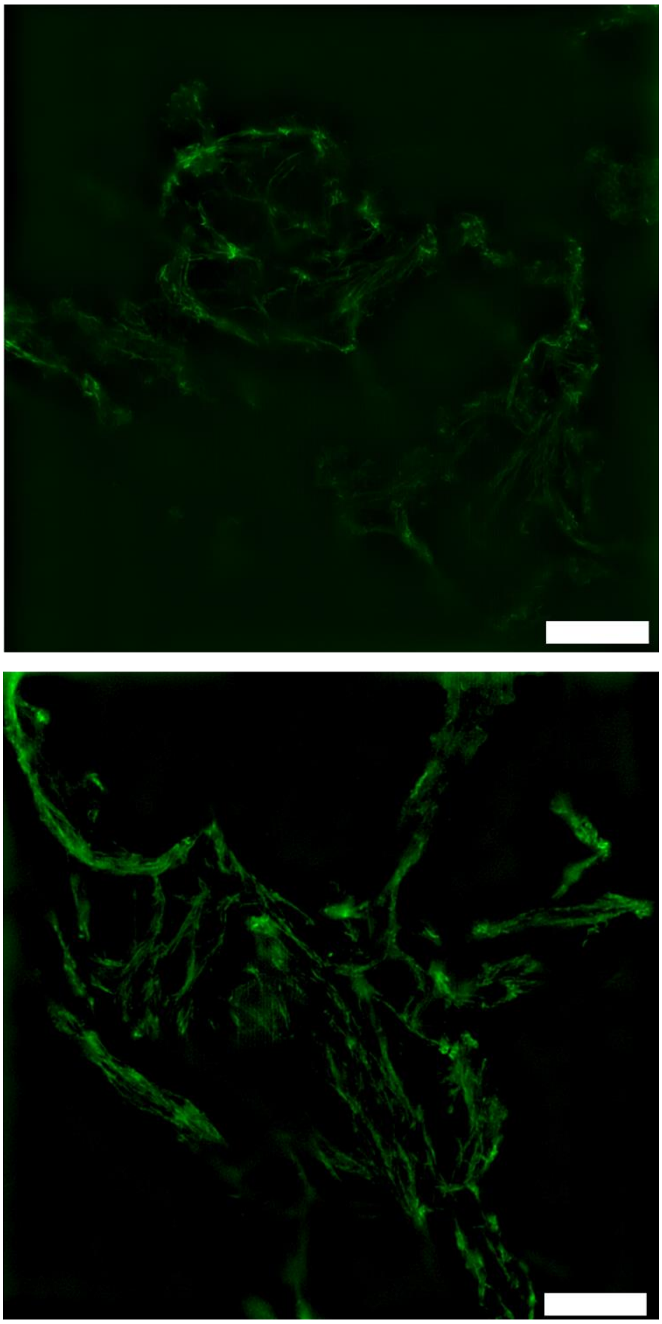

**Figure 6.10. | Confocal microscopy images of 1%-alginate/10%-collagen CLEX hydrogel after crosslinking.** Green structures imaged corresponds to the collagen network formed post-crosslinking. Scale bars = 300 µm.

### 6.3.3. Addition of MO-EVs to CLEX hydrogels

Following the successful preparation of bioinks incorporating both alginate and collagen I with the crosslinking of both components validated, the addition of MO-EVs was then explored.

Using the Z-stack function of the confocal microscope, a 3D representative image of a collagenous region of interest of the alginate/collagen CLEX hydrogel was obtained as displayed in Figure 6.11. Centered around the collagen fibril, a large collagenous structure in green appears at the centre of the box. PKH26-labelled MO-EVs in red appeared well distributed all across the 3D environment with no notable colocalization in the collagen region suggesting a non-collagen specific location.

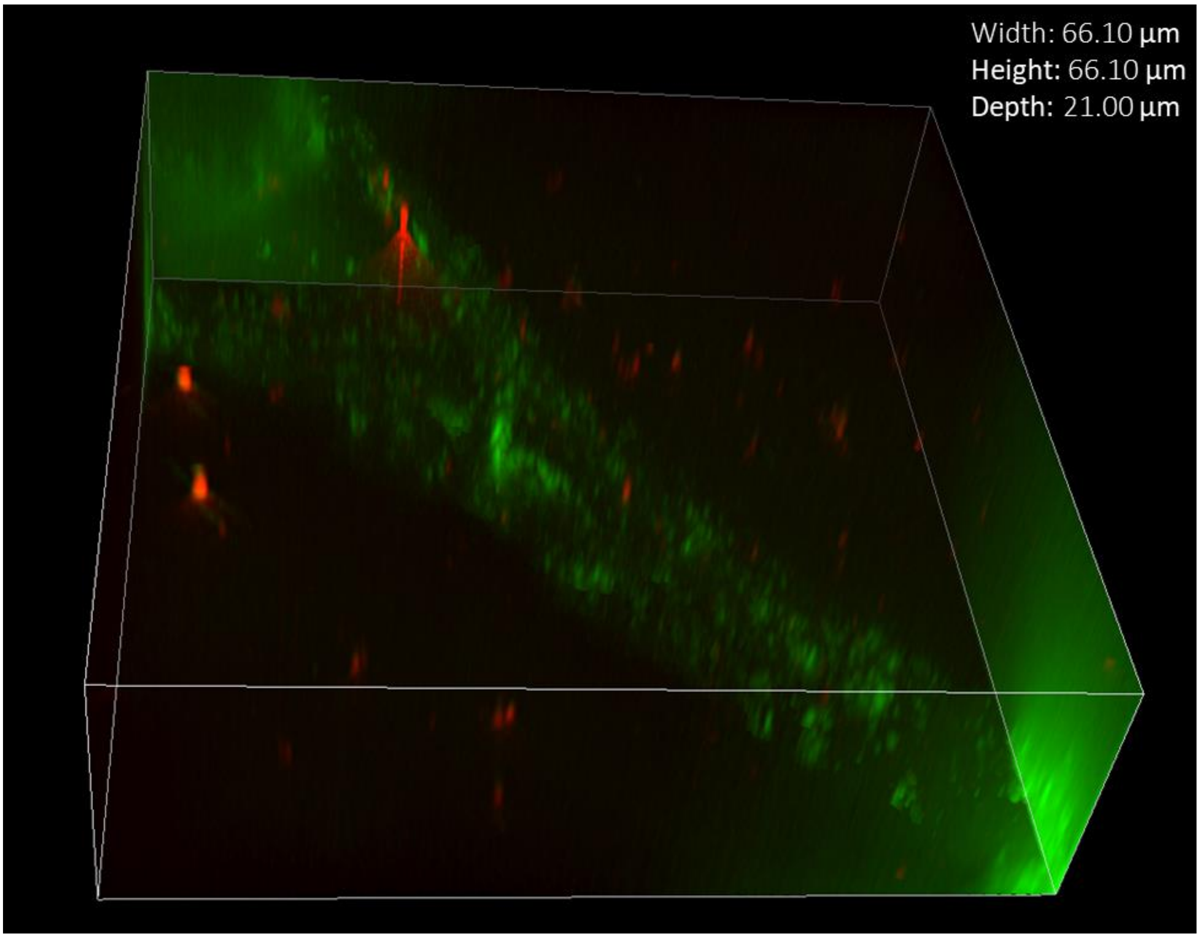

**Figure 6.11. | Confocal microscopy image of MO-EVs after loading in 1%-alginate/10%-collagen CLEX hydrogel.** PKH26 lipid-stained MO-EVs can be observed in red whereas the collagen structure can be observed in green. Scale is displayed on the image as 3D measurements of the box.

### 6.3.4. Evaluation of MO-EV release from alginate-collagen CLEX hydrogels

In this first MO-EV release study, BCA assay was used in order to quantify EV protein in the release media. In Figure 6.12A, the short-term release between 0.5 and 12 h was evaluated and showed no significant difference between control hydrogels (empty) and MO-EV loaded hydrogels. All concentrations were ranging between 20 and 40 µg/mL (Fig 6.12A). Similarly at longer time points (Day 1, 3 and 7), no significant differences were observed between groups with protein concentrations >20 µg/mL determined for all samples (Fig 6.12B).

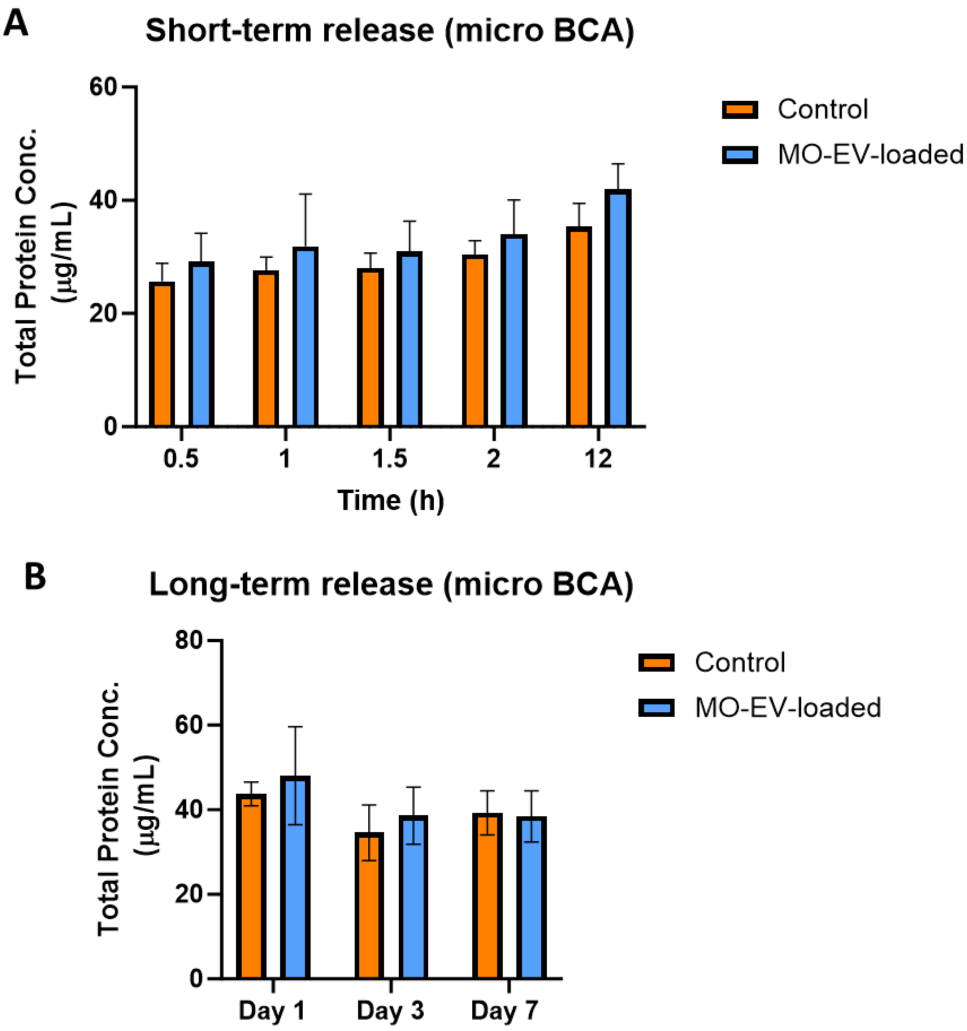

**Figure 6.12. | Determination of EV release from CLEX-alginate hydrogels via microBCA. A)** Short-term release from 0.5 to 12h. **B)** Long-term release after 1, 3 and 7 days. Data presented as mean ± SD (n=3) with statistical significance presented as *P ≤ 0.05, **P ≤ 0.01 and ***P ≤ 0.001.

Following the initial pilot release study, flow cytometry was used as an alternative to protein content in order to obtain an enhanced resolution by quantifying nanoparticle with a single-particle resolution.

As showed in Figure 6.13., a burst release of nanoparticles has been observed after 2 h with a high amount of nanoparticles (>3 x $10^6$) released from all hydrogels from 0% to 10% collagen concentrations. Importantly, all the groups containing collagen released a significantly higher number of nanoparticles (>10-fold increase) compared to alginate-only hydrogels.

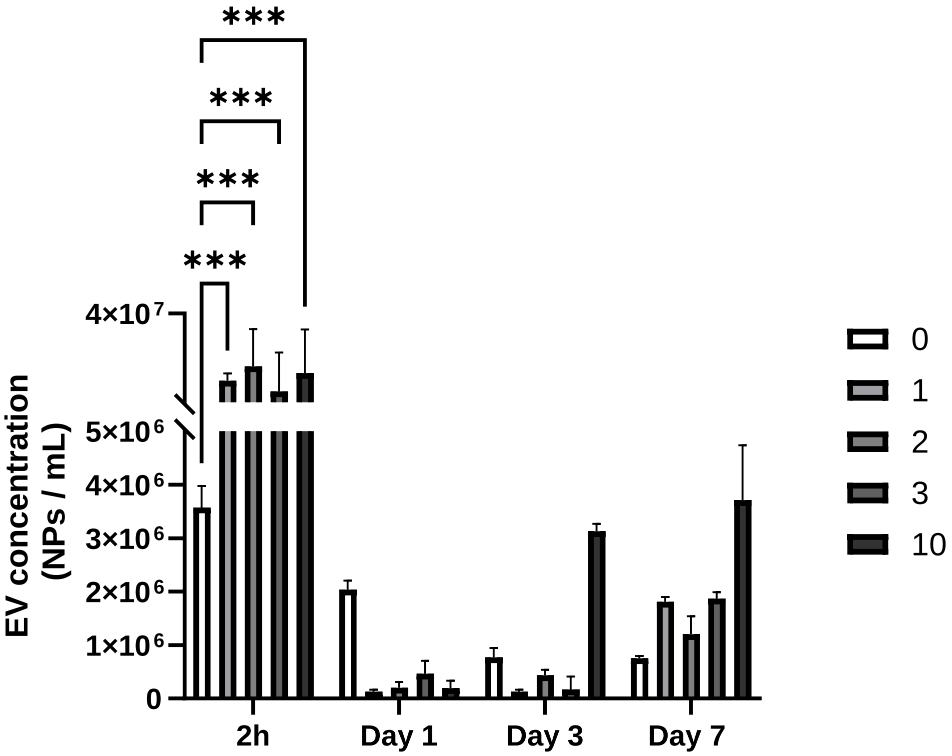

**Figure 6.13. | Determination of MO-EV release profile from alginate/collagen CLEX hydrogels via flow cytometry.** Data presented as mean ± SD (n=3) with statistical significance presented as *P ≤ 0.05, **P ≤ 0.01 and ***P ≤ 0.001.

Based on the results obtained via flow cytometry, a final alternative was investigated in order to better understand the release profile of MO-EVs from this hydrogel system. An ExoELISA specific to CD63 was employed while adding an unloaded hydrogel control to reinforce the experimental design. This specific marker found abundantly in MO-EVs allowed the discrimination of MO-EVs from other nanoparticles that can originate from the biomaterials themselves. Interestingly, a completely different release profile was observed showing no release after 2h and 24h (Fig 6.14.). From Day 3, EV release has been demonstrated for hydrogel containing 3 and 10% collagen only sustaining this release at end point Day 7. Notably, significantly less MO-EVs were released from the 10% collagen hydrogels compared to the 3% hydrogels at both Day 3 (p<0.01) and Day 7 (p<0.001) (Fig 6.14.).

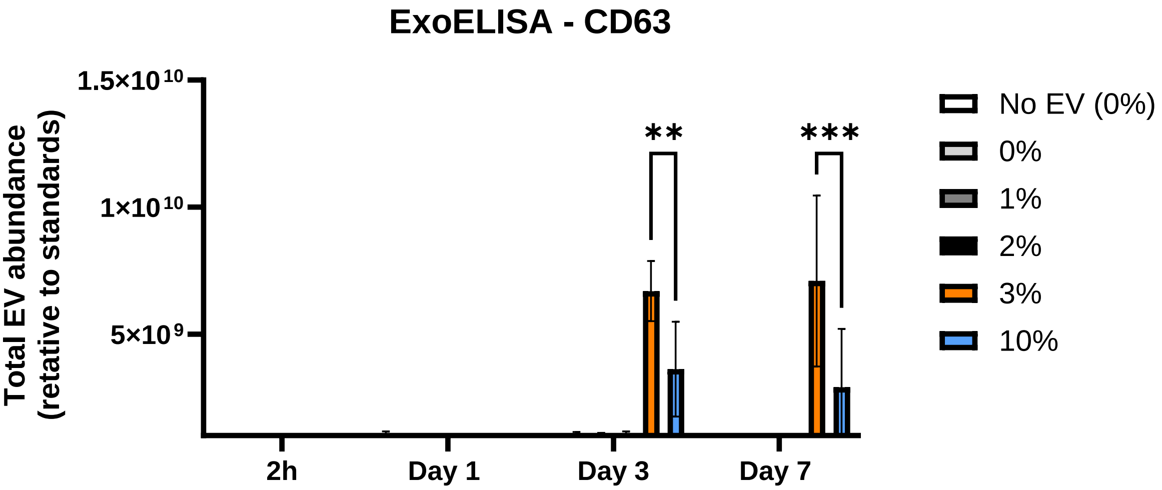

**Figure 6.14. | Determination of MO-EV release profile from alginate/collagen CLEX hydrogels *via* CD63 ExoELISA.** Data presented as mean ± SD (n=3) with statistical significance presented as *P ≤ 0.05, **P ≤ 0.01 and ***P ≤ 0.001.

### 6.3.5. Assessment of the printability of alginate/collagen CLEX hydrogels

After the characterisation of MO-EV release profile, the printability of the 1%-alginate-10%-collagen CLEX hydrogels was experimented. Using a custom 3D bioprinter (Fig 6.15), cylinder shaped hydrogels mimicking their moulded counterparts were successfully bioprinted after mixing CLEX A and B solutions in a single syringe allowing to print within 15 min prior to gelation *in situ*. In Figure 6.15C, an example of the successfully 3D printed hydrogel was displayed. The print was performed with a 20-gauge needle, however, the CLEX solutions were found easily extruded through multiple sizes from 16- to 30-gauge.

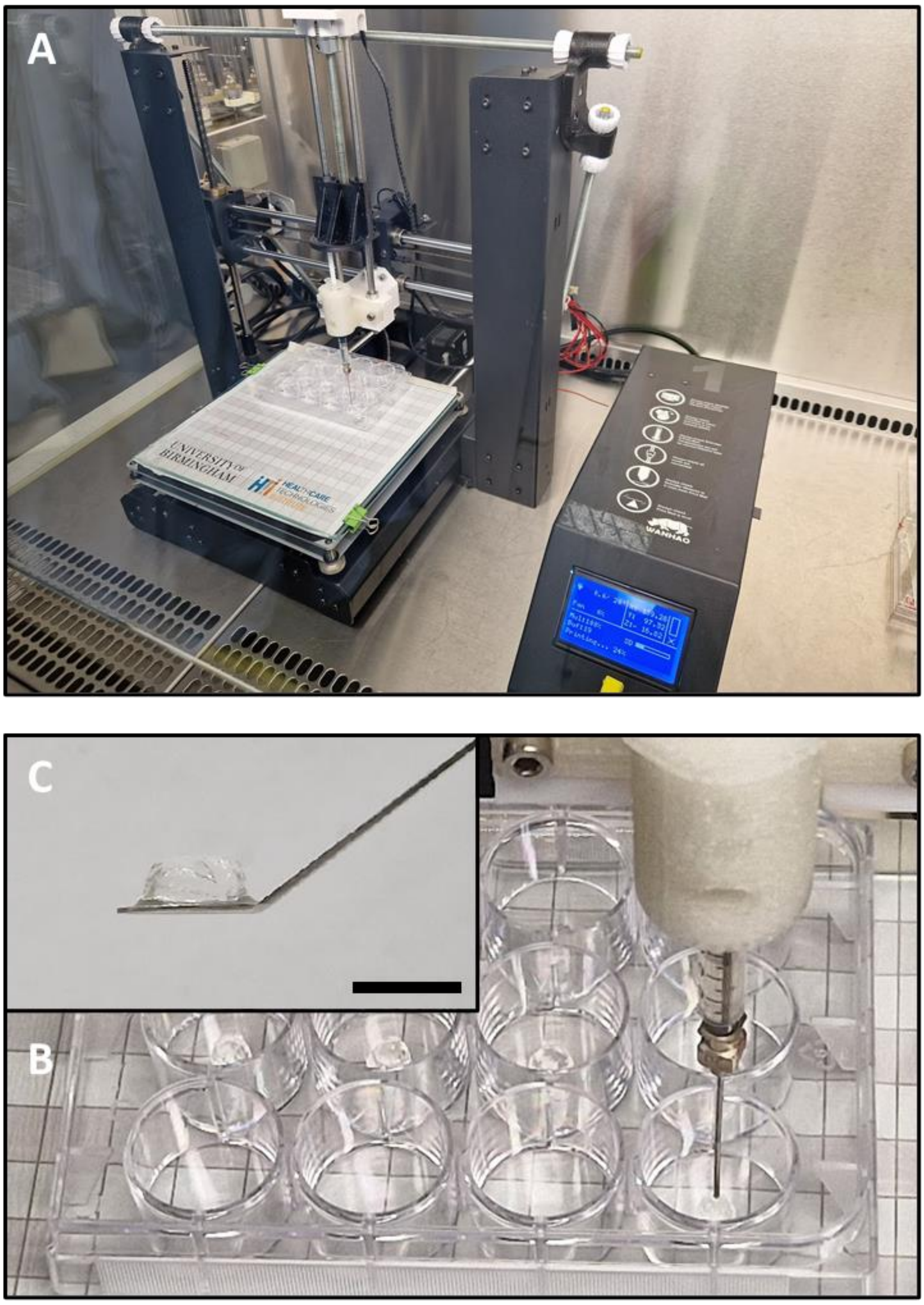

**Figure 6.15. | Macroscopic images of the 3D-printing of alginate/collagen CLEX hydrogel.** A) Overview of the 3D printer. B) Image of the plate during hydrogel printing. C) Side view of the resulting hydrogel obtained. Scale bar = 3 mm.

### 6.3.6. Development of a model to control the spatio temporal delivery of MO-EVs

As a further step towards the use of the validated MO-EV hydrogel system, a more sophisticated mould has been developed including a 48-well plate-sized insert (Fig 6.16A). Once added to each well before the addition of the bioinks, crosslinking then occurs all around the insert creating a smaller cylinder at the core of the hydrogel representing 30% of the volume of the total hydrogel. This negative volume can was then filled with an additional bioink loaded with MO-EVs offering a platform to study the spatio-temporally controlled delivery of nanovesicles (Fig 6.16.).

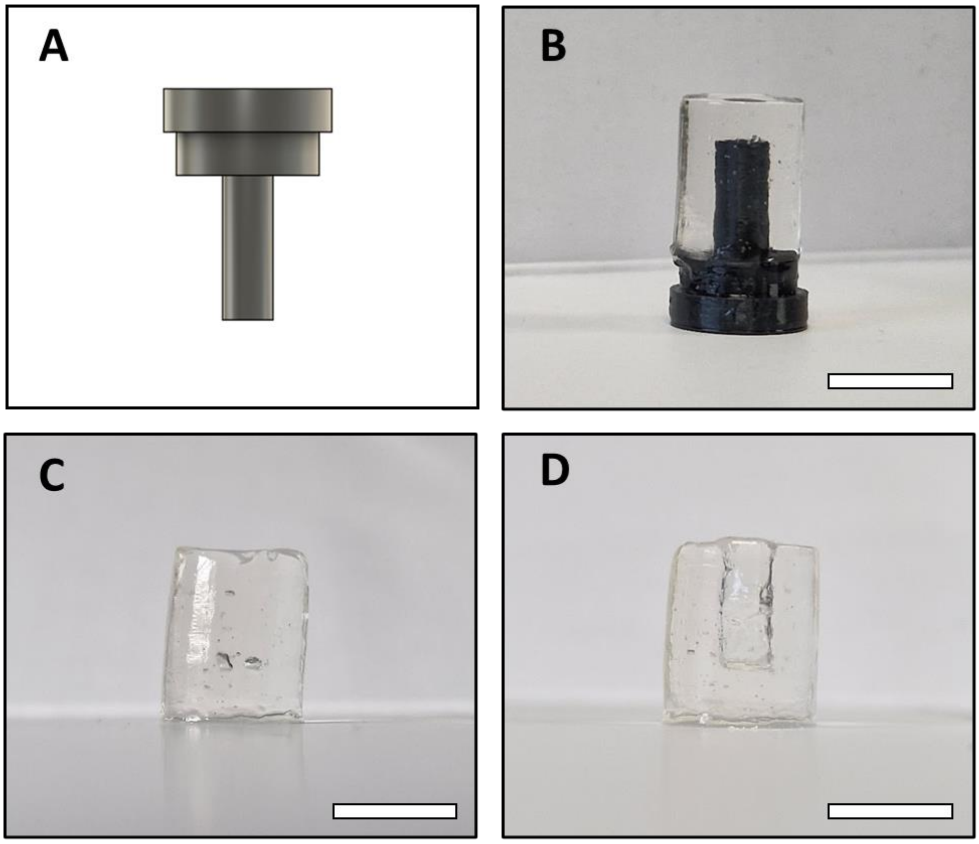

**Figure 6.16. | Creation of an inner core structure with alginate-collagen CLEX hydrogels.** With **A)** 3D representation of the insert. **B)** Gelation with the presence of the insert. Representative images of hydrogel formed **C)** without or **D)** with the use of the insert. Scale bars = 10 mm.

## 6.4. Discussion

### ***CLEX gelation was chosen to replace traditional crosslinking of alginate-collagen hydrogels.***

In Figure 6.5. and 6.6., the crosslinking of alginate and collagen was verified as these two starting materials were at the foundation of this work. Despite their full crosslinking, 100% collagen hydrogels at all concentrations appeared weak and easily degradable. These low mechanical properties are well established due to the absence of covalent bonds in the network (Sarrigiannidis *et al.*, 2021). On the other hand, the crosslinking of alginate using $CaCl_2$ as the ionic initiator of crosslinking was very efficient. However, stiffness of the resulting hydrogels formed a gradient from the contact surface with the liquid solutions to the bottom of the well. Moreover, the hydrogels formed showed important irregularities of shape due to the mixing of $CaCl_2$ with the alginate solution before crosslinking. To solve all these problems at once, the potential of competitive ligand exchange crosslinking was harnessed and adapted to this particular application.

pH has been introduced as one of the most important parameters for CLEX gelation as the displacement of pH outside the 7.4-8.0 range would induce an immediate gelation of alginate and a burst release of ions from their respective chelator would occur. In Figure 6.7., it was confirmed that the addition of sodium alginate to the CLEX solutions was not disrupting pH. This had to be thoroughly troubleshooted as it appeared that the mixing time of each ion to their chelators was an important factor to obtain more stable solutions. Additionally, best results were always obtained when all stock solutions were prepared fresh on the day. The use of a 1% concentration of alginate was chosen based on the work of Dr Laurence Hill (data not shown) in our lab who optimised the mechanical properties and the biocompatibility of alginate within CLEX bioinks.

Regarding the addition of collagen, it was showed in Figure 6.8., that all concentrations of collagen introduced from 0.5% onwards were significantly increasing pH ($p<0.001$) (Fig 6.6.). Fortunately, this increase remained in the working concentration range of CLEX solutions which did not induce spontaneous crosslinking. In Figure 6.9., only 10% collagen hydrogels increased the absorbance values beyond baseline suggesting that fibril formation only occurred using this concentration. Due to difficulties to assess collagen fibril formation visually using methods such as brightfield microscopy or polarised light microscopy, it was decided to use fluorescent collagen which was produced using the method developed by Doyle *et al*. (2018). In Figure 6.10., it was visually confirmed that collagen fibril formation occurred in 10% collagen CLEX hydrogel only.

### ***The MO-EV release from alginate-collagen CLEX hydrogels is influenced by the concentration of collagen present in the composite.***

Using hydrogel for bone repair applications, it is key to understand the release profile of MO-EVs from the hydrogel system considering its design as an EV delivery system. A growing number of studies have explored the release profile of EVs after their loading in 3D-hydrogel systems (Riau *et al.*, 2019). First, in Figure 6.11., the incorporation of MO-EVs was validated qualitatively observing an even distribution across the hydrogel. However, in the absence of colocalization with collagen, the specific binding of EVs to the ECM mimetic cannot be demonstrated.

In this particular system, a step-by-step approach had to be used due to the complexity of the evaluation of MO-EV release from an alginate/collagen composite and the presence of collagen. Several studies have commonly quantified EV release by quantifying the protein content in release media as EVs were the only source of protein. As showed in Figure 6.12., this methodology was not suitable for our application as BCA assay returned quantities of protein superior to the original amount loaded into the hydrogels (20 µg). This indicate that collagen is being release from the hydrogel system, thus, rending the sole quantification of MO-EVs impossible. Additionally, it was found that the HEPES buffer used in the preparation of the hydrogel is also part of the BCA assay manufacturer's list of interfering substances preventing us to use this simple and high-throughput approach for MO-EV release studies (Man *et al.*, 2021b).

NTA appeared as an obvious replacement allowing the determination of nanoparticle concentration. Nevertheless, the time of analysis per sample coupled with its high threshold of detection didn't suit the needs of an EV release study. As previously optimised for the characterisation of proteoliposomes, flow cytometry was then chosen as the method of choice to quantify MO-EVs without any fluorescent labelling to quantify the bulk of all nanoparticles released. This approach benefited from the high resolution of detection using only small volumes and allowed absolute quantification by controlling the injection the same volume of sample across the analysis. The main drawback of this method, which would have been shared with NTA, is that the detection was EV specific, and the other component of the hydrogel may release particles within the same size range as MO-EVs.

As a final strategy, the use of ExoELISA was found successful as it allowed MO-EV detection due to the presence of CD63 at their surface without the undesired co-detection of all the other nanoparticles. Interestingly, EV release was only observed at day 3 and day 7 and only by the hydrogels containing 3% or 10% collagen. At this stage, no final conclusions can be drawn. It is hypothesised that the fibril formation of collagen induced a disruption of the alginate network allowing a faster initiation of release. However, if MO-EV were to be specially bound to collagen, the degradation of the collagen fibrils overtime might lead to a forced release of EVs remaining attached to collagen fibers. Further investigations are required to monitor release for longer time to better understand the release kinetics of MO-EVs.

However, there is two critical limitations using ExoELISA to take into account. Being specific to a single EV marker which is not present on the totality of the nanoparticles, the quantification of EVs remains partial and relative. Moreover, as the quantification is based on the use of standards, the minimum detection threshold set by the manufacturer might prevent the detection of low concentrations of EVs which might occurred in earlier time points.

***The bioinks developed were found injectable and suitable for 3D-printing.***

In a final part, the injectability of the CLEX bioinks was evaluated demonstrating no issues with extrusion using multiple syringe/ needle sizes. Using a custom system, the mixing of the CLEX solutions allowed a 15-min window for the print corresponding to the gelation time of the two bioinks present in the syringe. For larger prints or simply for ease of use, the system employed by O'Dwyer *et al.* (2020) could be adapted to this application. They used a double-syringe injection system maintaining each component of the bioink separated until extrusion. Trying to replicate the cylindrical shape previously obtain with the moulds, the printing of 10%-collagen/1%-alginate CLEX hydrogels was successful. Together, this evaluation demonstrated the injectability of our bioink while showcasing the potential of this hydrogel system for bioprinting with for example the evaluation of the biocompatibility of this system with bone cells cultures in 3D (Lee *et al.*, 2012).

Finally, the EV delivery system introduced remains at an very early stage of development. Using the insert-system developed in Figure 6.16., the interaction of MO-EVs to hydrogel networks could be thoroughly investigated. In addition to the release kinetics, the migration of EVs through the hydrogel system could explored through a variety of bioink compositions. Also, harnessing the potential of bioprinting, this concept could be adapted from 2 phases with the current insert to multiple layers, from the core of the scaffold to its periphery. Loading relevant EVs at the different layers of the hydrogel, we could adapt the EV population released from the hydrogel overtime matching the needs of the different stages of bone fracture healing.

## 6.5. Conclusion

In the present Chapter, CLEX gelation was successfully applied to the generation of alginate-collagen composite incorporating MO-EVs. The evaluation of MO-EV release kinetics demonstrated a complex release profile linked to the degradation of the hydrogel releasing other types of nanoparticles. The printability of the CLEX hydrogels was validated offering an injectable bioink well-suited to explore bone repair applications . Finally, an insert was designed to generated hydrogels with a loadable core creating further opportunities to study the behaviour of MO-EVs inside various CLEX hydrogels. Together, these findings showed the development of a promising hydrogel technological platform to deliver MO-EVs.

# Chapter VII

-

# General Conclusion and Future Work

## 7.1 Summary of findings

This project has extensively characterised MO-EVs in line with the MISEV guidelines to offer a standardised approach allowing to provide robust and reproducible data. Focused on a single population of MO-EVs with defined isolation parameters, MO-EVs were successfully isolated using defining differential UC as the method of choice due to specific features of mineralising cultures. MO-EVs' physico-chemical characteristics and morphology aligned with the existing literature. The presence of EV biomarker was comprehensively assessed using a range of state-of-the-art methodologies. In particular, the adaptation of SP-IRIS via the ExoView platform demonstrated the potential of this all-in-one EV characterisation approach. In a pilot study, the benefits of the use of lyophilisation with cryoprotectant was showed inviting researchers to explore storage strategies further. Finally, an extensive compositional analysis provided a unique dataset proving valuable insights into MO-EVs potential mechanism of action. In particular, the abundant presence of proteins such as annexins and collagens associated with the detection of minerals in their cargo advocate for the role of MO-EVs as a driver of biomineralisation in line with current evidence associated with MVs.

After having thoroughly examined MO-EVs, their function was assessed *in vitro* with a focus on their influence of biomineralisation. Evaluated for the first time on MC3T3-E1 osteoblasts, MO-EVs were rapidly uptaken by the cells and were found to be osteoinductive as their treatment (10 µg/mL) significantly enhanced ALP activity, calcium deposition and ECM production in 2D cultures of osteoblasts. To further explore their pro-osteogenic properties, a µ-XRF based method was developed offering a unique new strategy to evaluate the influence of MO-EVs on mineralising osteoblast. This method was applied to a dose-response study on early biomineralisation and revealed that MO-EVs were modulating biomineralisation in a time and concentration dependent manner by increased mineral coverage and the degree of maturity of the mineral produced in the culture. Developing a standardised approach to identify the Ca/P ratio of *in vitro* ECM, this technique showed encouraging capabilities to be used in a variety of applications and to develop the non-destructive assessment of mineral production in *in vitro* settings.

Based on the body of evidence combining the characterisation and functional evaluation of MO-EVs, the development of synthetic MO-EVs was successfully performed. Generated *via* serial extrusion, MO-NVs were directly compared to MO-EVs and shared key structural features and similar biocompatibility profile. Obtained for the first time from osteoblasts, NVs were found able to be characterised via SP-IRIS, thus, further extending the potential of this characterisation platform to synthetic EVs. Nevertheless, MO-NVs did not exhibit any pro-osteogenic potency, therefore, requiring further investigations to modulate their composition for therapeutic purposes. Allowing a better control over their composition, EV-sized proteoliposomes harboring annexin VI and ALP were successfully manufactured. After their characterisation showing incorporation efficiency >30%, a flow cytometry assessment was performed for the first time to obtain single-particle resolution and showed the need for more robust approaches to fully characterise synthetic EVs. Moreover, the comparative biomineralisation study highlighted the variability of osteoblast cell line models, requiring further investigations to conclude on the influence of ALP and annexin VI on biomineralisation.

Finally, to prepare MO-EVs and their mimetics to their potential clinical use, a hydrogel-based delivery system was developed harnessing the potential of CLEX gelation to create an injectable bioink. Based on an alginate-collagen composite formulation, the feasibility of the incorporation of both collagen and MO-EVs to an alginate-CLEX bioink was reported. Furthermore, the evaluation of the release kinetics of MO-EVs from the hydrogel-system demonstrated the heterogeneity of the nature of the nanoparticles that can be released from such system requiring the use of specialised methods such as nano flow cytometry and EV-specific ELISA. Data provided indicated a burst release of nanoparticles from the hydrogels themselves whereas MO-EV release appeared to start only after 3 days. However, further characterisation is required to evaluate their release kinetics for longer timepoints.

## 7.2. Future work

Based on the current knowledge on MO-EVs, immediate future work should be focused on the determination of the difference between secreted vesicles and matrix vesicles. To achieve this distinction, the binding affinity of MVs to ECM and the presence of well-known enriched surface markers present at the surface of these particles could be employed. Obtaining these two separate populations of nanovesicles would allow key mechanistic studies *in vitro* to finally shed the light on a question that has divided the research community for over half a century.

This project has solely focused on the study of osteoblast-derived EVs, however, there is great potential in comparing the activity of EVs sourced from a variety of bone cells to either explore the potential effects of combination treatments or to use co-culture models. Additionally, biomineralisation being a relatively slow physiological phenomenon, the influence of time on the secreted EV population could be a promising focus as osteoblasts might release various population of EVs upon the maturity of the mineral phase. Moreover, the evaluation of the effects of MO-EVs should not be limited to osteoblasts themselves. As bone repair is driven by a multitude of coordinated events such as peripheral nerve repair, vascularisation or inflammation, there is tremendous potential of probing the effects of osteoblast-derived EVs on other cell types to understand potential multitargeting effects of these vesicles.

Having developed the µ-XRF method for the sole purpose for exploring the effects of MO-EVs on biomineralisation, there is a great need to explore the applications of this methods to others fields. In this work, Ca, P and S elements were selected for their relevance in mineralisation, however, XRF provide with greater possibilities looking at a multitude of elements at once such Mg or K.

Regarding cell-derived nanovesicles, the stimulation of the parental osteoblasts would be an interesting approach to augment their therapeutic potency. Moreover, there is a strong incentive to load exogenous molecules within NVs as the extrusion process offers a great opportunity for simple cargo loading during the self-assembly process. Importantly, there is great need for an extensive multi-OMICs analysis investigating the difference of composition between NVs and EVs.

Proteoliposomes investigations should remain focused on improving existing characterisation methods. Limited by the biological complexity achievable in these current models, the development of proteoliposomes should mainly be perceived as a technology allowing to isolate single features of EVs to determine their mechanism of action. Fusogenic liposomes, hybrid particles resulting from the fusion of EVs and liposomes, has recently been developed and could be applied to proteoliposomes research to modulate the protein composition of EVs.

## 7.3. General Conclusion

The overall aim of this thesis was to investigate the potential of MO-EVs as an innovative therapeutic solution for bone repair. To that end, the extensive characterisation and functional assessment of MO-EVs demonstrated their potential as a novel acellular therapy augmenting the osteoinductive properties of osteoblasts. Using bioengineering strategies, MO-EV biomimetics were investigated for the first time with the successful development of MO-NVs and bioinspired proteoliposomes offering a stepping stone towards the clinical translation of EV-based therapeutics for bone repair. Finally, in an attempt to create a hydrogel MO-EV delivery system, an innovative CLEX gelation appraoch was adapted to produce an injectable ECM mimetic hydrogel successfully loaded with MO-EVs offering the technological basis for further investigations.

# Bibliography

The following reference list has been indexed and generated using the reference manager software Mendeley (Mendeley Ltd., UK) in its v 1.19.8.

Alvarez, K., & Nakajima, H. (2009). Metallic Scaffolds for Bone Regeneration. Materials, 2(3), 790. https://doi.org/10.3390/MA2030790

Alvarez, S., Suazo, C., Boltansky, A., Ursu, M., Carvajal, D., Innocenti, G., Vukusich, A., Hurtado, M., Villanueva, S., Carreño, J. E., Rogelio, A., & Irarrazabal, C. E. (2013). Urinary Exosomes as a Source of Kidney Dysfunction Biomarker in Renal Transplantation. Transplantation Proceedings, 45(10), 3719–3723. https://doi.org/10.1016/J.TRANSPROCEED.2013.08.079

Alvarez-Erviti, L., Seow, Y., Yin, H., Betts, C., Lakhal, S., & Wood, M. J. A. (2011). Delivery of siRNA to the mouse brain by systemic injection of targeted exosomes. Nature Biotechnology 2011 29:4, 29(4), 341–345. https://doi.org/10.1038/nbt.1807

Anderson, H. C. (1967). Electron microscopic studies of induced cartilage development and calcification. The Journal of Cell Biology, 35(1), 81–101. https://doi.org/10.1083/JCB.35.1.81

Anderson H. C. (2003). Matrix vesicles and calcification. Current rheumatology reports, 5(3), 222–226. https://doi.org/10.1007/s11926-003-0071-z

Andreu, Z., & Yáñez-Mó, M. (2014). Tetraspanins in extracellular vesicle formation and function. Frontiers in Immunology, 5(SEP), 109543. https://doi.org/10.3389/FIMMU.2014.00442/BIBTEX

Ansari, S., de Wildt, B. W. M., Vis, M. A. M., de Korte, C. E., Ito, K., Hofmann, S., & Yuana, Y. (2021). Matrix Vesicles: Role in Bone Mineralization and Potential Use as Therapeutics. Pharmaceuticals, 14(4), 289. https://doi.org/10.3390/PH14040289

Anselmo, A. C., & Mitragotri, S. (2019). Nanoparticles in the clinic: An update. Bioengineering & Translational Medicine, 4(3). https://doi.org/10.1002/BTM2.10143

Bachurski, D., Schuldner, M., Nguyen, P. H., Malz, A., Reiners, K. S., Grenzi, P. C., Babatz, F., Schauss, A. C., Hansen, H. P., Hallek, M., & Pogge von Strandmann, E. (2019). Extracellular vesicle measurements with nanoparticle tracking analysis - An accuracy and repeatability comparison between NanoSight NS300 and ZetaView. Journal of Extracellular Vesicles, 8(1). https://doi.org/10.1080/20013078.2019.1596016

Baghban, N., Kodam, S. P., & Ullah, M. (2023). Role of CD9 Sensing, AI, and Exosomes in Cellular Communication of Cancer. International Journal of Stem Cell Research and Therapy, 10(1). https://doi.org/10.23937/2469-570X/1410079

Bahraminasab, M., Talebi, A., Doostmohammadi, N., Arab, S., Ghanbari, A., & Zarbakhsh, S. (2022). The healing of bone defects by cell-free and stem cell-seeded 3D-printed PLA tissue-engineered scaffolds. Journal of Orthopaedic Surgery and Research, 17(1), 1–17. https://doi.org/10.1186/S13018-022-03213-2/TABLES/2

Baht, G. S., Vi, L., & Alman, B. A. (2018). The Role of the Immune Cells in Fracture Healing. Current osteoporosis reports, 16(2), 138–145. https://doi.org/10.1007/s11914-018-0423-2

Bai, X., Gao, M., Syed, S., Zhuang, J., Xu, X., & Zhang, X. Q. (2018). Bioactive hydrogels for bone regeneration. Bioactive Materials, 3(4), 401–417. https://doi.org/10.1016/J.BIOACTMAT.2018.05.006

Balcerzak, M., Malinowska, A., Thouverey, C., Sekrecka, A., Dadlez, M., Buchet, R., & Pikula, S. (2008). Proteome analysis of matrix vesicles isolated from femurs of chicken embryo. Proteomics, 8(1), 192–205. https://doi.org/10.1002/PMIC.200700612

Bassett, D. C., Håti, A. G., Melø, T. B., Stokke, B. T., & Sikorski, P. (2013). Competitive ligand exchange of crosslinking ions for ionotropic hydrogel formation. J. Name, 00, 1–3. https://doi.org/10.1039/C6TB01812B

Bella, E. Della, Buetti-Dinh, A., Licandro, G., Ahmad, P., Basoli, V., Alini, M., & Stoddart, M. J. (2021). Dexamethasone induces changes in osteogenic differentiation of human mesenchymal stromal cells via sox9 and pparg, but not runx2. International Journal of Molecular Sciences, 22(9). https://doi.org/10.3390/IJMS22094785/S1

Bolean, M., Borin, I. A., Simão, A. M. S., Bottini, M., Bagatolli, L. A., Hoylaerts, M. F., Millán, J. L., & Ciancaglini, P. (2017). Topographic analysis by atomic force microscopy of proteoliposomes matrix vesicle mimetics harboring TNAP and AnxA5. Biochimica et Biophysica Acta. Biomembranes, 1859(10), 1911–1920. https://doi.org/10.1016/J.BBAMEM.2017.05.010

Bonewald L. F. (2011). The amazing osteocyte. Journal of bone and mineral research : the official journal of the American Society for Bone and Mineral Research, 26(2), 229–238. https://doi.org/10.1002/jbmr.320

Bonucci, E. (1967). Fine structure of early cartilage calcification. Journal of Ultrastructure Research, 20(1), 33–50. https://doi.org/10.1016/S0022-5320(67)80034-0

Boonrungsiman, S., Gentleman, E., Carzaniga, R., Evans, N. D., McComb, D. W., Porter, A. E., & Stevens, M. M. (2012). The role of intracellular calcium phosphate in osteoblast-mediated bone apatite formation. Proceedings of the National Academy of Sciences of the United States of America, 109(35), 14170–14175. https://doi.org/10.1073/PNAS.1208916109/-/DCSUPPLEMENTAL/SM01.MOV

Borjesson, J., Barregard, L., Sallsten, G., Schutz, A., Jonson, R., Alpsten, M., & Mattsson, S. (1995). In vivo XRF analysis of mercury: the relation between concentrations in the kidney and the urine. Physics in Medicine & Biology, 40(3), 413. https://doi.org/10.1088/0031-9155/40/3/006

Bosch, S., De Beaurepaire, L., Allard, M., Mosser, M., Heichette, C., Chrétien, D., Jegou, D., & Bach, J. M. (2016). Trehalose prevents aggregation of exosomes and cryodamage. Scientific Reports, 6. https://doi.org/10.1038/SREP36162

Bottini, M., Mebarek, S., Anderson, K. L., Strzelecka-Kiliszek, A., Bozycki, L., Simão, A. M. S., Bolean, M., Ciancaglini, P., Pikula, J. B., Pikula, S., Magne, D., Volkmann, N., Hanein, D., Millán, J. L., & Buchet, R. (2017). Matrix vesicles from chondrocytes and osteoblasts: Their biogenesis, properties, functions and biomimetic models. Biochimica et Biophysica Acta. General Subjects, 1862(3), 532–546. https://doi.org/10.1016/J.BBAGEN.2017.11.005

Boyan, B. D., Asmussen, N. C., Lin, Z., & Schwartz, Z. (2022). The Role of Matrix-Bound Extracellular Vesicles in the Regulation of Endochondral Bone Formation. Cells 2022, Vol. 11, Page 1619, 11(10), 1619. https://doi.org/10.3390/CELLS11101619

Brambilla, D., Sola, L., Ferretti, A. M., Chiodi, E., Zarovni, N., Fortunato, D., Criscuoli, M., Dolo, V., Giusti, I., Murdica, V., Kluszczyńska, K., Czernek, L., Düchler, M., Vago, R., & Chiari, M. (2021). EV Separation: Release of Intact Extracellular Vesicles Immunocaptured on Magnetic Particles. Analytical Chemistry, 93(13), 5476–5483. https://doi.org/10.1021/

Brisson, A. R., Tan, S., Linares, R., Gounou, C., & Arraud, N. (2017). Extracellular vesicles from activated platelets: a semiquantitative cryo-electron microscopy and immuno-gold labeling study. Platelets, 28(3), 263–271. https://doi.org/10.1080/09537104.2016.1268255

Brunner, J. D., & Schenck, S. (2019). Preparation of Proteoliposomes with Purified TMEM16 Protein for Accurate Measures of Lipid Scramblase Activity. Methods in Molecular Biology, 1949, 181–199. https://doi.org/10.1007/978-1-4939-9136-5_14

Burnouf, T., Agrahari, V., & Agrahari, V. (2019). Extracellular Vesicles As Nanomedicine: Hopes And Hurdles In Clinical Translation. International Journal of Nanomedicine, 14, 8847–8859. https://doi.org/10.2147/IJN.S225453

Buzas, E. I. (2022). The roles of extracellular vesicles in the immune system. Nature Reviews Immunology 2022 23:4, 23(4), 236–250. https://doi.org/10.1038/s41577-022-00763-8

Buzas, E. I. (2023). The roles of extracellular vesicles in the immune system. Nature Reviews. Immunology, 23(4), 236–250. https://doi.org/10.1038/S41577-022-00763-8

Buzás, E. I., Tóth, E., Sódar, B. W., & Szabó-Taylor, K. (2018). Molecular interactions at the surface of extracellular vesicles. Seminars in Immunopathology 2018 40:5, 40(5), 453–464. https://doi.org/10.1007/S00281-018-0682-0

Cai, H., Yang, X., Gao, Y., Xu, Z., Yu, B., Xu, T., Li, X., Xu, W., Wang, X., & Hua, L. (2019). Exosomal MicroRNA-9-3p Secreted from BMSCs Downregulates ESM1 to Suppress the Development of Bladder Cancer. Molecular Therapy. Nucleic Acids, 18, 787. https://doi.org/10.1016/J.OMTN.2019.09.023

Cao, Z., Qin, Z., Duns, G. J., Huang, Z., Chen, Y., Wang, S., Deng, R., Nie, L., & Luo, X. (2024). Repair of Infected Bone Defects with Hydrogel Materials. Polymers 2024, Vol. 16, Page 281, 16(2), 281. https://doi.org/10.3390/POLYM16020281

Cappariello, A., Loftus, A., Muraca, M., Maurizi, A., Rucci, N., & Teti, A. (2018). Osteoblast-Derived Extracellular Vesicles Are Biological Tools for the Delivery of Active Molecules to Bone. Journal of Bone and Mineral Research, 33(3), 517–533. https://doi.org/10.1002/JBMR.3332

Cappariello, A., Loftus, A., Muraca, M., Maurizi, A., Rucci, N., & Teti, A. (2018). Osteoblast-Derived Extracellular Vesicles Are Biological Tools for the Delivery of Active Molecules to Bone. Journal of Bone and Mineral Research : The Official Journal of the American Society for Bone and Mineral Research, 33(3), 517–533. https://doi.org/10.1002/JBMR.3332

Capulli, M., Paone, R., & Rucci, N. (2014). Osteoblast and osteocyte: games without frontiers. Archives of biochemistry and biophysics, 561, 3–12. https://doi.org/10.1016/j.abb.2014.05.003

Che, Y., Shi, X., Shi, Y., Jiang, X., Ai, Q., Shi, Y., Gong, F., & Jiang, W. (2019). Exosomes Derived from miR-143-Overexpressing MSCs Inhibit Cell Migration and Invasion in Human Prostate Cancer by Downregulating TFF3. Molecular Therapy. Nucleic Acids, 18, 232–244. https://doi.org/10.1016/J.OMTN.2019.08.010

Chen, Y., Feng, Y., Deveaux, J. G., Masoud, M. A., Chandra, F. S., Chen, H., Zhang, D., & Feng, L. (2019). Biomineralization Forming Process and Bio-inspired Nanomaterials for Biomedical Application: A Review. Minerals 2019, Vol. 9, Page 68, 9(2), 68. https://doi.org/10.3390/MIN9020068

Chertok, B., Moffat, B. A., David, A. E., Yu, F., Bergemann, C., Ross, B. D., & Yang, V. C. (2008). Iron oxide nanoparticles as a drug delivery vehicle for MRI monitored magnetic targeting of brain tumors. Biomaterials, 29(4), 487–496. https://doi.org/10.1016/

Chiang, C. Y., & Chen, C. (2019). Toward characterizing extracellular vesicles at a single-particle level Tse-Hua Tan. Journal of Biomedical Science, 26(1), 1–10. https://doi.org/10.1186/S12929-019-0502-4/FIGURES/1

Chistiakov, D. A., Myasoedova, V. A., Melnichenko, A. A., Grechko, A. V., & Orekhov, A. N. (2017). Calcifying Matrix Vesicles and Atherosclerosis. BioMed Research International, 2017. https://doi.org/10.1155/2017/7463590

Chhoy, P., Brown, C. W., Amante, J. J., & Mercurio, A. M. (2021). Protocol for the separation of extracellular vesicles by ultracentrifugation from in vitro cell culture models. STAR protocols, 2(1), 100303. https://doi.org/10.1016/j.xpro.2021.100303

Chuo, S. T. Y., Chien, J. C. Y., & Lai, C. P. K. (2018). Imaging extracellular vesicles: Current and emerging methods. Journal of Biomedical Science, 25(1), 1–10. https://doi.org/10.1186/S12929-018-0494-5/

Ciancaglini, P., Simão, A. M. S., Bolean, M., Millán, J. L., Rigos, C. F., Yoneda, J. S., Colhone, M. C., & Stabeli, R. G. (2012). Proteoliposomes in nanobiotechnology. Biophysical Reviews, 4(1), 67. https://doi.org/10.1007/S12551-011-0065-4

Ciancaglini, P., Yadav, M. C., Simão, A. M. S., Narisawa, S., Pizauro, J. M., Farquharson, C., Hoylaerts, M. F., & Millán, J. L. (2010). Kinetic Analysis of Substrate Utilization by Native and TNAP-, NPP1-, or PHOSPHO1-Deficient Matrix Vesicles. Journal of Bone and Mineral Research, 25(4), 716. https://doi.org/10.1359/JBMR.091023

Cieza, A., Causey, K., Kamenov, K., Hanson, S. W., Chatterji, S., & Vos, T. (2021). Global estimates of the need for rehabilitation based on the Global Burden of Disease study 2019: a systematic analysis for the Global Burden of Disease Study 2019. Lancet (London, England), 396(10267), 2006–2017. https://doi.org/10.1016/S0140-6736(20)32340-0

Clarke, B. (2008). Normal bone anatomy and physiology. Clinical Journal of the American Society of Nephrology : CJASN, 3 Suppl 3(Suppl 3). https://doi.org/10.2215/CJN.04151206

Clos-Sansalvador, M., Monguió-Tortajada, M., Roura, S., Franquesa, M., & Borràs, F. E. (2022). Commonly used methods for extracellular vesicles’ enrichment: Implications in downstream analyses and use. European Journal of Cell Biology, 101(3), 151227. https://doi.org/10.1016/J.EJCB.2022.151227

Cmoch, A., Strzelecka-Kiliszek, A., Palczewska, M., Groves, P., & Pikula, S. (2011). Matrix vesicles isolated from mineralization-competent Saos-2 cells are selectively enriched with annexins and S100 proteins. Biochemical and Biophysical Research Communications, 412(4), 683–687. https://doi.org/10.1016/J.BBRC.2011.08.025

Cong, B., Sun, T., Zhao, Y., & Chen, M. (2023). Current and Novel Therapeutics for Articular Cartilage Repair and Regeneration. Therapeutics and Clinical Risk Management, 19, 485. https://doi.org/10.2147/TCRM.S410277

Console, L., Tolomeo, M., Colella, M., Barile, M., & Indiveri, C. (2019). Reconstitution in Proteoliposomes of the Recombinant Human Riboflavin Transporter 2 (SLC52A2) Overexpressed in E. coli. International Journal of Molecular Sciences 2019, Vol. 20, Page 4416, 20(18), 4416. https://doi.org/10.3390/IJMS20184416

Crasto, G. J., Kartner, N., Reznik, N., Spatafora, M. V., Chen, H., Williams, R., Burns, P. N., Clokie, C., Manolson, M. F., & Peel, S. A. F. (2016). Controlled bone formation using ultrasound-triggered release of BMP-2 from liposomes. Journal of Controlled Release, 243, 99–108. https://doi.org/10.1016/J.JCONREL.2016.09.032

Cross, J., Rai, A., Fang, H., Claridge, B., & Greening, D. W. (2023). Rapid and in-depth proteomic profiling of small extracellular vesicles for ultralow samples. PROTEOMICS, 2300211. https://doi.org/10.1002/PMIC.202300211

Croucher, P. I., McDonald, M. M., & Martin, T. J. (2016). Bone metastasis: the importance of the neighbourhood. Nature Reviews Cancer 2016 16:6, 16(6), 373–386. https://doi.org/10.1038/nrc.2016.44

Cui, L., Houston, D. A., Farquharson, C., & MacRae, V. E. (2016). Characterisation of matrix vesicles in skeletal and soft tissue mineralisation. Bone, 87, 147–158. https://doi.org/10.1016/J.BONE.2016.04.007

Cui, Z. K., Kim, S., Baljon, J. J., Doroudgar, M., Lafleur, M., Wu, B. M., Aghaloo, T., & Lee, M. (2017). Design and Characterization of a Therapeutic Non-Phospholipid Liposomal Nanocarrier with Osteoinductive Characteristics to Promote Bone Formation. ACS Nano, 11(8), 8055. https://doi.org/10.1021/ACSNANO.7B02702

Danaei, M., Dehghankhold, M., Ataei, S., Hasanzadeh Davarani, F., Javanmard, R., Dokhani, A., Khorasani, S., & Mozafari, M. R. (2018). Impact of Particle Size and Polydispersity Index on the Clinical Applications of Lipidic Nanocarrier Systems. Pharmaceutics, 10(2), 57. https://doi.org/10.3390/pharmaceutics10020057

Datta, H. K., Ng, W. F., Walker, J. A., Tuck, S. P., & Varanasi, S. S. (2008). The cell biology of bone metabolism. Journal of clinical pathology, 61(5), 577–587. https://doi.org/10.1136/jcp.2007.048868

Davies, O. G., Cox, S. C., Williams, R. L., Tsaroucha, D., Dorrepaal, R. M., Lewis, M. P., & Grover, L. M. (2017). Annexin-enriched osteoblast-derived vesicles act as an extracellular site of mineral nucleation within developing stem cell cultures. Scientific Reports 2017 7:1, 7(1), 1–13. https://doi.org/10.1038/s41598-017-13027-6

Davies, O. G. (2023). Extracellular vesicles: From bone development to regenerative orthopedics. Molecular Therapy, 31(5), 1251–1274. https://doi.org/10.1016/J.YMTHE.2023.02.021

de Jong, O. G., van Balkom, B. W. M., Schiffelers, R. M., Bouten, C. V. C., & Verhaar, M. C. (2014). Extracellular Vesicles: Potential Roles in Regenerative Medicine. Frontiers in Immunology, 5(DEC). https://doi.org/10.3389/FIMMU.2014.00608

Delaisse, J. M., Andersen, T. L., Kristensen, H. B., Jensen, P. R., Andreasen, C. M., & Søe, K. (2020). Re-thinking the bone remodeling cycle mechanism and the origin of bone loss. Bone, 141, 115628. https://doi.org/10.1016/j.bone.2020.115628

De Sousa, K. P., Rossi, I., Abdullahi, M., Ramirez, M. I., Stratton, D., & Inal, J. M. (2023). Isolation and characterization of extracellular vesicles and future directions in diagnosis and therapy. Wiley Interdisciplinary Reviews. Nanomedicine and Nanobiotechnology, 15(1). https://doi.org/10.1002/WNAN.1835

Deng, L., Wang, Y., Peng, Y., Wu, Y., Ding, Y., Jiang, Y., Shen, Z., & Fu, Q. (2015). Osteoblast-derived microvesicles: A novel mechanism for communication between osteoblasts and osteoclasts. Bone, 79, 37–42. https://doi.org/10.1016/J.BONE.2015.05.022

Deville, S., Berckmans, P., Van Hoof, R., Lambrichts, I., Salvati, A., & Nelissen, I. (2021). Comparison of extracellular vesicle isolation and storage methods using high-sensitivity flow cytometry. PLOS ONE, 16(2), e0245835. https://doi.org/10.1371/JOURNAL.PONE.0245835

Di Maggio, N., & Banfi, A. (2022). The osteo-angiogenic signaling crosstalk for bone regeneration: harmony out of complexity. Current opinion in biotechnology, 76, 102750. https://doi.org/10.1016/j.copbio.2022.102750

Ding, Q., Zhang, S., Liu, X., Zhao, Y., Yang, J., Chai, G., Wang, N., Ma, S., Liu, W., & Ding, C. (2023). Hydrogel Tissue Bioengineered Scaffolds in Bone Repair: A Review. Molecules 2023, Vol. 28, Page 7039, 28(20), 7039. https://doi.org/10.3390/MOLECULES28207039

Dixon, D. T., & Gomillion, C. T. (2021). Conductive Scaffolds for Bone Tissue Engineering: Current State and Future Outlook. Journal of Functional Biomaterials 2022, Vol. 13, Page 1, 13(1), 1. https://doi.org/10.3390/JFB13010001

Doyle, A. D. (2018). Fluorescent Labeling of Rat-tail Collagen for 3D Fluorescence Imaging. Bio-Protocol, 8(13). https://doi.org/10.21769/BIOPROTOC.2919

Doyle, L. M., & Wang, M. Z. (2019). Overview of Extracellular Vesicles, Their Origin, Composition, Purpose, and Methods for Exosome Isolation and Analysis. Cells, 8(7), 727. https://doi.org/10.3390/CELLS8070727

Du, S., Guan, Y., Xie, A., Yan, Z., Gao, S., Li, W., Rao, L., Chen, X., & Chen, T. (2023). Extracellular vesicles: a rising star for therapeutics and drug delivery. Journal of Nanobiotechnology 2023 21:1, 21(1), 1–51. https://doi.org/10.1186/S12951-023-01973-5

Eichholz, K. F., Woods, I., Riffault, M., Johnson, G. P., Corrigan, M., Lowry, M. C., Shen, N., Labour, M. N., Wynne, K., O'Driscoll, L., & Hoey, D. A. (2020). Human bone marrow stem/stromal cell osteogenesis is regulated via mechanically activated osteocyte-derived extracellular vesicles. Stem Cells Translational Medicine, 9(11), 1431–1447. https://doi.org/10.1002/SCTM.19-0405

El Baradie, K. B. Y., Nouh, M., O'Brien, F., Liu, Y., Fulzele, S., Eroglu, A., & Hamrick, M. W. (2020). Freeze-Dried Extracellular Vesicles From Adipose-Derived Stem Cells Prevent Hypoxia-Induced Muscle Cell Injury. Frontiers in Cell and Developmental Biology, 8, 181. https://doi.org/10.3389/FCELL.2020.00181/BIBTEX

Elkhoury, K., Chen, M., Koçak, P., Enciso-Martínez, E., Bassous, N. J., Lee, M. C., Byambaa, B., Rezaei, Z., Li, Y., Ubina López, M. E., Gurian, M., Sobahi, N., Hussain, M. A., Sanchez-Gonzalez, L., Leijten, J., Hassan, S., Arab-Tehrany, E., Ward, J. E., & Shin, S. R. (2022). Hybrid extracellular vesicles-liposome incorporated advanced bioink to deliver microRNA. Biofabrication, 14(4). https://doi.org/10.1088/1758-5090/AC8621

Enrich, C., Lu, A., Tebar, F., Rentero, C., & Grewal, T. (2022). Annexins Bridging the Gap: Novel Roles in Membrane Contact Site Formation. Frontiers in Cell and Developmental Biology, 9, 797949. https://doi.org/10.3389/FCELL.2021.797949/BIBTEX

Eriksen E. F. (1986). Normal and pathological remodeling of human trabecular bone: three dimensional reconstruction of the remodeling sequence in normals and in metabolic bone disease. Endocrine reviews, 7(4), 379–408. https://doi.org/10.1210/edrv-7-4-379

Erwin, N., Serafim, M. F., & He, M. (2023). Enhancing the Cellular Production of Extracellular Vesicles for Developing Therapeutic Applications. Pharmaceutical Research, 40(4), 833. https://doi.org/10.1007/S11095-022-03420-W

Fan, L., Ren, Y., Emmert, S., Vučković, I., Stojanovic, S., Najman, S., Schnettler, R., Barbeck, M., Schenke-Layland, K., & Xiong, X. (2023). The Use of Collagen-Based Materials in Bone Tissue Engineering. International Journal of Molecular Sciences, 24(4). https://doi.org/10.3390/IJMS24043744

Fang, F., Yang, J., Wang, J., Li, T., Wang, E., Zhang, D., Liu, X., & Zhou, C. (2024). The role and applications of extracellular vesicles in osteoporosis. Bone Research, 12(1). https://doi.org/10.1038/S41413-023-00313-5

Fernando, I. P. S., Lee, W. W., Han, E. J., & Ahn, G. (2020). Alginate-based nanomaterials: Fabrication techniques, properties, and applications. Chemical Engineering Journal, 391, 123823. https://doi.org/10.1016/J.CEJ.2019.123823

Fiori, M. C., Figueroa, V., Zoghbi, M. E., Saéz, J. C., Reuss, L., & Altenberg, G. A. (2012). Permeation of calcium through purified connexin 26 hemichannels. The Journal of Biological Chemistry, 287(48), 40826–40834. https://doi.org/10.1074/JBC.M112.383281

Florencio-Silva, R., Sasso, G. R. D. S., Sasso-Cerri, E., Simões, M. J., & Cerri, P. S. (2015). Biology of Bone Tissue: Structure, Function, and Factors That Influence Bone Cells. BioMed Research International, 2015. https://doi.org/10.1155/2015/421746

Frade, B. B., Dias, R. B., Piperni, S. G., & Bonfim, D. C. (2023). The role of macrophages in fracture healing: a narrative review of the recent updates and therapeutic perspectives. Stem Cell Investigation, 10, 4–4. https://doi.org/10.21037/SCI-2022-038

Franz-Odendaal, T. A., Hall, B. K., & Witten, P. E. (2006). Buried alive: how osteoblasts become osteocytes. Developmental dynamics : an official publication of the American Association of Anatomists, 235(1), 176–190. https://doi.org/10.1002/dvdy.20603

Garcés-Ortíz, M., Ledesma-Montes, C., & Reyes-Gasga, J. (2013). Presence of matrix vesicles in the body of odontoblasts and in the inner third of dentinal tissue: a scanning electron microscopic study. Medicina Oral, Patologia Oral y Cirugia Bucal, 18(3). https://doi.org/10.4317/MEDORAL.18650

Garcia, S. G., Clos-Sansalvador, M., Sanroque-Muñoz, M., Pan, L., & Franquesa, M. (2024). Functional and potency assays for mesenchymal stromal cell–extracellular vesicles in kidney disease. Current Opinion in Physiology, 38, 100746. https://doi.org/10.1016/J.COPHYS.2024.100746

García-Manrique, P., Gutiérrez, G., & Blanco-López, M. C. (2018). Fully Artificial Exosomes: Towards New Theranostic Biomaterials. Trends in Biotechnology, 36(1), 10–14. https://doi.org/10.1016/J.TIBTECH.2017.10.005

García-Romero, N., Madurga, R., Rackov, G., Palacín-Aliana, I., Núñez-Torres, R., Asensi-Puig, A., Carrión-Navarro, J., Esteban-Rubio, S., Peinado, H., González-Neira, A., González-Rumayor, V., Belda-Iniesta, C., & Ayuso-Sacido, A. (2019). Polyethylene glycol improves current methods for circulating extracellular vesicle-derived DNA isolation. Journal of Translational Medicine, 17(1). https://doi.org/10.1186/S12967-019-1825-3

Ge, M., Ke, R., Cai, T., Yang, J., & Mu, X. (2015). Identification and proteomic analysis of osteoblast-derived exosomes. Biochemical and Biophysical Research Communications, 467(1), 27–32. https://doi.org/10.1016/J.BBRC.2015.09.135

Ge, M., Wu, Y., Ke, R., Cai, T., Yang, J., & Mu, X. (2017). Value of Osteoblast-Derived Exosomes in Bone Diseases. The Journal of Craniofacial Surgery, 28(4), 866–870. https://doi.org/10.1097/SCS.0000000000003463

Genge, B. R., Wu, L. N. Y., & Wuthier, R. E. (2007). In Vitro Modeling of Matrix Vesicle Nucleation: SYNERGISTIC STIMULATION OF MINERAL FORMATION BY ANNEXIN A5 AND PHOSPHATIDYLSERINE. Journal of Biological Chemistry, 282(36), 26035–26045. https://doi.org/10.1074/JBC.M701057200

Gerke, V., & Moss, S. E. (2002). Annexins: from structure to function. Physiological Reviews, 82(2), 331–371. https://doi.org/10.1152/PHYSREV.00030.2001

Gkioni, K., Leeuwenburgh, S. C. G., Douglas, T. E. L., Mikos, A. G., & Jansen, J. A. (2010). Mineralization of hydrogels for bone regeneration. Tissue Engineering. Part B, Reviews, 16(6), 577–585. https://doi.org/10.1089/TEN.TEB.2010.0462

Goh, W. J., Zou, S., Ong, W. Y., Torta, F., Alexandra, A. F., Schiffelers, R. M., Storm, G., Wang, J. W., Czarny, B., & Pastorin, G. (2017). Bioinspired Cell-Derived Nanovesicles versus Exosomes as Drug Delivery Systems: a Cost-Effective Alternative. Scientific Reports 2017 7:1, 7(1), 1–10. https://doi.org/10.1038/s41598-017-14725-x

Ghodasara, A., Raza, A., Wolfram, J., Salomon, C., & Popat, A. (2023). Clinical Translation of Extracellular Vesicles. Advanced healthcare materials, 12(28), e2301010. https://doi.org/10.1002/adhm.202301010

Görgens, A., Corso, G., Hagey, D. W., Jawad Wiklander, R., Gustafsson, M. O., Felldin, U., Lee, Y., Bostancioglu, R. B., Sork, H., Liang, X., Zheng, W., Mohammad, D. K., van de Wakker, S. I., Vader, P., Zickler, A. M., Mamand, D. R., Ma, L., Holme, M. N., Stevens, M. M., … EL Andaloussi, S. (2022). Identification of storage conditions stabilizing extracellular vesicles preparations. Journal of Extracellular Vesicles, 11(6), 11. https://doi.org/10.1002/JEV2.12238

Gregoriadis, G. (2016). Liposomes in Drug Delivery: How It All Happened. Pharmaceutics, 8(2). https://doi.org/10.3390/PHARMACEUTICS8020019

Groß, R., Reßin, H., von Maltitz, P., Albers, D., Schneider, L., Bley, H., Hoffmann, M., Cortese, M., Gupta, D., Deniz, M., Choi, J.-Y., Jansen, J., Preußer, C., Seehafer, K., Pöhlmann, S., Voelker, D. R., Goffinet, C., Pogge-von Strandmann, E., Bunz, U., … Müller, J. A. (2024). Phosphatidylserine-exposing extracellular vesicles in body fluids are an innate defence against apoptotic mimicry viral pathogens. Nature Microbiology 2024 9:4, 9(4), 905–921. https://doi.org/10.1038/s41564-024-01637-6

Gul, B., Syed, F., Khan, S., Iqbal, A., & Ahmad, I. (2022). Characterization of extracellular vesicles by flow cytometry: Challenges and promises. Micron, 161, 103341. https://doi.org/10.1016/J.MICRON.2022.103341

Hao, D., Lu, L., Song, H., Duan, Y., Chen, J., Carney, R., Li, J. J., Zhou, P., Nolta, J., Lam, K. S., Leach, J. K., Farmer, D. L., Panitch, A., & Wang, A. (2022). Engineered extracellular vesicles with high collagen-binding affinity present superior in situ retention and therapeutic efficacy in tissue repair. Theranostics, 12(13), 6021–6037. https://doi.org/10.7150/thno.70448

Håti, A. G., Bassett, D. C., Ribe, J. M., Sikorski, P., Weitz, D. A., & Stokke, B. T. (2016). Versatile, cell and chip friendly method to gel alginate in microfluidic devices. Lab on a chip, 16(19), 3718–3727. https://doi.org/10.1039/c6lc00769d

Henderson, S. W., Nakayama, Y., Whitelaw, M. L., Bruning, J. B., Anderson, P. A., Tyerman, S. D., Ramesh, S. A., Martinac, B., & Yool, A. J. (2023). Proteoliposomes reconstituted with human aquaporin-1 reveal novel single-ion-channel properties. https://doi.org/10.1016/j.bpr.2023.100100

Herrmann, I. K., Wood, M. J. A., & Fuhrmann, G. (2021). Extracellular vesicles as a next-generation drug delivery platform. Nature Nanotechnology 2021 16:7, 16(7), 748–759. https://doi.org/10.1038/s41565-021-00931-2

Herrmann, M., Diederichs, S., Melnik, S., Riegger, J., Trivanović, D., Li, S., Jenei-Lanzl, Z., Brenner, R. E., Huber-Lang, M., Zaucke, F., Schildberg, F. A., & Grässel, S. (2020). Extracellular Vesicles in Musculoskeletal Pathologies and Regeneration. Frontiers in Bioengineering and Biotechnology, 8, 624096. https://doi.org/10.3389/FBIOE.2020.624096

Hessle, L., Johnson, K. A., Anderson, H. C., Narisawa, S., Sali, A., Goding, J. W., Terkeltaub, R., & Millán, J. L. (2002). Tissue-nonspecific alkaline phosphatase and plasma cell membrane glycoprotein-1 are central antagonistic regulators of bone mineralization. Proceedings of the National Academy of Sciences of the United States of America, 99(14), 9445–9449. https://doi.org/10.1073/PNAS.142063399

Hicok, K. C., Thomas, T., Gori, F., Rickard, D. J., Spelsberg, T. C., & Riggs, B. L. (1998). Development and Characterization of Conditionally Immortalized Osteoblast Precursor Cell Lines from Human Bone Marrow Stroma. Journal of Bone and Mineral Research, 13(2), 205–217. https://doi.org/10.1359/JBMR.1998.13.2.205

Holkar, K., Kale, V., Pethe, P., & Ingavle, G. (2024). The symbiotic effect of osteoinductive extracellular vesicles and mineralized microenvironment on osteogenesis. Journal of Biomedical Materials Research. Part A, 112(2), 155–166. https://doi.org/10.1002/JBM.A.37600

Houschyar, K. S., Tapking, C., Borrelli, M. R., Popp, D., Duscher, D., Maan, Z. N., Chelliah, M. P., Li, J., Harati, K., Wallner, C., Rein, S., Pförringer, D., Reumuth, G., Grieb, G., Mouraret, S., Dadras, M., Wagner, J. M., Cha, J. Y., Siemers, F., Lehnhardt, M., … Behr, B. (2019). Wnt Pathway in Bone Repair and Regeneration - What Do We Know So Far. Frontiers in cell and developmental biology, 6, 170. https://doi.org/10.3389/fcell.2018.00170

Hu, H., Dong, L., Bu, Z., Shen, Y., Luo, J., Zhang, H., Zhao, S., Lv, F., & Liu, Z. (2020). miR-23a-3p-abundant small extracellular vesicles released from Gelma/nanoclay hydrogel for cartilage regeneration. Journal of Extracellular Vesicles, 9(1). https://doi.org/10.1080/20013078.2020.1778883

Hu, F., Gao, Q., Liu, J., Chen, W., Zheng, C., Bai, Q., Sun, N., Zhang, W., Zhang, Y., & Lu, T. (2023a). Smart microneedle patches for wound healing and management. Journal of materials chemistry. B, 11(13), 2830–2851. https://doi.org/10.1039/d2tb02596e

Hu, X., Zhang, Z., Wu, H., Yang, S., Zhao, W., Che, L., Wang, Y., Cao, J., Li, K., & Qian, Z. (2023b). Progress in the application of 3D-printed sodium alginate-based hydrogel scaffolds in bone tissue repair. Biomaterials Advances, 152, 213501. https://doi.org/10.1016/J.BIOADV.2023.213501

Huleihel, L., Hussey, G. S., Naranjo, J. D., Zhang, L., Dziki, J. L., Turner, N. J., Stolz, D. B., & Badylak, S. F. (2016). Matrix-bound nanovesicles within ECM bioscaffolds. Science Advances, 2(6). https://doi.org/10.1126/SCIADV.1600502/SUPPL_FILE/1600502_SM.PDF

Hwang, P. W., & Horton, J. A. (2019). Variable osteogenic performance of MC3T3-E1 subclones impacts their utility as models of osteoblast biology. Scientific reports, 9(1), 8299. https://doi.org/10.1038/s41598-019-44575-8

Iijima, K., & Otsuka, H. (2020). Cell Scaffolds for Bone Tissue Engineering. Bioengineering, 7(4), 1–11. https://doi.org/10.3390/BIOENGINEERING7040119

Imai, T., Takahashi, Y., Nishikawa, M., Kato, K., Morishita, M., Yamashita, T., Matsumoto, A., Charoenviriyakul, C., & Takakura, Y. (2015). Macrophage-dependent clearance of systemically administered B16BL6-derived exosomes from the blood circulation in mice. Journal of Extracellular Vesicles, 4(2015), 1–8. https://doi.org/10.3402/JEV.V4.26238

Izu, Y., Ezura, Y., Koch, M., Birk, D. E., & Noda, M. (2016). Collagens VI and XII form complexes mediating osteoblast interactions during osteogenesis. Cell and Tissue Research, 364(3), 623–635. https://doi.org/10.1007/S00441-015-2345-Y

Izumiya, M., Haniu, M., Ueda, K., Ishida, H., Ma, C., Ideta, H., Sobajima, A., Ueshiba, K., Uemura, T., Saito, N., & Haniu, H. (2021). Evaluation of mc3t3-e1 cell osteogenesis in different cell culture media. International Journal of Molecular Sciences, 22(14). https://doi.org/10.3390/IJMS22147752/S1

Jacobs, J. J., Skipor, A. K., Patterson, L. M., Hallab, N. J., Paprosky, W. G., Black, J., & Galante, J. O. (1998). Metal release in patients who have had a primary total hip arthroplasty. A prospective, controlled, longitudinal study. The Journal of Bone and Joint Surgery. American Volume, 80(10), 1447–1458. https://doi.org/10.2106/00004623-199810000-00006

Jakobsen, K. R., Paulsen, B. S., Bæk, R., Varming, K., Sorensen, B. S., & Jørgensen, M. M. (2015). Exosomal proteins as potential diagnostic markers in advanced non-small cell lung carcinoma. Journal of Extracellular Vesicles, 4(2015), 1–10. https://doi.org/10.3402/JEV.V4.26659

James, A. W., LaChaud, G., Shen, J., Asatrian, G., Nguyen, V., Zhang, X., Ting, K., & Soo, C. (2016). A Review of the Clinical Side Effects of Bone Morphogenetic Protein-2. Tissue Engineering. Part B, Reviews, 22(4), 284. https://doi.org/10.1089/TEN.TEB.2015.0357

Jang M. (2010). Application of portable X-ray fluorescence (pXRF) for heavy metal analysis of soils in crop fields near abandoned mine sites. Environmental geochemistry and health, 32(3), 207–216. https://doi.org/10.1007/s10653-009-9276-z

Jia, Y., Zhu, Y., Qiu, S., Xu, J., & Chai, Y. (2019). Exosomes secreted by endothelial progenitor cells accelerate bone regeneration during distraction osteogenesis by stimulating angiogenesis. Stem Cell Research and Therapy, 10(1), 1–13. https://doi.org/10.1186/S13287-018-1115-7/FIGURES/10

Jiao, Y., Liu, Y., Du, J., Xu, J., Luo, Z., Liu, Y., & Guo, L. (2024). Advances in the Study of Extracellular Vesicles for Bone Regeneration. International Journal of Molecular Sciences, 25(6), 3480. https://doi.org/10.3390/IJMS25063480

Jilka R. L. (2003). Biology of the basic multicellular unit and the pathophysiology of osteoporosis. Medical and pediatric oncology, 41(3), 182–185. https://doi.org/10.1002/mpo.10334

Johnell, O., & Kanis, J. A. (2006). An estimate of the worldwide prevalence and disability associated with osteoporotic fractures. Osteoporosis International, 17(12), 1726–1733. https://doi.org/10.1007/S00198-006-0172-4/METRICS

Ju, Y., Hu, Y., Yang, P., Xie, X., & Fang, B. (2023). Extracellular vesicle-loaded hydrogels for tissue repair and regeneration. Materials Today Bio, 18. https://doi.org/10.1016/J.MTBIO.2022.100522

Jung, J. H., Back, W., Yoon, J., Han, H., Kang, K. W., Choi, B., Jeong, H., Park, J., Shin, H., Hur, W., Choi, Y., Hong, S., Kim, H. K., Park, Y., & Park, J. H. (2021). Dual size-exclusion chromatography for efficient isolation of extracellular vesicles from bone marrow derived human plasma. Scientific Reports 2021 11:1, 11(1), 1–9. https://doi.org/10.1038/s41598-020-80514-8

Jung, H. H., Kim, J. Y., Lim, J. E., & Im, Y. H. (2020). Cytokine profiling in serum-derived exosomes isolated by different methods. Scientific reports, 10(1), 14069. https://doi.org/10.1038/s41598-020-70584-z

Kaddour, H., Tranquille, M., & Okeoma, C. M. (2021). The Past, the Present, and the Future of the Size Exclusion Chromatography in Extracellular Vesicles Separation. Viruses, 13(11). https://doi.org/10.3390/V13112272

Kalamegam, G., Memic, A., Budd, E., Abbas, M., & Mobasheri, A. (2018). A Comprehensive Review of Stem Cells for Cartilage Regeneration in Osteoarthritis. Advances in Experimental Medicine and Biology, 1089, 23–36. https://doi.org/10.1007/5584_2018_205

Kang, M., Huang, C. C., Lu, Y., Shirazi, S., Gajendrareddy, P., Ravindran, S., & Cooper, L. F. (2020). Bone regeneration is mediated by macrophage extracellular vesicles. Bone, 141. https://doi.org/10.1016/J.BONE.2020.115627

Kangari, P., Talaei-Khozani, T., Razeghian-Jahromi, I., & Razmkhah, M. (2020). Mesenchymal stem cells: amazing remedies for bone and cartilage defects. Stem Cell Research & Therapy 2020 11:1, 11(1), 1–21. https://doi.org/10.1186/S13287-020-02001-1

Karimian, A., Khoshnazar, S. M., Kazemi, T., Asadi, A., & Abdolmaleki, A. (2023). Role of secretomes in cell-free therapeutic strategies in regenerative medicine. Cell and Tissue Banking, 1–16. https://doi.org/10.1007/S10561-023-10073-5/

Kapustin, A. N., Davies, J. D., Reynolds, J. L., McNair, R., Jones, G. T., Sidibe, A., Schurgers, L. J., Skepper, J. N., Proudfoot, D., Mayr, M., & Shanahan, C. M. (2011). Calcium regulates key components of vascular smooth muscle cell-derived matrix vesicles to enhance mineralization. Circulation research, 109(1), e1–e12. https://doi.org/10.1161/CIRCRESAHA.110.238808

Kenkre, J. S., & Bassett, J. H. D. (2018). The bone remodelling cycle. Annals of Clinical Biochemistry, 55(3), 308–327. https://doi.org/10.1177/0004563218759371

Kong, H. J., Kaigler, D., Kim, K., & Mooney, D. J. (2004). Controlling rigidity and degradation of alginate hydrogels via molecular weight distribution. Biomacromolecules, 5(5), 1720–1727. https://doi.org/10.1021/bm049879r

Koniusz, S., Andrzejewska, A., Muraca, M., Srivastava, A. K., Janowski, M., & Lukomska, B. (2016). Extracellular vesicles in physiology, pathology, and therapy of the immune and central nervous system, with focus on extracellular vesicles derived from mesenchymal stem cells as therapeutic tools. Frontiers in Cellular Neuroscience, 10(MAY), 109. https://doi.org/10.3389/FNCEL.2016.00109/BIBTEX

Konoshenko, M. Y., Lekchnov, E. A., Vlassov, A. V., & Laktionov, P. P. (2018). Isolation of Extracellular Vesicles: General Methodologies and Latest Trends. BioMed Research International, 2018. https://doi.org/10.1155/2018/8545347

Kooijmans, S. A. A., Schiffelers, R. M., Zarovni, N., & Vago, R. (2016). Modulation of tissue tropism and biological activity of exosomes and other extracellular vesicles: New nanotools for cancer treatment. Pharmacological Research, 111, 487–500. https://doi.org/10.1016/J.PHRS.2016.07.006

Kou, P. M., & Babensee, J. E. (2011). Macrophage and dendritic cell phenotypic diversity in the context of biomaterials. Journal of Biomedical Materials Research - Part A, 96 A(1), 239–260. https://doi.org/10.1002/JBM.A.32971

Kumar, M. A., Baba, S. K., Sadida, H. Q., Marzooqi, S. Al, Jerobin, J., Altemani, F. H., Algehainy, N., Alanazi, M. A., Abou-Samra, A. B., Kumar, R., Al-Shabeeb Akil, A. S., Macha, M. A., Mir, R., & Bhat, A. A. (2024). Extracellular vesicles as tools and targets in therapy for diseases. Signal Transduction and Targeted Therapy 2024 9:1, 9(1), 1–41. https://doi.org/10.1038/s41392-024-01735-1

Kusuma, G. D., Barabadi, M., Tan, J. L., Morton, D. A. V., Frith, J. E., & Lim, R. (2018). To Protect and to Preserve: Novel Preservation Strategies for Extracellular Vesicles. Frontiers in Pharmacology, 9, 1199. https://doi.org/10.3389/fphar.2018.01199

Kusuma, G. D., Li, A., Zhu, D., McDonald, H., Inocencio, I. M., Chambers, D. C., Sinclair, K., Fang, H., Greening, D. W., Frith, J. E., & Lim, R. (2022). Effect of 2D and 3D Culture Microenvironments on Mesenchymal Stem Cell-Derived Extracellular Vesicles Potencies. Frontiers in Cell and Developmental Biology, 10, 819726. https://doi.org/10.3389/FCELL.2022.819726/BIBTEX

Lee, K. Y., & Mooney, D. J. (2012). Alginate: properties and biomedical applications. Progress in Polymer Science, 37(1), 106. https://doi.org/10.1016/J.PROGPOLYMSCI.2011.06.003

Lee, S. S., Du, X., Kim, I., & Ferguson, S. J. (2022). Scaffolds for bone-tissue engineering. Matter, 5(9), 2722–2759. https://doi.org/10.1016/J.MATT.2022.06.003

Levent, A., Suero, E. M., Gehrke, T., & Citak, M. (2021). Risk Factors for Aseptic Loosening After Total Knee Arthroplasty with a Rotating-Hinge Implant: A Case-Control Study. The Journal of Bone and Joint Surgery. American Volume, 103(6), 517–523. https://doi.org/10.2106/JBJS.20.00788

Levy, D., Jeyaram, A., Born, L. J., Chang, K. H., Abadchi, S. N., Hsu, A. T. W., Solomon, T., Aranda, A., Stewart, S., He, X., Harmon, J. W., & Jay, S. M. (2023). Impact of storage conditions and duration on function of native and cargo-loaded mesenchymal stromal cell extracellular vesicles. Cytotherapy, 25(5), 502–509. https://doi.org/10.1016/J.JCYT.2022.11.006

Li, Y. F., Arnold, R. J., Tang, H., & Radivojac, P. (2010). The importance of peptide detectability for protein identification, quantification, and experiment design in MS/MS proteomics. Journal of proteome research, 9(12), 6288–6297. https://doi.org/10.1021/pr1005586

Li, M., Fang, F., Sun, M., Zhang, Y., Hu, M., & Zhang, J. (2022). Extracellular vesicles as bioactive nanotherapeutics: An emerging paradigm for regenerative medicine. Theranostics, 12(11), 4879. https://doi.org/10.7150/THNO.72812

Li, Y. J., Wu, J. Y., Liu, J., Xu, W., Qiu, X., Huang, S., Hu, X. Bin, & Xiang, D. X. (2021). Artificial exosomes for translational nanomedicine. Journal of Nanobiotechnology 2021 19:1, 19(1), 1–20. https://doi.org/10.1186/S12951-021-00986-2

Lin, I., Wiles, L., Waller, R., Goucke, R., Nagree, Y., Gibberd, M., Straker, L., Maher, C. G., & O'Sullivan, P. P. B. (2020). What does best practice care for musculoskeletal pain look like? Eleven consistent recommendations from high-quality clinical practice guidelines: systematic review. British journal of sports medicine, 54(2), 79–86. https://doi.org/10.1136/bjsports-2018-099878

Lindner, U., Kramer, J., Rohwedel, J., & Schlenke, P. (2010). Mesenchymal Stem or Stromal Cells: Toward a Better Understanding of Their Biology? Transfusion Medicine and Hemotherapy : Offizielles Organ Der Deutschen Gesellschaft Fur Transfusionsmedizin Und Immunhamatologie, 37(2), 75–83. https://doi.org/10.1159/000290897

Liu, D., Cui, C., Chen, W., Shi, J., Li, B., & Chen, S. (2023a). Biodegradable Cements for Bone Regeneration. Journal of Functional Biomaterials, 14(3). https://doi.org/10.3390/JFB14030134

Liu, H., Wu, Y., Wang, F., Wang, S., Ji, N., Wang, M., Zhou, G., Han, R., Liu, X., Weng, W., Tan, H., Jing, Y., Zhang, W., Zhang, H., Shi, Z., & Su, J. (2023b). Bone-targeted engineered bacterial extracellular vesicles delivering miRNA to treat osteoporosis. Composites Part B: Engineering, 267, 111047. https://doi.org/10.1016/J.COMPOSITESB.2023.111047

Liu, J., Han, G., Pan, S., Ge, Y., Feng, H., & Shen, Z. (2015). Biomineralization stimulated peri-titanium implants prepared by selective laser melting. Journal of Materiomics, 1(3), 253–261. https://doi.org/10.1016/J.JMAT.2015.07.008

Liu, J., Yang, L., Liu, K., & Gao, F. (2023). Hydrogel scaffolds in bone regeneration: Their promising roles in angiogenesis. Frontiers in Pharmacology, 14, 1050954. https://doi.org/10.3389/FPHAR.2023.1050954/

Liu, L., Xiang, Y., Wang, Z., Yang, X., Yu, X., Lu, Y., Deng, L., & Cui, W. (2019). Adhesive liposomes loaded onto an injectable, self-healing and antibacterial hydrogel for promoting bone reconstruction. NPG Asia Materials 2019 11:1, 11(1), 1–18. https://doi.org/10.1038/s41427-019-0185-z

Liu, Y., Song, B., Wei, Y., Chen, F., Chi, Y., Fan, H., Liu, N., Li, Z., Han, Z., & Ma, F. (2018a). Exosomes from mesenchymal stromal cells enhance imatinib-induced apoptosis in human leukemia cells via activation of caspase signaling pathway. Cytotherapy, 20(2), 181–188. https://doi.org/10.1016/J.JCYT.2017.11.006

Liu, Y., Lin, L., Zou, R., Wen, C., Wang, Z., & Lin, F. (2018b). MSC-derived exosomes promote proliferation and inhibit apoptosis of chondrocytes via lncRNA-KLF3-AS1/miR-206/GIT1 axis in osteoarthritis. Cell Cycle (Georgetown, Tex.), 17(21–22), 2411–2422. https://doi.org/10.1080/15384101.2018.1526603

Liu, Z., Zhuang, Y., Fang, L., Yuan, C., Wang, X., & Lin, K. (2023). Breakthrough of extracellular vesicles in pathogenesis, diagnosis and treatment of osteoarthritis. Bioactive Materials, 22, 423–452. https://doi.org/10.1016/J.BIOACTMAT.2022.10.012

Loeser, R. F., Goldring, S. R., Scanzello, C. R., & Goldring, M. B. (2012). Osteoarthritis: a disease of the joint as an organ. Arthritis and Rheumatism, 64(6), 1697–1707. https://doi.org/10.1002/ART.34453

Logozzi, M., Di Raimo, R., Mizzoni, D., & Fais, S. (2020). Immunocapture-based ELISA to characterize and quantify exosomes in both cell culture supernatants and body fluids. Methods in Enzymology, 645, 155. https://doi.org/10.1016/BS.MIE.2020.06.011

Maguire, C. M., Rösslein, M., Wick, P., & Prina-Mello, A. (2018). Characterisation of particles in solution – a perspective on light scattering and comparative technologies. Science and Technology of Advanced Materials, 19(1), 732. https://doi.org/10.1080/14686996.2018.1517587

Makarczyk, M. J. (2023). Cell Therapy Approaches for Articular Cartilage Regeneration. Organogenesis, 19(1). https://doi.org/10.1080/15476278.2023.2278235

Man, K., Alcala, C., Mekhileri, N. V., Lim, K. S., Jiang, L. H., Woodfield, T. B. F., & Yang, X. B. (2022a). GelMA Hydrogel Reinforced with 3D Printed PEGT/PBT Scaffolds for Supporting Epigenetically-Activated Human Bone Marrow Stromal Cells for Bone Repair. Journal of Functional Biomaterials, 13(2). https://doi.org/10.3390/JFB13020041

Man, K., Barroso, I. A., Brunet, M. Y., Peacock, B., Federici, A. S., Hoey, D. A., & Cox, S. C. (2022b). Controlled Release of Epigenetically-Enhanced Extracellular Vesicles from a GelMA/Nanoclay Composite Hydrogel to Promote Bone Repair. International Journal of Molecular Sciences, 23(2). https://doi.org/10.3390/IJMS23020832

Man, K., Brunet, M. Y., Federici, A. S., Hoey, D. A., & Cox, S. C. (2022c). An ECM-Mimetic Hydrogel to Promote the Therapeutic Efficacy of Osteoblast-Derived Extracellular Vesicles for Bone Regeneration. Frontiers in Bioengineering and Biotechnology, 10, 829969. https://doi.org/10.3389/FBIOE.2022.829969/

Man, K., Brunet, M. Y., Fernandez-Rhodes, M., Williams, S., Heaney, L. M., Gethings, L. A., Federici, A., Davies, O. G., Hoey, D., & Cox, S. C. (2021a). Epigenetic reprogramming enhances the therapeutic efficacy of osteoblast-derived extracellular vesicles to promote human bone marrow stem cell osteogenic differentiation. Journal of Extracellular Vesicles, 10(9). https://doi.org/10.1002/JEV2.12118

Man, K., Brunet, M. Y., Jones, M. C., & Cox, S. C. (2020). Engineered Extracellular Vesicles: Tailored-Made Nanomaterials for Medical Applications. Nanomaterials, 10(9), 1–30. https://doi.org/10.3390/NANO10091838

Man, K., Brunet, M. Y., Louth, S., Robinson, T. E., Fernandez-Rhodes, M., Williams, S., Federici, A. S., Davies, O. G., Hoey, D. A., & Cox, S. C. (2021b). Development of a Bone-Mimetic 3D Printed Ti6Al4V Scaffold to Enhance Osteoblast-Derived Extracellular Vesicles' Therapeutic Efficacy for Bone Regeneration. Frontiers in Bioengineering and Biotechnology, 9, 757220. https://doi.org/10.3389/FBIOE.2021.757220/BIBTEX

Man, K., Lawlor, L., Jiang, L. H., & Yang, X. B. (2021c). The Selective Histone Deacetylase Inhibitor MI192 Enhances the Osteogenic Differentiation Efficacy of Human Dental Pulp Stromal Cells. International Journal of Molecular Sciences, 22(10). https://doi.org/10.3390/IJMS22105224

Man, K., Mekhileri, N. V., Lim, K. S., Jiang, L. H., Woodfield, T. B. F., & Yang, X. B. (2021d). MI192 induced epigenetic reprogramming enhances the therapeutic efficacy of human bone marrows stromal cells for bone regeneration. Bone, 153. https://doi.org/10.1016/J.BONE.2021.116138

Martinez-Lostao, L., García-Alvarez, F., Basáñez, G., Alegre-Aguarón, E., Desportes, P., Larrad, L., Naval, J., Martínez-Lorenzo, M. J., & Anel, A. (2010). Liposome-bound APO2L/TRAIL is an effective treatment in a rabbit model of rheumatoid arthritis. Arthritis and Rheumatism, 62(8), 2272–2282. https://doi.org/10.1002/ART.27501

Mathieu, M., Névo, N., Jouve, M., Valenzuela, J. I., Maurin, M., Verweij, F. J., Palmulli, R., Lankar, D., Dingli, F., Loew, D., Rubinstein, E., Boncompain, G., Perez, F., & Théry, C. (2021). Specificities of exosome versus small ectosome secretion revealed by live intracellular tracking of CD63 and CD9. Nature Communications 2021 12:1, 12(1), 1–18. https://doi.org/10.1038/s41467-021-24384-2

Meggiolaro, A., Moccia, V., Brun, P., Pierno, M., Mistura, G., Zappulli, V., & Ferraro, D. (2023). Microfluidic Strategies for Extracellular Vesicle Isolation: Towards Clinical Applications. Biosensors, 13(1). https://doi.org/10.3390/BIOS13010050

Mendt, M., Kamerkar, S., Sugimoto, H., McAndrews, K. M., Wu, C. C., Gagea, M., Yang, S., Blanko, E. V. R., Peng, Q., Ma, X., Marszalek, J. R., Maitra, A., Yee, C., Rezvani, K., Shpall, E., LeBleu, V. S., & Kalluri, R. (2018). Generation and testing of clinical-grade exosomes for pancreatic cancer. JCI Insight, 3(8), 99263. https://doi.org/10.1172/JCI.INSIGHT.99263

Midekessa, G., Godakumara, K., Ord, J., Viil, J., Lättekivi, F., Dissanayake, K., Kopanchuk, S., Rinken, A., Andronowska, A., Bhattacharjee, S., Rinken, T., & Fazeli, A. (2020). Zeta Potential of Extracellular Vesicles: Toward Understanding the Attributes that Determine Colloidal Stability. ACS omega, 5(27), 16701–16710. https://doi.org/10.1021/acsomega.0c01582

Minoia, A., Dalle Carbonare, L., Schwamborn, J. C., Bolognin, S., & Valenti, M. T. (2022). Bone Tissue and the Nervous System: What Do They Have in Common? Cells 2023, Vol. 12, Page 51, 12(1), 51. https://doi.org/10.3390/CELLS12010051

Mizukami, Y., Kawao, N., Takafuji, Y., Ohira, T., Okada, K., Jo, J. I., Tabata, Y., & Kaji, H. (2023). Matrix vesicles promote bone repair after a femoral bone defect in mice. PLOS ONE, 18(4). https://doi.org/10.1371/JOURNAL.PONE.0284258

Montanha, G. S., Rodrigues, E. S., Romeu, S. L. Z., de Almeida, E., Reis, A. R., Lavres, J., Jr, & Pereira de Carvalho, H. W. (2020). Zinc uptake from ZnSO4 (aq) and Zn-EDTA (aq) and its root-to-shoot transport in soybean plants (Glycine max) probed by time-resolved in vivo X-ray spectroscopy. Plant science : an international journal of experimental plant biology, 292, 110370. https://doi.org/10.1016/j.plantsci.2019.110370

Morrell, A. E., Brown, G. N., Robinson, S. T., Sattler, R. L., Baik, A. D., Zhen, G., Cao, X., Bonewald, L. F., Jin, W., Kam, L. C., & Guo, X. E. (2018). Mechanically induced Ca2+ oscillations in osteocytes release extracellular vesicles and enhance bone formation. Bone Research 2018 6:1, 6(1), 1–11. https://doi.org/10.1038/s41413-018-0007-x

Müller, W. E. G., Schröder, H. C., Tolba, E., Diehl-Seifert, B., & Wang, X. (2016). Mineralization of bone-related SaOS-2 cells under physiological hypoxic conditions. The FEBS Journal, 283(1), 74–87. https://doi.org/10.1111/FEBS.13552

Murphy, C., Withrow, J., Hunter, M., Liu, Y., Tang, Y. L., Fulzele, S., & Hamrick, M. W. (2018). Emerging role of extracellular vesicles in musculoskeletal diseases. Molecular Aspects of Medicine, 60, 123–128. https://doi.org/10.1016/J.MAM.2017.09.006

Mussunoor, S., & Murray, G. I. (2008). The role of annexins in tumour development and progression. The Journal of Pathology, 216(2), 131–140. https://doi.org/10.1002/PATH.2400

Nandi, S. K., Fielding, G., Banerjee, D., Bandyopadhyay, A., & Bose, S. (2018). 3D printed β-TCP bone tissue engineering scaffolds: Effects of chemistry on in vivo biological properties in a rabbit tibia model. Journal of Materials Research, 33(14), 1939. https://doi.org/10.1557/JMR.2018.233

Nasiry, D., & Khalatbary, A. R. (2023). Stem cell-derived extracellular vesicle-based therapy for nerve injury: A review of the molecular mechanisms. World Neurosurgery: X, 19, 100201. https://doi.org/10.1016/J.WNSX.2023.100201

Neupane, Y. R., Huang, C., Wang, X., Chng, W. H., Venkatesan, G., Zharkova, O., Wacker, M. G., Czarny, B., Storm, G., Wang, J. W., & Pastorin, G. (2021). Lyophilization Preserves the Intrinsic Cardioprotective Activity of Bioinspired Cell-Derived Nanovesicles. Pharmaceutics, 13(7), 1052. https://doi.org/10.3390/pharmaceutics13071052

O'Dwyer, J., Cullen, M., Fattah, S., Murphy, R., Stefanovic, S., Kovarova, L., Pravda, M., Velebny, V., Heise, A., Duffy, G. P., & Cryan, S. A. (2020). Development of a Sustained Release Nano-In-Gel Delivery System for the Chemotactic and Angiogenic Growth Factor Stromal-Derived Factor 1α. Pharmaceutics, 12(6), 513. https://doi.org/10.3390/pharmaceutics12060513

Ong, S. G., & Wu, J. C. (2015). Exosomes as Potential Alternatives to Stem Cell Therapy in Mediating Cardiac Regeneration. Circulation Research, 117(1), 7–9. https://doi.org/10.1161/CIRCRESAHA.115.306593

Otsuka, E., Yamaguchi, A., Hirose, S., & Hagiwara, H. (1999). Characterization of osteoblastic differentiation of stromal cell line ST2 that is induced by ascorbic acid. The American Journal of Physiology, 277(1). https://doi.org/10.1152/AJPCELL.1999.277.1.C132

Pang, L., Jin, H., Lu, Z., Xie, F., Shen, H., Li, X., Zhang, X., Jiang, X., Wu, L., Zhang, M., Zhang, T., Zhai, Y., Zhang, Y., Guan, H., Su, J., Li, M., & Gao, J. (2023). Treatment with Mesenchymal Stem Cell-Derived Nanovesicle-Containing Gelatin Methacryloyl Hydrogels Alleviates Osteoarthritis by Modulating Chondrogenesis and Macrophage Polarization. Advanced Healthcare Materials, 12(17). https://doi.org/10.1002/ADHM.202300315

Parisse, P., Rago, I., Ulloa Severino, L., Perissinotto, F., Ambrosetti, E., Paoletti, P., Ricci, M., Beltrami, A. P., Cesselli, D., & Casalis, L. (2017). Atomic force microscopy analysis of extracellular vesicles. European Biophysics Journal : EBJ, 46(8), 813–820. https://doi.org/10.1007/S00249-017-1252-4

Patel, S. R., Papadopoulos, N. E., Plager, C., Linke, K. A., Moseley, S. H., Spirindonidis, C. H., & Benjamin, R. (1996). Phase II study of paclitaxel in patients with previously treated osteosarcoma and its variants. Cancer, 78(4), 741–744. https://doi.org/10.1002/(SICI)1097-0142(19960815)78:4<741::AID-CNCR8>3.0.CO;2-H

Patel, N. J., Ashraf, A., & Chung, E. J. (2023). Extracellular Vesicles as Regulators of the Extracellular Matrix. Bioengineering, 10(2). https://doi.org/10.3390/BIOENGINEERING10020136

Perez, G. I., Bernard, M. P., Vocelle, D., Zarea, A. A., Saleh, N. A., Gagea, M. A., Schneider, D., Bauzon, M., Hermiston, T., & Kanada, M. (2023). Phosphatidylserine-Exposing Annexin A1-Positive Extracellular Vesicles: Potential Cancer Biomarkers. Vaccines, 11(3). https://doi.org/10.3390/VACCINES11030639/S1

Piffoux, M., Silva, A. K. A., Wilhelm, C., Gazeau, F., & Tareste, D. (2018). Modification of Extracellular Vesicles by Fusion with Liposomes for the Design of Personalized Biogenic Drug Delivery Systems. ACS Nano, 12(7), 6830–6842. https://doi.org/10.1021/acsnano.8b02053

Pitt, J. M., Kroemer, G., & Zitvogel, L. (2016). Extracellular vesicles: masters of intercellular communication and potential clinical interventions. The Journal of Clinical Investigation, 126(4), 1139. https://doi.org/10.1172/JCI87316

Pokhrel, R., Gerstman, B. S., Hutcheson, J. D., & Chapagain, P. P. (2018). In Silico Investigations of Calcium Phosphate Mineralization in Extracellular Vesicles. Journal of Physical Chemistry B, 122(14), 3782–3789. https://doi.org/10.1021/ACS.JPCB.8B00169/SUPPL_FILE/JP8B00169_SI_003.MPG

Pringle, J. K., Jeffery, A. J., Ruffell, A., Stimpson, I. G., Pirrie, D., Bergslien, E., Madden, C., Oliver, I., Wisniewski, K. D., Cassella, J. P., Lamont, N., Gormley, S., & Partridge, J. (2022). The use of portable XRF as a forensic geoscience non-destructive trace evidence tool for environmental and criminal investigations. Forensic Science International, 332, 111175. https://doi.org/10.1016/J.FORSCIINT.2022.111175

Quarto, R., & Giannoni, P. (2016). Bone Tissue Engineering: Past-Present-Future. Methods in Molecular Biology (Clifton, N.J.), 1416, 21–33. https://doi.org/10.1007/978-1-4939-3584-0_2

Rabinowits, G., Gerçel-Taylor, C., Day, J. M., Taylor, D. D., & Kloecker, G. H. (2009). Exosomal microRNA: a diagnostic marker for lung cancer. Clinical Lung Cancer, 10(1), 42–46. https://doi.org/10.3816/CLC.2009.N.006

Raposo, G., & Stoorvogel, W. (2013). Extracellular vesicles: exosomes, microvesicles, and friends. The Journal of Cell Biology, 200(4), 373–383. https://doi.org/10.1083/JCB.201211138

Ravi, S. P., Shamiya, Y., Chakraborty, A., Coyle, A., Zahid, A. A., Wang, J., Boutilier, M. S. H., Ho, E. A., & Paul, A. (2022). Controlling Differentiation of Adult Stem Cells Via Cell-Derived Nanoparticles: Implications in Bone Repair. ACS Applied Nano Materials, 5(12), 17468–17475. https://doi.org/10.1021/ACSANM.2C03657/SUPPL_FILE/AN2C03657_SI_001.PDF

Re, F., Borsani, E., Rezzani, R., Sartore, L., & Russo, D. (2023). Bone Regeneration Using Mesenchymal Stromal Cells and Biocompatible Scaffolds: A Concise Review of the Current Clinical Trials. Gels, 9(5). https://doi.org/10.3390/GELS9050389

Riau, A. K., Ong, H. S., Yam, G. H. F., & Mehta, J. S. (2019). Sustained Delivery System for Stem Cell-Derived Exosomes. Frontiers in Pharmacology, 10. https://doi.org/10.3389/FPHAR.2019.01368

Ridder, K., Keller, S., Dams, M., Rupp, A. K., Schlaudraff, J., Del Turco, D., Starmann, J., Macas, J., Karpova, D., Devraj, K., Depboylu, C., Landfried, B., Arnold, B., Plate, K. H., Höglinger, G., Sültmann, H., Altevogt, P., & Momma, S. (2014). Extracellular vesicle-mediated transfer of genetic information between the hematopoietic system and the brain in response to inflammation. PLoS Biology, 12(6). https://doi.org/10.1371/JOURNAL.PBIO.1001874

Riester, O., Borgolte, M., Csuk, R., & Deigner, H. P. (2021). Challenges in Bone Tissue Regeneration: Stem Cell Therapy, Biofunctionality and Antimicrobial Properties of Novel Materials and Its Evolution. International Journal of Molecular Sciences, 22(1), 1–25. https://doi.org/10.3390/IJMS22010192

Rizzo, F., & Kehr, N. S. (2021). Recent Advances in Injectable Hydrogels for Controlled and Local Drug Delivery. Advanced Healthcare Materials, 10(1). https://doi.org/10.1002/ADHM.202001341

Roefs, M. T., Sluijter, J. P. G., & Vader, P. (2020). Extracellular Vesicle-Associated Proteins in Tissue Repair. Trends in Cell Biology, 30(12), 990–1013. https://doi.org/10.1016/J.TCB.2020.09.009

Rohde, E., Pachler, K., & Gimona, M. (2019). Manufacturing and characterization of extracellular vesicles from umbilical cord-derived mesenchymal stromal cells for clinical testing. Cytotherapy, 21(6), 581–592. https://doi.org/10.1016/J.JCYT.2018.12.006

Rosso, G., & Cauda, V. (2023). Biomimicking Extracellular Vesicles with Fully Artificial Ones: A Rational Design of EV-BIOMIMETICS toward Effective Theranostic Tools in Nanomedicine. ACS Biomaterials Science and Engineering, 9(11), 5924–5932. https://doi.org/10.1021/ACSBIOMATERIALS.2C01025/ASSET/IMAGES/LARGE/AB2C01025_0002.JPEG

Sabokbar, A., Millett, P. J., Myer, B., & Rushton, N. (1994). A rapid, quantitative assay for measuring alkaline phosphatase activity in osteoblastic cells in vitro. Bone and Mineral, 27(1), 57–67. https://doi.org/10.1016/S0169-6009(08)80187-0

Sanchez, M. A., Felice, B., Sappia, L. D., Lima Moura, S., Martí, M., & Pividori, M. I. (2020). Osteoblastic exosomes. A non-destructive quantitative approach of alkaline phosphatase to assess osteoconductive nanomaterials. Materials Science and Engineering: C, 115, 110931. https://doi.org/10.1016/J.MSEC.2020.110931

Sarrigiannidis, S. O., Rey, J. M., Dobre, O., González-García, C., Dalby, M. J., & Salmeron-Sanchez, M. (2021). A tough act to follow: collagen hydrogel modifications to improve mechanical and growth factor loading capabilities. Materials Today Bio, 10, 100098. https://doi.org/10.1016/J.MTBIO.2021.100098

Sartori, M., Giavaresi, G., Parrilli, A., Ferrari, A., Aldini, N. N., Morra, M., Cassinelli, C., Bollati, D., & Fini, M. (2015). Collagen type I coating stimulates bone regeneration and osteointegration of titanium implants in the osteopenic rat. International orthopaedics, 39(10), 2041–2052. https://doi.org/10.1007/s00264-015-2926-0

Scalise, M., Pochini, L., Giangregorio, N., Tonazzi, A., & Indiveri, C. (2013). Proteoliposomes as Tool for Assaying Membrane Transporter Functions and Interactions with Xenobiotics. Pharmaceutics 2013, Vol. 5, Pages 472-497, 5(3), 472–497. https://doi.org/10.3390/PHARMACEUTICS5030472

Schindelin, J., Arganda-Carreras, I., Frise, E., Kaynig, V., Longair, M., Pietzsch, T., Preibisch, S., Rueden, C., Saalfeld, S., Schmid, B., Tinevez, J. Y., White, D. J., Hartenstein, V., Eliceiri, K., Tomancak, P., & Cardona, A. (2012). Fiji: an open-source platform for biological-image analysis. Nature Methods 2012 9:7, 9(7), 676–682. https://doi.org/10.1038/nmeth.2019

Schlesinger, P. H., Blair, H. C., Stolz, D. B., Riazanski, V., Ray, E. C., Tourkova, I. L., & Nelson, D. J. (2020). Landmark Review: Cellular and extracellular matrix of bone, with principles of synthesis and dependency of mineral deposition on cell membrane transport. American Journal of Physiology - Cell Physiology, 318(1), C111. https://doi.org/10.1152/AJPCELL.00120.2019

Schlundt, C., Saß, R. A., Bucher, C. H., Bartosch, S., Hauser, A. E., Volk, H. D., Duda, G. N., & Schmidt-Bleek, K. (2023). Complex Spatio-Temporal Interplay of Distinct Immune and Bone Cell Subsets during Bone Fracture Healing. Cells, 13(1), 40. https://doi.org/10.3390/cells13010040

Schoenmaker, L., Witzigmann, D., Kulkarni, J. A., Verbeke, R., Kersten, G., Jiskoot, W., & Crommelin, D. J. A. (2021). mRNA-lipid nanoparticle COVID-19 vaccines: Structure and stability. International Journal of Pharmaceutics, 601, 120586. https://doi.org/10.1016/J.IJPHARM.2021.120586

Schoger, E., Bleckwedel, F., Germena, G., Rocha, C., Tucholla, P., Sobitov, I., Möbius, W., Sitte, M., Lenz, C., Samak, M., Hinkel, R., Varga, Z. V., Giricz, Z., Salinas, G., Gross, J. C., & Zelarayán, L. C. (2023). Single-cell transcriptomics reveal extracellular vesicles secretion with a cardiomyocyte proteostasis signature during pathological remodeling. Communications Biology 2023 6:1, 6(1), 1–17. https://doi.org/10.1038/s42003-022-04402-9

Scott, H. L., Heberle, F. A., Katsaras, J., & Barrera, F. N. (2019). Phosphatidylserine Asymmetry Promotes the Membrane Insertion of a Transmembrane Helix. Biophysical journal, 116(8), 1495–1506. https://doi.org/10.1016/j.bpj.2019.03.003

Sekaran, S., Selvaraj, V., & Thangavelu, L. (2021). The Physiological and Pathological Role of Tissue Nonspecific Alkaline Phosphatase beyond Mineralization. Biomolecules, 11(11). https://doi.org/10.3390/BIOM11111564

Sharma, U., Pal, D., & Prasad, R. (2014). Alkaline Phosphatase: An Overview. Indian Journal of Clinical Biochemistry, 29(3), 269. https://doi.org/10.1007/S12291-013-0408-Y

Shen, N., Maggio, M., Woods, I., C. Lowry, M., Almasri, R., Gorgun, C., Eichholz, K. F., Stavenschi, E., Hokamp, K., Roche, F. M., O'Driscoll, L., & Hoey, D. A. (2023). Mechanically activated mesenchymal-derived bone cells drive vessel formation via an extracellular vesicle mediated mechanism. Journal of Tissue Engineering, 14, 1–16. https://doi.org/10.1177/20417314231186918

Silva, A. M., Lázaro-Ibáñez, E., Gunnarsson, A., Dhande, A., Daaboul, G., Peacock, B., Osteikoetxea, X., Salmond, N., Friis, K. P., Shatnyeva, O., & Dekker, N. (2021). Quantification of protein cargo loading into engineered extracellular vesicles at single-vesicle and single-molecule resolution. Journal of Extracellular Vesicles, 10(10). https://doi.org/10.1002/JEV2.12130

Simão, A. M. S., Bolean, M., Favarin, B. Z., Veschi, E. A., Tovani, C. B., Ramos, A. P., Bottini, M., Buchet, R., Millán, J. L., & Ciancaglini, P. (2019). Lipid microenvironment affects the ability of proteoliposomes harboring TNAP to induce mineralization without nucleators. Journal of bone and mineral metabolism, 37(4), 607–613. https://doi.org/10.1007/s00774-018-0962-8

Simão, A. M. S., Yadav, M. C., Narisawa, S., Bolean, M., Pizauro, J. M., Hoylaerts, M. F., Ciancaglini, P., & Luis Milla, J. (2010). Proteoliposomes harboring alkaline phosphatase and nucleotide pyrophosphatase as matrix vesicle biomimetics. Journal of Biological Chemistry, 285(10), 7598–7609. https://doi.org/10.1074/JBC.M109.079830/ATTACHMENT/D30A0A59-638F-42B5-89A9-B65E27902689/MMC1.PDF

Skelton, A. M., Cohen, D. J., Boyan, B. D., & Schwartz, Z. (2023). Osteoblast-Derived Matrix Vesicles Exhibit Exosomal Traits and a Unique Subset of microRNA: Their Caveolae-Dependent Endocytosis Results in Reduced Osteogenic Differentiation. International Journal of Molecular Sciences, 24(16). https://doi.org/10.3390/IJMS241612770

Skliar, M., & Chernyshev, V. S. (2019). Imaging of Extracellular Vesicles by Atomic Force Microscopy. Journal of Visualized Experiments : JoVE, 2019(151). https://doi.org/10.3791/59254

Skotland, T., Sagini, K., Sandvig, K., & Llorente, A. (2020). An emerging focus on lipids in extracellular vesicles. Advanced Drug Delivery Reviews, 159, 308–321. https://doi.org/10.1016/J.ADDR.2020.03.002

Soares, S., Sousa, J., Pais, A., & Vitorino, C. (2018). Nanomedicine: Principles, properties, and regulatory issues. Frontiers in Chemistry, 6(AUG), 360. https://doi.org/10.3389/FCHEM.2018.00360/BIBTEX

Sohn, H. S., & Oh, J. K. (2019). Review of bone graft and bone substitutes with an emphasis on fracture surgeries. Biomaterials Research, 23(1). https://doi.org/10.1186/S40824-019-0157-Y

Staehlke, S., Rebl, H., & Nebe, B. (2019). Phenotypic stability of the human MG-63 osteoblastic cell line at different passages. Cell Biology International, 43(1), 22–32. https://doi.org/10.1002/CBIN.11073

Staufer, O., Dietrich, F., Rimal, R., Schröter, M., Fabritz, S., Boehm, H., Singh, S., Möller, M., Platzman, I., & Spatz, J. P. (2021). Bottom-up assembly of biomedical relevant fully synthetic extracellular vesicles. Science Advances, 7(36). https://doi.org/10.1126/SCIADV.ABG6666/SUPPL_FILE/SCIADV.ABG6666_MOVIES_S1_AND_S2.ZIP

Stone, N. R., Bicanic, T., Salim, R., & Hope, W. (2016). Liposomal Amphotericin B (AmBisome®): A review of the pharmacokinetics, pharmacodynamics, clinical experience and future directions. Drugs, 76(4), 485. https://doi.org/10.1007/S40265-016-0538-7

Su, G., Zhang, D., Li, T., Pei, T., Yang, J., Tu, S., Liu, S., Ren, J., Zhang, Y., Duan, M., Yang, X., Shen, Y., Zhou, C., Xie, J., & Liu, X. (2023). Annexin A5 derived from matrix vesicles protects against osteoporotic bone loss via mineralization. Bone Research 2023 11:1, 11(1), 1–16. https://doi.org/10.1038/s41413-023-00290-9

Sun, Y., Saito, K., & Saito, Y. (2022). Lipidomic Analysis of Extracellular Vesicles Isolated from Human Plasma and Serum. Methods in Molecular Biology (Clifton, N.J.), 2504, 157–173. https://doi.org/10.1007/978-1-0716-2341-1_12

Szatanek, R., Baj-Krzyworzeka, M., Zimoch, J., Lekka, M., Siedlar, M., & Baran, J. (2017). The Methods of Choice for Extracellular Vesicles (EVs) Characterization. International Journal of Molecular Sciences, 18(6). https://doi.org/10.3390/IJMS18061153

Tamura, T., Yoshioka, Y., Sakamoto, S., Ichikawa, T., & Ochiya, T. (2020). Extracellular Vesicles in Bone Metastasis: Key Players in the Tumor Microenvironment and Promising Therapeutic Targets. International Journal of Molecular Sciences 2020, Vol. 21, Page 6680, 21(18), 6680. https://doi.org/10.3390/IJMS21186680

Tanaka, Y., Maruo, A., Fujii, K., Nomi, M., Nakamura, T., Eto, S., & Minami, Y. (2000). Intercellular adhesion molecule 1 discriminates functionally different populations of human osteoblasts: characteristic involvement of cell cycle regulators. Journal of Bone and Mineral Research : The Official Journal of the American Society for Bone and Mineral Research, 15(10), 1912–1923. https://doi.org/10.1359/JBMR.2000.15.10.1912

Tao, Y., Chen, Y., Wang, S., Chen, W., Zhou, D., Chen, D., Zhang, C., Wu, Z., Yan, J., Zhang, H., Wei, Y., & Su, J. (2022). Optimizing the modification density of acid oligopeptides to enhance the bone-targeting activity of liposomes. Composites Part B: Engineering, 247, 110288. https://doi.org/10.1016/J.COMPOSITESB.2022.110288

Thirabanjasak, D., Tantiwongse, K., & Thorner, P. S. (2010). Angiomyeloproliferative lesions following autologous stem cell therapy. Journal of the American Society of Nephrology : JASN, 21(7), 1218–1222. https://doi.org/10.1681/ASN.2009111156

Theobald, J., Smith, P. D., Jacob, S. M., & Moss, S. E. (1994). Expression of annexin VI in A431 carcinoma cells suppresses proliferation: a possible role for annexin VI in cell growth regulation. Biochimica et biophysica acta, 1223(3), 383–390. https://doi.org/10.1016/0167-4889(94)90099-x

Théry, C., Witwer, K. W., Aikawa, E., Alcaraz, M. J., Anderson, J. D., Andriantsitohaina, R., Antoniou, A., Arab, T., Archer, F., Atkin-Smith, G. K., Ayre, D. C., Bach, J. M., Bachurski, D., Baharvand, H., Balaj, L., Baldacchino, S., Bauer, N. N., Baxter, A. A., Bebawy, M., … Zuba-Surma, E. K. (2018). Minimal information for studies of extracellular vesicles 2018 (MISEV2018): a position statement of the International Society for Extracellular Vesicles and update of the MISEV2014 guidelines. Journal of Extracellular Vesicles, 7(1). https://doi.org/10.1080/20013078.2018.1535750

Tian, Y., Wu, D., Wu, D., Cui, Y., Ren, G., Wang, Y., Wang, J., & Peng, C. (2022). Chitosan-Based Biomaterial Scaffolds for the Repair of Infected Bone Defects. Frontiers in Bioengineering and Biotechnology, 10, 899760. https://doi.org/10.3389/FBIOE.2022.899760/BIBTEX

Tominaga, N., Kosaka, N., Ono, M., Katsuda, T., Yoshioka, Y., Tamura, K., Lötvall, J., Nakagama, H., & Ochiya, T. (2015). Brain metastatic cancer cells release microRNA-181c-containing extracellular vesicles capable of destructing blood–brain barrier. Nature Communications, 6. https://doi.org/10.1038/NCOMMS7716

Trenkenschuh, E., & Friess, W. (2021). Freeze-drying of nanoparticles: How to overcome colloidal instability by formulation and process optimization. European journal of pharmaceutics and biopharmaceutics : official journal of Arbeitsgemeinschaft fur Pharmazeutische Verfahrenstechnik e.V, 165, 345–360. https://doi.org/10.1016/j.ejpb.2021.05.024

Tu, K. N., Lie, J. D., Wan, C. K. V., Cameron, M., Austel, A. G., Nguyen, J. K., Van, K., & Hyun, D. (2018). Osteoporosis: A Review of Treatment Options. P & T : a peer-reviewed journal for formulary management, 43(2), 92–104.

Turner, N. J., Quijano, L. M., Hussey, G. S., Jiang, P., & Badylak, S. F. (2022). Matrix Bound Nanovesicles Have Tissue-Specific Characteristics That Suggest a Regulatory Role. Tissue Engineering. Part A, 28(21–22), 879–892. https://doi.org/10.1089/TEN.TEA.2022.0091

Turturici, G., Tinnirello, R., Sconzo, G., & Geraci, F. (2014). Extracellular membrane vesicles as a mechanism of cell-to-cell communication: Advantages and disadvantages. American Journal of Physiology - Cell Physiology, 306(7), 621–633. https://doi.org/10.1152/

Uenaka, M., Yamashita, E., Kikuta, J., Morimoto, A., Ao, T., Mizuno, H., Furuya, M., Hasegawa, T., Tsukazaki, H., Sudo, T., Nishikawa, K., Okuzaki, D., Motooka, D., Kosaka, N., Sugihara, F., Boettger, T., Braun, T., Ochiya, T., & Ishii, M. (2022). Osteoblast-derived vesicles induce a switch from bone-formation to bone-resorption in vivo. Nature Communications 2022 13:1, 13(1), 1–13. https://doi.org/10.1038/s41467-022-28673-2

Vermeulen, S., Knoops, K., Duimel, H., Parvizifard, M., van Beurden, D., López-Iglesias, C., Giselbrecht, S., Truckenmüller, R., Habibović, P., & Tahmasebi Birgani, Z. (2023). An in vitro model system based on calcium- and phosphate ion-induced hMSC spheroid mineralization. Materials Today Bio, 23, 100844. https://doi.org/10.1016/J.MTBIO.2023.100844

Veschi, V., Mangiapane, L. R., Nicotra, A., Di Franco, S., Scavo, E., Apuzzo, T., Sardina, D. S., Fiori, M., Benfante, A., Colorito, M. L., Cocorullo, G., Giuliante, F., Cipolla, C., Pistone, G., Bongiorno, M. R., Rizzo, A., Tate, C. M., Wu, X., Rowlinson, S., Stancato, L. F., … Stassi, G. (2020). Targeting chemoresistant colorectal cancer via systemic administration of a BMP7 variant. Oncogene, 39(5), 987–1003. https://doi.org/10.1038/s41388-019-1047-4

Veziroglu, E. M., & Mias, G. I. (2020). Characterizing Extracellular Vesicles and Their Diverse RNA Contents. Frontiers in Genetics, 11. https://doi.org/10.3389/FGENE.2020.00700

Vizoso, F. J., Eiro, N., Cid, S., Schneider, J., & Perez-Fernandez, R. (2017). Mesenchymal Stem Cell Secretome: Toward Cell-Free Therapeutic Strategies in Regenerative Medicine. International Journal of Molecular Sciences, 18(9). https://doi.org/10.3390/IJMS18091852

Wang, J., Huang, C. ., Neupane, Y. ., Wang, X., Zharkova, O., Chong, S. ., Lee, C. ., Wacker, M. ., Storm, G., & Pastorin, G. (2020). Bioinspired cell-derived nanovesicles protect the heart from ischemia reperfusion injury. European Heart Journal, 41(Supplement_2). https://doi.org/10.1093/EHJCI/EHAA946.3659

Wang, Y., Hu, X., Zhang, L., Zhu, C., Wang, J., Li, Y., Wang, Y., Wang, C., Zhang, Y., & Yuan, Q. (2019). Bioinspired extracellular vesicles embedded with black phosphorus for molecular recognition-guided biomineralization. Nature Communications, 10(1). https://doi.org/10.1038/S41467-019-10761-5

Wei, R., Zhao, L., Kong, G., Liu, X., Zhu, S., Zhang, S., & Min, L. (2020a). Combination of Size-Exclusion Chromatography and Ultracentrifugation Improves the Proteomic Profiling of Plasma-Derived Small Extracellular Vesicles. Biological Procedures Online, 22(1). https://doi.org/10.1186/S12575-020-00125-5

Wei, Y., Tang, C., Zhang, J., Li, Z., Zhang, X., Miron, R. J., & Zhang, Y. (2020b). Extracellular vesicles derived from the mid-to-late stage of osteoblast differentiation markedly enhance osteogenesis in vitro and in vivo. Biochemical and Biophysical Research Communications, 514(1), 252–258. https://doi.org/10.1016/J.BBRC.2019.04.029

Welsh, J. A., Goberdhan, D. C. I., O'Driscoll, L., Buzas, E. I., Blenkiron, C., Bussolati, B., Cai, H., Di Vizio, D., Driedonks, T. A. P., Erdbrügger, U., Falcon-Perez, J. M., Fu, Q. L., Hill, A. F., Lenassi, M., Lim, S. K., M˜y, G. M., Mohanty, S., Möller, A., Nieuwland, R., … Zubair, H. (2024). Minimal information for studies of extracellular vesicles (MISEV2023): From basic to advanced approaches. Journal of Extracellular Vesicles, 13(2). https://doi.org/10.1002/JEV2.12404

Wen, Y., Fu, Q., Soliwoda, A., Zhang, S., Zheng, M., Mao, W., & Wan, Y. (2022). Cell-derived nanovesicles prepared by membrane extrusion are good substitutes for natural extracellular vesicles. Extracellular vesicle, 1, 100004. https://doi.org/10.1016/j.vesic.2022.100004

Wendler, S., Schlundt, C., Bucher, C. H., Birkigt, J., Schipp, C. J., Volk, H. D., Duda, G. N., & Schmidt-Bleek, K. (2019). Immune modulation to enhance bone healing-a new concept to induce bone using prostacyclin to locally modulate immunity. Frontiers in Immunology, 10(APR), 440179. https://doi.org/10.3389/FIMMU.2019.00713/BIBTEX

Wiklander, O. P. B., Brennan, M., Lötvall, J., Breakefield, X. O., & Andaloussi, S. E. L. (2019). Advances in therapeutic applications of extracellular vesicles. Science Translational Medicine, 11(492), 8521. https://doi.org/10.1126/SCITRANSLMED.AAV8521/ASSET/C2FC48F8-B5D0-490F-A007-7C170E7AA561/ASSETS/GRAPHIC/AAV8521-F3.JPEG

Williams, J. K., Ngo, J. M., Lehman, I. M., & Schekman, R. (2023). Annexin A6 mediates calcium-dependent exosome secretion during plasma membrane repair. ELife, 12. https://doi.org/10.7554/ELIFE.86556

Wrobel, E., Leszczynska, J., & Brzoska, E. (2016). The Characteristics Of Human Bone-Derived Cells (HBDCS) during osteogenesis in vitro. Cellular and Molecular Biology Letters, 21(1), 1–15. https://doi.org/10.1186/S11658-016-0027-8/FIGURES/6

Wu, B., Chen, X., Wang, J., Qing, X., Wang, Z., Ding, X., Xie, Z., Niu, L., Guo, X., Cai, T., Guo, X., & Yang, F. (2020). Separation and characterization of extracellular vesicles from human plasma by asymmetrical flow field-flow fractionation. Analytica Chimica Acta, 1127, 234–245. https://doi.org/10.1016/J.ACA.2020.06.071

Wu, D., Qin, H., Wang, Z., Yu, M., Liu, Z., Peng, H., Liang, L., Zhang, C., & Wei, X. (2022). Bone Mesenchymal Stem Cell-Derived sEV-Encapsulated Thermosensitive Hydrogels Accelerate Osteogenesis and Angiogenesis by Release of Exosomal miR-21. Frontiers in bioengineering and biotechnology, 9, 829136. https://doi.org/10.3389/fbioe.2021.829136

Xu, H., Zhao, G., Zhang, Y., Jiang, H., Wang, W., Zhao, D., Hong, J., Yu, H., & Qi, L. (2019). Mesenchymal stem cell-derived exosomal microRNA-133b suppresses glioma progression via Wnt/β-catenin signaling pathway by targeting EZH2. Stem Cell Research & Therapy, 10(1). https://doi.org/10.1186/S13287-019-1446-Z

Yan, H. C., Yu, T. T., Li, J., Qiao, Y. Q., Wang, L. C., Zhang, T., Li, Q., Zhou, Y. H., & Liu, D. W. (2020). The Delivery of Extracellular Vesicles Loaded in Biomaterial Scaffolds for Bone Regeneration. Frontiers in Bioengineering and Biotechnology, 8, 559524. https://doi.org/10.3389/FBIOE.2020.01015/BIBTEX

Yáñez-Mó, M., Barreiro, O., Gordon-Alonso, M., Sala-Valdés, M., & Sánchez-Madrid, F. (2009). Tetraspanin-enriched microdomains: a functional unit in cell plasma membranes. Trends in Cell Biology, 19(9), 434–446. https://doi.org/10.1016/J.TCB.2009.06.004

Yang, J., Pei, T., Su, G., Duan, P., & Liu, X. (2023). AnnexinA6: a potential therapeutic target gene for extracellular matrix mineralization. Frontiers in Cell and Developmental Biology, 11, 1201200. https://doi.org/10.3389/FCELL.2023.1201200/BIBTEX

Yamamoto, K., Yuguchi, Y., Stokke, B. T., Sikorski, P., & Bassett, D. C. (2019). Local Structure of Ca2+ Alginate Hydrogels Gelled via Competitive Ligand Exchange and Measured by Small Angle X-Ray Scattering. Gels (Basel, Switzerland), 5(1), 3. https://doi.org/10.3390/gels5010003

Yuan, F., Li, Y. M., & Wang, Z. (2021). Preserving extracellular vesicles for biomedical applications: consideration of storage stability before and after isolation. Drug Delivery, 28(1), 1501–1509. https://doi.org/10.1080/10717544.2021.1951896

Zavatti, M., Beretti, F., Casciaro, F., Bertucci, E., & Maraldi, T. (2020). Comparison of the therapeutic effect of amniotic fluid stem cells and their exosomes on monoiodoacetate-induced animal model of osteoarthritis. BioFactors (Oxford, England), 46(1), 106–117. https://doi.org/10.1002/BIOF.1576

Zhang, L., Jiao, G., Ren, S., Zhang, X., Li, C., Wu, W., Wang, H., Liu, H., Zhou, H., & Chen, Y. (2020a). Exosomes from bone marrow mesenchymal stem cells enhance fracture healing through the promotion of osteogenesis and angiogenesis in a rat model of nonunion. Stem Cell Research and Therapy, 11(1), 1–15. https://doi.org/10.1186/S13287-020-1562-9/FIGURES/9

Zhang, M., & Zhao, X. (2020b). Alginate hydrogel dressings for advanced wound management. International Journal of Biological Macromolecules, 162, 1414–1428. https://doi.org/10.1016/J.IJBIOMAC.2020.07.311

Zhang, X., Zhao, Q., Zhou, N., Liu, Y., Qin, K., Buhl, E. M., Wang, X., Hildebrand, F., Balmayor, E. R., & Greven, J. (2023). Osteoblast derived extracellular vesicles induced by dexamethasone: A novel biomimetic tool for enhancing osteogenesis in vitro. Frontiers in Bioengineering and Biotechnology, 11, 349. https://doi.org/10.3389/FBIOE.2023.1160703/BIBTEX

Zhang, Y., Chopp, M., Meng, Y., Katakowski, M., Xin, H., Mahmood, A., & Xiong, Y. (2015). Effect of exosomes derived from multipluripotent mesenchymal stromal cells on functional recovery and neurovascular plasticity in rats after traumatic brain injury. Journal of Neurosurgery, 122(4), 856–867. https://doi.org/10.3171/2014.11.JNS14770

Zhang, Y., Wu, D., Zhao, X., Pakvasa, M., Tucker, A. B., Luo, H., Qin, K. H., Hu, D. A., Wang, E. J., Li, A. J., Zhang, M., Mao, Y., Sabharwal, M., He, F., Niu, C., Wang, H., Huang, L., Shi, D., Liu, Q., … El Dafrawy, M. (2020). Stem Cell-Friendly Scaffold Biomaterials: Applications for Bone Tissue Engineering and Regenerative Medicine. Frontiers in Bioengineering and Biotechnology, 8, 598607. https://doi.org/10.3389/FBIOE.2020.598607/BIBTEX

Zhao, R., Shen, Y., Deng, X., Tang, Y., Ge, Z., Wang, D., Xiong, Z., Fang, Q., Zhang, Z., Li, X., Du, X., Lin, W., Zhao, S., & Wang, G. (2023). From brain to bone: Harnessing extracellular vesicles released from TBI to enhance osteogenesis by 3D-Printed hydrogel scaffold. Composites Part B: Engineering, 264, 110909. https://doi.org/10.1016/J.COMPOSITESB.2023.110909

Zhou, B., Jiang, X., Zhou, X., Tan, W., Luo, H., Lei, S., & Yang, Y. (2023). GelMA-based bioactive hydrogel scaffolds with multiple bone defect repair functions: therapeutic strategies and recent advances. Biomaterials Research, 27(1), 1–49. https://doi.org/10.1186/S40824-023-00422-6/FIGURES/17

Zhu, L., Gangadaran, P., Kalimuthu, S., Oh, J. M., Baek, S. H., Jeong, S. Y., Lee, S. W., Lee, J., & Ahn, B. C. (2018). Novel alternatives to extracellular vesicle-based immunotherapy – exosome mimetics derived from natural killer cells. Https://Doi.Org/10.1080/21691401.2018.1489824, 46(sup3), S166–S179. https://doi.org/10.1080/21691401.2018.1489824